МИСИС
УНИВЕРСИТЕТ НАУКИ И ТЕХНОЛОГИЙ

СибГИУ
Сибирский государственный индустриальный университет

ISSN 0368-0797
eISSN 2410-2091

ИЗВЕСТИЯ ВЫСШИХ УЧЕБНЫХ ЗАВЕДЕНИЙ ЧЕРНАЯ МЕТАЛЛУРГИЯ

IZVESTIYA. FERROUS METALLURGY

fermet.misis.ru

2023 Том Vol. 66 № No. 4

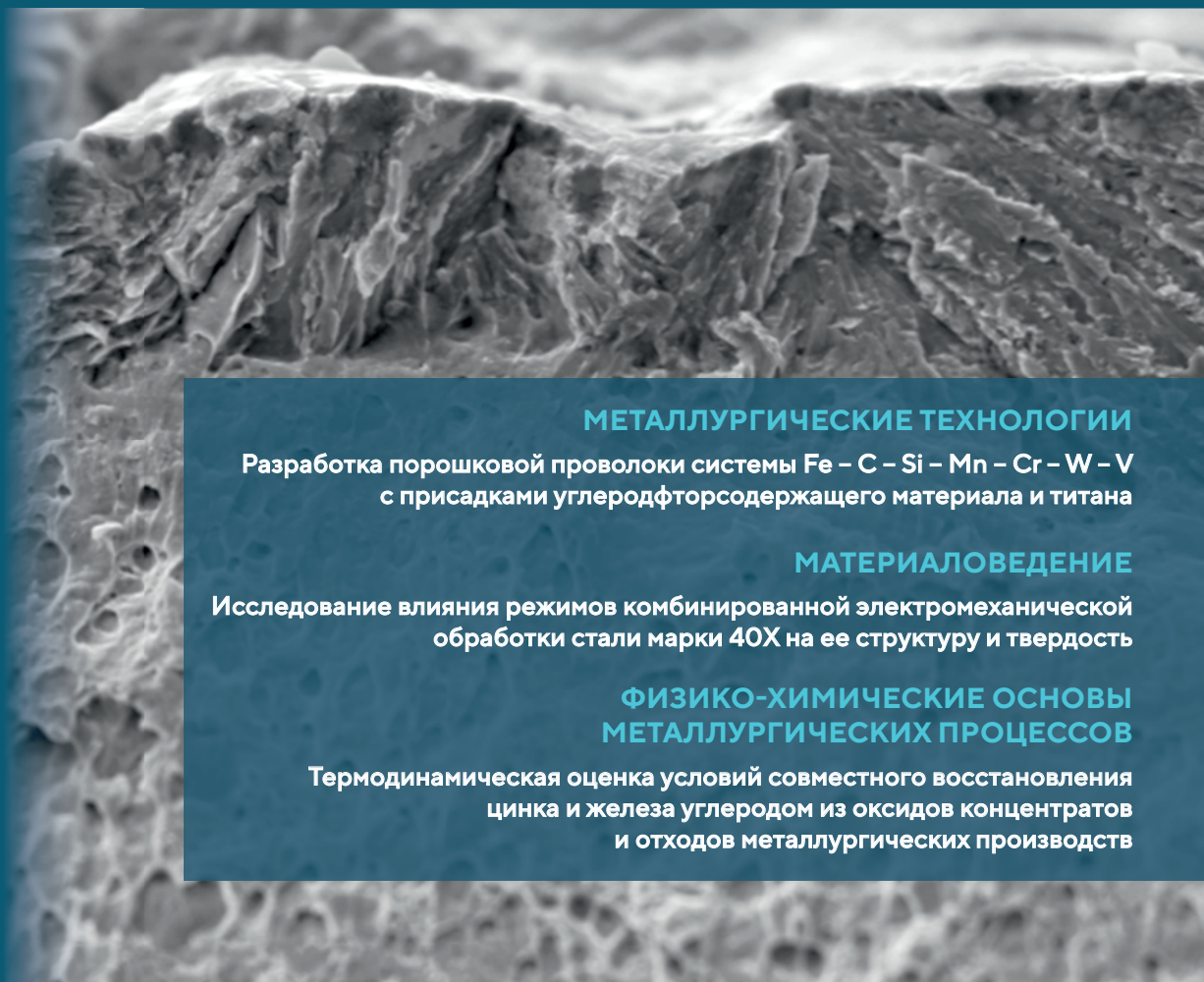

ISSN 0368-0797
eISSN 2410-2091

ИЗВЕСТИЯ ВЫСШИХ УЧЕБНЫХ ЗАВЕДЕНИЙ ЧЕРНАЯ МЕТАЛЛУРГИЯ

Научно-технический журнал

Издается с января 1958 г. Выпускается 6 раз в год

2023 Том Vol. 66 № No. 4

IZVESTIYA FERROUS METALLURGY

Scientific and Technical Journal

Published since January 1958. Issued 6 times a year

ИЗВЕСТИЯ ВЫСШИХ УЧЕБНЫХ ЗАВЕДЕНИЙ ЧЕРНАЯ МЕТАЛЛУРГИЯ

www.fermet.misis.ru

ISSN 0368-0797 *(Print)* ISSN 2410-2091 *(Online)*

Варианты названия:

Известия вузов. Черная металлургия

Izvestiya. Ferrous Metallurgy

Учредители:

МИСИС УНИВЕРСИТЕТ НАУКИ И ТЕХНОЛОГИЙ

СибГИУ Сибирский государственный индустриальный университет

Издатель:

Национальный исследовательский технологический университет «МИСИС»

Адреса подразделений редакций:

в Москве
Россия, 119049, Москва, Ленинский просп., д. 4, стр. 1
Национальный исследовательский технологический университет «МИСИС»
Тел.: +7 (495) 638-44-11 *E-mail*: ferrous@misis.ru

в Новокузнецке
Россия, 654007, Новокузнецк,
Кемеровская обл. – Кузбасс, ул. Кирова, зд. 42
Сибирский государственный индустриальный университет
Тел.: +7 (3843) 74-86-28 *E-mail:* redjizvz@sibsiu.ru

В соответствии п. 5 Правил формирования перечня ВАК журнал «Известия вузов. Черная металлургия» входит в перечень ведущих рецензируемых научных журналов и изданий, публикация в которых учитывается при защитах кандидатских и докторских диссертаций как индексируемый в МБД.

Индексирование: Scopus, Russian Science Citation Index (RSCI), Research Bible, Chemical Abstracts, OCLC и Google Scholar

Зарегистрирован Федеральной службой по надзору в сфере связи и массовых коммуникаций **ПИ № ФС77-35456**.

IZVESTIYA FERROUS METALLURGY

www.fermet.misis.ru

ISSN 0368-0797 *(Print)* ISSN 2410-2091 *(Online)*

Alternative title:

Izvestiya vuzov. Chernaya metallurgiya

Founders:

MISIS UNIVERSITY OF SCIENCE AND TECHNOLOGY

SibSIU Siberian State Industrial University

Publisher:

National University of Science and Technology "MISIS"

Editorial Office Address:

in Moscow
4 Leninskii Ave., Moscow 119049, Russian Federation
National University of Science and Technology "MISIS"
Tel.: +7 (495) 638-44-11
E-mail: fermet.misis@mail.ru, ferrous@misis.ru

in Novokuznetsk
42 Kirova Str., Novokuznetsk, Kemerovo Region – Kuzbass
654007, Russian Federation
Siberian State Industrial University
Tel.: +7 (3843) 74-86-28 *E-mail*: redjizvz@sibsiu.ru

In accordance with paragraph 5 of the Rules for the formation of the Higher Attestation Comission list journal "Izvestiya. Ferrous metallurgy" is included in the list of leading peer-reviewed scientific journals, publication in which is taken into account in the defense of candidate and doctoral dissertations, as indexed in internatonal data bases.

Indexed: Scopus, Russian Science Citation Index (RSCI), Research Bible, Chemical Abstracts, OCLC and Google Scholar

Registered in Federal Service for Supervision in the Sphere of Mass Communications **PI number FS77-35456**.

СОДЕРЖАНИЕ / CONTENTS

МЕТАЛЛУРГИЧЕСКИЕ ТЕХНОЛОГИИ

METALLURGICAL TECHNOLOGIES

МАТЕРИАЛОВЕДЕНИЕ

MATERIAL SCIENCE

ФИЗИКО-ХИМИЧЕСКИЕ ОСНОВЫ МЕТАЛЛУРГИЧЕСКИХ ПРОЦЕССОВ

PHYSICO-CHEMICAL BASICS OF METALLURGICAL PROCESSES

СОДЕРЖАНИЕ *(продолжение)*

ИННОВАЦИИ В МЕТАЛЛУРГИЧЕСКОМ ПРОМЫШЛЕННОМ И ЛАБОРАТОРНОМ ОБОРУДОВАНИИ, ТЕХНОЛОГИЯХ И МАТЕРИАЛАХ

ЭКОНОМИЧЕСКАЯ ЭФФЕКТИВНОСТЬ МЕТАЛЛУРГИЧЕСКОГО ПРОИЗВОДСТВА

CONTENTS *(Continuation)*

INNOVATIONS IN METALLURGICAL INDUSTRIAL AND LABORATORY EQUIPMENT, TECHNOLOGIES AND MATERIALS

ECONOMIC EFFICIENCY OF METALLURGICAL PRODUCTION

Metallurgical technologies / Металлургические технологии

UDC 669.162.263
DOI 10.17073/0368-0797-2023-4-394-402

Original article
Оригинальная статья

Reduction of specific coke consumption in blast furnace by impact on thermal reverse zone

A. S. Kharchenko[1], M. I. Sibagatullina[1], E. O. Kharchenko[1], I. V. Makarova[1], S. K. Sibagatullina[1], V. A. Beginyuk[2]

[1] **Nosov Magnitogorsk State Technical University** (38 Lenina Ave., Magnitogorsk, Chelyabinsk Region 455000, Russian Federation)
[2] **PJSC "Magnitogorsk Metallurgical Plant"** (93 Kirova Str., Magnitogorsk, Chelyabinsk Region 455000, Russian Federation)

as.mgtu@mail.ru

Abstract. At the blast furnace of PJSC "Magnitogorsk Metallurgical Plant" (MMK), the specific consumption of coke was reduced by impact on thermal reverse zone (TRZ) by increasing the consumption of natural gas above 120 m^3/t of cast iron under conditions of increased reactivity and reduced hot strength of coke. In the first pair of periods, an increase in CRI from 38.4 to 39.3 % with a decrease in CSR from 36.3 to 34.6 % was accompanied by an increase in the ratio of natural gas consumption and total oxygen entering the furnace from 0.43 to 0.45 by increasing the specific gas consumption from 123.2 to 133.5 m^3/t of cast iron. The set of actions increased the TRZ length towards the blast-furnace mouth by 1.9 % with its unchanged location along the lower part. Reducing the heat consumption in the TRZ increased the temperature difference between gas and materials there by an average of 36 °C. In the second pair of periods, the consumption of natural gas was 143.9 m^3/t of cast iron with a decrease in the oxygen content in the blast from 27.6 to 27.0. They were accompanied by the following changes in the processes under consideration: an increase in the length of the TRZ towards the blast-furnace mouth by 2.6 % and the distance from the tuyere hearth by 3.4 %, an increase in the degree of carbon reduction from 32.0 to 33.3 %, an insignificant (on average 0.3 °C) increase in the temperature difference of gas and materials in the TRZ. In the first pair of periods, reduction in the coke specific consumption was 4.7 kg/t of cast iron with an increase in furnace productivity by 27 t/day. Conditions and course of the processes of the second pair ensured a decrease in the coke specific consumption by 1.6 kg/ton of cast iron and led to a decrease in cast iron production by 41 t/day.

Keywords: blast furnace smelting, coke, cast iron, natural gas, heat transfer

Acknowledgements: The article was supported by a grant of the President of the Russian Federation No. MD-1064.2022.4.

For citation: Kharchenko A.S., Sibagatullina M.I., Kharchenko E.O., Makarova I.V., Sibagatullin S.K., Beginyuk V.A. Reduction of specific coke consumption in blast furnace by impact on thermal reverse zone. *Izvestiya. Ferrous Metallurgy*. 2023;66(4):394–402.
https://doi.org/10.17073/0368-0797-2023-4-394-402

Снижение удельного расхода кокса в доменной печи воздействием на зону замедленного теплообмена

А. С. Харченко[1], М. И. Сибагатуллина[1], Е. О. Харченко[1], И. В. Макарова[1], С. К. Сибагатуллин[1], В. А. Бегинюк[2]

[1] **Магнитогорский государственный технический университет им. Г.И. Носова** (Россия, 455000, Челябинская обл., Магнитогорск, пр. Ленина, 38)
[2] **ПАО «Магнитогорский металлургический комбинат»** (Россия, 455000, Челябинская обл., Магнитогорск, ул. Кирова, 93)

as.mgtu@mail.ru

Аннотация. На доменной печи ПАО «Магнитогорский металлургический комбинат» удельный расход кокса снижали воздействием на зону замедленного теплообмена (ЗЗТ), увеличивая потребление природного газа выше 120 м^3/т чугуна в условиях повышенной реакционной способности и пониженной горячей прочности кокса. В первой паре периодов рост CRI от 38,4 до 39,3 % с уменьшением CSR от 36,3 до 34,6 % осуществили одновременно с увеличением отношения расходов природного газа и всего поступающего в печь кислорода от 0,43 до 0,45 путем повышения удельного расхода газа от 123,2 до 133,5 м^3/т чугуна. Применение комплекса действий увеличило протяженность зоны замедленного теплообмена в сторону колошника на 1,9 % при неизменном ее расположении по нижней части. Уменьшение потребления тепла в ЗЗТ увеличило разность температур газа и материалов в среднем на 36 °С. Во второй паре периодов

потребление природного газа довели до 143,9 м^3/т чугуна при снижении содержания кислорода в дутье с 27,6 до 27,0. Это сопровождалось следующими изменениями рассматриваемых процессов: увеличением протяженности ЗЗТ в сторону колошника на 2,6 % и отдаленности от фурменного очага на 3,4 %; повышением степени восстановления углеродом с 32,0 до 33,3 %; незначительным (в среднем 0,3 °С) ростом разности температур газа и материалов в зоне ЗЗТ. В первой паре периодов уменьшение удельного расхода кокса составило 4,7 кг/т чугуна с повышением производительности печи на 27 т/сут. Условия и ход процессов второй пары обеспечили уменьшение удельного расхода кокса на 1,6 кг/т чугуна и привели к снижению производства чугуна на 41 т/сут.

Ключевые слова: доменная плавка, кокс, чугун, природный газ, теплообмен

Благодарности: Работа выполнена при поддержке гранта Президента Российской Федерации № МД-1064.2022.4.

Для цитирования: Харченко А.С., Сибагатуллина М.И., Харченко Е.О., Макарова И.В., Сибагатуллин С.К., Бегинюк В.А. Снижение удельного расхода кокса в доменной печи воздействием на зону замедленного теплообмена. *Известия вузов. Черная металлургия*. 2023;66(4): 394–402. https://doi.org/10.17073/0368-0797-2023-4-394-402

Introduction

The question of determining the rational parameters for combined blast during blast furnace smelting, in alignment with the developmental goals of ferrous metallurgy, remains pertinent [1 – 4]. The simultaneous utilization of reducing additives in the form of natural gas and pulverized coal fuel, with the ratio of their flow rates to that of the process oxygen ranging from 0.9 to 1.2, has contributed to the stabilization of theoretical combustion temperature and other process parameters. The degrees of direct and indirect reduction are notable factors in these processes [5]. Upon analyzing the operation of blast furnaces at PJSC "Magnitogorsk Metallurgical Plant" (MMK), the significant role of the reactivity index and coke strength after the reaction was further confirmed [6]. In the context of blast furnaces in Japan, it becomes imperative to estimate the initial gasification temperature of carbonaceous materials as the thermal reverse zone (TRZ) takes shape. The study presented in reference [7] delves into the injection of hydrogen as a reducing agent, replacing carbon, with the aim of mitigating CO_2 oxide emissions. Simultaneously, this approach enhances the efficiency of reduction through CO gaseous oxide. The experiment demonstrated that the reduction of CO_2 oxide emissions from the blast furnace is achieved within a hydrogen concentration range of up to 20 %.

The papers [8 – 11] underscore the vital role of mathematical models due to the scarcity of information on process parameters such as temperature, pressure, and reduction levels along height of the furnace. The processes that arise and evolve within the TRZ, leading to a substantial increase in iron reduction, are pivotal elements within these evolving mathematical models. These models are currently in development and implementation. The kinetic modeling, encompassing an evaluation of the thermal reverse zone's impact on blast furnace operations, is congruent with this perspective [7]. An investigation was conducted to assess the influence of material temperature upon charging into the furnace, their reductibility, and gas pressure at the furnace's mouth on the outcomes of blast furnace smelting. The findings revealed that as gases become more actively utilized within the furnace, the temperature at the onset of the thermal reverse zone decreases [9]. The paper [12] has illustrated that the specific consumption of coke diminishes with an increase in the duration of time the charged materials spend within the TRZ. A noteworthy reduction of 3.6 kg/t of cast iron was achieved [13] by mitigating heat outflow from the region where $W_{ch}/W_g \geq 1$ to the area where $W_{ch}/W_g < 1$, with W_{ch} and W_g representing the heat capacities of charge and gas flows, respectively. In the thermal reverse stage ($W_{ch} \approx W_g$), the temperature registered a decline of 2.5 °C, while the temperature differential between the gas and the charge contracted by 1.3 °C.

An evaluation of rational approaches concerning blast furnaces at MMK has unveiled the substantial significance of coke reactivity index and post-reaction strength in relation to the adjustment of natural gas consumption [6]. This complements prior explorations of these phenomena [14 – 19]. Theoretical and experimental investigations have contributed to the recognition of the importance of temperature boundaries distinguishing between indirect, mixed, and direct reduction regions [14]. The values characterizing these boundaries exhibit interrelationships with the rates of oxide reduction by gases such as CO and H_2, as well as the rates of carbon gasification by gaseous reduction products, CO_2 and H_2O [16].

In laboratory experiments, where the charge was maintained under identical temperature and time conditions as those in the upper section of the blast furnace shaft, a comparison was conducted between charcoal and coke concerning their influence on the degree of sinter reduction by a gas mixture comprising 29 % CO, 2 % H_2 and 60 % N_2 [16]. The results obtained were as follows:

Temperature, °C	600	700	750	800	850	900
Heating time, min	37	72	107	132	150	165
Reduction degree by oxygen removal, %:						
when using charcoal	2	8	17	24	32	67
when using coke	1.5	6	15	20	22	25

Based to these data, at temperatures corresponding to intense heat exchange in the upper section of the furnace (up to 750 °C), the reduction degree exhibited only a marginal increase, with fuel reactivity nearly unchanged. Simultaneously, the flue gas composition contained approximately 10.4 – 10.8 % CO_2. At temperatures corresponding

to the initiation and progression of the thermal reverse zone (above 750 °C), a portion of CO_2 oxide engaged in interactions with carbon from the fuel, leading to the formation of CO oxide. The formation of CO oxide by charcoal, a fuel with a higher reactivity index, contributed more significantly to the enhancement of sinter reduction compared to its formation by coke. This effect assumed considerable importance in the optimization of the blast furnace process as natural gas consumption increased [18].

Experiments that involved the examination of coke samples extracted from the pilot blast furnace unveiled four different reactivity pathways. The outcome of these pathways includes the potential reduction of coke-specific consumption and the augmentation of blast intensity. Furthermore, the ability of coke carbon to react with CO_2 oxide was also observed to increase [20 – 22]. In practical applications, these findings can be implemented by incorporating machine vision systems for both the upper and lower sections of the blast furnace [23 – 29]. Additionally, they align with concepts associated with the electronic theory of iron reduction from oxides [30; 31].

Materials and methods

Using the insights gathered from the works [1 – 31], we successfully reduced coke-specific consumption within a blast furnace with a production capacity of 1370 m^3. This reduction was achieved by strategically manipulating the thermal reverse zone, primarily through an increase in natural gas-specific consumption, while concurrently adjusting the coke reactivity index (CRI) and coke strength after reaction (CSR) in opposite direction. The most important operational characteristics of the furnace are depicted in Fig. 1 – 4.

The vertical pressure behavior (active weight P_a) of materials along both the height and the cross-section of the furnace is presented in Fig. 1 and 2.

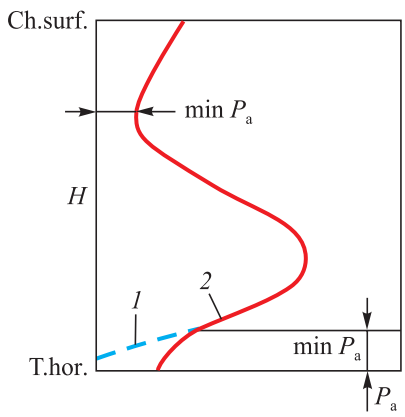

Fig. 1. Vertical pressure of materials from charge surface (Ch. surf.) along the furnace height (H) to tuyeres' horizon (T.hor.):
1 – over loose part of tuyere hearth; *2* – on average in the furnace

Рис. 1. Вертикальное давление материалов от поверхности шихты (Ch. surf.) по высоте печи (H) до горизонта фурм (T.hor.):
1 – над рыхлой частью фурменного очага; *2* – в среднем по печи

Average temperature trends along the height of the blast furnace are depicted in Fig. 3, while those concerning temperature distribution by radius are illustrated in Fig. 4 and 5. These figures are constructed based on the findings and insights from the referenced papers [14; 17; 22].

When temperatures fall below the range of 850 – 900 °C, it is observed that the heat capacity of the gas flow surpasses that of the charge flow ($W_g > W_{ch}$), while the W_{ch}/W_g ratio

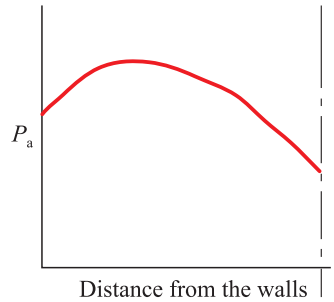

Fig. 2. Vertical pressure of materials from lining to the blast furnace axis

Рис. 2. Вертикальное давление материалов от футеровки до оси доменной печи

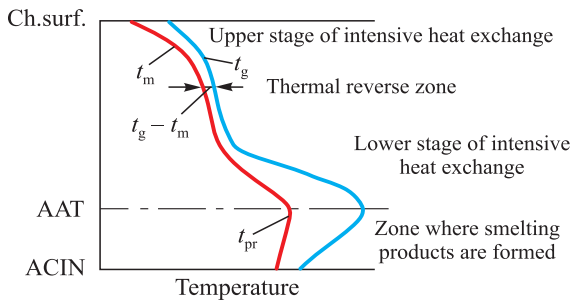

Fig. 3. Scheme of temperature changes of materials (t_m) and gases (t_g) along the blast furnace height:
AAT – axis of the air tuyeres; ACIN – axis of the cast iron notch;
t_{pr} – temperature of the smelting products

Рис. 3. Схема изменения температур материалов (t_m) и газов (t_g) по высоте доменной печи:
AAT – ось воздушных фурм; ACIN – ось чугунных леток;
t_{pr} – температура продуктов плавки

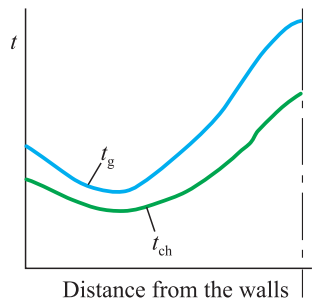

Fig. 4. Diagram of changes in temperatures of the charge (t_{ch}) and gases (t_g) from walls to axis of the blast furnace

Рис. 4. Схема изменения температур шихты (t_{ch}) и газов (t_g) от стен до оси доменной печи

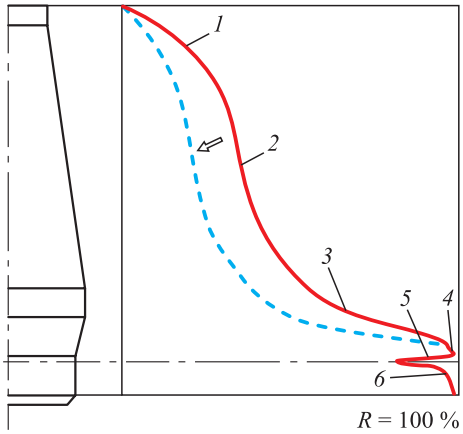

Fig. 5. Nature of changes in reduction degree along the blast furnace height

Рис. 5. Характер изменения степени восстановления по высоте доменной печи

remains within the range of 0.7 – 0.9. This surplus heat in the upper heat exchange phase, not absorbed by the charge, finds application in low-temperature processes without necessitating an increase in the quantity of coke introduced into the furnace. Notably, no additional coke is required for moisture evaporation.

Fig. 5 illustrates the portion of oxygen from all oxides extracted from the charged materials by various reducing agents. In the figure: *1* – accelerated reduction occurring in the upper part of the blast furnace, which is attributed to the low stability of the chemical bond of Fe_2O_3 and Fe_3O_4; *2* – reduction taking place in the conditions of the thermal reverse zone, which are highly conducive to reactions $FeO + CO = Fe + CO_2$ and $FeO + H_2 = Fe + H_2O$, with each unit of temperature change significantly influencing the reduction process; *3* – accelerated reduction due to the intensity of its direct progression ($FeO + C = Fe + CO$); *4* – slower reduction occurring as the process reaches its conclusion, with only a few unreduced oxides remaining; *5* – a decrease in the reduction degree due to the oxidation of smelting products in tuyere hearths; *6* – rapid reduction of elements, mainly iron, previously oxidized in tuyere hearths. The solid line in the figure corresponds to modern blast furnace smelting conditions, while the dashed line signifies potential advancements in blast furnace smelting technology.

Results and discussion

At the blast furnace of MMK, the reduction in coke-specific consumption was achieved by elevating the utilization of hydrogen and augmenting the degree of iron reduction from FeO oxide. This was accomplished by influencing the thermal reverse zone, leading to an increase in natural gas consumption exceeding 120 m^3/t of cast iron. The study focused on two paired periods: *I* and *II* (the first pair) and *III* and *IV* (the second pair). The periods within each pair were contiguous, primarily spanning seven days each.

During period *I* of the first pair, under the initial conditions, the natural gas flow rate stood at 123.2 m^3/t of cast iron. When the blast contained 27.2 % of oxygen, the ratio of gas and oxygen consumption equated to 0.43 (Table 1). In the second pair (base period *III*), these values increased to 135.8 m^3/t of cast iron; 27.6 % oxygen and a ratio of 0.47, respectively.

In both pairs of periods, several key parameters experienced growth, including the mass of the gas-air mixture per tuyere, its kinetic energy of efflux, and the extent of the loose portion of the tuyere hearth. Notably, these parameters exhibited more pronounced changes in the first pair of periods.

The coke strength after reaction CSR under the baseline conditions of the first pair of periods amounted to 36.3 %, with a reactive index (CRI) of 38.4 %. During the renewed smelting mode, CRI increased by 0.9 % to reach 39.3 %. In the basic conditions of the second pair, CSR was 39.5 %, and CRI was 39.1 %, with a variation reducing CRI to 37.8 % (Table 2).

In period *II*, as compared to period *I*, CSR decreased from 36.3 to 34.6 %, and CRI increased from 38.4 to 39.3 %. This change resulted in an increase in the ratio of natural gas consumption to the total oxygen entering the furnace, rising from 0.43 to 0.45. The gas-specific consumption also increased from 123.2 to 133.5 m^3/t of cast iron. Additionally, the oxygen content in the blast increased from 27.2 to 28.4 %. These alterations facilitated an increase in hydrogen reduction from 31.9 to 37.2 % (Table 3) and an enhancement in its utilization, from 45.3 to 48.8 %. Meanwhile, the length of the TRZ increased towards the blast furnace mouth by 1.9 %, while its position at the bottom remained unchanged. A significant reduction in carbon reduction, from 30.7 to 24.4 %, led to a decrease in heat consumption within the TRZ, resulting in an average temperature difference $t_g - t_{ch}$ (Fig. 3) increasing by 36 °C.

In period *IV*, in comparison to period *III*, the main factors pertaining to smelting conditions underwent the following changes:

– an increase in natural gas consumption from 135.8 to 143.9 m^3/t of cast iron;

– a decrease in the oxygen content in the blast from 27.6 to 27.0 %;

– an increase in the ratio of natural gas consumption to the total oxygen entering the furnace from 0.47 to 0.51;

– a decrease in CRI from 39.1 to 37.8 %;

– an increase in CSR from 39.5 to 40.2 %.

As a result, several changes in the studied processes during period *IV*, compared to period *III*, were observed:

– an increase in the length of the TRZ towards the blast-furnace mouth by 2.6 % and the distance from the tuyere hearth by 3.4 %;

– an increase in the degree of carbon reduction from 32.0 to 33.3 %;

Table 1

Parameters of the blast and blast-furnace gas

Таблица 1. **Параметры дутья и колошникового газа**

Indicator	Indicator value in the period			
	I	*II*	*III*	*IV*
Consumption of:				
blast, m^3/t of cast iron	1044	1056	1053	1087
natural gas, m^3/t of cast iron	123.2	133.5	135.8	143.9
Hot blast pressure, kPa	271	272	269	272
Blast temperature, °C	1155	1152	1154	1154
Water vapor flow rate, g/m^3	3.13	3.72	2.21	1.99
Oxygen content, %	27.2	28.4	27.6	27.0
Ratio of natural gas consumption to total oxygen consumption	0.43	0.45	0.47	0.51
Degree of utilization, %:				
CO	42.6	42.5	42.8	42.0
H_2	45.3	48.8	43.5	44.3
Gas temperature in gas vents, °C	235	246	217	233
Blast-furnace gas pressure (exc.), kPa	141.8	142.2	141.9	142.0
Actual stock line, м	1.73	1.87	1.69	1.65
Gas temperature along the radius, °C:				
at the periphery (T_{per})	247	263	233	264
in the "ore ridge" (T_r)	213	234	196	218
in the center of the furnace (T_c)	384	370	390	410
Dynamic gas head on the empty section of the furnace under operating conditions in terms of temperature and pressure, n/m^2:				
in the blast furnace mouth	2.05	2.26	2.12	2.25
in the belly	0.98	1.04	1.05	1.08
in the top part of the hearth	1.30	1.45	1.39	1.42

Table 2

Quality indicators of the charge materials

Таблица 2. **Показатели качества шихтовых материалов**

Indicator	Indicator value in the period			
	I	*II*	*III*	*IV*
Content of 0 – 5 mm fraction in sinter, %	8.47	9.34	8.35	8.23
Ash content in coke, %	12.57	12.64	12.52	12.58
Coke basis strength, %:				
M10	8.13	8.11	8.06	7.83
M25	87.62	87.82	87.47	87.67
Coke strength after reaction CSR, %	36.3	34.6	39.5	40.2
Coke reactivity index CRI, %	38.4	39.3	39.1	37.8

– a slight, albeit insignificant, increase in the temperature difference $t_g - t_{ch}$ (Fig. 3), averaging only 0.3 °C.

The key thermal performance characteristics accompanying these alterations are detailed in Table 4.

In terms of the recorded parameters, the temperature in the axial zone of the blast-furnace mouth decreased by 14 °C in period *II* when compared to period *I*, and conversely, it increased by 20 °C in period *IV* when compared to period *III* (Table 1).

The series of modifications within the processes, encompassing the ratios T_{per}/T_g, T_{per}/T_c, T_c/T_g, resulted in a reduction in coke-specific consumption in period *II*

Table 3

Reduction distribution indicators

Таблица 3. **Показатели распределения восстановления**

Indicator	Indicator value in the period			
	I	*II*	*III*	*IV*
Ratio of utilization rates H_2 and CO	1.06	1.15	1.02	1.05
Degree of Fe reduction from FeO by different reducing agents, %:				
carbon	30.7	24.4	32.0	33.3
carbonic oxide CO	37.4	38.4	34.6	30.8
hydrogen	31.9	37.2	33.4	35.9

Table 4

Heat consumption indicators

Таблица 4. **Показатели потребления тепла**

Indicator	Indicator value in the period			
	I	*II*	*III*	*IV*
Ratio of heat capacities of charge and gas flows:				
in the upper stage of intensive heat exchange	0.756	0.742	0.777	0.757
in the lower stage of intensive heat exchange	1.763	1.763	1.715	1.656
Total heat consumption for all processes in the zone determining coke consumption (Q_Σ), MJ/t of cast iron	2663	2759	2650	2643

Table 5

Main technological indicators of the furnace

Таблица 5. **Основные технологические показатели работы печи**

Indicator	Indicator value in the period			
	I	*II*	*III*	*IV*
Duration of the period, days	7	6	7	7
Specific consumption of dry coke, kg/t of cast iron	434.9	430.2	437.5	435.9
Ratio of specific consumption of solid (C_{SCP}) and gaseous (NG_{SP}) fuels, kg/m^3	3.53	3.15	3.22	3.06
Capacity, t/day	3467	3490	3512	3471
Consumption, kg/t of cast iron:				
raw materials	1694	1681	1678	1665
including				
quartzite	2.4	34.8	0	44.2
manganese ore	23.7	18.1	23.9	13.0
Share of pellets from IORM, %	34.1	31.1	37.7	39.6
Ore load, t/t	3.895	3.889	3.835	3.782
Fe content in the charge, %	57.32	57.77	57.86	58.32

compared to period *I* from 434.9 to 430.2 kg/t of cast iron, while in period *IV*, in comparison to period *III*, from 437.5 to 435.9 kg/t of cast iron (Table 5). During the first pair of periods, furnace productivity increased by 27 t/day; however, the conditions and progression of the processes during the second pair led to a decrease in cast iron production by 41 t/day (Table 5).

The shift of the coke carbon gasification process in period *II*, in comparison to period *I*, led to a 6.9 % reduction in the factor of charge and its product's resistance to gas movement in the lower part of the bosh (Fig. 1, the region of minimal P_a value). This shift also facilitated smelting with an 11.5 % increase in lift force of the gas flow (Table 1). The shift of the coke carbon gasification region in

period *IV* compared to period *III* to the region of lower temperatures led to a decrease in the coke specific consumption and the processes rate, resulting in decline of the furnace output (Table 5).

Conclusions

The parameters, such as length, height location, temperature, and the temperature difference between rising gases and descending materials within the blast furnace's TRZ, exert significant influence on coke-specific consumption. The formation of the TRZ is contingent on various factors, including the coke reactivity index (CRI), coke strength before reaction (CSR), natural gas consumption, and process oxygen consumption.

At the blast furnace of MMK, a series of smelting operations were conducted, categorized into two pairs of periods: the first pair serving as the base period and the second as the experimental period.

The first pair of periods witnessed an increase in natural gas consumption, rising from 123.2 to 133.5 m^3/t of cast iron. The length of the TRZ extended towards the blast furnace mouth by 1.9 %, maintaining its position at the bottom unchanged. Simultaneously, the temperature gradient between the gas and materials surged by 36 °C. Conversely, in the second pair of periods, natural gas consumption increased from 135.8 to 143.9 m^3/t of cast iron. The TRZ expanded towards the blast furnace mouth by 2.6 %, and the distance from the tuyere hearth extended by 3.4 %. However, the temperature difference between the gas and materials within the TRZ registered a negligible increase, averaging just 0.3 °C.

In the first pair of periods, a reduction in coke-specific consumption by 4.7 kg/t of cast iron was achieved, resulting in a notable increase in furnace productivity by 27 t/day. However, in the second pair, coke-specific consumption decreased by 1.6 kg/t of cast iron, leading to a decrease in cast iron production by 41 t/day.

References / Список литературы

1. Grigorovich K.V. Metallurgy of the 21st century: Challenges and tasks of modernizing the industry in the Russian Federation. In: *Physico-Chemical Bases of Metallurgical Processes (FHOMP 2022). Proceedings of the Int. Sci. Conf. named after Academician A.M. Samarin*. Vyksa: Publ. house of JSC "Vyksa Metallurgical Plant"; 2022:37–44. (In Russ.).

   Григорович К.В. Металлургия XXI века: вызовы и задачи модернизации отрасли в РФ. В кн.: *Физико-химические основы металлургических процессов (ФХОМП 2022). Сборник трудов международной научной конференции имени академика А.М. Самарина*. Выкса: Изд-во АО «Выксунский металлургический завод»; 2022:37–44.
2. Elanskii D.G. Carbon-free ferrous metallurgy – paths and their cost. In: *Proceedings of the XVI Int. Congress of Steelmakers and Metal Producers*. Yekaterinburg; 2021:51–56. (In Russ.).

   Еланский Д.Г. Безуглеродная черная металлургия – пути и их стоимость. В кн.: *Сборник трудов. XVI Международный конгресс сталеплавильщиков и производителей металлов*. Екатеринбург; 2021:51–56.
3. Nedelin S.V. Prospects for development of ferrous metallurgy taking into account environmental restrictions. In: *Proceedings of the XVI Int. Congress of Steelmakers and Metal Producers*. Yekaterinburg; 2021:38–44. (In Russ.).

   Неделин С.В. Перспективы развития черной металлургии с учетом экологических ограничений. В кн.: *Сборник трудов. XVI Международный конгресс сталеплавильщиков и производителей металлов*. Екатеринбург; 2021:38–44.
4. Torokhov G.V., Travyanov A.Ya., Golubev O.V., Chernousov P.I. Modern state and prospects for iron metallurgy. In: *Proceedings of the XVI Int. Congress of Steelmakers and Metal Producers*. Yekaterinburg; 2021:26–37. (In Russ.).

   Торохов Г.В., Травянов А.Я., Голубев О.В., Черноусов П.И. Современное состояние и перспективы металлургии железа. В кн.: *Сборник трудов. XVI Международный конгресс сталеплавильщиков и производителей металлов*. Екатеринбург; 2021:26–37.
5. Chernousov P.I., Seregin S.N., Grishin R.E., Chikalova A.N. Investigation of blast-furnace process with multi-component blast. *Chernye metally*. 2021;(12):4–10. (In Russ.).

   Черноусов П.И., Серегин С.Н., Гришин Р.Е., Чикалова А.Н. Исследование доменного процесса с применением многокомпонентного дутья. *Черные металлы*. 2021;(12):4–10.
6. Kharchenko A.S., Sibagatullin S.K., Pavlov A.V., Polinov A.A. Rational technological solutions for production of cast iron in blast furnaces of PJSC MMK. *Chernye metally*. 2021;(12):10–15. (In Russ.).

   Харченко А.С., Сибагатуллин С.К., Павлов А.В., Полинов А.А. Рациональные технологические решения при производстве чугуна в доменных печах ПАО «ММК». *Черные металлы*. 2021;(12):10–15.
7. Yokoyava Hirokazu, Kasai Eiki, Naitou Masaaki. Reduction of CO_2 emissions from blast furnace applying reactive coke agglomerate and hydrogen reduction. *Tetsu-to-Hagane*. 2022;108(6):335–342.
   https://doi.org/10.2355/tetsutohagane.TETSU-2021-118
8. Dmitriev A.N., Vit'kina G.Yu., Alektorov R.V., Zolotykh M.O., Vyaznikova E.A. Proposals for the use of information technologies in improving blast-furnace process. In: *Int. Forum. Dialogue of Metallurgists: Forecast for the Development of the industry until 2030. Price and Technology Solutions. April 21-22.* Moscow; 2022:11–14. (In Russ.).

   Дмитриев А.Н., Витькина Г.Ю., Алекторов Р.В., Золотых М.О., Вязникова Е.А. Предложения по использованию информационных технологий при совершенствовании доменного процесса. В кн.: *Международный форум. Диалог металлургов: Прогноз развития отрасли до 2030 года. Ценовые и технологические решения. 21-22 апреля*. Москва; 2022:11–14.
9. Dmitriev A.N., Vitkina G.Yu, Chesnokov Yu.A. Mathematical modeling and practical tasks solution of blast furnace smelting and adjacent repartitions. *Proceeding of Shechtman International Symposium*. 2016;3:369–376.
10. Dmitriev A.N., Chesnokov Yu.A., Chen K., Ivanov O.Yu., Zolotykh M.O. Monitoring the wear of the refractory lining

in the blast-furnace hearth. *Steel in Translation*. 2013;43(11): 732–739. https://doi.org/10.3103/S0967091213110041

11. Dmitriev A.N., Chesnokov Yu.A., Chen K., Ivanov O.Yu., Zolotykh M.O. New monitoring system of firebrick lining deterioration of blast furnace devil in metallurgical plants of China. *Advanced Materials Research*. 2013; 834-836:939–943. https://doi.org/10.4028/www.scientific.net/AMR.834-836.939

12. Stefanovich M.A., Baertuev A.A., Sibagatullin S.K. Role of optimization of blast-furnace domain process with combined blast. In: *Problems of Automated Management of Blast-Furnace Production*. Kiev: Institut avtomatiki; 1973;3:31–32. (In Russ.).

Стефанович М.А., Баертуев А.А., Сибагатуллин С.К. Роль оптимизации доменного процесса при применении комбинированного дутья. В кн.: *Проблемы автоматизированного управления доменным производством*. Киев: Институт автоматики; 1973;3:31–32.

13. Sibagatullin S.K., Kharchenko A.S., Minikaev S.R., Iglikova U.Zh., Polinov A.A., Gushchin D.N. Study of influence of iron-magnesia ore addition to sinter charge on blast furnace heat indices. *Ferrous Metallurgy. Bulletin of Scientific, Technical and Economic Information*. 2020;76(9):910–920. (In Russ.).

Сибагатуллин С.К., Харченко А.С., Миникаев С.Р., Игликова У.Ж., Полинов А.А., Гущин Д.Н. Исследование влияния ввода железомагнезиальной руды в агломерационную шихту на показатели доменной плавки. *Черная металлургия. Бюллетень научно-технической и экономической информации*. 2020;76(9):910–920.

14. Gurin I., Spirin N., Lavrov V. Automated information system for control and diagnostics of the blast furnace slag mode. *Lecture Notes in Electrical Engineering*. 2022;857:256–264. https://doi.org/10.1007/978-3-030-94202-1_25

15. Spirin N.A., Lavrov V.V., Rybolovlev V.Yu., Shnaider D.A., Krasnobaev A.V., Gurin I.A. Digital transformation of pyrometallurgical technologies: State, scientific problems and prospects of development. *Izvestiya. Ferrous Metallurgy*. 2021;64(8):588–598. https://doi.org/10.17073/0368-0797-2021-8-588-598

Спирин Н.А., Лавров В.В., Рыболовлев В.Ю., Шнайдер Д.А., Краснобаев А.В., Гурин И.А. Цифровая трансформация пирометаллургических технологий: состояние, научные проблемы и перспективы развития. *Известия вузов. Черная Металлургия*. 2021;64(8):588–598. https://doi.org/10.17073/0368-0797-2021-8-588-598

16. Gol'dshtein N.L., Zlatoustovskii D.M., Zvereva N.N., etc. Reactivity of coke in a blast furnace. *Stal'*. 1975;(11):977–981. (In Russ.).

Гольдштейн Н.Л., Златоустовский Д.М., Зверева Н.Н. и др. Реакционная способность кокса в доменной печи. *Сталь*. 1975;(11):977–981.

17. Babarykin N.N. *Theory and Technology of Blast-Furnace Process*. Magnitogorsk: MSTU; 2009:257. (In Russ.).

Бабарыкин Н.Н. *Теория и технология доменного процесса: Учебное пособие*. Магнитогорск: ГОУ ВПО «МГТУ»; 2009:257.

18. Sibagatullin S.K., Kharchenko A.S., Selivanov V.N., Beginyuk V.A., Chernov V.P. Improving the blast furnace process by raising the natural gas flow rate in the upper heat exchnage stage. *Vestnik of Nosov Magnitogorsk State Technical University*. 2017;15(1):37–44. (In Russ.). https://doi.org/10.18503/1995-2732-2017-15-1-37-44

Сибагатуллин С.К., Харченко А.С., Селиванов В.Н., Бегинюк В.А., Чернов В.П. Совершенствование хода доменного процесса повышением расхода природного газа по газодинамике в верхней ступени теплообмена. *Вестник Магнитогорского государственного технического университета им. Г.И. Носова*. 2017;15(1):37–44. https://doi.org/10.18503/1995-2732-2017-15-1-37-44

19. Dmitriev A.N., Spirin N.A. Use of modern information technologies to analyze and control the blast-furnace process. *Ferrous Metallurgy. Bulletin of Scientific, Technical and Economic Information*. 2014;1(1369):21–25. (In Russ.).

Дмитриев А.Н., Спирин Н.А. Использование современных информационных технологий для анализа и контроля доменного процесса. *Черная металлургия. Бюллетень научно-технической и экономической информации*. 2014;1(1369):21–25.

20. Abas R.A., Jakobson A., Hayashi M., etc. Studies on graphitisation of blast coke by X-ray diffraction analysis and thermal diffusivity measurements. *Steel Research International*. 2006;77(11):763–769. https://doi.org/10.1002/srin.200606460

21. Natsui T., Sunahara K., Ujisawa Y. Effects of gasification and smelting reductionon coke. *Tetsu-to-Hagane*. 2008;92(12):841–848. https://doi.org/10.2355/tetsutohagane1955.92.12_841

22. Mousa E., Senk D., Babich A. Reduction of pellets-nut coke mixture under simulating blast furnace conditions. *Steel Research International*. 2010;81(9):706–715. https://doi.org/10.1002/srin.201000047

23. Spirin N., Onorin O., Istomin A. Prediction of blast furnace thermal state in real-time operation. *Solid State Phenomena*. 2020;299:518–523. https://doi.org/10.4028/www.scientific.net/SSP.299.518

24. Spirin N.A., Rybolovlev V.Yu., Lavrov V.V., Shnaider D.A., Krasnobaev A.V., Onorin O.P. Improving metallurgical information systems: blast-furnace applications. *Steel in Translation*. 2019;49(2):118–122. https://doi.org/10.3103/S0967091219020141

25. Pavlov A.V., Polinov A.A., Spirin N.A., Onorin O.P., Lavrov V.V., Gurin I.A. Decision-making support in blast-furnace operation. *Steel in Translation*. 2019;49(3):185–193. https://doi.org/10.3103/S0967091219030082

26. Teng Z., Cheng S., Du P., Guo X. Mathematical model of burden distribution for the bell-less top of a blast furnace. *International Journal of Minerals, Metallurgy, and Materials*. 2013;20(7):620–626.

27. Jiménez J., Mochón J., Sainz de Ayala J. Mathematical model of gas flow distribution in a scale model of a blast furnace shaft. *ISIJ International*. 2004;44(3): 518–526. https://doi.org/10.2355/isijinternational.44.518

28. Sibagatullin S.K., Kharchenko A.S., Logachev G.N. The rational mode of nut coke charging into the blast furnace by compact trough-type charging device. *International Journal of Advanced Manufacturing Technology*. 2016;86:531–537. https://doi.org/10.1007/s00170-015-8184-x

29. Kharchenko A.S., Sibagatullin S.K., Kolosov A.V. Neuronetwork modeling application for study of gas dynamics mode at down part of blast furnace, working with uniformly sized coke. *Izvestiya. Ferrous Metallurgy*. 2011;54(11):23–26. (In Russ.).

Харченко А.С., Сибагатуллин С.К., Колосов А.В. Использование нейросетевого моделирования для изучения газодинамического режима в нижней части доменной печи в условиях ее работы с коксовым орешком. *Известия вузов. Черная металлургия*. 2011;54(11):23–26.

30. Roshchin V.E., Gamov P.A., Roshchin A.V., Salikhov S.P. Electron theory of metals reduction: Theory and methods of metals extraction from various types of ore. *Izvestiya. Ferrous Metallurgy*. 2019;62(5):407–417. (In Russ.). https://doi.org/10.17073/0368-0797-2019-5-407-417

Рощин В.Е., Гамов П.А., Рощин А.В., Салихов С.П. Электронная теория восстановления: следствия для теории и практики извлечения металлов из руд. *Известия вузов. Черная металлургия*. 2019;62(5):407–417. https://doi.org/10.17073/0368-0797-2019-5-407-417

31. Smirnov K.I., Gamov P.A., Roshchin V.E. Distribution of solid-phase reduction of iron in a layer of ilmenite concentrate. *Izvestiya. Ferrous Metallurgy*. 2020;63(2):116–121. (In Russ.). https://doi.org/10.17073/0368-0797-2020-2-116-121

Смирнов К.И., Гамов П.А., Рощин В.Е. Распространение твердофазного восстановления железа в слое ильменитового концентрата. *Известия вузов. Черная металлургия*. 2020;63(2):116–121. https://doi.org/10.17073/0368-0797-2020-2-116-121

Information about the Authors

***Aleksandr S. Kharchenko**, Dr. Sci. (Eng.), Assist. Prof., Head of the Chair of Metallurgy and Chemical Technologies,* Nosov Magnitogorsk State Technical University
ORCID: 0000-0002-0454-6399
E-mail: as.mgtu@mail.ru

***Margarita I. Sibagatullina**, Postgraduate of the Chair of Metallurgy and Chemical Technologies,* Nosov Magnitogorsk State Technical University
E-mail: margarita-sibaga@mail.ru

***Elena O. Kharchenko**, Cand. Sci. (Eng.), Assistant of the Chair of Metallurgy and Chemical Technologies,* Nosov Magnitogorsk State Technical University
E-mail: eo.mgtu@mail.ru

***Irina V. Makarova**, Cand. Sci. (Eng.), Prof. of the Chair of Metallurgy and Chemical Technologies,* Nosov Magnitogorsk State Technical University
E-mail: m.irina1976@mail.ru

***Salavat K. Sibagatullin**, Dr. Sci. (Eng.), Prof. of the Chair of Metallurgy and Chemical Technologies,* Nosov Magnitogorsk State Technical University
E-mail: 10tks@mail.ru

***Vitalii A. Beginyuk**, Leading Specialist of the Technological Group of the Blast Furnace Shop,* PJSC "Magnitogorsk Metallurgical Plant"
E-mail: beginyuk.va@mmk.ru

Сведения об авторах

***Александр Сергеевич Харченко**, д.т.н., доцент, заведующий кафедрой металлургии и химических технологий,* Магнитогорский государственный технический университет им. Г.И. Носова
ORCID: 0000-0002-0454-6399
E-mail: as.mgtu@mail.ru

***Маргарита Ильдаровна Сибагатуллина**, аспирант кафедры металлургии и химических технологий,* Магнитогорский государственный технический университет им. Г.И. Носова
E-mail: margarita-sibaga@mail.ru

***Елена Олеговна Харченко**, к.т.н., ассистент кафедры металлургии и химических технологий,* Магнитогорский государственный технический университет им. Г.И. Носова
E-mail: eo.mgtu@mail.ru

***Ирина Владимировна Макарова**, к.т.н., доцент кафедры металлургии и химических технологий,* Магнитогорский государственный технический университет им. Г.И. Носова
E-mail: m.irina1976@mail.ru

***Салават Камилович Сибагатуллин**, д.т.н., профессор кафедры металлургии и химических технологий,* Магнитогорский государственный технический университет им. Г.И. Носова
E-mail: 10tks@mail.ru

***Виталий Александрович Бегинюк**, ведущий специалист технологической группы доменного цеха,* ПАО «Магнитогорский металлургический комбинат»
E-mail: beginyuk.va@mmk.ru

Contribution of the Authors

A. S. Kharchenko – setting the task, preparing experiments, analysis of the research results, formulation of conclusions.
M. I. Sibagatullina – conducting experiments, analyzing data, participating in analysis of the research results, performing calculations.

E. O. Kharchenko – processing of production data, analysis of the research results.
I. V. Makarova – processing of production data, analysis of the research results.
S. K. Sibagatullin – organization of the research, conducting calculations, establishing the interconnections of blast-furnace process course, analysis of the research results.
V. A. Beginyuk – conducting the research on blast furnaces of PJSC ММК

Вклад авторов

А. С. Харченко – постановка задачи, подготовка экспериментов, анализ результатов исследований, формулировка выводов.
М. И. Сибагатуллина – проведение экспериментов, анализ данных, участие в анализе результатов исследований, выполнение расчетов.
Е. О. Харченко – обработка производственных данных, анализ результатов.
И. В. Макарова – обработка производственных данных, анализ результатов.
С. К. Сибагатуллин – организация комплекса исследований, выполнение расчетов, установление взаимосвязей хода доменного процесса, анализ результатов.
В. А Бегинюк – проведение исследований на доменных печах ПАО «ММК».

Received 27.01.2023
Revised 02.03.2023
Accepted 03.03.2023

Поступила в редакцию 27.01.2023
После доработки 02.03.2023
Принята к публикации 03.03.2023

Metallurgical technologies / Металлургические технологии

UDC 621.762.04:624.567.1:669
DOI 10.17073/0368-0797-2023-4-403-409

Original article
Оригинальная статья

Development of flux-cored wire of Fe – C – Si – Mn – Cr – W – V system with additives of carbon-fluorine-containing material and titanium

A. A. Usol'tsev [1], **N. A. Kozyrev** [2], **L. P. Bashchenko** [1], **R. E. Kryukov** [1], **A. V. Zhukov** [1]

[1] **Siberian State Industrial University** (42 Kirova Str., Novokuznetsk, Kemerovo Region – Kuzbass 654007, Russian Federation)
[2] **I.P. Bardin Central Research Institute of Ferrous Metallurgy** (23/9 Radio Str., Moscow 105005, Russian Federation)

n.kozyrev@chermet.net

Abstract. The paper considers research of quality of the electric arc coating obtained using flux-cored wire of the Fe–C–Si–Mn–Cr–W–V system with additives of carbon-fluorine-containing material and titanium. The formation of an electric arc coating was carried out using an automatic arc welding machine ASAW-1250 with a new chromium-containing flux-cored wire on plates made of St3 steel. To exclude mixing of the deposited metal with the substrate steel, multilayer surfacing was conducted. The surfacing mode was calculated and refined experimentally. The authors studied the composition and properties of the surface of the electric arc coating after surfacing. As a substitute for amorphous carbon they used a carbon-fluorine-containing material (dust of gas purification of aluminum production). Surfacing was carried out under a flux made from slag produced by silicomanganese with a high content of sulfur. A regression analysis of influence of the deposited layer's chemical composition on its hardness and wear rate was carried out and mathematical models of the investigated performance characteristics of the electric arc coating were obtained. With an increase in the content of chromium, tungsten, carbon and silicon, hardness of the deposited metal and its resistance to abrasive wear increase. The results of the conducted research make it possible to develop measures ensuring the required level of performance characteristics of the electric arc coating and can be used to make a forecast of hardness of the deposited layer and its wear resistance when the chemical composition of the metal changes, to predict the operational resistance of rolling rolls deposited with wires of the PP-Np-35V9Kh3SF type. Mathematical models of hardness of the deposited layer and its wear resistance help to clarify the mechanism of hardening and formation of protective properties of the surface layers of rolling rolls by means of electric arc coatings deposited with flux-cored wires.

Keywords: flux-cored wire, electric arc coating, multilayer surfacing, rolling rolls, hardness, wear rate

For citation: Usol'tsev A.A., Kozyrev N.A., Bashchenko L.P., Kryukov R.E., Zhukov A.V. Development of flux-cored wire of Fe – C – Si – Mn – Cr – W – V system with additives of carbon-fluorine-containing material and titanium. *Izvestiya. Ferrous Metallurgy*. 2023;66(4):403–409. https://doi.org/10.17073/0368-0797-2023-4-403-409

Разработка порошковой проволоки системы Fe – C – Si – Mn – Cr – W – V с присадками углеродфторсодержащего материала и титана

А. А. Усольцев [1], **Н. А. Козырев** [2], **Л. П. Бащенко** [1], **Р. Е. Крюков** [1], **А. В. Жуков** [1]

[1] **Сибирский государственный индустриальный университет** (Россия, 654007, Кемеровская обл. – Кузбасс, Новокузнецк, ул. Кирова, 42)
[2] **Центральный научно-исследовательский институт черной металлургии им. И.П. Бардина** (Россия, 105005, Москва, ул. Радио, 23/9)

n.kozyrev@chermet.net

Аннотация. В работе исследуется качество электродугового покрытия, полученного с использованием порошковой проволоки системы Fe–C–Si–Mn–Cr–W–V с присадками углеродфторсодержащего материала и титана. Формирование электродугового покрытия осуществляется с помощью аппарата для автоматической дуговой сварки ASAW-1250 с применением новой хромсодержащей порошковой проволоки на пластины из стали марки Ст3. Для исключения перемешивания наплавляемого металла со сталью подложки проводят

многослойную наплавку. Режим наплавки рассчитывается и уточняется экспериментальным путем. Авторы исследовали состав и свойства поверхности электродугового покрытия после наплавки. В качестве заменителя аморфного углерода используется углеродфторсодержащий материал (пыль газоочистки алюминиевого производства). Наплавку осуществляли под флюсом, изготовленным из шлака производства силикомарганца с повышенным содержанием серы. Проведенный регрессионный анализ показывает влияние химического состава наплавленного слоя на его твердость и скорость износа. В работе получены математические модели исследуемых эксплуатационных характеристик электродугового покрытия. При увеличении содержания хрома, вольфрама, углерода и кремния повышаются твердость наплавленного металла и устойчивость его к абразивному износу. Результаты проведенных исследований позволяют выработать мероприятия для обеспечения требуемого уровня эксплуатационных характеристик электродугового покрытия и могут использоваться для составления прогноза твердости наплавленного слоя и его износостойкости при изменении химического состава металла, прогнозировать эксплуатационную стойкость прокатных валков, наплавленных проволоками типа ПП-Нп-35В9Х3СФ. Математические модели твердости наплавленного слоя и его износостойкости позволяют уточнить механизм упрочнения и формирования защитных свойств поверхностных слоев прокатных валков посредством электродуговых покрытий, наплавленных порошковыми проволоками.

Ключевые слова: порошковая проволока, электродуговое покрытие, многослойная наплавка, прокатные валки, твердость, скорость износа

Для цитирования: Усольцев А.А., Козырев Н.А., Бащенко Л.П., Крюков Р.Е., Жуков А.В. Разработка порошковой проволоки системы Fe – C – Si – Mn – Cr – W – V с присадками углеродфторсодержащего материала и титана. *Известия вузов. Черная металлургия*. 2023;66(4):403–409. https://doi.org/10.17073/0368-0797-2023-4-403-409

Introduction

Rolling rolls constitute the primary technological tool in the steel mill rolling process. During their operation, amidst the plastic deformation of the metal, these rolls endure significant specific pressures and thermal effects, leading to intensive wear [1 – 3]. In light of this, the issue of roller repair quality has become more critical. Recently, there has been a notable increase in the widespread application of restorative arc surfacing to repair rolling mill rolls, using powder wires [2; 4; 5]. However, the use of flux-cored wires for surface welding comes with various drawbacks. In order to ensure the execution of high-quality repair procedures, there arises an essential need to enhance the composition of the wire charge and refine its application technique [6 – 8]. Consequently, the theoretical and experimental exploration of the physical characteristics, processes, and mechanisms involved in reinforcing and developing protective properties within the surface layers of rolls through electric arc coatings, deposited using flux-cored wires, remains relevant and holds scientific and practical significance.

It is worth mentioning that the utilization of presently employed flux-cored wires for the surfacing of rolling rolls is linked to a series of defects that emerge during the surfacing process. These include the high cost and scarcity of surfacing materials, along with the imperfect nature of surfacing technologies [9 – 11]. Identifying and rectifying the flawed structure of these coatings, which contributes to their premature deterioration, holds significant importance [12 – 14]. The advancement of technological surfacing materials [15 – 17], capable of yielding low-carbon martensite structures in the deposited metal, is a subject of interest.

Flux-cored wires within the Fe – C – Si – Mn – Cr – W – V system find extensive application in the surfacing of rolling rolls [18 – 20]. Simultaneously, for the restoration of rolls that operate under the most demanding conditions, the flux-cored wires of the PP-Np-35V9Kh3SF grade in accordance with the State Standard GOST 26101–84 are predominantly employed [19 – 21]. By modifying the composition of the charge within these flux-cored wires and incorporating several elements into their makeup, it becomes feasible to enhance the wear resistance of the deposited layer and extend the operational lifespan of the deposited rolls. Enhancing and altering the chemical composition of the flux-cored wires employed in surfacing presents a multifaceted scientific and manufacturing challenge, requiring a solution that meets the criteria of both economic viability and environmental sustainability [21 – 23].

The objective of this study is to establish patterns governing the augmentation of wear resistance and hardness in electric arc coatings applied to rolling rolls via the use of flux-cored wires within the Fe – C – Si – Mn – Cr – W – V system. This enhancement is achieved through the introduction of titanium and carbon-fluorine-containing material into their composition.

Materials and methods

The processes involved in surfacing and the fabrication of flux-cored wire, as well as the formulation of the filler for the flux-cored wire under investigation and the welding flux, are elaborated upon in references [20 – 22].

In the pursuit of developing a new flux-cored wire, a comparative benchmark was established using wire PP-Np-35V9Kh3SF, produced with graphite grade GL-1 (sample *1*). Subsequently, adjustments were made to the concentrations of titanium (samples *2 – 4*) and the carbon-fluorine-containing material (samples *5 – 9*) for comparison.

Before commencing the production of flux-cored wires, the quantities of powder materials were preliminarily calculated. These materials were meticulously weighed using laboratory analytical scales AUX 120. The blending of the powders was conducted on laboratory rotary mixers for a minimum of 30 min. The manufacturing of the flux-cored wire was executed using a laboratory machine: the strip was drawn through a die, resulting in the formation of the flux-cored wire, which was then wound onto a drum.

The surfacing of electric arc coatings was conducted using an ASAW-1250 welding tractor, employing a custom-made flux-cored wire on steel plates in five distinct

layers. This stratification aimed to prevent the mingling of the deposited metal with the underlying substrate steel. The surfacing parameters were calculated and fine-tuned through experimental adjustments. Post-surfacing, an analysis of the composition and properties of the resulting electric arc coatings were undertaken.

The chemical composition of the deposited coatings was determined using *X*-ray fluorescence via an XRF-1800 spectrometer and atomic emission analysis with a DFS-71 spectrometer. For several samples, the metal's chemical composition was ascertained using chemical techniques: carbon content was measured in accordance with State Standard GOST 12344–2003, sulfur levels were determined following State Standard GOST 12345–2001, and phosphorus content was evaluated adhering to State Standard GOST 12347–77.

Samples designated for macro- and microstructure examination, hardness testing, and wear resistance analysis were prepared using a methodology encompassing cutting via a KKS 315L cutting machine, subsequent grinding on a 3D725 surface grinder, and final polishing utilizing a FROMMIA 835 SE polishing machine.

The configuration of sample cutting is depicted in Fig. 1.

In order to assess the mechanical properties, macro-sections measuring 20×55×14 mm were derived from the cut samples. Hardness measurements were conducted using the Rockwell method on a TK-14-250 hardness tester, following the specifications outlined in State Standard GOST 9013–59. This involved indenting a conical diamond tip with an apex angle of 120°.

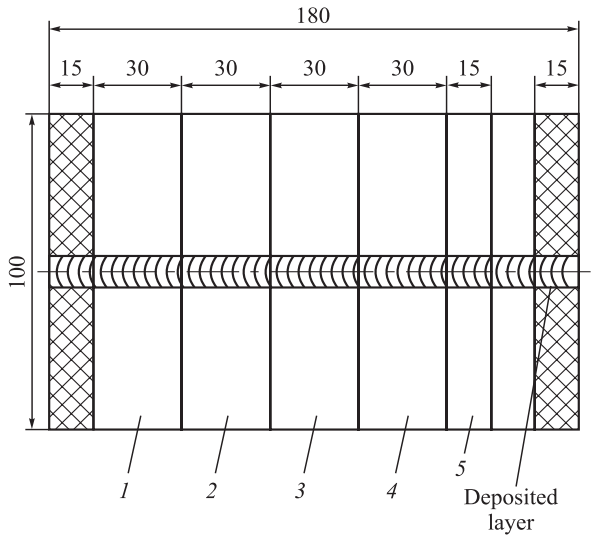

Fig. 1. Scheme of samples cutting for testing:
1 and *2* – for obtaining macro- and micro-plates;
3 and *4* – for tests on hardness and wear resistance;
5 – for hydrogen content determination

Рис. 1. Схема вырезки образцов
для проведения испытаний и анализа:
1 и *2* – для изготовления макро- и микрошлифов;
3 и *4* – для испытаний на твердость и износостойкость;
5 – для определения содержания водорода

Wear tests are presently conducted in accordance with State Standard GOST 23.208–79. This standard pertains to both metallic materials and metallic coatings, stipulating the method for evaluating their resistance to abrasive wear during friction against loosely bound abrasive particles. The core of this method involves rubbing test and reference material samples against abrasive particles introduced into the friction zone and pressed onto the sample by a rotating rubber roller. The wear of these test and reference material samples is measured, with the wear resistance of the test material estimated through a comparison of the wear on the reference and test samples. The outcomes are processed based on the recorded weight of the samples prior to and post the tests, determining the arithmetic mean values of weight loss for both the reference sample and the samples under study.

In order to analyze the influence of the chemical composition of flux-cored wires on the wear rate (degree) and hardness of electric arc coatings, we employed multifactorial correlation analysis. This approach enables us to scrutinize the patterns of changes in specific indicators as a function of various factors. Initially, we identified the factors affecting the indicator in question, selecting the most significant among them. Subsequently, we examined the initial data for reliability, uniformity, and adherence to the normal distribution law. This allowed us to formulate a model of the factor system, using deterministic factor analysis given the presence of independent factor characteristics in the systems being studied.

The rate of abrasion of the deposited layer of the test samples was determined through wear tests performed on a 2070 SMT-1 machine. The fundamental kinematic diagram of this machine is presented in Fig. 2. The lower sample's shaft rotation frequency measurement range (range *A*) was 75 – 750 min^{-1}, while the friction torque measurement range (range *I*) spanned 1 – 10 N·m. The friction machine 2070 SMT-1 can function with both closed and open power circuits, and operates as follows: power is transmitted from the electric motor *2* to both the lower *5* and upper *6* samples via a belt drive *10*. Sample *6* is mounted on the shaft of the folding carriage *7*, which is counterbalanced by the spring mechanism *8*. An elastic torsion sensor *9* for friction torque, along with a non-contact current collector, is installed on the drive shaft of the lower sample, with its signal relayed control panel.

The samples are subjected to loading through a spring bar mechanism *4*. The applied normal force is adjusted by manipulating the loading unit's handle, with the measurements conveyed to the control panel via a flexible link connected to a resistor situated within this unit.

The rotation speed is measured utilizing a rate generator *3*, positioned on the engine shaft, while the rotations of the lower sample *5* are counted by means of a non-contact sensor *1*. The shaft-bushing employed for sample wear, which is crafted from P18 steel, is incorporated.

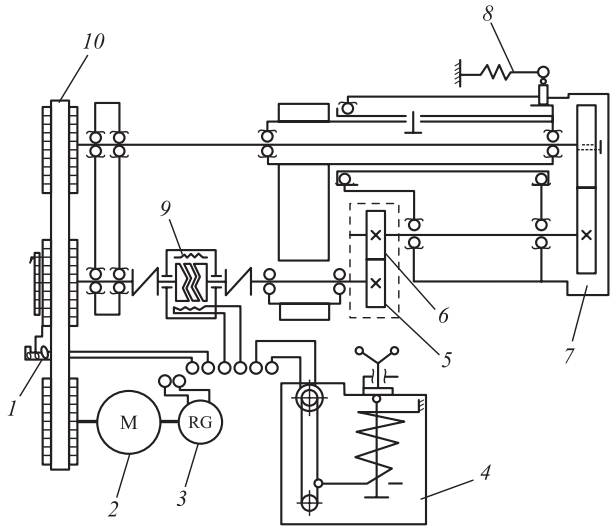

Fig. 2. Basic kinematic scheme of the 2070 CMT-1 machine:
1 – contactless speed sensor; *2* – electric motor; *3* – rate generator;
4 – loading unit (spring mechanism);
5 and *6* – lower and upper samples; *7* – carriage;
8 – spring mechanism; *9* – friction torque sensor;
10 – flat-toothed belt drive

Рис. 2. Принципиальная кинематическая схема машины 2070 СМТ-1:
1 – бесконтактный датчик количества оборотов;
2 – электродвигатель; *3* – тахогенератор;
4 – узел нагружения (пружинный механизм);
5 и *6* – нижний и верхний образцы; *7* – каретка;
8 – пружинный механизм; *9* – датчик момента трения;
10 – плоскозубая ременная передача

Results and discussion

The chemical composition of the deposited layer obtained using the experimental powder wire is outlined in Table 1, and the wear rates of the samples are summarized in Table 2.

Variations in hardness and wear rate concerning the content of different elements are visualized in Fig. 3.

The utilization of mathematical and statistical methods has facilitated the development of a mathematical model depicting the influence of the chemical composition of the deposited layer on its hardness and wear rate.

The validity of the acquired relationships was assessed through the mean approximation error, calculated as follows

$$\tilde{\varepsilon} = \frac{1}{m}\sum_{i=1}^{m}\left|\frac{Y_i - \tilde{Y}_i}{Y_i}\right|100,$$

where m represents the number of observations; $\tilde{Y}_i$ stands for the calculated resultant indicator; $\tilde{Y}_i$ corresponds to the actual value of resultant indicator.

Regression analysis of the influence of the chemical composition of the deposited layer on its hardness and wear rate is expressed by the following equations:

– HRC hardness:

$$-39.056 + 58.725C + 4.983Si + 37.87Mn +$$
$$+ 6.058Cr - 7.096Cu - 107.503Mo - 0.341V - 0.435W$$

(approximation error is 0.0012 %);

– wear rate, g/rot:

$$-0.0000741 + 0.00042C - 0.00043Si +$$
$$+ 0.000258Mn - 0.00022Cr + 0.000398Cu +$$
$$+ 0.00419Mo - 0.00019V + 0.0000372W$$

(approximation error is 0.0011 %).

The hardness and resistance to abrasive wear of the deposited metal exhibit an increase with an escala-

Table 1

Chemical composition of the deposited layers

Таблица 1. **Химический состав наплавленных слоев**

Sample	Content of elements, wt. %															HRC
	C	Si	Mn	Cr	Cu	Mo	V	W	Ni	P	S	Al	Co	Nb	Ti	
1	0.39	1.26	1.69	3.43	0.14	0.11	0.21	8.76	0.12	0.037	0.022	0.060	0.04	0.010	0.020	58.2
2	0.37	1.31	1.74	3.25	0.13	0.11	0.20	8.19	0.12	0.034	0.021	0.110	0.04	0.010	0.030	58.4
3	0.39	1.23	1.76	3.35	0.17	0.10	0.20	8.38	0.10	0.032	0.022	0.100	0.03	0.020	0.030	54.5
4	0.35	1.18	1.73	3.03	0.18	0.09	0.19	7.42	0.13	0.031	0.021	0.090	0.04	0.020	0.030	57.0
5	0.17	0.92	1.76	1.43	0.06	0.05	0.06	3.68	0.07	0.018	0.029	0.020	0.02	0.010	0.006	43.4
6	0.18	0.83	1.55	0.84	0.06	0.03	0.04	2.23	0.06	0.014	0.033	0.009	0.01	0.010	0.007	34.8
7	0.15	0.96	1.66	1.12	0.07	0.03	0.06	3.31	0.07	0.017	0.036	0.008	0.01	0.006	0.007	39.0
8	0.09	0.76	1.46	0.60	0.06	0.02	0.03	1.50	0.06	0.013	0.033	0.004	0.01	0.006	0.006	25.7
9	0.10	1.03	1.75	1.12	0.07	0.05	0.05	3.48	0.07	0.019	0.046	0.004	0.02	0.007	0.006	37.6

Table 2

Wear rate of the samples

Таблица 2. **Скорость износа образцов**

Sample	Sample weight, g			Number of rotations (V_{rot})	Wear resistance $\Delta m \cdot 10^{-5}$
	before wear, m_1	after wear, m_2	difference		
1	86.0384	85.9819	0.0565	2500	2.26
2	90.1120	90.0561	0.0559	2445	2.29
3	102.6680	102.5870	0.0810	2780	2.91
4	105.5680	105.5010	0.0668	2580	2.59
5	85.6461	85.4218	0.2243	2300	9.75
6	100.0260	99.8323	0.1939	2300	8.43
7	115.5400	115.4650	0.0757	3380	2.24
8	94.4399	94.3375	0.1024	2570	3.98
9	112.6090	112.3920	0.2170	2500	8.68

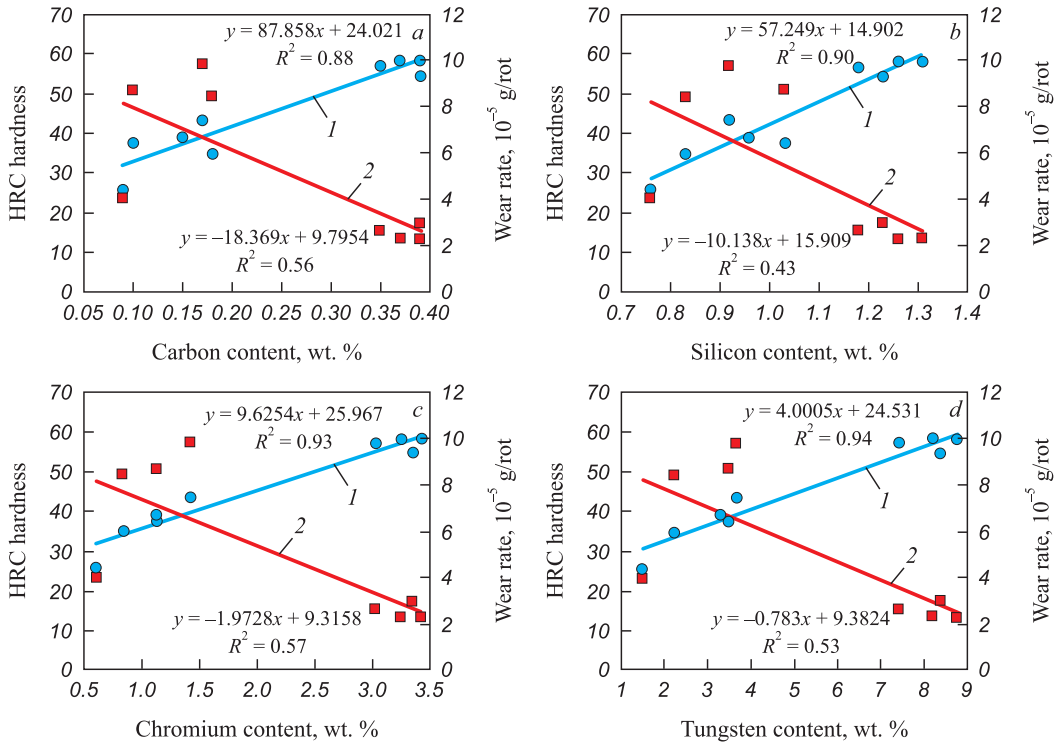

Fig. 3. Dependences of the deposited metal properties on content of carbon (*a*), silicon (*b*), chromium (*c*) and tungsten (*d*): ■ – hardness; ● – wear rate; *1* – linear hardness; *2* – linear wear rate

Рис. 3. Зависимости свойств наплавленного металла от содержания углерода (*a*), кремния (*b*), хрома (*c*) и вольфрама (*d*): ■ – твердость; ● – скорость износа; *1* – линейная твердость; *2* – линейная скорость износа

tion in the concentration of chromium, tungsten, carbon, and silicon. The depicted relationships facilitate the prediction of hardness and wear rate outcomes when modifying the chemical composition of the deposited layers.

Conclusions

A regression analysis was undertaken to investigate the impact of the chemical composition of the deposited layer on both its hardness and wear rate. Consequently, mathematical models were derived to represent the examined operational attributes of the electric arc coating. Notably, the hardness of the deposited metal and its resistance to abrasive wear exhibit an augmentation with an increase in the concentrations of chromium, tungsten, carbon, and silicon.

The findings from these studies offer the potential to formulate strategies aimed at guaranteeing the desired level of operational attributes for the electric arc coat-

ing. Furthermore, they can be employed to prognosticate the hardness of the deposited layer and its wear resistance in response to variations in the chemical composition of the deposited metal. Additionally, they enable the anticipation of the operational longevity of rolls coated with wires of the PP-Np-35V9Kh3SF grade.

The mathematical models delineating the hardness of the deposited layer and its wear resistance provide insights that aid in clarifying the mechanism underlying the strengthening and development of protective properties within the surface layers of rolling rolls, achieved through the application of electric arc coatings deposited using flux-cored wires.

References / Список литературы

1. Metlitskii V.A. Flux-cored wires for arc welding and surfacing of cast iron. *Welding International*. 2008;22(11):796–800. https://doi.org/10.1080/09507110802593646
2. Filippov M.A., Shumyakov V.I., Balin S.A., Zhilin A.S., Lehchilo V.V., Rimer G.A. Structure and wear resistance of deposited alloys based on metastable chromium-carbon austenite. *Welding International*. 2015;29(10):819–822. https://doi.org/10.1080/09507116.2014.986891
3. Liu D.S., Liu R.P., Wei Y.H. Influence of tungsten on microstructure and wear resistance of iron base hardfacing alloy. *Materials Science and Technology*. 2014;30(3):316–322. https://doi.org/10.1179/1743284713Y.0000000359
4. Kejžar R., Grum J. Hardfacing of wear-resistant deposits by MAG welding with a flux-cored wire having graphite in its filling. *Materials and Manufacturing Processes*. 2005;20(6):961–976. https://doi.org/10.1081/AMP-200060424
5. Li R., He D.Y., Zhou Z., Wang Z.J., Song X.Y. Wear and high temperature oxidation behavior of wire arc sprayed iron based coatings. *Surface Engineering*. 2014;30(11):784–790. https://doi.org/10.1179/1743294414Y.0000000331
6. Ma H.R., Chen X.Y., Li J.W., Chang C.T., Wang G., Li H., Wang X.M., Li R.W. Fe-based amorphous coating with high corrosion and wear resistance. *Surface Engineering*. 2017;33(1):56–62. https://doi.org/10.1080/02670844.2016.1176718
7. Lim S.C., Gupta M., Goh Y.S., Seow K.C. Wear resistant WC – Co composite hard coatings. *Surface Engineering*. 1997;13(3):247–250. https://doi.org/10.1179/sur.1997.13.3.247
8. Zhuk Yu. Super-hard wear-resistant coating systems. *Materials Technology*. 1999;14(3):126–129. https://doi.org/10.1080/10667857.1999.11752827
9. Hardell J., Yousfi A., Lund M., Pelcastre L., Prakash B. Abrasive wear behaviour of hardened high strength boron steel. *Tribology – Materials, Surfaces and Interfaces*. 2014;8(2): 90–97. https://doi.org/10.1179/1751584X14Y.0000000068
10. Deng X.T., Fu T.L., Wang Z.D., Misra R.D.K., Wang G.D. Epsilon carbide precipitation and wear behaviour of low alloy wear resistant steels. *Materials Science and Technology*. 2016;32(4):320–327. https://doi.org/10.1080/02670836.2015.1137410
11. Kirchgaßner M., Badisch E., Franek F. Behaviour of iron-based hardfacing alloys under abrasion and impact. *Wear*. 2008;265(5-6):772–779. https://doi.org/10.1016/j.wear.2008.01.004
12. Hasui A., Morigaki O. *Surfacing and Spraying*. Moscow: Mashinostroenie; 1985:240. (In Russ.).

    Хасуи А., Моригаки О. *Наплавка и напыление*. Москва: Машиностроение; 1985:240.
13. Paton B.E. *Technology of Electric Welding of Metals and Alloys by Melting*. Moscow: Kniga po Trebovaniyu; 2021:769. (In Russ.).

    Патон Б.Е. *Технология электрической сварки металлов и сплавов плавлением*. Москва: Книга по Требованию; 2021:769.
14. Gulyaev A.P. *Metals Science. Textbook for Universities*. Moscow: Metallurgiya; 1986:544. (In Russ.).

    Гуляев А.П. *Металловедение. Учебник для вузов*. Москва: Металлургия; 1986:544.
15. Khrushchov M.M., Babichev M.A. *Abrasive Wear*. Moscow: Nauka; 1970:251. (In Russ.).

    Хрущов М.М., Бабичев М.А. *Абразивное изнашивание*. Москва: Наука; 1970:251.
16. Elagina O.Yu. *Technological Methods of Increasing the Wear Resistance of Machine Parts*. Moscow: Logos; 2009:488. (In Russ.).

    Елагина О.Ю. *Технологические методы повышения износостойкости деталей машин*. Москва: Логос; 2009:488.
17. Tylkin M.A. *Improving the Durability of Metallurgical Equipment Parts*. Moscow: Metallurgiya; 1971:608. (In Russ.).

    Тылкин М.А. *Повышение долговечности деталей металлургического оборудования*. Москва: Металлургия; 1971:608.
18. Danil'chenko B.V. Selection of wear-resistant deposited metal for operation under abrasive wear. *Svarochnoe proizvodstvo*. 1992;(5):31–35. (In Russ.).

    Данильченко Б.В. Выбор износостойкого наплавленного металла для работы в условиях абразивного изнашивания. *Сварочное производство*. 1992;(5):31–35.
19. Gusev A.I., Romanov D.A., Kozyrev N.A., Gromov V.E., Ivanov Yu.F. Structure of weld of wear-resistant surfacing by flux-cored wire of Fe – C – Si – Mn – Cr – Ni – Mo system. *Bulletin of the Siberian State Industrial University*. 2021;(2(36)):3–10. (In Russ.).

    Гусев А.И., Романов Д.А., Козырев Н.А., Громов В.Е., Иванов Ю.Ф. Структура сварного шва износостойкой наплавки порошковой проволокой системы Fe – C – Si – Mn – Cr – Ni – Mo. *Вестник Сибирского государственного индустриального университета*. 2021;(2(36)):3–10.
20. Kozyrev N.A., Titov D.A., Kibko N.V. The study of the influence of the composition of flux-cored wire ПП-Нп-35В9Х3СФ on the properties surfaced roller. *Actual Problems in Machine Building*. 2016;3(3):60–64. (In Russ.).

    Козырев Н.А., Титов Д.А., Кибко Н.В. Изучение влияния состава порошковой проволоки ПП-Нп-35В9Х3СФ на свойства наплавляемого валика. *Актуальные проблемы в машиностроении*. 2016;3(3):60–64.
21. Umanskii A.A., Kozyrev N.A., Titov D.A. The experimental investigations into the influence of the compositions of the cored wires of the C–Si–Mn–Cr–V–Mo and C–Si–Mn–Cr–W–V alloying systems on the build-up mill roll layer structure. *Ferrous Metallurgy. Bulletin of Scientific, Technical and Economic Information*. 2016;(4):74–78. (In Russ.).

Уманский А.А., Козырев Н.А., Титов Д.А. Экспериментальные исследования влияния состава порошковых проволок систем легирования C–Si–Mn–Cr–V–Mo и C–Si–Mn–Cr–W–V на структуру наплавленного слоя прокатных валков. *Черная металлургия. Бюллетень научно-технической и экономической информации*. 2016;(4):74–78.

22. Umanskii A.A., Kozyrev N.A., Titov D.A. Research and development of new compositions of flux-cored wire for surfacing of rolling rolls providing an increase in operational characteristics of the deposited metal. *Proizvodstvo prokata*. 2016;5:43–47. (In Russ.).

Уманский А.А., Козырев Н.А., Титов Д.А. Исследование и разработка новых составов порошковой проволоки для наплавки прокатных валков, обеспечивающих повышение эксплуатационных характеристик наплавленного металла. *Производство проката*. 2016;(5):43–47.

23. Kozyrev N.A., Gusev A.I., Galevskii G.V., Kryukov R.E., Osetkovskii I.V., etc. *Flux-Cored Wire*. Pat. RF 2641590. 2018. (In Russ.).

Пат. 2641590 РФ. МПК[8] B23 K35/36 B 23 K35/36 *Порошковая проволока* / Н.А. Козырев, А.И. Гусев, Г.В. Галевский, Р.Е. Крюков, И.В. Осетковский и др. Заявл. 22.06.2016; опубл. 18.01.2018.

Information about the Authors

Aleksandr A. Usol'tsev, *Cand. Sci. (Eng.), Assist. Prof. of the Chair of Ferrous Metallurgy,* Siberian State Industrial University
ORCID: 0000-0001-6220-7910
E-mail: a.us@rambler.ru

Nikolai A. Kozyrev, *Dr. Sci. (Eng.), Deputy Director of the Scientific Center for High-Quality Steels,* I.P. Bardin Central Research Institute of Ferrous Metallurgy
ORCID: 0000-0002-7391-6816
E-mail: n.kozyrev@chermet.net

Lyudmila P. Bashchenko, *Cand. Sci. (Eng.), Assist. Prof. of the Chair "Thermal Power and Ecology",* Siberian State Industrial University
ORCID: 0000-0003-1878-909X
E-mail: luda.baschenko@gmail.com

Roman E. Kryukov, *Dr. Sci. (Eng.), Assist. Prof. of the Chair of Ferrous Metallurgy,* Siberian State Industrial University
ORCID: 0000-0002-3394-7941
E-mail: rek_nzrmk@mail.ru

Andrei V. Zhukov, *Postgraduate of the Chair of Ferrous Metallurgy,* Siberian State Industrial University
E-mail: Svarka42@mail.ru

Сведения об авторах

Александр Александрович Усольцев, *к.т.н., доцент кафедры металлургии черных металлов,* Сибирский государственный индустриальный университет
ORCID: 0000-0001-6220-7910
E-mail: a.us@rambler.ru

Николай Анатольевич Козырев, *д.т.н., заместитель директора научного центра качественных сталей,* Центральный научно-исследовательский институт черной металлургии им. И.П. Бардина
ORCID: 0000-0002-7391-6816
E-mail: n.kozyrev@chermet.net

Людмила Петровна Бащенко, *к.т.н., доцент кафедры теплоэнергетики и экологии,* Сибирский государственный индустриальный университет
ORCID: 0000-0003-1878-909X
E-mail: luda.baschenko@gmail.com

Роман Евгеньевич Крюков, *д.т.н., доцент кафедры металлургии черных металлов,* Сибирский государственный индустриальный университет
ORCID: 0000-0002-3394-7941
E-mail: rek_nzrmk@mail.ru

Андрей Владимирович Жуков, *аспирант кафедры металлургии черных металлов,* Сибирский государственный индустриальный университет
E-mail: Svarka42@mail.ru

Contribution of the Authors

A. A. Usol'tsev – formation of the main research idea, development of the work methodology, analysis of research results.

N. A. Kozyrev – formation of the main research idea, development of the research plan, setting the tasks, analysis of the research results.

L. P. Bashchenko – collection of the research data, analysis of the research results, preparation of materials for the article.
R. E. Kryukov – development of the research plan, organization of samples testing, collection of the research data, analysis of the research results.
A. V. Zhukov – organization of samples testing, collection of the research data, analysis of the research results.

Вклад авторов

А. А. Усольцев – формирование основной идеи исследований, разработка методологии работы, анализ результатов исследований.
Н. А. Козырев – формирование основной идеи исследований, разработка плана исследований, постановка задач, анализ результатов исследований.
Л. П. Бащенко – сбор данных исследований, анализ результатов исследований, подготовка материалов для статьи.
Р. Е. Крюков – разработка плана исследований, организация испытаний образцов, сбор данных исследований, анализ результатов исследований.
А. В. Жуков – организация испытаний образцов, сбор данных исследований, анализ результатов исследований.

Received 20.04.2022
Revised 31.10.2022
Accepted 12.12.2022

Поступила в редакцию 20.04.2022
После доработки 31.10.2022
Принята к публикации 12.12.2022

Metallurgical technologies / Металлургические технологии

UDC 621.762:669.017.15
DOI 10.17073/0368-0797-2023-4-410-414

Original article
Оригинальная статья

Sintered powder high-entropy target cathodes for wear-resistant coatings

S. N. Grigor'ev, M. Sh. Migranov, M. A. Volosova, A. S. Gusev

Moscow State University of Technology "STANKIN" (1 Vadkovskii Lane, Moscow 127055, Russian Federation)

migmars@mail.ru

Abstract. Modern machine-building production equipped with high-performance mechatronic systems and numerically-controlled and adaptive control machines for blade cutting of heat-resistant chromium-nickel and titanium alloys requires increasing the operating properties of cutting tools working at high temperature-force loads in the contact zone, respectively with a significant stress-strain state of the cutting wedge. It is possible to solve the problem of increasing wear resistance and serviceability by developing and introducing new tooling material, as well as by applying wear-resistant coatings. The paper presents the results on development of technology for obtaining high-entropy target cathodes by spark plasma sintering with subsequent application of wear-resistant coatings on metal-cutting tools by both magnetron and ion-plasma methods. Samples of sintered high-entropy target cathodes of different compositions (more than fourteen) and at different modes of their sintering (depending on temperature in five modes) with their subsequent optimization and two standard sizes (20 and 80 mm) were obtained for further application of wear-resistant coatings on the magnetron unit. The authors carried out structural and phase analysis and studied physicomechanical properties of the obtained high-entropy target cathodes: density, hardness, electrical conductivity, emissivity. The possibility of obtaining high-entropy target cathodes by spark plasma sintering was confirmed experimentally, and the effect of sintering temperature on structure and properties of the sintered samples of high-entropy target cathodes was established. Dependence of physicomechanical and electrophysical parameters of target cathodes on technological modes of spark plasma sintering is shown.

Keywords: sintered powder high-entropy target cathodes, spark plasma sintering, composition, hardness, electrical conductivity, density, structural-phase composition

Acknowledgements: The study was supported by the Russian Science Foundation, grant No. 22-19-00670, https://rscf.ru/project/22-19-00670/.

For citation: Grigor'ev S.N., Migranov M.Sh., Volosova M.A., Gusev A.S. Sintered powder high-entropy target cathodes for wear-resistant coatings. *Izvestiya. Ferrous Metallurgy*. 2023;66(4):410–414. https://doi.org/10.17073/0368-0797-2023-4-410-414

Спеченные порошковые высокоэнтропийные катоды-мишени для износостойких покрытий

С. Н. Григорьев, М. Ш. Мигранов, М. А. Волосова, А. С. Гусев

Московский государственный технологический университет «СТАНКИН» (Россия, 127055, Москва, Вадковский пер., 1)

migmars@mail.ru

Аннотация. Современное машиностроительное производство, оснащенное высокопроизводительными мехатронными системами и станками с числовым программным и адаптивным управлением для лезвийной обработки резанием жаропрочных хромоникелевых и титановых сплавов, требует повышения эксплуатационных свойств режущего инструмента, работающего при высоких температурно-силовых нагрузках в контактной зоне и, соответственно, при существенном напряженно-деформированном состоянии режущего клина. Решение вопроса повышения износостойкости и работоспособности возможно как путем разработки и внедрения нового инструментального материала, так и применения износостойких покрытий. В работе представлены результаты по разработке технологии получения высокоэнтропийных катодов-мишеней путем искрового плазменного спекания с последующим нанесением износостойких покрытий на металлорежущий инструмент магнетронным и ионно-плазменными методами. Получены образцы спеченных высокоэнтропийных катодов-мишеней различных по составу композиций (более четырнадцати) при разных режимах спекания (в зависимости от температуры в пяти режимах) с последующей их оптимизацией, а также двух типоразмеров (20 и 80 мм) для дальнейшего использования для нанесения износостойких покрытий на магнетронной установке. Проведены структурный и фазовый анализы, а также исследование физико-механических свойств полученных высокоэнтропийных катодов-мишеней: плотности, твердости, электропроводности, эмиссионной способности. Экспериментально подтверждена возможность получения высокоэнтропийных катодов-мишеней методом

искрового плазменного спекания, при этом показано влияние температуры спекания на структуру и свойства спеченных образцов высокоэнтропийных катодов-мишеней. Установлены зависимости физико-механических и электрофизических параметров катодов-мишеней от технологических режимов процесса искрового плазменного спекания.

Ключевые слова: спеченные порошковые высокоэнтропийные катоды-мишени, искровое плазменное спекание, композиция, твердость, электропроводность, плотность, структурно-фазовый состав

Благодарности: Исследование выполнено при поддержке гранта Российского научного фонда № 22-19-00670, https://rscf.ru/project/22-19-00670/.

Для цитирования: Григорьев С.Н., Мигранов М.Ш., Волосова М.А., Гусев А.С. Спеченные порошковые высокоэнтропийные катоды-мишени для износостойких покрытий. *Известия вузов. Черная металлургия*. 2023;66(4):410–414.
https://doi.org/10.17073/0368-0797-2023-4-410-414

Introduction

Today, manufacturers are dedicated to enhancing the durability and reliability of their products because it directly impacts efficiency and market competitiveness. One effective approach to achieve this is by improving the metal-cutting process. Even in the case of advanced high-performance NC machine tools, the cutting tool often becomes the bottleneck. It constrains both the machine tool's capability and the quality of the machined surface. Conventional wear-resistant coatings for cutting tools, deposited using one to four solid cathodes, no longer meet current requirements. Such coatings are indispensable for high-speed machining, tools operating under elevated temperatures and loads in the contact zone, and the machining of high-strength, heat-resistant Cr–Ni and Ti alloys.

Additionally, advanced power metallurgy processes have garnered significant attention [1 – 3] because they facilitate the manufacturing of highly intricate components with improved performance [4; 5].

The objective of this study is to develop a powder spark plasma sintering process and assess the properties of multi-component wear-resistant coatings applied to metal cutting tools, along with evaluating the service life of the target cathode.

High-entropy alloys, known for their high-temperature resistance, wear resistance, hardness, and strength [6 – 9], are of considerable interest. The properties of such coatings are contingent on the elemental composition and deposition process, which necessitate optimization. Another crucial factor is the characteristics of high-entropy target cathodes [10; 11] employed in depositing wear-resistant coatings on cutting tools.

High-entropy alloys have been the subject of intensive research [12 – 15]. They possess distinctive features, including:

– elevated entropy of mixing (S_{mix}) compared to conventional multi-component materials [16];

– unique mechanical properties resulting from specific thermal processes, atom diffusion under certain structural and phase [17];

– significant influence on the crystal lattice due to the content of iron, nickel, molybdenum, aluminum, among other elements;

– binary or ternary phase diagrams are used to estimate the phase composition [18];

– while alloying elements initiate solid solution hardening and discrete phase separation [19];

– as a result, these alloys are classified as a special category [20].

As mentioned in [5; 9; 15], certain high-entropy alloys exhibit exceptional properties, including hardness, heat resistance, thermal stability, corrosion resistance, and wear resistance.

Materials and Methods

Casting and melting are the primary processes employed in the production of high-entropy alloys [20]. However, powder sintering, particularly spark plasma sintering (SPS), holds significant promise as well [6; 7; 12]. The testing process was divided into two phases, conducted at the Spark Plasma Sintering Lab, Center for New Materials and Technologies, National Engineering Center, STANKIN University. In Phase 1, our focus was on the production of high-entropy target cathodes, while in Phase 2, we deposited the coatings and conducted tests to assess their properties. The results of Phase 1, which involved the manufacturing of powder high-entropy cathodes, are summarized below.

In order to determine the optimal powder composition for spark plasma sintering of the target cathodes, we conducted an analysis of a wear-resistant mixture comprising more than 12 commercially available metal powders. After establishing the quantitative and qualitative composition based on the Yum-Roseri rule, we followed these steps:

– preparation of the powder mixture with a specified particle size distribution;

– pre-compaction of the powder mixture in a mold using a 3851 Manual BenchTOP 12 manual hydraulic lab press (Carver, USA);

– utilization of a A KCE-FCT-H-HP-D25-SD furnace (FCT, Germany) for spark plasma sintering, with variations ranging from 500 to 1600 °C in 50 °C increments;

– application of compaction forces at 25, 50, 80, and 100 kN;

– adjustment of the heating rate to either 50 or 100 °C/min;

– implementation of holding times at 1, 2, 3, 4, and 5 min;

– usage of sample sizes measuring 20 and 80 mm.

Following this, we conducted an examination of the properties exhibited by the resulting target cathodes, employing the following methodologies:

– measurement of density using the hydrostatic technique;

– utilization of a Wilson Rockwell 574 hardness tester (Germany) to measure hardness;

– estimation of electrical conductivity through the phase-sensitive eddy current method using a portable Fischer SIGMASCOPE instrument (Helmut Fischer GmbH+Co.KG, Germany);

– application of scanning electron microscopy (SEM) to determine the elemental, qualitative, and quantitative compositions of the samples. For this purpose, we utilized a Phenom ProX microscope (Netherlands) and a Difray 401K desktop *X*-ray diffractometer (Russia).

Results and Discussion

The manufactured samples of the high-entropy target cathodes, with compositions including:

– $Al_{20}–Ti_{20}–Zr_{15}–V_{15}–Cr_{15}–Nb_{15}$;
– $Al_{20}–Hf_{15}–Mo_{15}–Co_{15}–Ta_{10}–W_{10}–Zr_{15}$;
– $Al_{20}–Hf_{15}–V_{15}–Cr_{15}–Ti_{15}–Ta_{10}–W_{10}$;
– $Al_{20}–Hf_{10}–Ni_{15}–Ti_{25}–W_{10}–Zr_{20}$;
– $Mo_{20}–Nb_{20}–Ni_{20}–Ta_{20}–W_{20}$;
– $Nb_{20}–Hf_{20}–Ti_{20}–Zr_{20}–Ta_{20}$

and others, subjected to testing for their suitability in depositing nano-coatings on cutting tools. The key properties of these target cathodes, aside from the particle size distribution of the powder mixture, encompass density, hardness, electrical conductivity, as well as elemental, qualitative, and quantitative compositions (refer to the table). The test results reveal that higher sintering temperatures lead to increased relative density, hardness, and electrical conductivity.

Conclusion

Based on the test results, we successfully developed a spark plasma sintering process for the production of high-entropy target cathodes, essential for depositing wear-resistant coatings on cutting tools. Through our research, we pinpointed the optimal compositions and sintering conditions necessary to achieve the desired coating structure, as well as the desired physical and

Results under sintering conditions: sintering temperature 1200 °C; pressing pressure 25 kN; holding time 1 min; heating rate 100 °C/min; sample diameter 20 mm

Результаты ипсытаний при режимах спекания: температура спекания 1200 °C; давление прессования 25 кН; время выдержки 1 мин; скорость нагрева 100 °C/мин; диаметр образца 20 мм

Density, g/cm^3	Hardness, HB	Electrical conductivity, MSm/m^2	SEM			
			element	atomic number	content, %	
					at.	wt.
$Al_{20}–Ti_{20}–Zr_{15}–V_{15}–Cr_{15}–Nb_{15}$						
8.60	104.6	0.67 – 0.74	Ti	22	29.71	32.28
			Al	13	43.64	26.73
			Zr	40	10.71	22.18
			Cr	24	15.93	18.80
$Al_{20}–Hf_{15}–Mo_{15}–Co_{15}–Ta_{10}–W_{10}–Zr_{15}$						
9.99	110.2	0.64 – 1.20	Mo	42	26.50	26.07
			Co	27	26.12	15.78
			Zr	40	14.36	13.43
			Hf	72	10.38	19.00
			W	74	9.53	17.96
			Br	35	8.84	7.24
			C	6	4.27	0.53

mechanical properties. Our findings confirm the feasibility of employing spark plasma sintering for the creation high-entropy target cathodes. Furthermore, we identified the influence of sintering temperature on the structure and properties of high-entropy target cathode samples, as well as the interrelationships between the physical and mechanical properties of these samples and the variables of the SPS process. The introduction of target cathodes crafted through this process promises to enhance high-speed machining efficiency when utilizing cutting tools with wear-resistant coatings. Such tools have the potential to form secondary and diamond-like structures within the contact zone, leading to the adaptation and self-organization of friction and wear processes.

References / Список литературы

1. Cantor B. Multicomponent and high entropy alloys. *Entropy*. 2014;16 (9):4749–4768. http://doi.org/10.3390/e16094749
2. Murty B.S., Yeh J.-W., Ranganathan S., Bhattacharjee P.P. *High-Entropy Alloys*. Amsterdam: Elsevier; 2019:374.
3. Gao M.C., Yeh J.-W., Liaw P.K., Zhang Y. *High-Entropy Alloys: Fundamentals and Applications*. Cham: Springer International Publishing; 2016:524.
4. Zhang Y., Zuo T.T., Tang Z., Gao M.C., Dahmen K.A., Liaw P.K., Lu Z.P. Microstructures and properties of high-entropy alloys. *Progress in Materials Science*. 2014;61:1–93. http://doi.org/10.1016/j.pmatsci.2013.10.001
5. Firstov S.A., Gorban' V.F., Krapivka N.A., Pechkovskii E.P. New class of materials – high-entropic alloys and coatings. *Vestnik Tambovskogo universiteta. Seriya: Estestvennye i tekhnicheskie nauki*. 2013;18(4–2):1938–1940. (In Russ.).

   Фирстов С.А., Горбань В.Ф., Крапивка Н.А., Печковский Э.П. Новый класс материалов – высокоэнтропийные сплавы и покрытия. *Вестник Тамбовского университета. Серия: Естественные и технические науки*. 2013;18(4–2):1938–1940.
6. Kochetov N.A., Rogachev A.S., Shchukin A.S., Vadchenko S.G., Kovalev I.D. Mechanical alloying with partial amorphization of Fe–Cr–Co–Ni–Mn multicomponent powder mixture and its spark plasma sintering for compact high-entropy material production. *Powder Metallurgy and Functional Coatings*. 2018;(2):35–42. (In Russ.). http://doi.org/10.17073/1997-308X-2018-2-35-42

   Кочетов Н.А., Рогачев А.С., Щукин А.С., Вадченко С.Г., Ковалев И.Д. Механическое сплавление с частичной аморфизацией многокомпонентной порошковой смеси Fe–Cr–Co–Ni–Mn и ее электроискровое плазменное спекание для получения компактного высокоэнтропийного материала. *Известия вузов. Порошковая металлургия и функциональные покрытия*. 2018;(2):35–42. http://doi.org/10.17073/1997-308X-2018-2-35-42
7. Chen W., Anselmi-Tamburini U., Garay J.E., Groza J.R., Munir Z.A. Fundamental investigations on the spark plasma sintering/synthesis process. I. Effect of dc pulsing on reactivity. *Materials Science and Engineering: A*. 2005;394(1–2): 132–138. https://doi.org/10.1016/j.msea.2004.11.020
8. Yeh J.-W., Chen Y.-L., Lin S.-J., Chen S.-K. High-entropy alloys – A new era of exploitation. *Materials Science Forum*. 2007; 560:1–9. http://doi.org/10.4028/www.scientific.net/MSF.560.1
9. Miracle D.B., Senkov O.N. A critical review of high entropy alloys and related concepts. *Acta Materialia*. 2017;122: 448–511. http://doi.org/10.1016/j.actamat.2016.08.081
10. Zhang W., Liaw P.K., Zhang Y. Science and technology in high-entropy alloys. *Science China Materials*. 2018;61(1): 2–22. http://doi.org/10.1007/s40843-017-9195-8
11. George E.P., Raabe D., Ritchie R.O. High-entropy alloys. *Nature Reviews Materials*. 2019;4:515–534. http://doi.org/10.1038/s41578-019-0121-4
12. Rogachev A.S. Structure, stability and properties of high-entropy alloys. *The Physics of Metals and Metallography*. 2020;121(8):733–764. http://doi.org/10.1134/S0031918X20080098

    Рогачев А.С. Структура, стабильность и свойства высокоэнтропийных сплавов. *Физика металлов и металловедение*. 2020;121(8):807–841. http://doi.org/10.31857/S0015323020080094
13. Singh S., Wanderka N., Glatzel U., Banhart J. Decomposition in multi-component AlCoCrCuFeNi high-entropy alloy. *Acta Materialia*. 2011;59(1):182–190. http://doi.org/10.1016/j.actamat.2010.09.023
14. Senkov O.N., Wilks G.B., Scott J.M., Miracle D.B. Mechanical properties of $Nb_{25}Mo_{25}Ta_{25}W_{25}$ and $V_{20}Nb_{20}Mo_{20}Ta_{20}W_{20}$ refractory high entropy alloys. *Intermetallics*. 2011;19(5): 698–706. http://doi.org/10.1016/j.intermet.2011.01.004
15. Firstov S.A., Gorban' V.F., Danilenko N.I., Karpets M.V., Andreev A.A., Makarenko E.S. Thermal stability of superhard nitride coatings based on multicomponent high-entropy alloy of the TiVZrNbHf system. *Poroshkovaya metallurgiya*. 2013;(9/10):93–102. (In Russ.).

    Фирстов С.А., Горбань В.Ф., Даниленко Н.И., Карпец М.В., Андреев А.А., Макаренко Е.С. Термостабильность сверхтвердых нитридных покрытий на основе многокомпонентного высокоэнтропийного сплава системы TiVZrNbHf. *Порошковая металлургия*. 2013;(9/10):93–102.
16. Oates W.A. Configurational entropies of mixing in solid alloys. *Journal of Phase Equilibria and Diffusion*. 2007;28:79–89. http://doi.org/10.1007/s11669-006-9008-3
17. Otto F., Yang Y., Bei H., George E.P. Relative effects of enthalpy and entropy on the phase stability of equiatomic high-entropy alloys. *Acta Materialia*. 2013;61(7):2628–2638. http://doi.org/10.1016/j.actamat.2013.01.042
18. Tong C.-J., Chen Y.-L., Yeh J.-W., Lin S.-J., Chen S.-K., Shun T.-T., Tsau C.-H., Chang S.-Y. Microstructure characterization of $Al_xCoCrCuFeNi$ high-entropy alloy system with multiprincipal elements. *Metallurgical and Materials Transactions A*. 2005;36(4):881–893. https://doi.org/10.1007/s11661-005-0283-0
19. Tsai M.-H., Yeh J.-W. High-entropy alloys: a critical review. *Materials Research Letters*. 2014;2(3):107–123. http://doi.org/10.1080/21663831.20 14.912690
20. Gelchinski B.R., Balyakin I.A., Yuryev A.A., Rempel A.A. High-entropy alloys: properties and prospects of application as protective coatings. *Russian Chemical Reviews*. 2022;91(6):RCR5023. http://doi.org/10.1070/RCR5023

Information about the Authors

Sergei N. Grigor'ev, *Dr. Sci. (Eng.), Prof., Head of the Chair of Highly Efficient Processing Technologies,* Moscow State University of Technology "STANKIN"
ORCID: 0000-0002-8239-5354
E-mail: s.grigoriev@stankin.ru

Mars Sh. Migranov, *Dr. Sci. (Eng.), Prof. of the Chair of Highly Efficient Processing Technologies,* Moscow State University of Technology "STANKIN"
ORCID: 0000-0002-7075-5500
E-mail: migmars@mail.ru

Marina A. Volosova, *Cand. Sci. (Eng.), Assist. Prof. of the Chair of Highly Efficient Processing Technologies,* Moscow State University of Technology "STANKIN"
ORCID: 0000-0002-5302-5442
E-mail: volosova1978@gmail.com

Andrei S. Gusev, *Junior Researcher of the Chair of Highly Efficient Processing Technologies,* Moscow State University of Technology "STANKIN"
ORCID: 0000-0002-5629-4998
E-mail: gusev.angrey@bk.ru

Сведения об авторах

Сергей Николаевич Григорьев, *д.т.н., профессор, заведующий кафедрой высокоэффективных технологий обработки,* Московский государственный технологический университет «СТАНКИН»
ORCID: 0000-0002-8239-5354
E-mail: s.grigoriev@stankin.ru

Марс Шарифуллович Мигранов, *д.т.н., профессор кафедры высокоэффективных технологий обработки,* Московский государственный технологический университет «СТАНКИН»
ORCID: 0000-0002-7075-5500
E-mail: migmars@mail.ru

Марина Александровна Волосова, *к.т.н., доцент кафедры высокоэффективных технологий обработки,* Московский государственный технологический университет «СТАНКИН»
ORCID: 0000-0002-5302-5442
E-mail: volosova1978@gmail.com

Андрей Сергеевич Гусев, *младший научный сотрудник кафедры высокоэффективных технологий обработки,* Московский государственный технологический университет «СТАНКИН»
ORCID: 0000-0002-5629-4998
E-mail: gusev.angrey@bk.ru

Contribution of the Authors

S. N. Grigor'yev – statement and solution of the problem of increasing the wear resistance of metal-cutting tools by developing the technology of obtaining high-entropy target cathodes for application of innovative wear-resistant coatings.

M. Sh. Migranov – theoretical and experimental analysis of methods for obtaining high-entropy target cathodes, justification of choice and modes of spark plasma sintering of high-entropy target cathodes, formulation of conclusions.

M. A. Volosova – development of experimental research methods, selection of necessary equipment for full-scale tests.

A. S. Gusev – performance of experimental tests, processing of the results.

Вклад авторов

С. Н. Григорьев – постановка и решение задачи по повышению износоустойчивости металлорежущего инструмента путем разработки технологии получения высокоэнтропийных катодов-мишеней для нанесения инновационных износостойких покрытий.
М. Ш. Мигранов – теоретико-экспериментальный анализ методов получения высокоэнтропийных катодов-мишеней, обоснование выбора и режимов искрового плазменного спекания высокоэнтропийных катодов-мишеней, формулирование выводов по результатам исследований.
М. А. Волосова – разработка методик экспериментальных исследований, подбор необходимого оборудования для натурных испытаний.
А. С. Гусев – проведение экспериментальных испытаний, обработка результатов.

Received 29.06.2023
Revised 06.07.2023
Accepted 30.07.2023

Поступила в редакцию 29.06.2023
После доработки 06.07.2023
Принята к публикации 30.07.2023

Metallurgical technologies / Металлургические технологии

UDC 669.16.22:621.793
DOI 10.17073/0368-0797-2023-4-415-420

Original article
Оригинальная статья

Effect of ring groove in a heat-insulating insert on efficiency of its work in blast channel of blast furnace tuyere

S. V. Albul[1], **O. A. Kobelev**[1, 2], **I. A. Levitskii**[1]

[1] **National University of Science and Technology "MISIS"** (4 Leninskii Ave., Moscow 119049, Russian Federation)
[2] **JSC Russian State Research Center "CNIITMASH"** (4 Sharikopodshipnikovskaya Str., Moscow 115088, Russian Federation)

albul@misis.ru

Abstract. One of the main disadvantages when supplying natural gas to the air tuyere of a blast furnace is low intensity of its combustion inside the tuyere blast channel. Ring groove on the surface of blast channel improves the mixing of natural gas with blast and increases completeness of gas combustion in it, but reduces the tuyere durability. One of the ways to simultaneously solve these problems is to install a heat-insulating ceramic insert in the tuyere blast channel. The insert significantly reduces heat losses through the tuyere surface, improves natural gas combustion in the blast channel due to its contact with hot walls of the insert instead of cold copper walls in its absence. This increases the temperature of the hot blast at the tuyere outlet. In addition, the insert affects the tuyere durability by reducing the heat flow acting on the tuyere. In this work, we studied influence of the ring groove and its parts in the insert on efficiency of its work. In the Ansys 21.1 software, the processes occurring in the blast channel of a blast furnace tuyere with a ceramic insert installed in it, having a groove of a quadrangular section in the form of a ring or its part in the circumferential direction, were simulated. It was established that improvement of natural gas combustion in the tuyere blast channel is achieved using a ring groove or part of it from the side of gas supply.

Keywords: blast furnace, air tuyere, blast channel, ceramic insert, ring groove, Ansys modeling, heat transfer, natural gas combustion

Acknowledgements: The authors express their gratitude to Prof. Radyuk A.G. for his advice on the possibility of using a groove in a ceramic insert to increase the efficiency of its use in air tuyere of blast furnace.

For citation: Albul S.V., Kobelev O.A., Levitskii I.A. Effect of ring groove in a heat-insulating insert on efficiency of its work in blast channel of blast furnace tuyere. *Izvestiya. Ferrous Metallurgy*. 2023;66(4):415–420. https://doi.org/10.17073/0368-0797-2023-4-415-420

Влияние зоны кольцевой выборки в теплоизолирующей вставке на эффективность ее работы в дутьевом канале воздушной фурмы доменной печи

С. В. Албул[1], **О. А. Кобелев**[1, 2], **И. А. Левицкий**[1]

[1] **Национальный исследовательский технологический университет «МИСИС»** (Россия, 119049, Москва, Ленинский пр., 4)
[2] **Центральный научно-исследовательский институт технологии машиностроения, ОАО НПО «ЦНИИТМАШ»** (Россия, 115088, Москва, Шарикоподшипниковская ул., 4)

albul@misis.ru

Аннотация. Одним из основных недостатков при подаче природного газа в воздушную фурму доменной печи является низкая интенсивность его горения внутри дутьевого канала фурмы. Известно, что кольцевая выборка на поверхности дутьевого канала улучшает смешивание природного газа с дутьем и увеличивает полноту сгорания газа в нем, однако снижает стойкость фурмы. Одним из способов одновременного решения этих проблем является установка в дутьевой канал фурмы теплоизолирующей керамической вставки. Вставка значительно снижает тепловые потери через поверхность фурмы, улучшает горение природного газа в дутьевом канале за счет его контакта с горячими стенками вставки вместо холодных медных стенок при ее отсутствии, что увеличивает температуру горячего дутья на выходе из фурмы. Кроме того, вставка оказывает влияние на стойкость фурмы за счет снижения теплового потока, действующего на фурму. В данном исследовании изучено влияние кольцевой выборки и ее частей во вставке на эффективность ее работы. В среде Ansys 21.1 моделировали процессы, происходящие в дутьевом канале фурмы доменной печи с установленной в него керамической вставкой, имеющей выборку четырехугольного сечения в форме кольца или его части в окружном направлении. Установлено, что улучшение горения природного газа в дутьевом канале фурмы достигается с использованием кольцевой выборки или ее части со стороны подачи газа.

Ключевые слова: доменная печь, воздушная фурма, дутьевой канал, керамическая вставка, кольцевая выборка, моделирование в Ansys, теплообмен, горение природного газа

Благодарности: Авторы выражают благодарность проф. Радюк А.Г. за консультацию по возможности использования выборки в керамической вставке для повышения эффективности её применения в воздушной фурме доменной печи.

Для цитирования: Албул С.В., Кобелев О.А., Левицкий И.А. Влияние зоны кольцевой выборки в теплоизолирующей вставке на эффективность ее работы в дутьевом канале воздушной фурмы доменной печи. *Известия вузов. Черная металлургия*. 2023;66(4):415–420.
https://doi.org/10.17073/0368-0797-2023-4-415-420

Introduction

The air tuyeres supply a mixture of oxygen-enriched blast and natural gas [1 – 3] or natural gas and pulverized coal into the blast furnace. The injection of gas and coal reduces the coke consumption during pig iron manufacturing [4 – 6]. As the share of natural gas increases, its mixing with the blast deteriorates [7 – 9] and blowing efficiency decreases [10 – 12]. We have proposed solutions to enhance the ignition and combustion of natural gas in the tuyere blast channel [13 – 16]. Numerous improved technologies for mixing natural gas with the blast have been invented [17 – 20].

Gas preheating has been proven to be efficient [21; 22].

Another promising approach to improving gas/blast mixing is adding cavities to the blast channel to increase flow turbulence in the tuyere. Such elements could be a groove in the tuyere nose [23], blowpipe, [24], or in the natural gas feed tube [25]. However, more intense gas combustion in the tuyere blast channel may result in blowpipe deformation or burnout. For this reason, as gas combustion improves, the blowpipe should be heat protected. Durable insulating ceramic inserts [26 – 28, 29 – 31] can be used.

A large number of studies [32 – 34] are dedicated to modeling processes occurring in the air tuyere and the blast furnace tuyere zone, including the simultaneous supply of combustible natural gas and pulverized coal into the blast channel of the tuyere [35; 36].

Problem statement

We investigated the effects of a ring roove or its segments on ceramic insert performance.

The purpose of this study is to simulate the flow, heat exchange, and gas combustion in the blast channel. We considered the following ceramic insert designs:

– no groove in the insert (basic design);

– with a quadrangular section (3 mm deep, 40 mm wide) ring groove located 20 mm from the insert bottom;

– with a semi-ring groove of the same size located at the top (on the gas feed pipe side);

– with a semi-ring groove of the same size located at the bottom (opposite the gas feed pipe side).

The depth and width of the groove were selected to meet two conditions: provide a measurable improvement in the gas combustion process and maintain structural integrity. The groove was placed near the edge of the insert to intensify gas combustion in the area close to the tuyere nose and the tuyere zone.

We conducted CFD, combustion, and heat transfer simulations in Ansys Fluent 21.1 using the actual tuyere operating conditions and some simplifying assumptions proposed by Levitskii I. et al. [18]. The key assumptions are:

– extended boundary conditions include heat transfer to the cooling water;

– radiation heat exchange inside the air passage is neglected;

– the *Finite Rate / Eddy dissipation model* is employed to simulate chemical reactions and turbulence;

– to reduce computational costs, half of the symmetrical structure is simulated;

– the problem is assumed to be stationary;

– the pressure solver is utilized;

– the *realizable k-ε* turbulence model with standard wall functions is used to solve the energy and convective diffusion equations for the methane-air mixture, taking possible combustion into account.

In contrast to the approach presented in [18], our approach involved solving a combined heat transfer problem, explicitly analyzing heat transfer through solid bodies (specifically, the insert).

We constructed a symmetric geometric model using Design Modeler and subsequently generated the mesh using Ansys Meshing.

The simulation addressed a stationary problem. The components of the methane-air mixture were treated as perfect gases, meaning we assumed that density varies with pressure and temperature. The tuyere nose and the blowpipe were composed of copper, with their properties available in the Ansys Fluent database. The insert was fabricated from corundum, characterized by a density of 3583 kg/m^3, specific heat capacity of 1291 J/(kg·K), and thermal conductivity of 83 W/(m·K). The gap between the insert and the blowpipe was assumed to be filled with sealant, featuring a density of 1200 kg/m^3, specific

Table 1

Blast parameters in the inlet section

Таблица 1. **Параметры дутья во входном сечении**

Property	Value
Section type	mass flow inlet
Mixture composition	30 % O_2, 70 % N_2
Air temperature	1200 °C
Air mass flow	4.539 kg/s
Air pressure	405.3 kPa
Turbulent pulsations	5 %
Hydraulic diameter	0.18 m

Table 2

Parameters of natural gas in the inlet section

Таблица 2. **Параметры ПГ во входном сечении**

Property	Value
Section type	mass flow inlet
Composition	100 % CH_4
Natural gas mass flow rate	0.283 kg/s
Natural gas temperature	27 °C
Turbulent pulsations	5 %
Hydraulic diameter	0.033 m

heat capacity of 840 J/(kg·K), and thermal conductivity 0.4 W/(m·K).

The boundary conditions for the blast process are detailed in Table 1, while those for the natural gas feed are outlined in Table 2.

In order to account for the 2 mm thick gap and the 6 mm thick copper layer on the outer surface of the insert within the simulation domain, the boundary conditions on this surface were extended. Convective heat exchange with the environment occurred on the outer surface of the copper layer, maintaining a temperature of 27 °C and a heat conductivity of a = 5815 W/(m^2·K).

The boundary conditions at the fluid-to-tuyere nose interface were also extended due to the presence of a 14 mm thick copper layer. Similar to the 6 mm thick copper layer, there was convective heat exchange with the environment occurring on the outer surface of this copper layer.

Simulation results and discussion

Table 3 presents the crucial simulation results, and Figs. 1 and 2 illustrate the distribution of turbulent kinetic energy.

Both Table 3 and Figs. 1 and 2 indicate that the presence of a ring groove in the insert or a groove on the natural gas feed side enhances the mixing of natural gas and hot air. Consequently, this leads to increased gas combustion heat, higher CO_2 content, and as a result, elevated temperature and flow velocity at the tuyere out-

Table 3

Design parameters of the air tuyere

Таблица 3. **Расчетные параметры работы воздушной фурмы**

Variables*	Design options			
	without groove	with groove		
		ring	semi-ring, top	semi-ring, bottom
Q_{out}, kW	–3207.2	–3230.9	–3223.3	–3158.7
Q_{nose}, kW	–26.3	–27.8	–26.4	–26.5
Q_{comb}, kW	289.2	314.7	305.2	240.6
ΔQ, kW	–0.042	–0.018	0.019	0.012
T_{out}, K	1399.3	1407.2	1404.7	1385.7
$CO_{2\ out}$	0.0105	0.0114	0.0111	0.0088
υ_{out}, m/s	217.8	218.9	218.7	216.1
K_{out}, m^2/s^2	61.6	84.9	66.1	67.5

* Since the simulation domain represents half of the real structure, all the heat values should to be doubled.

Q_{out} is heat flux at the blast channel, kW; Q_{nose} is heat flux at the tuyere nose, kW; Q_{comb} is combustion heat, kW; ΔQ is heat disbalance, kW; T_{out} is average air temperature at the tuyere outlet, K; $CO_{2\ out}$ is mass fraction of CO_2 at the tuyere outlet; υ_{out} is average flow velocity at the tuyere outlet, m/s; K_{out} is turbulent kinetic energy at the tuyere outlet, m^2/s^2.

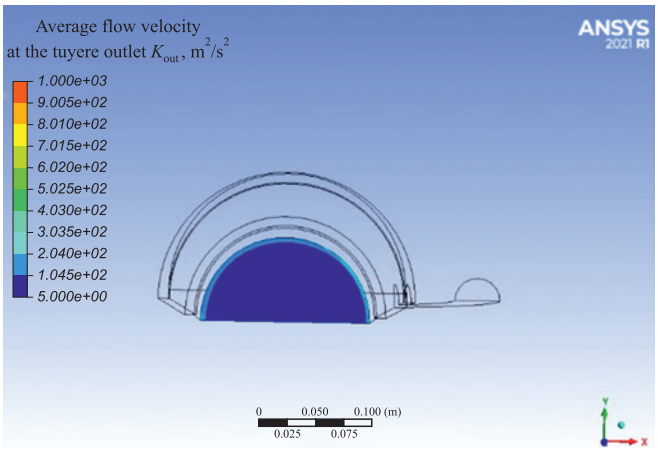

Fig. 1. Distribution of turbulence kinetic energy at the outlet of a serial tuyere

Рис. 1. Распределение кинетической энергии турбулентности на выходе из серийной фурмы

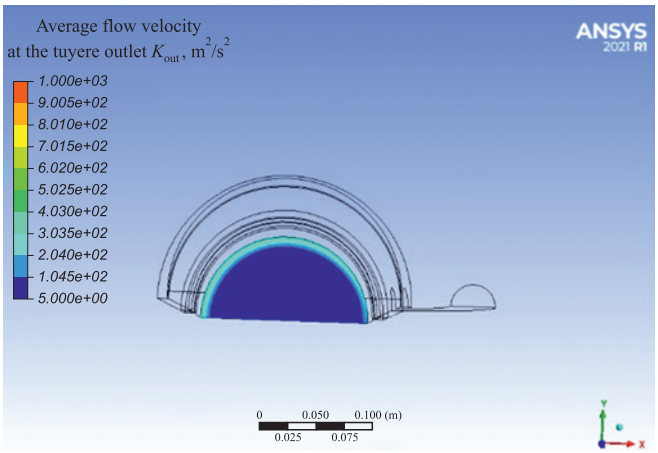

Fig. 2. Distribution of turbulence kinetic energy at the outlet of a tuyere with ring groove

Рис. 2. Распределение кинетической энергии турбулентности на выходе из фурмы с кольцевой выборкой

let. This implies that the natural gas ratio in the tuyere mixture can be raised.

Conclusions

The presence of a ring groove in the tuyere blowpipe's heat-insulating insert has a significant impact on gas combustion:

– a semi-ring groove located at the gas feed pipe side enhances gas/hot air mixing and accelerates combustion;

– an ring groove further improves the gas/hot air mixing and accelerates combustion;

– a semi-ring groove opposite the gas feed pipe side leads to a deterioration in gas/hot air mixing and combustion compared to the standard, no-groove design.

Список литературы / References

1. Radyuk A.G., Titlyanov A.E., Skripalenko M.M. Modeling of the temperature field of blast furnace tuyeres using Deform-2D software. *Metallurgist*. 2017;60(9–10):1011–1015. https://doi.org/10.1007/s11015-017-0400-5

   Радюк А.Г., Титлянов А.Е., Скрипаленко М.М. Моделирование температурного поля воздушных фурм доменных печей с помощью Deform 2D. *Металлург*. 2016;10:14–17.
2. Filatov S., Kurunov I., Tihonov D. Reserves for rising the efficiency of blast furnace process. *Proceedings of 7th European Coke and Ironmaking Congress – ECIC*. 2016;184–191.
3. Peacey J.G., Davenport W.G. *The Iron Blast Furnace: Theory and Practice*. Pergamon; 1989.
4. Majeski A., Runstedtler A., D'Alessio J., Macfadyen N. Injection of pulverized coal and natural gas into blast furnaces for iron-making: Lance positioning and design. *ISIJ International*. 2015;55(7):1377–1383. https://doi.org/10.2355/isijinternational.55.1377
5. Silaen A.K., Okosun T., Chen Y., Wu B., Zhao J., Zhao Y., D'Alessio J., Capo J., Zhou C.Q. Investigation of high rate natural gas injection through various lance designs in a blast furnace. *Iron and Steel Technology*. 2015;1(3):1536–1549.
6. Okosun T., Street S., Chen Y., Zhao J., Wu B., Zhou C.Q. Investigation of co-injection of natural gas and pulverized coal in a blast furnace. *Proceedings of the AISTech 2015*. 2015;1581–1594.
7. Murao A., Fukada K., Matsuno H., Sato M., Akaotsu S., Saito Y., Matsushita Y., Aoki H. Effect of natural gas injection point on combustion and gasification efficiency of pulverized coal under blast furnace condition. *Tetsu-to-Hagane*. 2018;104(5):243–252. https://doi.org/10.2355/tetsutohagane.TETSU-2017-087
8. Ueki Y., Yoshiie R., Naruse I., Matsuzaki S. Effect of hydrogen gas addition on combustion characteristics of pulverized coal. *Fuel Processing Technology*. 2017;161:289–294. https://doi.org/10.1016/j.fuproc.2017.02.034
9. Shen Y., Zhou Y., Zhu T., Duan G. Thermotechnical performance of an air-cooled tuyere with air cooling channels in series. *Heat and Mass Transfer*. 2017;53(1):81–98. https://doi.org/10.1007/s00231-016-1801-x
10. Pistorius P.C. Technical and economic evaluation of top gas recycling blast furnace ironmaking. *Proceedings of the Fray Int. Symp., 27 November – 1 December 2011, Cancun, Mexico.* 2011;5:223–232.
11. Filatov S.V., Kurunov I.F., Grachev S.N., etc. Blast furnace production at NLMK: Traditions, innovations, development *Ferrous Metallurgy. Bulletin of Scientific, Technical and Economic Information*. 2014;(10):30–34. (In Russ.).

    Филатов С.В., Курунов И.Ф., Грачев С.Н. и др. Доменное производство НЛМК: традиции, инновации, развитие. *Черная металлургия. Бюллетень научно-технической и экономической информации*. 2014;(10):30–34.
12. Jampani M. *Increased use of natural gas in blast furnace iron-making: Ph.D. Thesis*. Pittsburgh, PA: Carnegie Mellon University; 2016.
13. Liu X., Tang G., Silaen A.K., Street S.J., Zhou C.Q. Investigation of heat transfer phenomena in blast furnace tuyere/blowpipe region. *ASME 2017 Heat Transfer Summer Conf.* 2017:HT2017-4961. https://doi.org/10.1115/HT2017-4961

14. Zhou Z., Wang G. Effect of recycled gas temperature on coal combustion in oxygen blast furnace. *Proceedings of the 2017 6th Int. Conf. on Energy and Environmental Protection (ICEEP 2017), AER-Advances in Engineering Research*. 2017;143:1076–1079.
https://doi.org/10.2991/iceep-17.2017.186

15. Pistorius P.C., Gibson J., Jampani M. Natural gas utilization in blast furnace ironmaking: tuyere injection, shaft injection and prereduction. In: *Applications of Process Engineering Principles in Materials Processing, Energy and Environmental Technologies*. Wang S., Free M., Alam S., Zhang M., Taylor P. eds. The Minerals, Metals & Materials Series. Springer, Cham; 2017. https://doi.org/10.1007/978-3-319-51091-0_26

16. Wojewodka M.J., Keith J.P., Horvath S.D., Alter M.A., McGovern C.C. Natural gas injection maximization on C and D blast furnaces at ArcelorMittal Burns Harbor. *Proceedings of Iron & Steel Technology Conf. AISTech, 5-8 May 2014, Indianapolis, Indiana U.S.A.* 2014;767–780.

17. Loginov V.N., Netronin V.I., Shatlov V.A., etc. *Air tuyere of a blast furnace*. Patent RF no. 2191830 RF, S21V7/16; no. 2001129265/02. *Byulleten' izobretenii*. 2002;(30). (In Russ.).

Пат. 2191830 РФ, C21B7/16. *Воздушная фурма доменной печи* / Логинов В.Н., Нетронин В.И., Шатлов В.А. и др. № 2001129265/02; заявл. 30.10.01, опубл. 27.10.02; Бюл. № 30.

18. Levitskii I.A., Radyuk A.G., Titlyanov A.E., Sidorova T.Yu. Influence of the method of natural gas supplying on gas dynamics and heat transfer in air tuyere of blast furnace. *Izvestiya. Ferrous Metallurgy*. 2018;61(5):357–363. (In Russ.). https://doi.org/10.17073/0368-0797-2018-5-357-363

Левицкий И.А., Радюк А.Г., Титлянов А.Е., Сидорова Т.Ю. Влияние способа подачи природного газа на газодинамику и теплообмен в воздушной фурме доменной печи. *Известия вузов. Черная металлургия*. 2018;61(5):357–363.
https://doi.org/10.17073/0368-0797-2018-5-357-363

19. Loginov V.N., Sukhanov M.Yu., Ukhov A.D., etc. *Blowing tuyere of a blast furnace*. Patent RF no. 2245373 RF, S21V7/16; no. 2003111093/02. *Byulleten' izobretenii*. 2005;(3). (In Russ.).

Пат. 2245373 РФ, C21B7/16. *Дутьевая фурма доменной печи* / Логинов В.Н., Суханов М.Ю., Ухов А.Д. и др. № 2003111093/02; заявл. 17.04.03, опубл. 27.01.05; Бюл. № 3.

20. Gorbatyuk S.M., Tarasov Yu.S., Levitskii I.A., Radyuk A.G., Titlyanov A.E. Effect of a ceramic insert with swirler on gas dynamics and heat exchange in a blast furnace tuyere. *Izvestiya. Ferrous Metallurgy*. 2019;62(5):337-344. (In Russ.). https://doi.org/10.17073/0368-0797-2019-5-337-344

Горбатюк С.М., Тарасов Ю.С., Левицкий И.А., Радюк А.Г., Титлянов А.Е. Влияние керамической вставки с завихрителем на газодинамику и теплообмен в воздушной фурме доменной печи. *Известия вузов. Черная металлургия*. 2019;62(5):337–344.
https://doi.org/10.17073/0368-0797-2019-5-337-344

21. Zainullin L.A., Filatov S.V., Kushnarev A.V., etc. *Method of air blast tuyere cooling and supply of natural gas to a blast furnace and device for its implementation*. Patent RF no. 2449022 RF, S21V7/16; no. 2010123224/02. *Byulleten' izobretenii*. 2011;(35). (In Russ.).

Пат. 2449022 РФ, C21B7/16. *Способ охлаждения фурмы воздушного дутья и подачи природного газа в доменную печь и устройство для его осуществления* / Зайнуллин Л.А., Филатов С.В., Кушнарев А.В. и др. № 2010123224/02; заявл. 07.06.10, опубл. 20.12.11; Бюл. № 35.

22. Jampani M., Gibson J., Pistorius P.C. Increased use of natural gas in blast furnace ironmaking: Mass and energy balance calculations. *Metallurgical and Materials Transactions B*. 2019;50:1290–1299.
https://doi.org/10.1007/s11663-019-01538-8

23. Mokrinskii A.V., Shatlov V.A., Yur'ev A.B., etc. *Blast furnace air tuyere*. Patent RF no. 2280698 RF, S21V7/16; no. 2005104595/02. *Byulleten' izobretenii*. 2006;(21). (In Russ.).

Пат. 2280698 РФ, C21B7/16. *Воздушная фурма доменной* печи / Мокринский А.В., Шатлов В.А., Юрьев А.Б. и др. № 2005104595/02; заявл. 21.02.05, опубл. 27.07.06; Бюл. № 21.

24. Mikhailov A.A., Shirshov S.YA., Chernobrivets B.F. *Blast furnace air tuyere*. Certificate of authorship USSR no. 517638 СССР, C21B7/16. Publ. 15.06.76.

А.с. 517638 СССР, C21B7/16. *Фурма доменной печи* / Михайлов А.А., Ширшов С.Я., Чернобривец Б.Ф. и др. № 2103522; заявл. 10.02.75, опубл. 15.06.76.

25. Gimmel'farb A.A., Medvedev N.M., Dzhusov A.B., etc. *Blast furnace air tuyere*. Certificate of authorship USSR no. 910769 СССР, C21B7/16. Publ. 07.03.82.

А.с. 910769 СССР, C21B7/16. *Дутьевая фурма доменной печи* / Гиммельфарб А.А., Медведев Н.М., Джусов А.Б. и др. № 2956367; заявл. 21.07.80, опубл. 07.03.82.

26. Radyuk A.G., Titlyanov A.E., Yakoev A.G., Pedos S.I. Improvement in service life of blast furnace tuyeres due to gas thermal spraying. *Stal'*. 2002;(6):11–12.

27. Kirillova N.L., Radyuk A.G., Titlyanov A.E., Reducing heat loss through the surface of blast-furnace tuyeres. *Metallurgist*. 2014;57(9–10):878–882.
https://doi.org/10.1007/s11015-014-9816-3

Кириллова Н.Л., Радюк А.Г., Титлянов А.Е. Снижение тепловых потерь через поверхность воздушных фурм доменных печей. *Металлург*. 2013;(10):28–31.

28. Vinogradov E.N., Radyuk A.G., Volkov E.A., Terebov A.L., Sidorova T.Yu. Reducing heat losses through blast furnace tuyeres. *Steel in Translation*. 2019;49(11):778–782.
https://doi.org/10.3103/S0967091219110160

Виноградов Е.Н., Радюк А.Г., Волков Е.А., Теребов А.Л., Сидорова Т.Ю. Снижение тепловых потерь через воздушную фурму доменной печи. *Сталь*. 2019;(11):9–12.

29. Tarasov Yu.S., Skripalenko M.M., Radyuk A.G., Titlyanov A.E. Computer simulation of thermal and stress–strain state of blast furnace tuyeres. *Metallurgist*. 2019;62(11–12): 1083–1091. https://doi.org/10.1007/s11015-019-00760-8

Тарасов Ю.С., Скрипаленко М.М., Радюк А.Г., Титлянов А.Е. Моделирование теплового и напряженно-деформированного состояния воздушных фурм доменных печей. *Металлург*. 2018;(11):9–13.

30. Zainullin L.A., Epishin A.Y., Spirin N.A. Extending the life of blast-furnace air tuyeres. *Metallurgist*. 2018;62(3-4):322–325.
https://doi.org/10.1007/s11015-018-0663-5

Зайнуллин Л.А., Епишин А.Ю., Спирин Н.А. Повышение стойкости воздушных фурм доменных печей. *Металлург*. 2018;(4):26–28.

31. Radyuk A.G., Titlyanov A.E., Sidorova T.Yu. Effect of slurry coating on the resistance of thermal insulation insert in blast furnace air tuyere. *Metallurgist*. 2020;63(11–12):1153–1159. https://doi.org/10.1007/s11015-020-00935-8

Радюк А.Г., Титлянов А.Е., Сидорова Т.Ю. Влияние шликерного покрытия на стойкость теплоизолирующей вставки в воздушной фурме доменной печи. *Металлург*. 2019;(11):21–25.

32. Fu D., Tang G., Zhao Y., D'Alessio J., Zhou C.Q. Integration of tuyere, raceway and shaft models for predicting blast furnace process. *JOM*. 2018;70(6):951–957. https://doi.org/10.1007/s11837-017-2614-1

33. Dong Z., Wang J., Zuo H., She X., Xue Q. Analysis of gas-solid flow and shaft-injected gas distribution in an oxygen blast furnace using a discrete element method and computational fluid dynamics coupled model. *Particuology*. 2017;32:63–72. https://doi.org/10.1016/j.partic.2016.07.008

34. Radyuk A.G., Titlyanov A.E., Sidorova T.Y. Thermal state of air tuyeres in blast furnaces. *Steel in Translation*. 2016;46(9): 624–628. https://doi.org/10.3103/S0967091216090084

35. Yeh C.P., Du S.W., Tsai C.H., Yang R.J. Numerical analysis of flow and combustion behavior in tuyere and raceway of blast furnace fueled with pulverized coal and recycled top gas. *Proceedings of the ICE – Energy*. 2012;42(1):233–240. https://doi.org/10.1016/j.energy.2012.03.065

36. Chen Y., Fu D., Zhou C.Q. Numerical simulation of the co-injection of natural gas and pulverized coal in blast furnace. *Proceedings of the AISTech 2013*. 2013;573–580. https://doi.org/10.13140/RG.2.1.2948.2967

Information about the Authors

Sergei V. Albul, *Senior Lecturer of the Chair "Engineering of Technological Equipment",* National University of Science and Technology "MISIS"
ORCID: 0000-0003-1802-7378
E-mail: albul@misis.ru

Oleg A. Kobelev, *Dr. Sci. (Eng.), Prof.,* National University of Science and Technology "MISIS", *Chief Specialist of State Corporation "ROSATOM",* JSC Russian State Research Center "CNIITMASH"
E-mail: oakobelev@cniitmash.com

Igor' A. Levitskii, *Cand. Sci. (Eng.), Assist. Prof. of the Chair "Energy-Efficient and Resource-Saving Industrial Technologies",* National University of Science and Technology "MISIS"
ORCID: 0000-0002-9345-3628
E-mail: lewwwis@mail.ru

Сведения об авторах

Сергей Валерьевич Албул, *старший преподаватель кафедры «Инжиниринг технологического оборудования»,* Национальный исследовательский технологический университет «МИСИС»
ORCID: 0000-0003-1802-7378
E-mail: albul@misis.ru

Олег Анатольевич Кобелев, *д.т.н., профессор,* Национальный исследовательский технологический университет «МИСИС», *главный специалист ГК «РОСАТОМ»,* Центральный научно-исследовательский институт технологии машиностроения, ОАО НПО «ЦНИИТМАШ»
E-mail: oakobelev@cniitmash.com

Игорь Анисимович Левицкий, *к.т.н., доцент кафедры энергоэффективных и ресурсосберегающих промышленных технологий,* Национальный исследовательский технологический университет «МИСИС»
ORCID: 0000-0002-9345-3628
E-mail: lewwwis@mail.ru

Contribution of the Authors

S. V. Albul – calculations and modeling, analysis of the research results, writing the text.
O. A. Kobelev – setting the research goals and objectives, research analysis, scientific guidance.
I. A. Levitskii – concept formation, setting the research goals and objectives, scientific guidance.

Вклад авторов

С. В. Албул – проведение расчетов и моделирования, анализ результатов исследований, подготовка текста.
О. А. Кобелев – постановка целей и задач исследования, анализ исследования, научное руководство.
И. А. Левицкий – формирование концепции, постановка целей и задач исследования, научное руководство.

Received 08.06.2023
Revised 22.06.2023
Accepted 30.07.2023

Поступила в редакцию 08.06.2023
После доработки 22.06.2023
Принята к публикации 30.07.2023

Material science / Материаловедение

UDC 621.787:621.9.048
DOI 10.17073/0368-0797-2023-4-421-426

Original article
Оригинальная статья

Influence of combined electromechanical processing modes of 40Kh steel on its structure and hardness

A. S. Simachev, **T. N. Oskolkova, R. A. Shevchenko**

Siberian State Industrial University (42 Kirova Str., Novokuznetsk, Kemerovo Region – Kuzbass 654007, Russian Federation)

simachev_as@mail.ru

Abstract. The paper considers the effect of combined electromechanical processing in three different modes on the structure and hardness of the surface layers of 40Kh steel, which was in a normalized state (the original structure). The modes differ from each other by the different applied load and the number of pulses. The applied load in modes *1* and *2* (current strength 39 kA, pulse time 0.02 s, number of pulses 1) is 100 and 250 MPa, respectively. A distinctive feature of mode *3* compared to mode *2* is a greater number of pulses (two). Metallographically it was established that in all three cases a hardened surface layer of different thickness (from 300 to 1200 μm) with a hardness of 593 – 598 HV is formed, consisting of two zones (a surface zone with a structure of fine-needle martensite; a transition zone smoothly transitioning into the initial ferrite structure). The transition zone (treatment according to mode *1*) in its structure contains martensite and ferrite. The transition zone (mode *2* processing) consists of a Widemannstett structure. A more substantial surface heating zone according to this mode (700 μm) in comparison with the processing according to mode *1* (300 μm) in combination with intensive heat removal contributed to the formation of a Widmanstett structure, which is defective and unacceptable for operation. The transition zone with the processing according to mode *3* has the structure of martensite and ferrite. The formation of a defective Widmanstett structure in the transition zone does not occur, since 2 times more pulses are used during processing than in mode *2*. This contributes to the heating of the surface layer to a greater depth (1200 μm), and, consequently, the structure formation in the transition zone occurs from the intercritical interval $Ag_3 – Ag_1$.

Keywords: steel, hardness, microstructure, surface combined electromechanical processing

For citation: Simachev A.S., Oskolkova T.N., Shevchenko R.A. Influence of combined electromechanical processing modes of 40Kh steel on its structure and hardness. *Izvestiya. Ferrous Metallurgy*. 2023;66(4):421–426. https://doi.org/10.17073/0368-0797-2023-4-421-426

Исследование влияния режимов комбинированной электромеханической обработки стали марки 40Х на ее структуру и твердость

А. С. Симачёв, **Т. Н. Осколкова, Р. А. Шевченко**

Сибирский государственный индустриальный университет (Россия, 654007, Кемеровская обл. – Кузбасс, Новокузнецк, ул. Кирова, 42)

simachev_as@mail.ru

Аннотация. В работе рассмотрено влияние комбинированной электромеханической обработки по трем различным режимам на структуру и твердость поверхностных слоев стали марки 40Х в нормализованном состоянии (исходная структура). Режимы отличаются друг от друга разной приложенной нагрузкой и количеством импульсов. Приложенная нагрузка по режимам *1* и *2* (сила тока 39 кА, время импульса 0,02 с, количество импульсов 1) составляет 100 и 250 МПа. Отличительной особенностью режима *3* по сравнению с режимом *2* является большее количество импульсов (два). Металлографически установлено, что во всех трех случаях формируется упрочненный поверхностный слой разной толщины (от 300 до 1200 мкм) с твердостью 593 – 598 HV, состоящий из двух зон (поверхностной зоны со структурой мелкоигольчатого мартенсита; переходной зоны, плавно переходящей в исходную феррито-перлитную структуру). Переходная зона (обработка по режиму *1*) в своей структуре содержит мартенсит и феррит. Переходная зона (обработка по режиму *2*) состоит из видманштеттовой структуры. Более существенная по толщине поверхностная зона разогрева по этому режиму (700 мкм) по сравнению с обработкой по режиму *1* (300 мкм) в сочетании и интенсивным отводом тепла поспособствовали формированию видманштеттовой структуры, которая является дефектной и недопустимой для эксплуатации. Переходная зона при обработке по режиму *3* имеет структуру мартенсит и феррит. Формирования дефектной видманштеттовой структуры в переходной зоне не происходит, поскольку при обработке применяется в два раза больше импульсов, чем по режиму *2*. Это способствует прогреву поверхностного слоя на большую глубину (1200 мкм), и, следовательно, структурообразование в переходной зоне происходит из межкритического интервала $Ar_3 – Ar_1$.

Ключевые слова: сталь, твердость, микроструктура, поверхностная комбинированная электромеханическая обработка

Для цитирования: Симачев А.С., Осколкова Т.Н., Шевченко Р.А. Исследование влияния режимов комбинированной электромеханической обработки стали марки 40Х на ее структуру и твердость. *Известия вузов. Черная металлургия*. 2023;66(4):421–426.
https://doi.org/10.17073/0368-0797-2023-4-421-426

Introduction

The advancement of mechanical engineering in Russia is inconceivable without the integration of medium-carbon improved steels. These considered steels predominantly function under tribotechnical conditions, thus the establishment of hardened surface layers holds immense potential for substantially enhancing the dependability and longevity of machine components [1 – 3], alongside bolstering surface hardness [4; 5]. Such enhancements invariably result in an augmentation of the overall wear resistance exhibited by the utilized steel. To illustrate, the primary challenge faced by the metalworking industry lies in augmenting the wear resistance of cutting tools [6 – 8].

Currently, achieving high levels of surface hardness predominantly relies on employing diverse methodologies to harden component surfaces, aimed at generating layers and coatings with specific properties [9; 10]. An analysis of published data reveals the existence of numerous techniques for surface hardening of steels, encompassing approaches such as combined electro-mechanical and ultrasonic treatment, as well as electromechanical treatment involving dynamic force application [11 – 13].

In the context of [14; 15], the utilization of combined electromechanical processing (CEMP) emerges as an effective technique for enhancing the surface integrity of machine parts. This approach results in surface hardening through a combination of electromechanical processing (EMP) and the induction of plastic deformation within the surface layer.

Experimental

In this study, samples measuring 10×10×20 mm were employed following normalization of 40Kh steel, with a chemical composition that adheres to the specifications outlined in State Standard GOST 4543 – 2016. The process of surface hardening for these samples was executed using the CEMP technique on a MR 2517 relief welding machine, utilizing the parameters outlined in Table and visually depicted in Fig. 1.

Treatment modes of 40Kh steel by combined electromechanical processing

Режимы обработок стали марки 40Х способом комбинированной ЭМО

Mode	Current, kA	Pulse duration, s	Number of pulses	Applied load, MPa
1	39	0.02	1	100
2	39	0.02	1	250
3	39	0.02	2	250

The MR 2517 AC machine features a solitary welding transformer with a rated welding current of 25 kA and is equipped with a pneumatic drive *1* for compressing the workpieces. The machine's welding structure is configured as a rigid bracket. Current modulation within the machine is facilitated by thyristor contactors, and this current traverses specialized electrodes *2* featuring a diminished cross-sectional area. This design facilitates the attainment of elevated electric current density on the treated surface of the sample *3*. For management of the CEMP cycle is executed through contactless hardware, allowing for precise control of current, modulation, and multi-pulse switching.

The CEMP technique encompasses the application of a substantial electric current and subsequent surface plastic deformation. This amalgamation leads to the elevation of the steel surface temperature to the range of 1000 – 1300 °C [16 – 18]. In the process of rapid surface cooling, facilitated by the dissipation of heat into both the material's interior and the surrounding environment, significant phase transformations take place, leading to the occurrence of superfast hardening. This phenomenon results in the formation of martensitic structures.

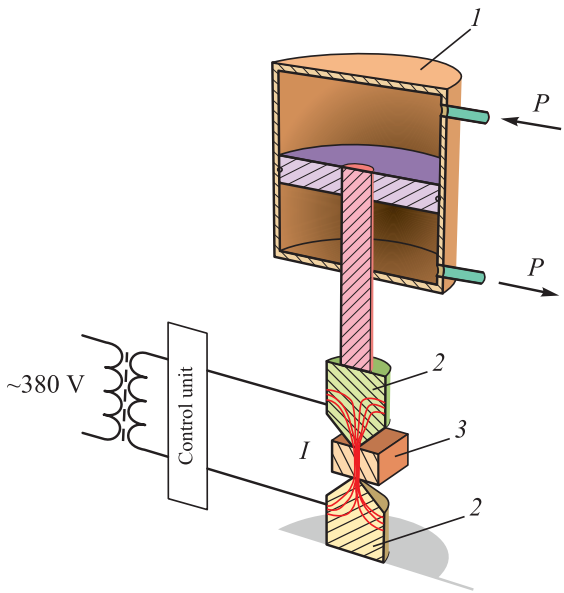

Fig. 1. Scheme of the installation for combined electromechanical processing

Рис. 1. Схема установки для комбинированной электромеханической обработки

In order to examine the hardened layers, metallographic analyses were conducted utilizing an OLIMPUS – GX 50 microscope and the HVS-1000 instrument, adhering to the protocols stipulated by State Standard GOST 2999 – 75 "Metals and Alloys. Vickers Hardness Test by Diamond Pyramid". The determination of grain size was executed following the guidelines of State Standard GOST 5639 – 82 "Steels and Alloys. Methods for Detection and Determination of Grain Size".

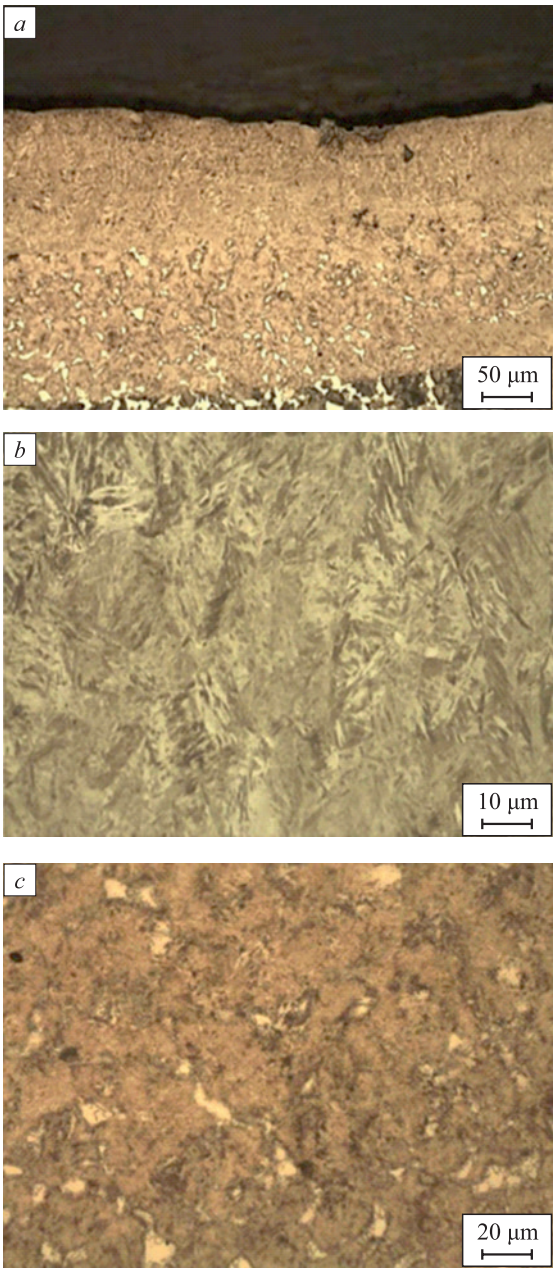

Fig. 2. Microstructure of 40Kh steel after combined electromechanical processing according to mode *1*:
a – appearance of the hardened layer;
б – external hardened zone; *в* – transition zone

Рис. 2. Микроструктура стали марки 40Х после комбинированной электромеханической обработки по режиму *1*:
а – внешний вид упрочненного слоя;
б – внешняя упрочненная зона; *в* – переходная зона

Results and discussion

The application of CEMP under mode *1* conditions (current: 39 kA, pulse duration 0.02 s, number of pulses 1, applied load 100 MPa) on the samples yielded insights through optical metallography. This analysis disclosed the development of a layer on the steel surface, encompassing two distinct zones with an aggregate thickness of 300 μm. Notably, this layer exhibited a modified microstructure when compared to the original state (Fig. 2). The initial zone, situated at the surface and extending 150 μm deep (Fig. 2, *a*, *b*), was found to comprise finely acicular martensite, characterized by a hardness value of 598 HV and a grain count of 8. In contrast, the subsequent transition zone, also 150 μm thick (Fig. 2, *a*, *c*), was identified as a composite of martensite and ferrite, exhibiting a hardness of 275 HV along with a grain count of 7. The underlying structure featured an initial composition of ferrite and pearlite, denoting a hardness level of 188 HV and a grain count of 6 [19; 20].

Samples subjected to CEMP under mode *2* conditions (current 39 kA, pulse duration 0.02 s, applied load 250 MPa, number of pulses 1) exhibit the development of a hardened layer with a substantial thickness of 700 μm (Fig. 3, *a*). This layer is characterized by a dual-zone composition: the initial (surface) zone, measuring 500 μm in depth, and possessing grain counts of 7 and 8, comprises finely acicular martensite (Fig. 3, *a*, *b*) characterized by a hardness value of 593 HV. Below lies a transition zone (Fig. 3, *a*, *c*), 200 μm in thickness, exhibiting a structure composed of pearlite and ferrite showcasing a Widmanstätten orientation. The hardness within this zone is measured at 233 HV, with grain counts of 4 and 5. The transition zone extends deeper, penetrating the initial ferrite-pearlite structure. It is important to highlight that the greater thickness of the surface heating zone observed in mode *2* (700 μm), in comparison to mode *1* (300 μm), in combination with the pronounced heat dissipation from this area, has contributed to the emergence of the Widmanstätten structure. However, this structure exhibits defects and proves unsuitable for operational use.

Processing under mode *3* was executed using the subsequent parameters: current 39 kA, pulse duration 0.02 s, applied load 250 MPa, and a pulse count of 2. The microstructural changes that emerged in the steel as a consequence of hardening through the CEMP method under mode *3* conditions are visibly presented in Fig. 4.

Upon conducting a metallographic analysis, a discernible augmentation in the thickness of the hardened layer up to 1200 μm was ascertained (Fig. 4, *a*). Analogous to preceding instances, this layer is comprised of two discernible zones. The initial zone, extending to a depth of 1000 μm from the surface and characterized by a grain count of 7, showcases a microstructure of finely acicular martensite

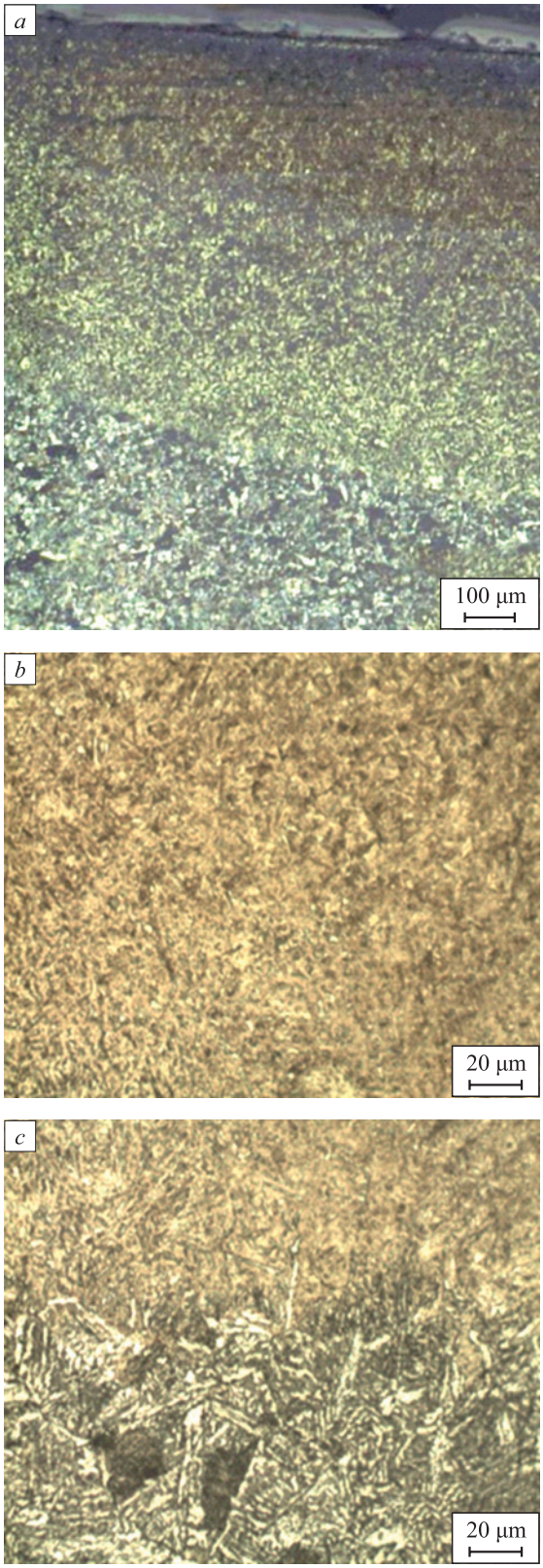

Fig. 3. Microstructure of 40Kh steel after combined electromechanical processing according to mode *2*:
a – appearance of the hardened layer;
б – external hardened zone; *в* – transition zone

Рис. 3. Микроструктура стали марки 40Х после комбинированной электромеханической обработки по режиму *2*:
а – внешний вид упрочненного слоя;
б – внешняя упрочненная зона; *в* – переходная зона

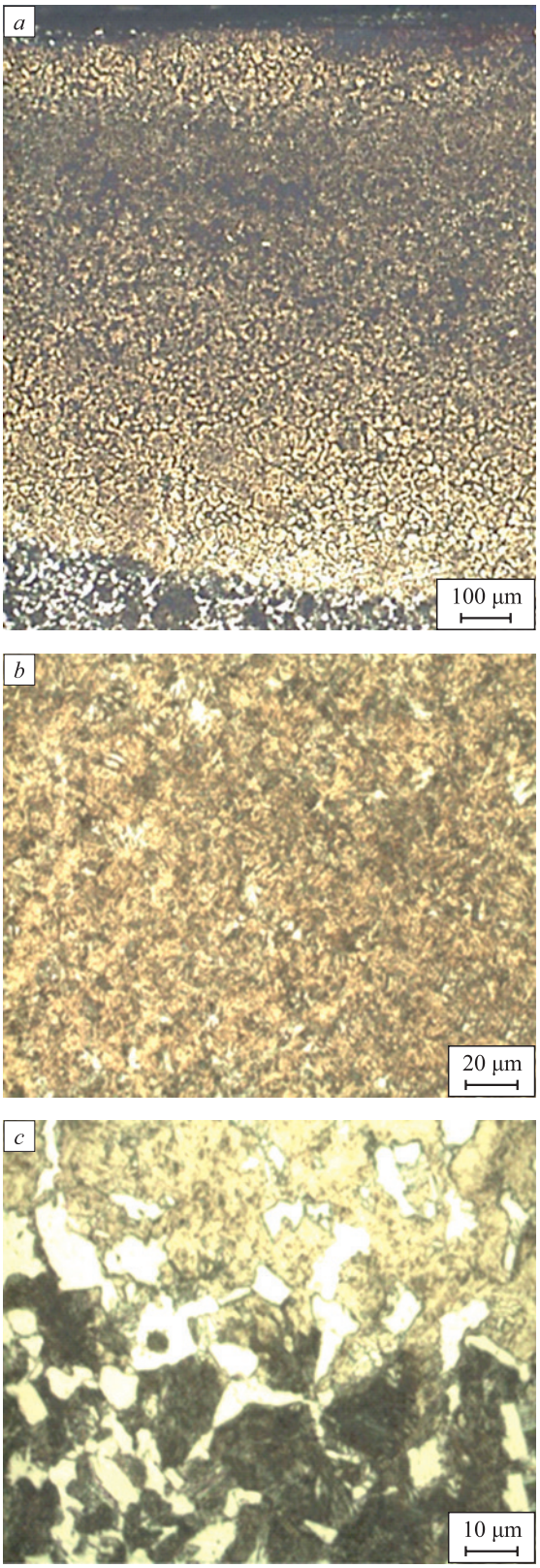

Fig. 4. Microstructure of 40Kh steel after combined electromechanical processing according to mode *3*:
a – appearance of the hardened layer;
б – external hardened zone; *в* – transition zone

Рис. 4. Микроструктура стали марки 40Х после комбинированной электромеханической обработки по режиму *3*:
а – внешний вид упрочненного слоя;
б – внешняя упрочненная зона; *в* – переходная зона

(Fig. 4, *b*), accentuated by a hardness rating of 598 HV. Beneath this surface zone, a transition zone spans 200 μm, displaying a composite structure of martensite and ferrite (with a hardness of 275 HV) and a grain count of 6 (Fig. 4, *c*). Subsequently, the hardened layer transitions seamlessly into the native ferrite and pearlite structure, marked by a grain count of 6 and a hardness of 190 HV.

A flawed Widmanstätten structure within the transition zone does not manifest as a discernible feature in metallographic analyses. This absence of identification arises from the fact that the application of treatment mode 3 on 40Kh steel leads to a more profound surface-layer heating, consequently inducing structure formation within the transition zone from the intercritical interval $Ar_3 – Ar_1$ (Fig. 4, *c*).

Conclusions

Surface layers characterized by thicknesses ranging from 300 to 1200 μm and featuring a finely acicular martensite structure exhibiting a hardness of 598 HV were successfully achieved on the 40Kh steel surface. This was accomplished through the application of combined electromechanical processing, particularly on steel structures initially present in a normalized state characterized by ferrite and pearlite. Detailed investigations underscored that the most effective treatment modes for the desired structure formation and subsequent enhancement in surface hardness are modes *1* and *3*. The surface layers obtained under these conditions consist predominantly of finely acicular martensite. Beneath this surface layer lies a transitional zone characterized by the coexistence of martensite and ferrite structures, which seamlessly transitions into the original ferrite-pearlite structure.

References / Список литературы

1. Panin S.V., Klimenov V.A., Seifullina M.P., Pochivalov Yu.I., Ovechkin B.B. Effect of ultrasonic treatment of fused gas-thermal coatings on the character of deformation and fracture of “coating – substrate” compositions at three-point bending. *Physical Mesomechanics*. 2004;7(1-2):107–116.
2. Varga G. Effects of technological parameters on the surface texture of burnished surfaces. *Engineering Materials*. 2014;581:403–408. https://doi.org/10.4028/www.scientific.net/KEM.581.403
3. Malaki M., Ding H. A review of ultrasonic peening treatment. *Materials and Design*. 2015;87:1072–1086. https://doi.org/10.1016/j.matdes.2015.11.108
4. Lu K., Lu J. Nanostructured surface layer on metallic materials induced by surface mechanical attrition treatment. *Materials Science and Engineering: A*. 2004;375–377:38–45. https://doi.org/10.1016/j.msea.2003.10.261
5. Wang Z., Lu K. Diffusion and surface alloying of gradient nanostructured metals. *Beilstein Journal of Nanotechnology*. 2017;8:547–560. https://doi.org/10.3762/bjnano.8.59
6. Sidashov A.V., Kozakov A.T., Yaresko S.I. Auger and X-Ray photoelectron spectroscopy study of the tribocontact surface after laser modification. *Materials Science Forum*. 2016;870:298–302. https://doi.org/10.4028/www.scientific.net/MSF.870.298
7. Yaresko S.I. Application features of the cutting tool, hardened by laser pulsed radiation. *Materials Science Forum*. 2016;870:46–51. https://doi.org/10.4028/www.scientific.net/MSF.870.46
8. Ogin P.A., Levashkin D.G., Yaresko S.I., Block-modular principle of build composition automatically changeable laser modules for CNC machines. *Procedia Engineering*. 2017;206:1298–1302. https://doi.org/10.1016/j.proeng.2017.10.634
9. Ivancivsky V.V., Zverev E.A., Vakhrushev N.V., Bandyurov I.V. Adhesion strength research of wear-resistant ceramic-metal plasma coatings. *Actual Problems in Machine Building*. 2016;(3):77–82.
10. Loginova M.V., Yakovlev V.I., Sitnikov A.A., Filimonov V.Yu., Sobachkin A.V., Negodyaev A.Z., Gradoboev A.V. Structural transformations in mechanically activated powder mixtures Ti + Al under the influence of γ-irradiation. *Actual Problems in Machine Building*. 2016;(3):398–404.
11. Edigarov V.R., Litau E.V., Morgunov A.P. The influence of process parameters of the electromechanical handling on its features. *Dynamics of Systems, Mechanisms and Machines (Dynamics)*. 2014:7005647. https://doi.org/10.1109/Dynamics.2014.7005647
12. Matlin M.M., Dudkina N.G., Dudkin A.D. Features of formation of the strengthened surface layer upon electromechanical treatment with dynamic effort. *Uprochnyayushchie tekhnologii i pokrytiya*. 2007;(6(30)):38–41. (In Russ.).

    Матлин М.М., Дудкина Н.Г., Дудкин А.Д. Особенности формирования упрочненного слоя при электромеханической обработке с динамическим силовым воздействием. *Упрочняющие технологии и покрытия*. 2007;(6(30)):38–41.
13. Kosogorov V.A., Bagmutov V.P., Zakharov I.N., Denisevich D.S., Kosogorova P.V. Combined surface hardening of steel based alloys on electromechanical and ultrasonic treatments. *Izvestiya Volgogradskogo gosudarstvennogo technicheskogo universiteta*. 2014;(1(128)):10–14. (In Russ.).

    Косогоров В.А., Багмутов В.П., Захаров И.Н., Денисевич Д.С., Косогорова П.В. Комбинированное поверхностное упрочнение стальных сплавов на основе электромеханической и ультразвуковой обработок. *Известия Волгоградского государственного технического университета*. 2014;(1(128)):10–14.
14. Edigarov V.R., Kilunin I.Yu., Degtyar’ V.V. Classification of combined processing methods based on electromechanical hardening. *Sovremennye naukoemkie tekhnologii*. 2012;(3):32–36. (In Russ.).

    Эдигаров В.Р., Килунин И.Ю., Дегтярь В.В. Классификация комбинированных методов обработки на основе электромеханического упрочнения. *Современные наукоемкие технологии*. 2012;(3):32–36.
15. Edigarov V.R., Malyi V.V. Improving wear resistance of details of multi-purpose tracked machines’ running gear by combined methods of electromechanical processing. *Vestnik Sibirskoi gosudarstvennoi avtomobil’no-dorozhnoi akademii*. 2014;(4(38)):57–64. (In Russ.).

    Эдигаров В.Р., Малый В.В. Повышение износостойкости деталей ходовой части многоцелевых гусеничных машин комбинированными методами электромеханичес-

кой обработки. *Вестник Сибирской государственной автомобильно-дорожной академии*. 2014;(4(38)):57–64.

16. Kirichek A.V., Soloviev D.L., Lazutkin A.G. *Technology and Equipment of Static Pulse Processing by Surface Plastic Deformation: Technologist's Library*. Moscow: Mashinostroenie; 2004:288. (In Russ.).

Киричек А.В., Соловьев Д.Л., Лазуткин А.Г. *Технология и оборудование статико-импульсной обработки поверхностным пластическим деформированием: библиотека технолога*. Москва: Машиностроение; 2004:288.

17. Edigarov V.R., Alimbaeva B.Sh., Perkov P.S. Hardening of blankets of details by electromechanical processing with additional deformation of a blanket. *Nauchnyi al'manakh*. 2016;10(3(24)):351–354. (In Russ.). https://doi.org/10.17117/na.2016.10.03.351

Эдигаров В.Р., Алимбаева Б.Ш., Перков П.С. Упрочнение поверхностных слоев деталей электромеханической обработкой с дополнительной деформацией поверхностного слоя. *Научный альманах*. 2016;10(3(24)):351–354. https://doi.org/10.17117/na.2016.10.03.351

18. Gorlenko A.O. Hardening of friction surfaces of machine parts during electromechanical processing. *Vestnik Bryanskogo gosudarstvennogo tekhnicheskogo universiteta*. 2011;(3(31)):4–8. (In Russ.).

Горленко А.О. Упрочнение поверхностей трения деталей машин при электромеханической обработке. *Вестник Брянского государственного технического университета*. 2011;(3(31)):4–8.

19. Kashin S.S., Shevchenko R.A., Oskolkova T.N. Hardening the surface of 40Kh steel by electromechanical processing. In: *Proceedings of the All-Russ. Sci. Conf. of Students, Postgraduates and Young Scientists "Science and Youth: Problems, Searches, Solutions. Part 2. Technical Sciences"*. Novokuznetsk, 2021;2:231–234. (In Russ.).

Кашин С.С., Шевченко Р.А., Осколкова Т.Н. Упрочнение поверхности стали марки 40Х способом электромеханической обработки. В кн.: *Сб. науч. трудов Всероссийской научной конференции студентов, аспирантов и молодых ученых «Наука и молодежь: проблемы, поиски, решения. Ч. 2. Технические науки»*. Новокузнецк: ИЦ СибГИУ, 2021:231–234.

20. Kashin S.S., Oskolkova T.N., Shevchenko R.A. Surface hardening of 40Kh steel by combined electromechanical processing. In: *Proceedings of the All-Russ. Sci. Conf. of Students, Postgraduates and Young Scientists "Science and Youth: Problems, Searches, Solutions. Part 2. Technical Sciences"*. Novokuznetsk, 2021;2:34–36. (In Russ.).

Кашин С.С., Осколкова Т.Н., Шевченко Р.А. Поверхностное упрочнение стали марки 40Х методом комбинированной электромеханической обработки. В кн.: *Сб. науч. трудов XXI Международной науч.-практич. конференции «Металлургия: технологии, инновации, качество. Ч. 2»*. Новокузнецк: ИЦ СибГИУ, 2021;2: 34–36.

Information about the Authors

Artem S. Simachev, *Cand. Sci. (Eng.), Assist. Prof. of the Chair "Metal Forming and Metal Science. "EVRAZ ZSMK"*, Siberian State Industrial University
ORCID: 0000-0002-9712-3757
E-mail: simachev_as@mail.ru

Tat'yana N. Oskolkova, *Dr. Sci. (Eng.), Prof. of the Chair "Metal Forming and Metal Science. "EVRAZ ZSMK"*, Siberian State Industrial University
ORCID: 0000-0003-1310-1284
E-mail: oskolkovatatiana@yandex.ru

Roman A. Shevchenko, *Cand. Sci. (Eng.), Assist. Prof. of the Chair of Ferrous Metallurgy*, Siberian State Industrial University
E-mail: shefn1200@mail.ru

Сведения об авторах

Артем Сергеевич Симачёв, *к.т.н. доцент кафедры обработки металлов давлением и металловедения. ЕВРАЗ ЗСМК*, Сибирский государственный индустриальный университет
ORCID: 0000-0002-9712-3757
E-mail: simachev_as@mail.ru

Татьяна Николаевна Осколкова, *д.т.н., профессор кафедры обработки металлов давлением и металловедения. ЕВРАЗ ЗСМК*, Сибирский государственный индустриальный университет
ORCID: 0000-0003-1310-1284
E-mail: oskolkovatatiana@yandex.ru

Роман Алексеевич Шевченко, *к.т.н., доцент кафедры металлургии черных металлов*, Сибирский государственный индустриальный университет
E-mail: shefn1200@mail.ru

Contribution of the Authors

A. S. Simachev – development of the concept of scientific research, carrying out hardening surface processing according to different modes, processing of the obtained results, writing the text.

T. N. Oskolkova – processing of the obtained results and their discussion.

R. A. Shevchenko – presentation of scheme of the installation for combined electromechanical processing, description of the principle of its operation.

Вклад авторов

А. С. Симачев – разработка концепции научных исследований, проведение упрочняющей поверхностной обработки по разным режимам, обработка полученных результатов, написание текста статьи.

Т. Н. Осколкова – обработка полученных результатов и их обсуждение.

Р. А. Шевченко – представление схемы установки для комбинированной электромеханической обработки, описание принципа ее работы.

Received 27.06.2022
Revised 10.11.2022
Accepted 14.11.2022

Поступила в редакцию 27.06.2022
После доработки 10.11.2022
Принята к публикации 14.11.2022

Material science / Материаловедение

UDC 536.425:539.25:539.351
DOI 10.17073/0368-0797-2023-4-427-433

Original article
Оригинальная статья

Structure and properties of HEA surface layer after electron-ion-plasma processing

Yu. F. Ivanov[1], **V. V. Shugurov**[1], **A. D. Teresov**[1], **E. A. Petrikova**[1], **M. O. Efimov**[2]

[1] **Institute of High Current Electronics, Siberian Branch of the Russian Academy of Sciences** (2/3 Akademicheskii Ave., Tomsk 634055, Russian Federation)
[2] **Siberian State Industrial University** (42 Kirova Str., Novokuznetsk, Kemerovo Region – Kuzbass 654007, Russian Federation)

yufi55@mail.ru

Abstract. High-entropy alloys (HEAs) are the most actively researched materials of recent decades. In the present work, the non-equiatomic AlCrFeCoNi wind turbine is manufactured using cold metal transfer technology and investigated by the methods of modern physical materials science. The authors analyzed the elemental and phase compositions, defective substructure and tribological properties of the HEA surface layer formed as a result of complex processing, which combines the deposition of a film (B + Cr) and irradiation with a pulsed electron beam in an argon medium. In the initial state, the alloy has a simple cubic lattice with a lattice parameter of 0.28795 μm, the average grain size of the HEA is 12.3 μm. Chemical composition of the HEA is as follows, at. %: 33.4 Al; 8.3 Cr; 17.1 Fe; 5.4 Co; 35.7 Ni. The elements are distributed quasi-periodically. The irradiation mode was revealed (electron-beam energy density 20 J/cm^2; irradiation duration 200 μs, number of pulses 3; pulse frequency 0.3 s^{-1}), which allows to increase microhardness (almost twice) and wear resistance (more than by five times), to reduce the friction coefficient by 1.3 times. At an electron-beam energy density of 20 J/cm^2, the surface is fragmented by a grid of microcracks. Size of the fragments varies between 40 – 200 μm. An increase in the electron-beam energy density leads to complete dissolution of the film (B + Cr). Regardless of the magnitude of the electron-beam energy density, the wind turbine is a single-phase material and has a simple cubic crystal lattice. High-speed crystallization of the surface layer leads to the formation of a subgrain structure (150 – 200 nm). It is suggested that an increase in the strength and tribological properties of wind turbines is due to a significant (by 4.5 times) decrease in the average grain size, formation of chromium and aluminum oxide particles, and introduction of boron atoms into the crystal lattice of wind turbines.

Keywords: high-entropy alloy, cold metal transfer technology, film/substrate system, electron-ion-plasma processing, elemental and phase composition, defect structure

Acknowledgements: The work was supported by the Russian Science Foundation (project No. 19-19-00183 – modification of HEA, study of the structure and properties of the modified HEA layer; and project No. 20-19-00452 – production of HEA samples using cold metal transfer technology).

For citation: Ivanov Yu. F., Shugurov V.V., Teresov A.D., Petrikova E.A., Efimov M.O. Structure and properties of HEA surface layer after electron-ion-plasma processing. *Izvestiya. Ferrous Metallurgy*. 2023;66(4):427–433. https://doi.org/10.17073/0368-0797-2023-4-427-433

Структура и свойства поверхностного слоя ВЭС после электронно-ионно-плазменной обработки

Ю. Ф. Иванов[1], **В. В. Шугуров**[1], **А. Д. Тересов**[1], **Е. А. Петрикова**[1], **М. О. Ефимов**[2]

[1] **Институт сильноточной электроники Сибирского отделения РАН** (Россия, 634055, Томск, пр. Академический, 2/3)
[2] **Сибирский государственный индустриальный университет** (Россия, 654007, Кемеровская обл. – Кузбасс, Новокузнецк, ул. Кирова, 42)

yufi55@mail.ru

Аннотация. Высокоэнтропийные сплавы (ВЭС) являются наиболее активно исследуемыми материалами последних десятилетий. В настоящей работе ВЭС неэквиатомного состава AlCrFeCoNi изготовлен по технологии холодного переноса металла и исследован методами современного физического материаловедения. Выполнен анализ элементного и фазового составов, дефектной субструктуры и трибологических свойств поверхностного слоя ВЭС, сформированного в результате комплексной обработки, которая сочетает напыление пленки (B + Cr) и облучение импульсным электронным пучком в среде аргона. В исходном состоянии сплав имеет простую кубическую

решетку с параметром 0,28795 мкм, средний размер зерна ВЭС составляет 12,3 мкм. Химический состав: 33,4 % Al; 8,3 % Cr; 17,1 % Fe; 5,4 % Co; 35,7 % Ni (ат.). Элементы распределены квазипериодически. Выявлен режим облучения (плотность энергии пучка электронов 20 Дж/см^2; длительность облучения 200 мкс, количество импульсов 3; частота импульсов 0,3 с$^{-1}$), который позволяет повысить микротвердость (почти в два раза) и износостойкость (более чем в пять раз), снизить коэффициент трения в 1,3 раза. При плотности энергии пучка электронов 20 Дж/см^2 поверхность фрагментируется сеткой микротрещин. Размеры фрагментов изменяются в пределах 40 – 200 мкм. Увеличение плотности энергии пучка электронов приводит к полному растворению пленки (B + Cr). Независимо от величины плотности энергии пучка электронов ВЭС является однофазным материалом, имеет простую кубическую кристаллическую решетку. Высокоскоростная кристаллизация поверхностного слоя приводит к формированию субзеренной структуры (150 – 200 нм). Высказывается предположение, что увеличение прочностных и трибологических свойств ВЭС обусловлено существенным (в 4,5 раза) снижением среднего размера зерна, формированием частиц оксиборидов хрома и алюминия, внедрением атомов бора в кристаллическую решетку ВЭС.

Ключевые слова: высокоэнтропийный сплав, технология холодного переноса металла, система пленка/подложка, электронно-ионно-плазменная обработка, элементный и фазовый состав, дефектная структура

Благодарности: Работа выполнена за счет гранта Российского научного фонда (проект № 19-19-00183), https://rscf.ru/project/19-19-00183/ – модифицирование ВЭС, исследование структуры и свойств модифицированного слоя ВЭС; при финансовой поддержке гранта Российского научного фонда (проект № 20-19-00452) – изготовление образцов ВЭС с помощью технологии холодного переноса металла.

Для цитирования: Иванов Ю.Ф., Шугуров В.В., Тересов А.Д., Петрикова Е.А., Ефимов М.О. Структура и свойства поверхностного слоя ВЭС после электронно-ионно-плазменной обработки. *Известия вузов. Черная металлургия*. 2023;66(4):427–433.
https://doi.org/10.17073/0368-0797-2023-4-427-433

Introduction

The development and study of high-entropy alloys (HEAs) are of significant scientific interest due to their unique microstructure [1; 2], composite composition [3], and mechanical properties [4 – 6]. In contrast to traditional alloys, which typically consist of one or two basic elements, HEAs are composed of several major elements (at least five) in equimolar or near-equimolar ratios. The original findings in the field of HEAs are extensively discussed in analytical reviews [7 – 9] and monographs (e.g., [10]). These publications describe the microstructure, properties, and thermodynamics, review the results of structural modeling, and explore novel methods for producing multi-component alloys. Substantial efforts have been dedicated to addressing the challenge of enhancing the mechanical properties of five-component alloys like MnCoCrFeNi and AlCoCrFeNi through grain boundary strengthening [11; 12], solid solution hardening [13 – 16], and interstitial solid-solution hardening [17]. Relevant theoretical developments are also in progress [18]. The paper [13] proposes a method to enhance strength through partial amorphization, as this structure lacks grain boundaries or dislocations. To improve surface properties, HEAs undergo various types of surface treatments. For example, the paper [19] reviews various processing methods and their impact on the surface of CoCrFeMnNi HEA obtained through selective laser melting. The considered treatments include electrolytic polishing, electro-erosion machining, milling, grinding, mechanical polishing with abrasives, and combinations of these methods. The results demonstrate that grinding smoothes the surface and increases microhardness, however, it leaves tool marks and residual stresses due to microstructure deformation. Mechanical polishing using abrasives enables the creation of an ultra-smooth surface without subsurface damage. Electro-erosion machining results in surface melting, leading to increased residual stresses and microhardness. When electrolytic polishing is combined with other methods, it removes residual stresses and damage caused by previous processing, thereby smoothing the surface. However, when electrolytic polishing is used in isolation from other methods, a micrometer-level surface roughness cannot be achieved. The paper [20] addresses the challenge of low strength and wear resistance in the CoCrFeMnNi alloy with an FCC crystal lattice by employing the powder-pack boriding method. This treatment results in a double layer enriched with silicon and boron, leading to increased microhardness and wear resistance in the borated samples. One of the most promising and highly efficient methods for surface hardening is electron-beam treatment [9; 10]. This treatment ensures ultrahigh heating rates of the surface layer (up to 10^6 K/s) to the specified temperatures, followed by cooling rates of 10^4 – 10^9 K/s through heat extraction into the bulk of the material. As a result, non-equilibrium submicro- and nanocrystalline structural-phase states emerge in the surface layer.

The aim of this research is to analyze the elemental and phase compositions, as well as the defect substructure of the HEA surface layer formed as a result of complex treatment, combining film deposition (B + Cr) and pulsed electron beam irradiation.

Materials and methods

The study material utilized was a HEA with the elemental composition AlCrFeCoNi, which was obtained using cold metal transfer technology [20]. The samples had dimensions of 15×15×5 mm. The surface treatment of the HEA samples was carried out in two steps: *1* – formation of a “film/substrate” system: a 0.5 μm thick boron film was deposited, and on top of it, a 0.5 μm thick chromium film was added; *2* – irradiation of the “film (B) + film (Cr)/HEA (substrate)” system with a pulsed electron beam.

The boron film was deposited onto the surface of HEA samples using plasma-assisted radio frequency sputtering (RF sputtering) of boron powder cathode. The following process parameters were applied: power W = 800 W; frequency f = 13.56 MHz; duration of processes t = 35 min (resulting in a 0.5 μm thick boron film); current of PINK plasma generator I_p = 50 A; heating current I_h = 145 A; bias voltage U_b = 50 V; duty cycle 75 %; bias frequency 50 kHz. Before applying the boron film, the surface of the HEA samples, following placement in the installation chamber and subsequent evacuation, underwent a brief 15-minute etching process with argon plasma. The 0.5 μm thick chromium film was deposited onto the samples with the boron film using an arc evaporator. The following process parameters were employed: samples with the boron film were placed opposite the arc evaporator, without rotation; arc evaporator current I_a = 80 A; plasma generator current I_p = 20 A; heating current I_h = 135 A; duty cycle 75 %; bias voltage U_b = 35 V; pressure p = 0.3 Pa; chromium deposition t = 10 min. The "film/substrate" system was then irradiated with an intense pulsed electron beam on the SOLO installation, employing the following process parameters: energy of accelerated electrons is 18 keV, energy density of the electron beam is 20 – 40 J/cm^2; pulse duration is 200 μs; number of pulses is 3; pulse repetition rate is 0.3 s^{-1}; pressure of the working gas (argon) is 0.02 Pa. Based on estimations [10], under these irradiation parameters, the temperature of the surface layer of the "film (B + Cr)/(HEA) substrate" system surpasses the melting point of the HEA. This leads to the expectation that the process of forming a molten surface layer of HEA samples alloyed with boron and chromium atoms (during rapid heating) and the subsequent development of a submicro- and nanocrystalline multiphase structure strengthened with metal borides (during rapid cooling) will occur.

The phase composition and the condition of the crystal lattice in the main phases of the sample's surface layer were investigated through *X*-ray phase and *X*-ray diffraction analysis. This analysis was conducted using a Shimadzu XRD 6000 *X*-ray diffractometer located in Kyoto, Japan. *X*-ray shooting utilized copper-filtered Cu$K_{\alpha 1}$ radiation and a CM-3121 monochromator. The phase composition was determined with reference to the PDF 4+ databases, and full-profile analysis was performed using the POWDER CELL 2.4 program. To achieve the desired film thickness, the deposition modes for the boron and chromium films were selected through experiments employing the Calotest CAT-S-0000 device, designed to determine film thickness. Material hardness was assessed using the Vickers method on a PMT-3 microhardness tester with a 0.5 N load. The tribological characteristics, including the friction coefficient and wear parameter of the material, were examined using a Pin on Disc and Oscillating TRIBOtester tribometer by TRIBOtechnic in Clichy, France. The tests were conducted with a ceramic Al_2O_3 ball, 6 mm in diameter, a 2 mm radius for the friction track, a 100 m path for the counter body's travel, a sample rotation speed of 25 mm/s, and an indenter load of 2 N. These tribological tests were performed under dry friction conditions at room temperature.

Results and discussion

The HEA produced through additive technology exhibits a dendritic structure. Dendrites are polycrystalline aggregates with an average grain size of 12.3 μm. *X*-ray microanalysis revealed that the HEA consists of the chemical elements Al, Cr, Fe, Co, and Ni in the following proportions at. %: Al 33.4; Cr 8.3; Fe 17.1; Co 5.4; Ni 35.7.

A mapping technique was employed to visualize the distribution of atoms within the alloy's bulk. The results indicate that the boundaries of grains and dendrites are enriched with chromium and iron atoms, while the volume of the grains contains higher concentrations of aluminum and nickel. Cobalt atoms are distributed in a quasi-homogeneous manner throughout the alloy's bulk.

X-ray phase analysis confirmed that the alloy in question possesses a simple cubic crystal lattice, with a crystal lattice parameter is 0.28795 nm.

Irradiation of the "film/substrate" system with a pulsed electron beam induces significant alterations in the mechanical and tribological properties of HEA samples. Firstly, there is a substantial increase in microhardness, with the maximum value achieved following irradiation of the "film/substrate" system with a pulsed electron beam having an electron beam energy density (E_s) of 20 J/cm^2 (Fig. 1, *a*). Secondly, the wear resistance of the samples improves, and the friction coefficient decreases, with the most favorable outcomes observed after irradiation of the "film/substrate" system with a pulsed electron beam having an energy density of 20 J/cm^2 (Fig. 1, *b*, *c*).

The alterations in the mechanical and tribological properties of the alloy are evidently attributed to changes in the structure of the surface layer of the samples. It was observed that when the "film/substrate" system is exposed to an electron beam with an energy density of 20 J/cm^2, the sample's surface undergoes fragmentation, forming a network of microcracks (Fig. 2, *a*). These microcracks vary in size from 40 to 200 μm, with an average size of 104 μm. Within the fragments, a grain structure becomes apparent (Fig. 2, *c*). The average grain size within the fragments measures 2.7 μm, which is 4.5 times smaller than the average grain size of the initial HEA.

With an increase in electron beam energy density, the average grain size of the HEA surface layer also increases, reaching 19 μm when E_s = 40 J/cm^2. it reaches 19 μm. It is evident that the significant reduction in the average grain size of the surface layer when

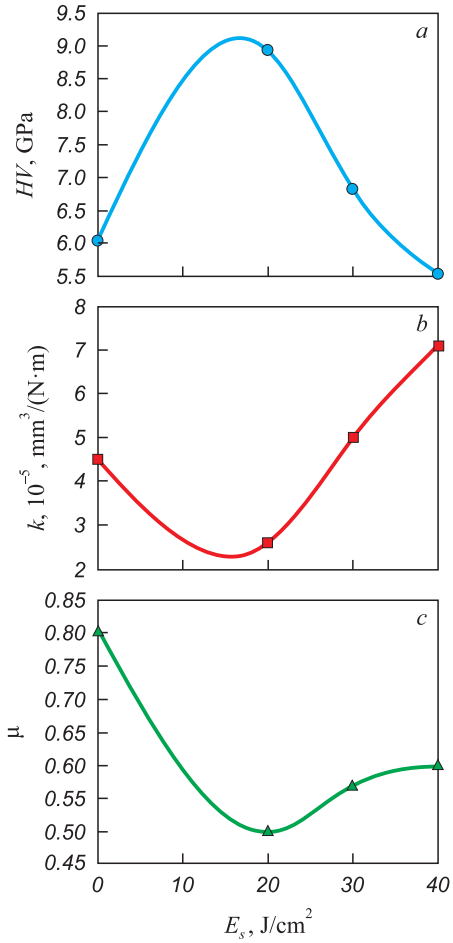

Fig. 1. Dependence of microhardness (*a*), wear parameter (*b*) and friction coefficient (*c*) of the film/substrate system surface layer on electron-beam energy density. In the initial state of wind turbine (without a sprayed film and irradiation), microhardness is 4.7 GPa, wear parameter is $14 \cdot 10^{-5}$ mm^3/(N·m), friction coefficient is 0.65

Рис. 1. Зависимость микротвердости (*a*), параметра износа (*b*) и коэффициента трения (*c*) поверхностного слоя системы «пленка/подложка» от плотности энергии пучка электронов. В исходном состоянии ВЭС (без напыленной пленки и без облучения) микротвердость 4,7 ГПа, параметр износа $14 \cdot 10^{-5}$ мм^3/(Н·м), коэффициент трения 0,65

$E_s = 20$ J/cm^2 is one of the reasons for the improvement in the alloy's strength properties, a phenomenon known as the Hall–Petch effect.

Irradiation of the "film/substrate" system with a pulsed electron beam at $E_s = 20$ J/cm^2 does not result to the complete dissolution of the film. Instead, we observe extended film interlayers within the bulk and along the boundaries of the fragments, as well as film islands situated at the junctions of the fragments (Fig. 2, *b*, *c*).

With the increase in electron beam energy density, reaching 30 J/cm^2 and subsequently 40 J/cm^2, the (B + Cr) film completely dissolves (Fig. 3). In these cases, the surface of the samples is once again fragmented by a network of microcracks, which signifies the formation of significant tensile stresses within the surface layer of the alloy as it is irradiated.

The rapid solidification of the surface layer results in the creation of a sub-grain structure, often referred to as a rapid solidification structure (Fig. 3, *c*). When $E_s = 20$ J/cm^2, the subgrain structure is infrequently observed, at $E_s = 30$ J/cm^2, it forms at the junctions of grain boundaries and fragments; and at $E_s = 40$ J/cm^2, subgrains are formed across the entire surface of the sample. The size of these subgrains remains consistent and ranges from 150 to 200 nm, independent of the energy density of the electron beam.

X-ray microanalysis was employed to demonstrate that the sections of the film that remain after irradiation of the "film/substrate" system with a pulsed elec-

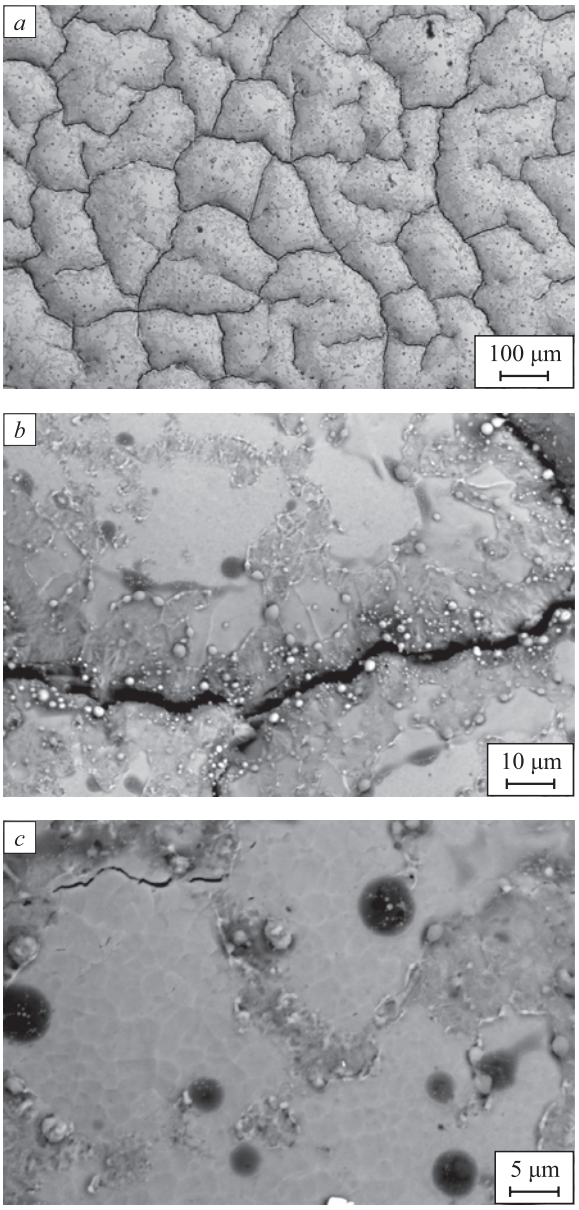

Fig. 2. Structure of the film/substrate system irradiated by a pulsed electron beam at energy density of 20 J/cm^2

Рис. 2. Структура системы «пленка/подложка», облученной импульсным электронным пучком при плотности энергии пучка электронов 20 Дж/см^2

tron beam at 20 J/cm^2 are enriched with chromium, boron, and oxygen atoms.

Additionally, extended interlayers along the fragment boundaries are observed to be enriched with oxygen and aluminum.

The islands that form on the HEA surface when the "film/substrate" system is irradiated with an electron beam, with an energy density of 30 and 40 J/cm^2, are found to be enriched with chromium, aluminum, and oxygen atoms. This indicates that, as a result of irradiation of the "film/substrate" system with a pulsed electron beam, chromium and aluminum oxiborides are formed on the HEA surface. The quantity of these oxiborides decreases as the energy density of the electron beam increases. The formation of oxiborides contributes to the enhancement of HEA microhardness and wear resistance.

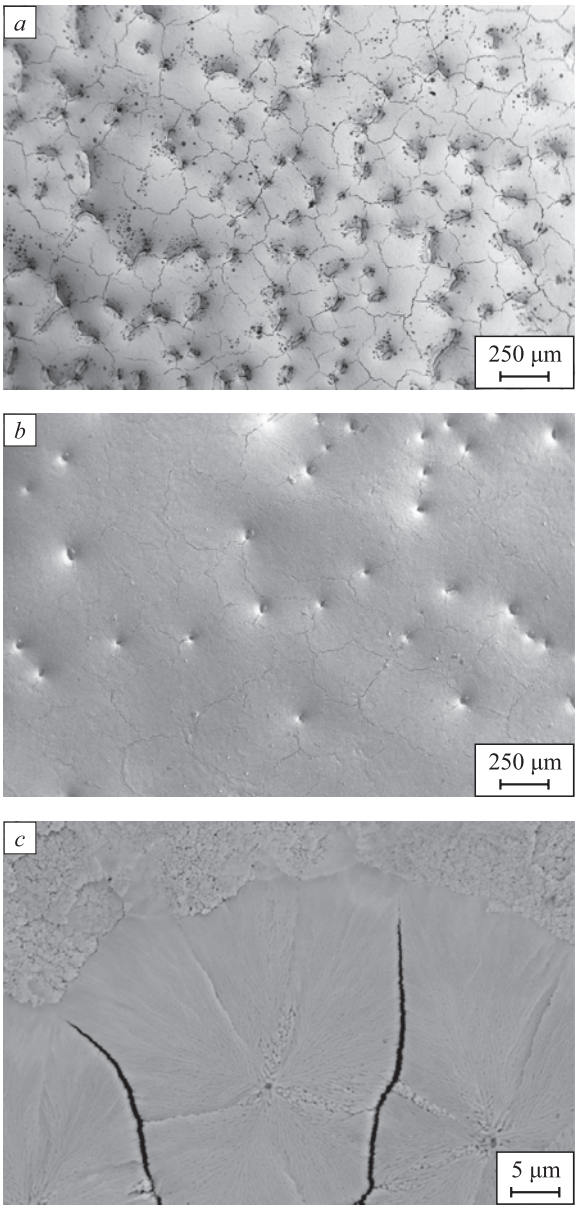

Fig. 3. Structure of the film/substrate system irradiated by a pulsed electron beam at energy density of 30 J/cm^2 (*a*) and 40 J/cm^2 (*b*, *c*)

Рис. 3. Структура системы «пленка/подложка», облученной импульсным электронным пучком при плотности энергии пучка электронов 30 Дж/см^2 (*a*) и 40 Дж/см^2 (*b*, *c*)

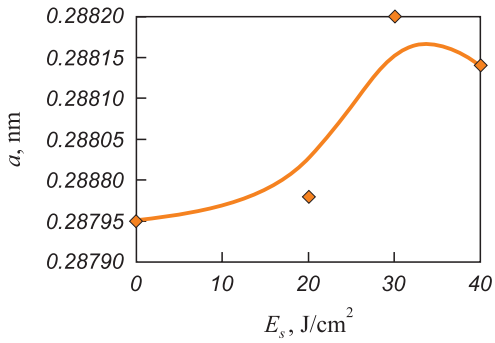

Fig. 4. Dependence of crystal lattice parameter of the film/substrate system surface layer on electron beam energy density

Рис. 4. Зависимость параметра кристаллической решетки поверхностного слоя системы «пленка/подложка» от плотности энергии пучка электронов

The phase composition of the HEA surface layer, modified due to irradiation of the "film/substrate" system with a pulsed electron beam, was investigated through *X*-ray phase analysis. Regardless of the value of E_s, the alloy remains a single-phase material with a simple cubic crystal lattice.

The lattice parameter exhibits an ambivalent dependence on the value of E_s (Fig. 4). One of the reasons for the variation in the crystal lattice parameter of the alloy is the incorporation of boron atoms into the samples, and their concentration within the bulk of the alloy increases as the energy density falls within the range $E_s = (20 – 30)$ J/cm^2. It is worth noting that the boron atoms within the HEA crystal lattice will occupy interstitial positions, leading to an increase in the lattice parameter. The formation of a solid interstitial solution is another physical mechanism contributing to the hardness of the alloy. The absence of detectable strengthening phases in the alloy under study by *X*-ray phase analysis may be attributed to their limited quantity.

Conclusions

HEA samples with non-equiatomic elemental composition AlCrFeCoNi were manufactured using cold metal transfer technology. A comprehensive treatment of the HEA samples' surface layer was carried out, combining the creation of the "film (Cr + B)/(HEA) substrate" system with subsequent irradiation using a pulsed electron beam at various electron beam energy density levels (ranging from 20 – 40 J/cm^2. The optimized irradiation mode (electron-beam energy density of 20 J/cm^2, irradiation duration of 200 μs, three pulses, pulse frequency of 0.3 s^{-1}) was identified, resulting in a significant increase in microhardness (almost double), enhanced wear

resistance (over fivefold improvement), and a 1.3-fold reduction in the friction coefficient. The conducted studies of the structure and phase composition suggested that the improvement in HEA strength and tribological properties is linked to a considerable reduction in average grain size (4.5 times smaller), the formation of chromium and aluminum oxyboride particles, and the incorporation of boron atoms into the HEA crystal lattice.

References / Список литературы

1. Shivam V., Basu J., Pandey V.K., Shadangi Y., Mukhopadhyay N.K. Alloying behaviour, thermal stability and phase evolution in quinary AlCoCrFeNi high entropy alloy. *Advanced Powder Technology*. 2018;29(9):2221–2230. https://doi.org/10.1016/j.apt.2018.06.006
2. Alshataif Y.A., Sivasankaran S., Al-Mufadi F.A., Alaboodi A.S., Ammar H.R. Manufacturing methods, microstructural and properties evolutions of high-entropy alloy: A review. *Metals and Materials International*. 2020;26:1099–1133. https://doi.org/10.1007/s12540-019-00565-z
3. Ganesh U.L., Raghavendra H. Review on the transition from conventional to multicomponent-based nano-high-entropy alloys-NHEAs. *Journal of Thermal Analysis and Calorimetry*. 2020;139:207–216. https://doi.org/10.1007/s10973-019-08360-z
4. George E.P., Curtin W.A., Tasan C.C. High entropy alloys: A focused review of mechanical properties and deformation mechanisms. *Acta Materialia*. 2020;188:435–474. https://doi.org/10.1016/j.actamat.2019.12.015
5. Cheng K.C., Chen J.H., Stadler S., Chen S.H. Properties of atomized AlCoCrFeNi high-entropy alloy powders and their phase-adjustable coatings prepared via plasma spray process. *Applied Surface Science*. 2019;478:478–486. https://doi.org/10.1016/j.apsusc.2019.01.203
6. Miracle D.B., Senkov O.N. A critical review of high entropy alloys and related concepts. *Acta Materialia*. 2017;122:448–511. https://doi.org/10.1016/j.actamat.2016.08.081
7. Zhang W., Liaw P.K., Zhang Y. Science and technology in high-entropy alloys. *Science China Materials*. 2018;61(1):2–22. https://doi.org/10.1007/s40843-017-9195-8
8. Osintsev K.A., Gromov V.E., Konovalov S.V., Ivanov Yu.F., Panchenko I.A. High-entropy alloys: Structure, mechanical properties, deformation mechanisms and application. *Izvestiya. Ferrous Metallurgy*. 2021;64(4):249–258. https://doi.org/10.17073/0368-0797-2021-4-249-258

   Осинцев К.А., Громов В.Е., Коновалов С.В., Иванов Ю.Ф., Панченко И.А. Высокоэнтропийные сплавы: структура, механические свойства, механизмы деформации и применение. *Известия вузов. Черная металлургия*. 2021;64(4):249–258. https://doi.org/10.17073/0368-0797-2021-4-249-258
9. Ivanov Yu.F., Gromov V.E., Zagulyaev D.V., Konovalov S.V., Rubannikova Yu.A., Semin A.P. Prospects for the application of surface treatment of alloys electron beams in state of the art technologies. *Progress in Physics of metals*. 2020;21(3):345–362. https://doi.org/10.15407/ufm.21.03.345

   Иванов Ю.Ф., Громов В.Е., Загуляев Д.В., Коновалов С.В., Рубанникова Ю.А., Семин А.П. Перспективы применения поверхностной обработки сплавов электронными пучками в современных технологиях. *Успехи физики металлов*. 2020;21(3):345–362. https://doi.org/10.15407/ufm.21.03.345
10. Gromov V.E., Konovalov S.V., Osintsev K.A. *Structure and Properties of High Entropy Alloys*. Springer; 2021;110.
11. Wu Z., Bei H., Pharr G.M., George E.P. Temperature dependence of the mechanical properties of equiatomic solid solution alloys with face-centered cubic crystal structures. *Acta Materialia*. 2014;81:428–441. https://doi.org/10.1016/j.actamat.2014.08.026
12. Schuh B., Mendez-Martin F., Völker B., George E.P., Clemens H., Pippan R., Hohenwarter A. Mechanical properties, microstructure and thermal stability of a nanocrystalline CoCrFeMnNi high-entropy alloy after severe plastic deformation. *Acta Materialia*. 2015;96:258–268. https://doi.org/10.1016/j.actamat.2015.06.025
13. Gali A., George E.P. Tensile properties of high- and medium-entropy alloys. *Intermetallics*. 2013;39:74–78. https://doi.org/10.1016/j.intermet.2013.03.018
14. Li Z., Tasan C.C., Springer H., Gault B., Raabe D. Interstitial atoms enable joint twinning and transformation induced plasticity in strong and ductile high-entropy alloys. *Scientific Reports*. 2017;7:40704. https://doi.org/10.1038/srep40704
15. Xiao L.L., Zheng Z.Q., Guo S.W., Huang P., Wang F. Ultra-strong nanostructured CrMnFeCoNi high entropy alloys. *Materials and Design*. 2020;194:108895. https://doi.org/10.1016/j.matdes.2020.108895
16. Coury F.G., Kaufman M., Clarke A.J. Solid-solution strengthening in refractory high entropy alloys. *Acta Materialia*. 2019;175:66–81. https://doi.org/10.1016/j.actamat.2019.06.006
17. Ikeda Y., Tanaka I., Neugebauer J., Körmann F. Impact of interstitial C on phase stability and stacking-fault energy of the CrMnFeCoNi high-entropy alloy. *Physical Review Materials*. 2019;3(11):113603. https://doi.org/10.1103/PhysRevMaterials.3.113603
18. Laplanche G., Kostka A., Horst O.M., Eggeler G., George E.P. Microstructure evolution and critical stress for twinning in the CrMnFeCoNi high-entropy alloy. *Acta Materialia*. 2016;118:152–163. https://doi.org/10.1016/j.actamat.2016.07.038
19. Guo J., Goh M., Zhu Z., Lee X., Nai M.L.S., Wei J. On the machining of selective laser melting CoCrFeMnNi high-entropy alloy. *Materials and Design*. 2018;153:211–220. https://doi.org/10.1016/j.matdes.2018.05.012
20. Lindner T., Löbel M., Sattler B., Lampke T. Surface hardening of FCC phase high-entropy alloy system by powder-pack boriding. *Surface and Coatings Technology*. 2019;371:389–394. https://doi.org/10.1016/j.surfcoat.2018.10.017

Information about the Authors

Yurii F. Ivanov, *Dr. Sci. (Phys.-Math.), Prof., Chief Researcher of the Laboratory of Plasma Emission Electronics,* Institute of High-Current Electronics, Siberian Branch of the Russian Academy of Sciences
ORCID: 0000-0001-8022-7958
E-mail: yufi55@mail.ru

Vladimir V. Shugurov, *Research Associate of the Laboratory of Plasma Emission Electronics,* Institute of High-Current Electronics, Siberian Branch of the Russian Academy of Sciences
ORCID: 0000-0001-6148-9442
E-mail: shugurov@inbox.ru

Anton D. Teresov, *Senior Researcher of the Laboratory of Plasma Emission Electronics,* Institute of High-Current Electronics, Siberian Branch of the Russian Academy of Sciences
ORCID: 0000-0002-5363-0108
E-mail: tad514@sibmail.com

Elizaveta A. Petrikova, *Junior Researcher of the Laboratory of Plasma Emission Electronics,* Institute of High-Current Electronics, Siberian Branch of the Russian Academy of Sciences
ORCID: 0000-0002-1959-1459
E-mail: elizmarkova@yahoo.com

Mikhail O. Efimov, *Candidates for a degree of Cand. Sci. (Eng.) of the Chair of Science named after V.M. Finkel',* Siberian State Industrial University
ORCID: 0000-0002-4890-3730
E-mail: moefimov@mail.ru

Сведения об авторах

Юрий Федорович Иванов, *д.ф.-м.н., профессор, главный научный сотрудник,* Институт сильноточной электроники Сибирского отделения РАН
ORCID: 0000-0001-8022-7958
E-mail: yufi55@mail.ru

Владимир Викторович Шугуров, *научный сотрудник лаборатории плазменной эмиссионной электроники,* Институт сильноточной электроники Сибирского отделения РАН
ORCID: 0000-0001-6148-9442
E-mail: shugurov@inbox.ru

Антон Дмитриевич Тересов, *старший научный сотрудник лаборатории плазменной эмиссионной электроники,* Институт сильноточной электроники Сибирского отделения РАН
ORCID: 0000-0002-5363-0108
E-mail: tad514@sibmail.com

Елизавета Алексеевна Петрикова, *младший научный сотрудник лаборатории плазменной эмиссионной электроники,* Институт сильноточной электроники Сибирского отделения РАН
ORCID: 0000-0002-1959-1459
E-mail: elizmarkova@yahoo.com

Михаил Олегович Ефимов, *соискатель степени к.т.н. кафедры естественнонаучных дисциплин им. проф. В.М. Финкеля,* Сибирский государственный индустриальный университет
ORCID: 0000-0002-4890-3730
E-mail: moefimov@mail.ru

Contribution of the Authors

Yu. F. Ivanov – scientific guidance, formation of the basic concept, goals and objectives of the study.
V. V. Shugurov – writing the text, obtaining and analyzing the data, reviewing publications on the article topic, obtaining data for analysis.
A. D. Teresov – obtaining and analyzing the data, finalizing the text.
E. A. Petrikova – analysis of the results of electron microscopic tests.

M. O. Efimov – conducting microhardness tests, data analysis.

Вклад авторов

Ю. Ф. Иванов – научное руководство, формирование основной концепции, цели и задачи исследования.
В. В. Шугуров – написание текста рукописи, получение и анализ данных, обзор публикаций по теме статьи, получение данных для анализа.
А. Д. Тересов – получение и анализ данных, доработка текста.
Е. А. Петрикова – анализ данных электронно-микроскопических исследований
М. О. Ефимов – проведение испытаний на микротвердость, анализ данных.

Received 20.07.2022
Revised 20.11.2022
Accepted 29.03.2023

Поступила в редакцию 20.07.2022
После доработки 20.11.2022
Принята к публикации 29.03.2023

Material science / Материаловедение

UDC 669.1
DOI 10.17073/0368-0797-2023-4-434-441

Original article
Оригинальная статья

Effect of morphology and volume fraction of δ-ferrite on hydrogen embrittlement of stainless steel produced by electron beam additive manufacturing

M. Yu. Panchenko, K. A. Reunova, A. S. Nifontov, E. A. Kolubaev, E. G. Astafurova

Institute of Strength Physics and Materials Science, Siberian Branch of Russian Academy of Sciences (2/4 Akademicheskii Ave., Tomsk 634055, Russian Federation)

elena.g.astafurova@ispms.ru

Abstract. The authors studied the influence of volume fraction and morphology of δ-ferrite on hydrogen embrittlement of austenitic stainless steel 08Kh19N9T obtained by electron beam additive manufacturing. It is experimentally shown that in additively-manufactured samples, long lamellae of δ-ferrite form a dense "net" of interphase boundaries (austenite/δ-ferrite, the volume fraction of the δ-phase is 20 %) and contribute to the hydrogen accumulation. Also, being the "easy" ways for the diffusion of hydrogen atoms, the dendritic lamellae of ferrite provide hydrogen transport deep into the samples. Post-production solid-solution treatment (at T = 1100 °C, 1 h) leads to a significant decrease in the fraction of δ-ferrite in steel (up to 5 %) and partial dissolution of dendritic lamellae. A decrease in the volume fraction of ferrite and a change in its morphology hinder the diffusion of hydrogen deep into the samples and its accumulation during electrolytic hydrogen-charging and subsequent deformation. It contributes to a decrease in the total concentration of hydrogen dissolved in the steel samples. Despite the lower concentration of dissolved hydrogen in the solid-solution treated samples, the solid-solution strengthening by hydrogen atoms is higher ($\Delta\sigma^{H}_{0.2}$ = 73 MPa) than for the initial samples with a high content of δ-ferrite ($\Delta\sigma^{H}_{0.2}$ = 55 MPa). The solid-solution treated samples are characterized by a smaller thickness of the brittle surface hydrogen-charged layer and a lower hydrogen embrittlement index compared to the post-produced samples (D_H = 55 ± 12 μm, I_H = 32 % for initial samples and D_H = 29 ± 7 μm, I_H = 24 % for samples after post-production solid-solution treatment).

Keywords: austenitic steel, additive technologies, hydrogen embrittlement, δ-ferrite, fracture, microstructure, mechanical properties

Acknowledgements: The work was performed within the framework of the state task of the Institute of Strength Physics and Materials Science, Siberian Branch of Russian Academy of Sciences, project No. FWRW-2022-0005. The study was conducted using the equipment of the Institute of Strength Physics and Materials Science, Siberian Branch of Russian Academy of Sciences ("Nanotech" center).
The authors express their gratitude to S.V. Astafurov, G.G. Maier, E.V. Mel'nikov, V.E. Rubtsov and S.Yu. Nikonov for their help in conducting experimental works and assistance in obtaining materials.

For citation: Panchenko M.Yu., Reunova K.A., Nifontov A.S., Kolubaev E.A. Astafurova E.G. Effect of morphology and volume fraction of δ-ferrite on hydrogen embrittlement of stainless steel produced by electron beam additive manufacturing. *Izvestiya. Ferrous Metallurgy*. 2023;66(4):434–441. https://doi.org/10.17073/0368-0797-2023-4-434-441

Влияние морфологии и объемной доли δ-феррита на водородное охрупчивание нержавеющей стали 08Х19Н9Т, полученной методом электронно-лучевого аддитивного производства

М. Ю. Панченко, К. А. Реунова, А. С. Нифонтов, Е. А. Колубаев, Е. Г. Астафурова

Институт физики прочности и материаловедения Сибирского отделения РАН (Россия, 634055, Томск, пр. Академический, 2/4)

elena.g.astafurova@ispms.ru

Аннотация. В настоящей работе изучено влияние объемной доли и морфологии δ-феррита на закономерности водородного охрупчивания образцов аустенитной нержавеющей стали 08Х19Н9Т, полученной методом электронно-лучевого аддитивного производства. Экспериментально показано, что в аддитивно-изготовленных образцах длинные дендритные ламели δ-феррита формируют плотную «сетку» межфазных границ (аустенит – δ-феррит, объемная доля δ-фазы составляет 20 %) и способствуют накоплению водорода. Дендритные ветви феррита являются «легкими» путями для диффузии атомов водорода и поэтому обеспечивают его транспорт в глубь образцов. Постпроизводственная термическая обработка (при температуре 1100 °C, в течение 1 ч) приводит к значительному уменьшению доли δ-феррита в аддитивно-полученной стали (до 5 %) и частичному растворению дендритных ламелей. Уменьшение объемной доли феррита и изменение его морфологии затрудняет диффузию водорода в глубь образца и его накопление в процессе электролитического насыщения и последующей деформации, способствует понижению общей концентрации растворенного в образцах водорода. Несмотря на меньшую концентрацию растворенного водорода в образцах, подвергнутых термообработке, твердорастворное упрочнение атомами водорода оказывается больше ($\Delta\sigma^{H}_{0,2}$ = 73 МПа), чем для исходных образцов с высокой долей δ-феррита ($\Delta\sigma^{H}_{0,2}$ = 55 МПа). Также образцы после постпроизводственной термической обработки характеризуются меньшей толщиной хрупкого поверхностного наводороженного слоя D_H и более низким коэффициентом водородного охрупчивания I_H по сравнению с исходными аддитивно-полученными образцами (D_H = 55 ± 12 мкм, I_H = 32 % для исходных образцов и D_H = 29 ± 7 мкм, I_H = 24 % для образцов после постпроизводственной термической обработки).

Ключевые слова: аустенитная сталь, аддитивные технологии, водородное охрупчивание, δ-феррит, разрушение, микроструктура, механические свойства

Благодарности: Работа выполнена в рамках государственного задания Института физики прочности и материаловедения Сибирского отделения РАН, тема № FWRW-2022-0005.
Исследования проведены с использованием оборудования ЦКП «Нанотех» (Институт физики прочности и материаловедения Сибирского отделения РАН). Авторы выражают благодарность к.ф.-м.н. С.В. Астафурову, к.ф.-м.н. Г.Г. Майер, Е.В. Мельникову, к.ф.-м.н. В.Е. Рубцову и к.ф.-м.н. С.Ю. Никонову за помощь в проведении экспериментальных исследований и получении материалов.

Для цитирования: Панченко М.Ю., Реунова К.А., Нифонтов А.С., Колубаев Е.А., Астафурова Е.Г. Влияние морфологии и объемной доли δ-феррита на водородное охрупчивание нержавеющей стали 08Х19Н9Т, полученной методом электронно-лучевого аддитивного производства. *Известия вузов. Черная металлургия*. 2023;66(4):435–441. https://doi.org/10.17073/0368-0797-2023-4-434-441

Introduction

Additive manufacturing (AM) represents a rapidly advancing domain encompassing both science and industry. It introduces a transformative approach to crafting intricate components and parts for mechanisms characterized by intricate configurations, a feat previously unattainable using conventional manufacturing techniques. The application of additive technologies holds significant potential within the burgeoning sphere of hydrogen energy. This encompasses endeavors related to hydrogen storage, transportation, and the fabrication of essential components like hydrogen fuel cells and vehicles. Stable austenitic stainless steels exhibit the highest resistance to hydrogen's adverse effects when compared to other steel categories [1; 2]. Their favorable weldability and moderate cost make them an appealing choice for utilization as foundational materials within additive technologies [3; 4]. Nevertheless, when devising components intended for operation in aggressive hydrogen-rich environments, it becomes imperative to consider the unique microstructural attributes intrinsic to this steel category that manifest during the AM process. These attributes take into account the anisotropic nature of grain structure [5; 6] and formation of the secondary phases [7 – 9].

Currently, the subject of hydrogen embrittlement in steel samples produced through AM techniques remains inadequately explored in published literature, with occasional inconsistencies in the available data. The study [10] revealed that austenitic steel AISI 304L, fabricated using laser powder AM technology, is more resistant to hydrogen embrittlement compared to conventionally obtained rolled steel. This enhanced resistance is attributed to the development of a stable austenitic phase that is resistant to phase transitions, as well as the distinctive texture of the steel brought about during powder sintering. Research presented in [11] demonstrated the heightened vulnerability of martensitic aging steel produced through selective laser melting to hydrogen embrittlement. Stainless steel 17-4 PH, featuring a coarse crystalline ferritic structure and manufactured via laser additive technologies, is more prone to the adverse effects of hydrogen than its cast counterpart [12]. Conversely, for ferritic steel 09G2S, additively produced steel using the electron beam AM method exhibits a weaker susceptibility to hydrogen embrittlement than its cast equivalent [13].

In comprehending the reasons behind the degradation of mechanical properties induced by hydrogen in additively manufactured austenitic steels – known for their resistance to hydrogen embrittlement – grasping the role of key microstructural aspects in these processes becomes crucial. Particularly, samples of austenitic steels generated through electron beam AM methods exhibit distinctive characteristics: an anisotropic grain structure and a notable proportion of the δ-phase (approximately 20 %) [6 – 8]. This study aims to strategically manipulate the morphology and volume fraction of δ-ferrite within 08Kh19N9T steel samples produced via electron beam additive manufacturing (EBAM), while keeping other structural parameters (primarily the size of austenite grains) unchanged [6].

The objective of this research is to establish patterns concerning the hydrogen embrittlement of austenitic steel

08Kh19N9T manufactured using the EBAM technique, contingent on the morphology and content of δ-ferrite in its structure.

Experimental methods

For the EBAM process, we utilized an industrial wire composed of austenitic stainless steel (ASS) 08Kh19N9T, with the following chemical composition (wt. %): Cr 17.7; Ni 9.7; Mn 1.1; Ti 0.8; Si 0.6; C 0.08; with iron constituting the remainder (wire diameter 1.2 mm). The electron beam additive manufacturing was executed within a vacuum chamber, employing the subsequent parameters: accelerating voltage of 30 kV, wire feed speed set at 180 mm/min, beam sweep spanning 45×45 mm, scanning frequency of 1 kHz, and electron beam current of 45 mA. The accumulation of material layers transpired atop an austenitic steel substrate, resulting in a final geometric configuration of the steel billet measuring 110×6×30 mm.

For the purpose of uniaxial static tension tests, flat samples resembling double blades were fashioned, with the working part dimensions at 12×3×1.5 mm. These samples were extracted from an additively manufactured steel wall. A portion of the samples were assessed in their initial state – directly following additive growth (AM-ASS) – while another subset underwent annealing at 1100°C for 1 hour, succeeded by water quenching (AM-ASS + HT). Surface treatment encompassed mechanical grinding and electrolytic polishing using a solution of 25 g CrO_3 and 200 ml H_3PO_4.

Microstructural analysis of the obtained samples was conducted using optical (OM) and transmission electron microscopy (TEM), utilizing Altami MET 1C and Jeol JEM 2100 microscopes, respectively. The magnetic phase analysis (MPA) technique was employed, specifically with an MVP-3 ferritometer (Kropus, Russia) to determine the volume fraction of the δ phase (V_δ).

Electrolytic hydrogenation was executed in a 3 % NaCl aqueous solution containing 3 g/L NH_4SCN. This procedure spanned 50 h at a current density of 50 mA/cm^2. Thermal desorption spectroscopy (TDS) investigations – centered on evaluating the rate of hydrogen liberation from specimens during gradual heating – were conducted using an automated Gas Reaction Controller LBP system (Advanced Materials Research, USA). This was executed with a heating rate of 360 °C/h, within a temperature span ranging from 25 to 400 °C. Tensile tests were carried out at room temperature, maintaining an initial strain rate of $5\cdot10^{-4}$ s^{-1}. The testing was performed employing an LFM-125 universal electromechanical testing machine (Walter+Bai AG, Switzerland). Subsequently, the fracture surfaces of the samples were meticulously analyzed using a LEO EVO 50 scanning electron microscope (SEM) (Zeiss, Germany). To estimate the thickness of the brittle hydrogen-induced layer, SEM images acquired from the fracture surfaces of hydrogenated samples were employed. The secant method was utilized for this purpose, wherein the secants were oriented perpendicular to the hydrogenated layer.

Results and discussion

Fig. 1 presents optical microscopy (OM) and transmission electron microscopy (TEM) images of samples produced via the EBAM process. Both categories of samples exhibit a dual-phase (γ + δ) configuration. Notably, the δ-ferrite lamellae emergence of the δ phase within the structure of additively manufactured samples is attributed to distinct characteristics of the EBAM process, encompassing the intricate, multistage thermal history of layers and the overall billet, as well as the diminution of nickel content within the melt, among other factors [7; 9; 14]. Subsequent heat treatment (1100 °C, 1 h) induces a reduction in the δ-ferrite con-

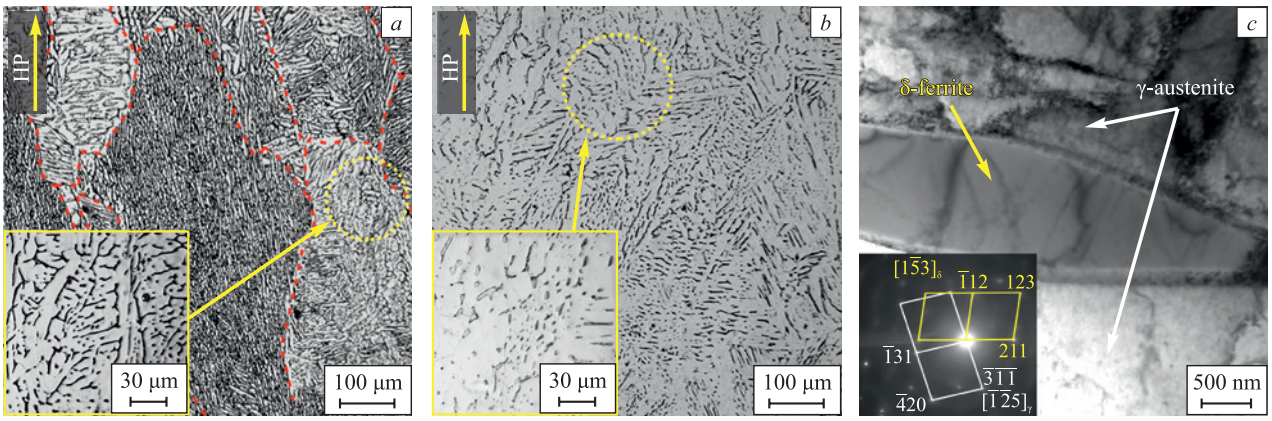

Fig. 1. OM images (*a*, *b*) and SEM image (*c*) of the samples of additive manufactured austenic stainless steel (AM-ASS) (*a*) and AM-ASS + heat treatment (HT) (*b*, *c*):
HP – direction of growth of the electron beam addive manufactured (EBAM) billet; --- – boundaries of austenitic grains

Рис. 1. ОМ-изображения (*a*, *b*) и ПЭМ-изображение (*c*) образцов АП-АНС (*a*) и АП-АНС + ТО (*b*, *c*):
НР – направление роста ЭЛАП-заготовки; --- – границы аустенитных зерен

tent while simultaneously altering its morphology – a phenomenon exhaustively elucidated in [6]. In specific, the heat treatment results in the formation of a dendritic structure of δ-ferrite, characterized by an average lamella thickness of 0.8 ± 0.4 μm within the AM-ASS samples. Following heat treatment, prolonged continuous branches (lamellae) of δ-ferrite experience partial dissolution, giving rise to non-equiaxed δ-phase grains (particles). These new grains exhibit an average thickness and length of 1.3 ± 0.5 and 6.2 ± 3.1 μm, respectively (Fig. 1, *b*). Consequently, the volume fraction of ferrite diminishes from 20 % to 5 % after the heat treatment, while the grain structure of the principal phase (austenite) remains unaffected [6]. Thus, the heat treatment exclusively influences the morphology and volume fraction of the ferrite phase, maintaining all other structural parameters unaltered.

For hydrogenated AM-ASS and AM-ASS + HT samples, their thermal desorption (TDS) spectra depict a sole peak at T_{max} = 160 – 165 °C (Fig. 2, *a*). This low-temperature peak corresponds to the release of hydrogen atoms from the crystal lattice and various weak, reversible traps possessing low activation energies. These encompass grain boundaries, interfacial (austenite – δ-ferrite) boundaries, dislocations, and similar features [15; 16]. The peak intensity for AM-ASS samples surpasses that of AM-ASS + HT samples, wherein the latter category bears a reduced proportion of the δ-phase. Hence, under analogous saturation conditions, a lesser amount of hydrogen dissolves within AM-ASS + HT samples. This disparity might arise due to the diminished presence of interphase boundaries in the annealed samples, which are capable of adsorbing hydrogen atoms. Given that the diffusion coefficient of hydrogen in δ-ferrite is significantly higher and its solubility lower than in the austenite phase [17; 18], the elevated volume fraction of the δ-phase, along with its morphology characterized by extended continuous lamellae in AM-ASS samples, expedites the profound penetration of hydrogen atoms into the samples during saturation. Put differently, the δ-ferrite branches serve as preferential conduits for the inward transport of hydrogen atoms, contributing to a more effective accumulation of hydrogen within the material (primarily within austenite). This proposition also correlates with the observation of the TDS peak shifting towards higher temperatures for AM-ASS samples in comparison to the peak for AM-ASS + HT samples. This shift could be attributed to a deeper saturation of the samples with hydrogen as the ferrite proportion increases.

Fig. 2, *b* delineates stress-strain diagrams in engineering coordinates for AM-ASS and AM-ASS + HT samples. Mechanical properties ($\sigma_{0.2}$ – yield strength; σ_u – ultimate strength; δ – elongation to fracture; $I_H = \left(\frac{\delta_0 - \delta_H}{\delta_0}\right) \cdot 100$ %; δ_0 and δ_H – elongation to fracture of unhydrogenated and hydrogenated samples) are summarized in Table.

Examination of the provided experimental data demonstrates that post-production heat treatment yields an increase in elongation to failure and a decrease in yield strength for the examined steel. This phenomenon can be attributed to a decrease in the volume fraction of δ-ferrite, as δ-ferrite possesses higher strength compared to austenite [19]. Additionally, there is a reduction in the density of interphase boundaries (austenite – δ-ferrite), which function as barriers to the movement of dislocations during deformation [6].

The process of hydrogen charging induces alterations in the mechanical properties of EBAM steel (outlined in Table). Irrespective of the ferrite content, the yield strength ($\sigma_{0.2}$) of hydrogen-charged samples surpasses that of the original samples (deformed without hydrogen charging). This experimental observation signifies solid-solution hardening of the auste-

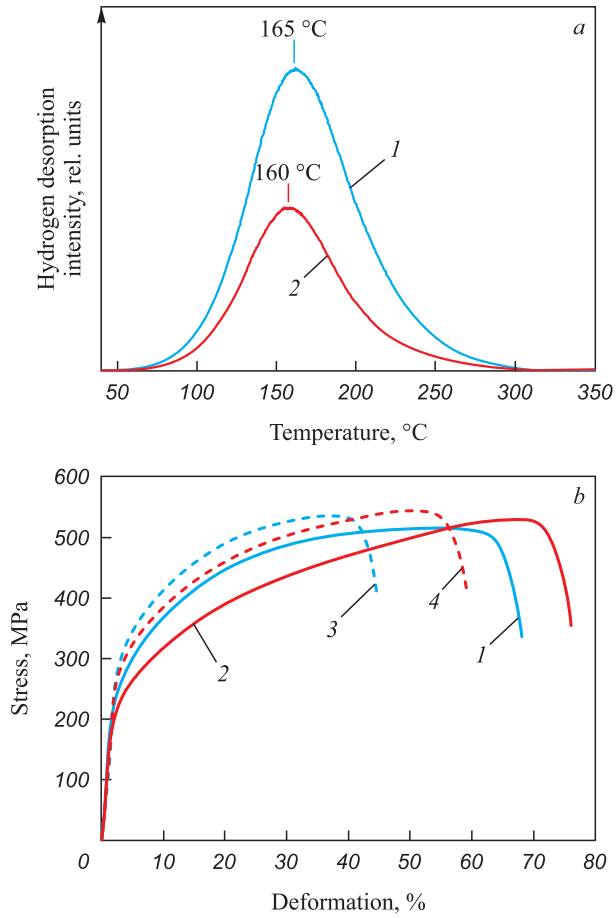

Fig. 2. Thermodesorbtion spectra (*a*) and stress–strain diagrams in engineering coordinates (*b*) (H – hydrogen-charging): *1* and *3* –AM-ASS before and after hydrogen-charging; *2* and *4* – AM-ASS + HT before and after hydrogen-charging

Рис. 2. ТДС-спектры (*a*), а также диаграммы напряжение – деформация в инженерных координатах (*b*) (H – наводороживание): *1* и *3* – АП-АНС до и после насыщения водородом; *2* и *4* – АП-АНС + ТО до и после насыщения водородом

nitic phase due to the presence of hydrogen atoms [20]. Notably, it's noteworthy that in AM-ASS + HT samples, the hydrogen-induced enhancement in yield strength ($\Delta\sigma^{H}_{0.2}$ = 73 MPa) exceeds that in AM-ASS samples ($\Delta\sigma^{H}_{0.2}$ = 55 MPa), even though, as per the results of TDS analysis, the hydrogen concentration in the latter is higher (Fig. 2, *a*). The presence of a limited volume fraction of ferrite and interfacial boundaries, which function as traps for hydrogen atoms [21], can lead to a heightened accumulation of hydrogen within the austenite grain bodies located near the saturable surface of AM-ASS + HT samples. This accumulation contributes to their solid solution hardening. On the contrary, hydrogen transport is more restricted in AM-ASS + HT samples due to the altered morphology and reduced volume fraction of ferrite, which leads to the suppression of hydrogen transport over long distances along ferrite dendrites and a decrease in the prevalence of interfacial boundaries. Consequently, AM-ASS samples amass a greater total hydrogen concentration. In these samples, the concentration gradient across depth is evidently smaller, subsequently yielding a lower level of solid solution strengthening in the austenite phase compared to AM-ASS + HT samples where hydrogen transport is curtailed. In addition to solid solution hardening, the hydrogen concentration gradient throughout the depth is intrinsically linked to the stress gradient within the tested samples – stemming from their heterogeneous hydrogen charging. This aspect becomes more pronounced in AM-ASS + HT samples where the transfer of hydrogen atoms during charging and subsequent deformation is hindered due to the alterations in morphology and the reduction in the volume fraction of ferrite [22; 23]. Therefore, even with a lower hydrogen adsorption concentration during hydrogen charging, the yield strength of AM-ASS + HT samples, wherein hydrogen transport is limited, displays increased susceptibility to hydrogen charging: the hydrogen-induced rise in yield strength is more significant in AM-ASS + HT samples compared to AM-ASS samples. However, the hydrogen embrittlement factor I_H, which quantifies the reduction in elongation to failure due to hydrogenation, is greater for AM-ASS samples (Table).

Effect of hydrogen-charging on mechanical properties of AM-ASS and AM-ASS +HT samples

Влияние наводороживания на механические свойства образцов АП-АНС и АП-АНС + ТО

Sample	$\sigma_{0.2}$, MPa	σ_u, MPa	δ, %	I_H, %
AM-ASS	220 ± 5	516 ± 7	62 ± 2	32
AM-ASS + H	275 ± 5	537 ± 2	42 ± 2	
AM-ASS + HT	192 ± 4	523 ± 8	73 ± 3	24
AM-ASS + HT + H	265 ± 3	544 ± 3	55 ± 2	

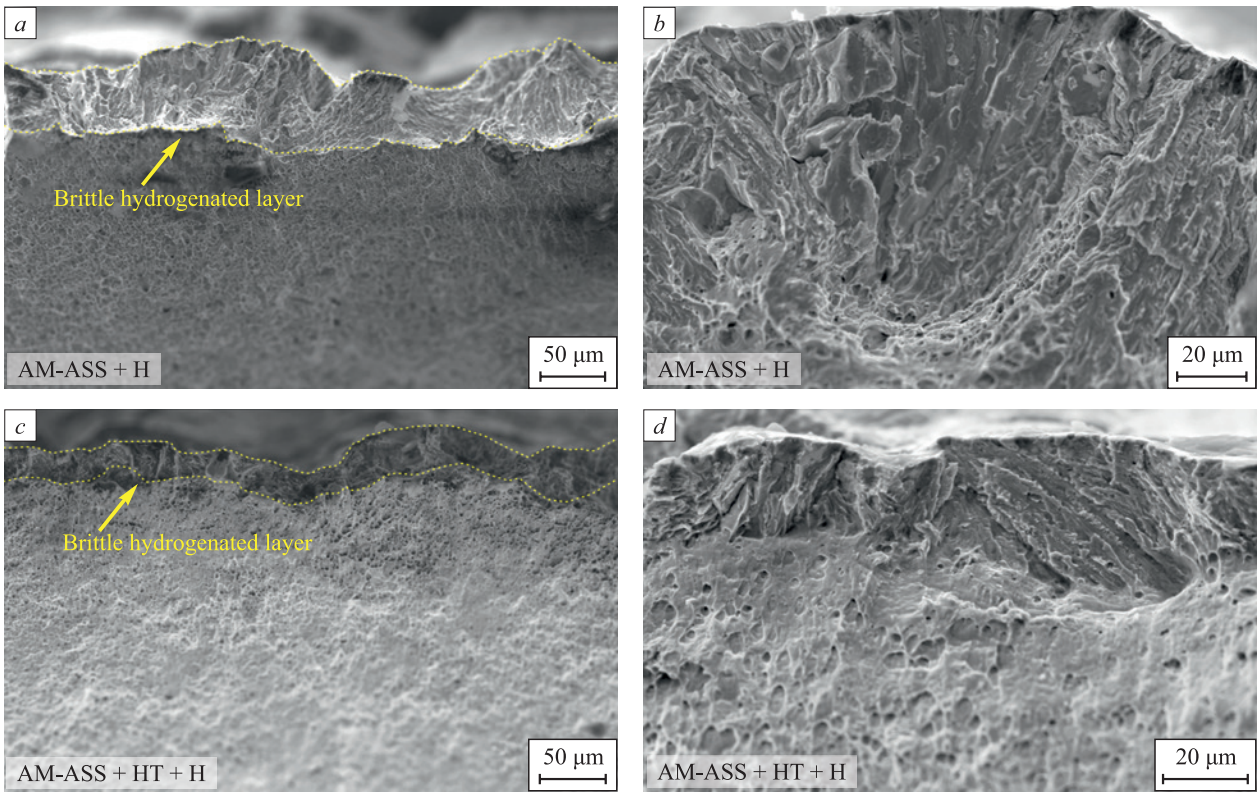

Fig. 3. SEM images of fracture surfaces of hydrogen-charged (H) AM-ASS (*a*, *b*) and AM-ASS + HT (*c*, *d*) samples

Рис. 3. СЭМ-изображения поверхностей разрушения наводороженных (H) АП-АНС (*a*, *b*) и АП-АНС + ТО (*c*, *d*) образцов

Fig. 3 portrays SEM images of fractured surfaces from both hydrogen-charged AM-ASS and AM-ASS + HT samples. Across all samples, hydrogen charging results in the formation of a brittle surface layer, while the remaining portions of the samples exhibit a ductile transcrystalline fracture mode, comparable to uncharged samples [14].

The fracture surfaces of the brittle hydrogenated layer exhibit features characteristic of both transcrystalline and intercrystalline fracture, including ridges and flat facets. The presence of intercrystalline cleavages aligns with the aforementioned mechanisms of hydrogen adsorption, specifically pointing towards the accumulation of hydrogen atoms at interphase boundaries. The transcrystalline nature of the fracture signifies the brittle fracture of hydrogen-saturated austenite grains, along with the formation of deformation-induced martensite within them, as documented in [2; 14; 23; 24].

The thickness of the brittle hydrogenated layer is notably greater for AM-ASS samples (D_H = 55 ± 12 μm) characterized by a higher initial proportion of ferrite – than for AM-ASS + HT samples (D_H = 29 ± 7 μm). This experimental observation corroborates the findings from TDS studies, mechanical tests, and the preceding discussions.

Conclusions

The investigation delved into the hydrogen embrittlement characteristics of austenitic chromium-nickel steel samples produced via electron beam additive manufacturing in two distinct states: immediately following additive growth and subsequent post-production heat treatment. Annealing the additively manufactured samples at 1100 °C for 1 h yielded a notable reduction in the volume fraction of δ-ferrite – from 20 % to 5 % – accompanied by an alteration in its morphology. Specifically, the state after EBAM exhibited thin extended lamellae of dendrites, while the heat-treated samples showcased isolated inclusions (particles) of ferrite. This transformation in phase composition and microstructure exerted an impact on the steel's susceptibility to hydrogen embrittlement, the solubility and distribution of hydrogen during the process of electrolytic saturation, and the dimensions of the brittle hydrogenated layer within the samples.

Even though the annealed samples with a lower proportion of ferrite contained a lower overall concentration of dissolved hydrogen, their hydrogen-induced increase in yield strength ($\Delta\sigma^H_{0.2}$ = 73 MPa), exceeded that of samples following EBAM, characterized by a higher proportion of dendritic ferrite ($\Delta\sigma^H_{0.2}$ = 55 MPa). This discrepancy can be attributed to the impedance of hydrogen transport deep into the samples along δ-ferrite dendrites due to modifications in their morphology and the reduction of interphase boundaries. These boundaries function as traps for hydrogen atoms within both the austenite crystal lattice and intergranular regions. Consequently, post heat treatment, hydrogen transport deep into the samples is curtailed, leading to its accumulation in the surface layers. This accumulation contributes to robust solid-solution hardening of the austenitic phase, thereby engendering a pronounced stress gradient due to the hydrogen concentration gradient in these samples.

The thickness of the brittle hydrogenated surface layer and the hydrogen embrittlement factor were found to be more significant for the initial additively manufactured steel samples (D_H = 55 ± 12 μm, I_H = 32 % for AM-ASS and D_H = 29 ± 7 μm, I_H = 24 % for AM-ASS + HT samples). The reduction in the volume fraction and the alteration in the morphology of δ-ferrite, brought about by post-production heat treatment, enhance the resistance of EBAM stainless steel to hydrogen embrittlement.

References / Список литературы

1. Michler T., Naumann J. Hydrogen embrittlement of Cr–Mn–N-austenitic stainless steels. *International Journal of Hydrogen Energy*. 2010;35(3):1485–1492. https://doi.org/10.1016/j.ijhydene.2009.10.050
2. Xu X., An J., Wen C., Niu J. Study on the hydrogen embrittlement susceptibility of AISI 321 stainless steel. *Engineering Failure Analysis*. 2021;122:105212. https://doi.org/10.1016/j.engfailanal.2020.105212
3. Bajaj P., Hariharan A., Kini A., Kurnsteiner P., Raabe D., Jagle E.A. Steels in additive manufacturing: A review of their microstructure and properties. *Materials Science and Engineering: A*. 2020;772:138633. https://doi.org/10.1016/j.msea.2019.138633
4. Li N., Huang S., Zhang G., Qin R.Y., Liu W., Xiong H., Shi G., Blackburn J. Progress in additive manufacturing on new materials: A review. *Journal of Materials Science & Technology*. 2019;35(2):242–269. https://doi.org/10.1016/j.jmst.2018.09.002
5. Tarasov S.Yu., Filippov A.V., Shamarin N.N., Fortuna S.V., Maier G.G., Kolubaev E.A. Microstructural evolution and chemical corrosion of electron beam wire-feed additively manufactured AISI 304 stainless steel. *Journal of Alloys and Compounds*. 2019;803:364–370. https://doi.org/10.1016/j.jallcom.2019.06.246
6. Astafurova E.G., Panchenko M.Yu., Moskvina V.A., Maier G.G., Astafurov S.V., Melnikov E.V., Fortuna A.S., Reunova K.A., Rubtsov V.E., Kolubaev E.A. Microstructure and grain growth inhomogeneity in austenitic steel produced by wire-feed electron beam melting: the effect of post-building solid-solution treatment. *Journal of Materials Science*. 2020;55:9211–9224. https://doi.org/10.1007/s10853-020-04424-w
7. Chen X., Li J., Cheng X., He B., Wang H., Huang Zh. Microstructure and mechanical properties of the austenitic stainless steel 316L fabricated by gas metal arc additive manufacturing. *Materials Science and Engineering: A*. 2017;703:567–677. https://doi.org/10.1016/j.msea.2017.05.024

8. Kolubaev E.A., Rubtsov V.E., Chumaevskii A.V., Astafurova E.G. Scientific approaches to micro-, meso- and macrostructural design of bulk metallic and polymetallic materials by wire-feed electron-beam additive manufacturing. *Fizicheskaya mezomekhanika*. 2022;25(4):5–18. (In Russ.). https://doi.org/10.55652/1683-805X_2022_25_4_5

Колубаев Е.А., Рубцов В.Е., Чумаевский А.В., Астафурова Е.Г. Научные подходы к микро-, мезо- и макроструктурному дизайну объемных металлических и полиметаллических материалов с использованием метода электронно-лучевого аддитивного производства. *Физическая мезомеханика*. 2022;25(4):5–18. https://doi.org/10.55652/1683-805X_2022_25_4_5

9. Astafurov S., Astafurova E. Phase composition of austenitic stainless steels in additive manufacturing: A review. *Metals*. 2021;11(7):1052. https://doi.org/10.3390/met11071052

10. Baek S.W., Song E.J., Kim J.H., Jung M., Baek U.B., Nahm S.H. Hydrogen embrittlement of 3-D printing manufactured austenitic stainless steel part for hydrogen service. *Scripta Materialia*. 2017;130:87–90. https://doi.org/10.1016/j.scriptamat.2016.11.020

11. Li S., Liu M., Ren Y., Wang Y. Hydrogen embrittlement behaviors of additive manufactured maraging steel investigated by in situ high-energy X-ray diffraction. *Materials Science and Engineering: A*. 2019;766:138341. https://doi.org/10.1016/j.msea.2019.138341

12. Alnajjar M., Christien F., Bosch C., Wolski K. A comparative study of microstructure and hydrogen embrittlement of selective laser melted and wrought 17–4PH stainless steel. *Materials Science & Engineering: A*. 2020;785:139363. https://doi.org/10.1016/j.msea.2020.139363

13. Panchenko M.Yu., Mel'nikov E.V., Astafurov S.V., Reunova K.A., Kolubaev E.A., Astafurova E.G. Features of hydrogen embrittlement of low-carbon steel obtained by electron beam additive manufacturing. *Izvestiya vuzov. Fizika*. 2022;65(6):53–60. (In Russ.). https://doi.org/10.17223/00213411/65/6/53

Панченко М.Ю., Мельников Е.В., Астафуров С.В., Реунова К.А., Колубаев Е.А., Астафурова Е.Г. Особенности водородного охрупчивания низкоуглеродистой стали, полученной методом электронно-лучевого аддитивного производства. *Известия вузов. Физика*. 2022;65(6):53–60. https://doi.org/10.17223/00213411/65/6/53

14. Yin Q., Chen G., Cao H., Zhang G., Zhang B., Wei S. Transformation law of microstructure evolution and mechanical properties of electron beam freeform fabricated 321 austenitic stainless steel. *Vacuum*. 2021;194:110594. https://doi.org/10.1016/j.vacuum.2021.110594

15. Depover T., Verbeken K. The effect of TiC on the hydrogen induced ductility loss and trapping behavior of Fe–C–Ti alloys. *Corrosion Science*. 2016;112:308–326. https://doi.org/10.1016/j.corsci.2016.07.013

16. Escobar P.D., Depover T., Duprez L., Verbeken K., Verhaege M. Combined thermal desorption spectroscopy, differential scanning calorimetry, scanning electron microscopy and X-ray diffraction study of hydrogen trapping in cold deformed TRIP steel. *Acta Materialia*. 2012;60(6-7):2593–2605. https://doi.org/10.1016/j.actamat.2012.01.026

17. Claeys L., Depover T., De Graeve I., Verbeken K. Electrochemical hydrogen charging of duplex stainless steel. *Corrosion*. 2019;75(8):880–887. https://doi.org/10.5006/2959

18. Owczarek E., Zakroczymski T. Hydrogen transport in a duplex stainless steel. *Acta Materialia*. 2000;48(12):3059–3070. https://doi.org/10.1016/S1359-6454(00)00122-1

19. Abraham D.P., Altstetter C.J. The effect of hydrogen on the yield and flow stress of an austenitic stainless steel. *Metallurgical and Materials Transactions A*. 1995;26:2849–2858. https://doi.org/10.1007/BF02669643

20. Alvarez-Armas I., Degallaix-Moreuil S. *Duplex Stainless Steels*. Wiley-ISTE; 2009:464.

21. Panchenko M.Yu., Melnikov E.V., Mikhno A.S., Maier G.G., Astafurov S.V., Moskvina V.A., Reunova K.A., Galchenko N.K., Astafurova E.G. The influence of intergranular and interphase boundaries and δ-ferrite volume fraction on hydrogen embrittlement of high-nitrogen steel. *International Journal of Hydrogen Energy*. 2021;46(59):30510–30522. https://doi.org/10.1016/j.ijhydene.2021.06.183

22. Brass A.M., Chêne J. Hydrogen uptake in 316L stainless steel: Consequences on the tensile properties. *Corrosion Science*. 2006;48(10):3222–3242. https://doi.org/10.1016/j.corsci.2005.11.004

23. Hahnenberger F., Smaga M., Eifler D. Influence of γ–α'-phase transformation in metastable austenitic steels on the mechanical behavior during tensile and fatigue loading at ambient and lower temperatures. *Advanced Engineering Materials*. 2012;14(10):853–858. https://doi.org/10.1002/adem.201100341

24. Koyama M., Tasan C.C., Tsuzaki K. Overview of metastability and compositional complexity effects for hydrogen-resistant iron alloys: Inverse austenite stability effects. *Engineering Fracture Mechanics*. 2019;214:123–133. https://doi.org/10.1016/j.engfracmech.2019.03.049

Information about the Authors

Marina Yu. Panchenko, *Junior Researcher of the Laboratory of Physics of Hierarchical Structures in Metals and Alloys,* Institute of Strength Physics and Materials Science, Siberian Branch of Russian Academy of Sciences
ORCID: 0000-0003-0236-2227
E-mail: Panchenko.marina4@gmail.com

Kseniya A. Reunova, *Postgraduate, Junior Researcher of the Laboratory of Physics of Hierarchical Structures in Metals and Alloys,* Institute of Strength Physics and Materials Science, Siberian Branch of Russian Academy of Sciences
ORCID: 0000-0002-1318-1010
E-mail: reunova.ksenya@mail.ru

Сведения об авторах

Марина Юрьевна Панченко, *младший научный сотрудник лаборатории физики иерархических структур в металлах и сплавах,* Институт физики прочности и материаловедения Сибирского отделения РАН
ORCID: 0000-0003-0236-2227
E-mail: Panchenko.marina4@gmail.com

Ксения Андреевна Реунова, *аспирант, младший научный сотрудник лаборатории физики иерархических структур в металлах и сплавах,* Институт физики прочности и материаловедения Сибирского отделения РАН
ORCID: 0000-0002-1318-1010
E-mail: reunova.ksenya@mail.ru

Aleksei S. Nifontov, *Research Laboratory Assistant of the Laboratory of Physics of Hierarchical Structures in Metals and Alloys,* Institute of Strength Physics and Materials Science, Siberian Branch of Russian Academy of Sciences
ORCID: 0000-0003-2473-8504
E-mail: trymailzero@gmail.com

Evgenii A. Kolubaev, *Dr. Sci. (Eng.), Director,* Institute of Strength Physics and Materials Science, Siberian Branch of the Russian Academy of Sciences
ORCID: 0000-0001-7288-3656
E-mail: eak@ispms.tsc.ru

Elena G. Astafurova, *Dr. Sci. (Phys.-Math.), Assist. Prof., Head of the Laboratory of Physics of Hierarchical Structures in Metals and Alloys,* Institute of Strength Physics and Materials Science, Siberian Branch of Russian Academy of Sciences
ORCID: 0000-0002-1995-4205
E-mail: elena.g.astafurova@ispms.ru

Алексей Сергеевич Нифонтов, *лаборант-исследователь лаборатории физики иерархических структур в металлах и сплавах,* Институт физики прочности и материаловедения Сибирского отделения РАН
ORCID: 0000-0003-2473-8504
E-mail: trymailzero@gmail.com

Евгений Александрович Колубаев, *д.т.н., директор,* Институт физики прочности и материаловедения Сибирского отделения РАН
ORCID: 0000-0001-7288-3656
E-mail: eak@ispms.tsc.ru

Елена Геннадьевна Астафурова, *д.ф.-м.н., доцент, заведующий лабораторией физики иерархических структур в металлах и сплавах,* Институт физики прочности и материаловедения Сибирского отделения РАН
ORCID: 0000-0002-1995-4205
E-mail: elena.g.astafurova@ispms.ru

Contribution of the Authors

M. Yu. Panchenko – literary review, analysis of the research results, writing the text, design of the article.
K. A. Reunova – literary review, conducting microstructural studies, analysis of the research results.
A. S. Nifontov – preparation of the test samples, analysis and graphical presentation of the research results.
E. A. Kolubaev – scientific guidance, reviewing and editing the article final version.
E. G. Astafurova – formation of the basic concept, scientific guidance, revision of the text.

Вклад авторов

М. Ю. Панченко – обзор литературы, анализ результатов, написание текста статьи, оформление статьи.
К. А. Реунова – обзор литературы, микроструктурные исследования и анализ результатов исследований.
А. С. Нифонтов – подготовка образцов для исследований, анализ и графическое представление результатов.
Е. А. Колубаев – научное руководство исследованиями, редактирование финальной версии статьи.
Е. Г. Астафурова – формирование основной концепции, научное руководство исследованиями, доработка текста.

Received 11.11.2022
Revised 25.11.2022
Accepted 20.04.2023

Поступила в редакцию 11.11.2022
После доработки 25.11.2022
Принята к публикации 20.04.2023

Material science / Материаловедение

UDC 669.15:621.78
DOI 10.17073/0368-0797-2023-4-442-444

Short report
Краткое сообщение

High-temperature strength of die steel with regulated austenitic transformation during exploitation after quenching and tempering

A. A. Kruglyakov[1], **S. O. Rogachev**[2, 3], **A. V. Molyarov**[2]

[1] **Scientific Production Association WBH** (106 b Friedrichstrasse, Berlin D-10117, Germany)
[2] **National University of Science and Technology "MISIS"** (4 Leninskii Ave., Moscow 119049, Russian Federation)
[3] **Baikov Institute of Metallurgy and Materials Science, Russian Academy of Sciences** (49 Leninskii Ave., Moscow 119991, Russian Federation)

csaap@mail.ru

Abstract. Steels with regulated austenitic transformation during exploitation (RATE) are a new class of ferritic-based tungsten-free tool steels for hot forming. The study obtained quantitative data on the high-temperature strength of RATE steel of new composition after quenching and tempering. The stress-strain curves are plotted and the tendency of steel to strain hardening at temperatures of 450 and 750 °C is estimated. It was established that at a temperature of 750 °C, corresponding to the operating temperature, RATE steel has a stronger tendency to work hardening than at a temperature of 450 °C.

Keywords: RATE steels, quenching, tempering, hot deformation

For citation: Kruglyakov A.A., Rogachev S.O., Molyarov A.V. High-temperature strength of die steel with regulated austenitic transformation during exploitation after quenching and tempering *Izvestiya. Ferrous Metallurgy*. 2023;66(4):442–444.
https://doi.org/10.17073/0368-0797-2023-4-442-444

Высокотемпературная прочность штамповой стали с регулируемым аустенитным превращением при эксплуатации после закалки и отпуска

А. А. Кругляков[1], **С. О. Рогачев**[2, 3], **А. В. Моляров**[2]

[1] **Научно-коммерческая фирма WBH** (Германия, D-10117, Берлин, Фридрихштрассе, 106 Б)
[2] **Национальный исследовательский технологический университет «МИСИС»** (Россия, 119049, Москва, Ленинский пр., 4)
[3] **Институт металлургии и материаловедения им. А.А. Байкова, РАН** (Россия, 119991, Москва, Ленинский пр., 49)

csaap@mail.ru

Аннотация. Стали с регулируемым аустенитным превращением при эксплуатации (РАПЭ) – новый класс безвольфрамовых инструментальных сталей на ферритной основе для горячей обработки давлением. В работе получены количественные данные по высокотемпературной прочности стали с РАПЭ нового состава после закалки и отпуска. Построены кривые деформации и проведена оценка склонности стали к деформационному упрочнению при температурах 450 и 750 °C. Установлено, что при температуре 750 °C, соответствующей эксплуатационной, сталь с РАПЭ обладает более сильной склонностью к деформационному упрочнению, чем при температуре 450 °C.

Ключевые слова: сталь с РАПЭ, закалка, отпуск, горячая деформация

Для цитирования: Кругляков А.А., Рогачев С.О., Моляров А.В. Высокотемпературная прочность штамповой стали с регулируемым аустенитным превращением при эксплуатации после закалки и отпуска. *Известия вузов. Черная металлургия*. 2023;66(4):442–444.
https://doi.org/10.17073/0368-0797-2023-4-442-444

Steels with regulated austenite transformation during exploitation (RATE) represent a novel category of tungsten-free ferritic steels designed for hot forming [1; 2]. These steels fall into either single-phase (γ) or two-phase (γ + α) region and demonstrate a propensity to maintain high-temperature hardening [3]. This effect enables the hot pre-hardening of the steel. Before being put into operation, the steel undergoes austenitization at 1150 °C, followed by a cooling process down to 450 °C. The steel retains its austenitic structure because the supercooled austenite is exceptionally stable. Subsequently, the steel becomes ready for shaping, resulting in sufficient hardness maintenance within the temperature range of 750 – 800 °C [4].

It is worth noting that RATE steels can operate at high temperatures even without pre-hardening, relying solely on quenching and tempering [5]. However, the newer, advanced RATE steel grades have not been extensively investigated in this context. Therefore, the objective of this study is to assess the high-temperature strength of the new RATE die steel after quenching and tempering.

We subjected the 5Kh2G4N3M2FSTB steel to guenching (1100 °C for 20 min in oil) and double tempering (590 °C for 2 h + 560 °C for 2 h in air) to achieve a hardness of 55 HRC [6]. The image depicts the Zwick machine employed for testing threaded cylindrical samples measuring 20 mm in length and 4 mm in diameter:

– the samples were heated to 450 °C, held for 15 min, and subsequently elongated until failure;

– the samples were heated to 450 °C, held for 15 min, and then elongated to 5 %,

– the samples were heated to 750 °C, held for 15 min, and then elongated to 5 %.

The strain hardening factor (n) was calculated as outlined in [3].

At 450 °C, the steel displayed a yield offset and ultimate strength of 1277 and 1379 MPa, respectively. The relative elongation reached 9% (as shown in the figure). This suggests that plastic deformation at 450 °C leads to strain hardening of the steel ($n = 0.03$). Under the maximum load, deformation is concentrated ultimately leading to sample failure. When the sample is deformed at 450 °C to a 5 % relative elongation, the steel hardens to 1335 MPa. Subsequent heating to 750 °C results in a significant reduction in strength, with the offset yield strength during deformation measuring 311 MPa (a quarter of that at 750 °C). However, further deformation at 750 °C enhances the steel's susceptibility to strain hardening ($n = 0.06$). The steel's strength reaches 356 MPa at approximately 2 % relative elongation, attributed to the steel's austenitization as a result of the α → γ transformation. The achieved hardening is maintained throughout further deformation, up to approximately 5 % relative elongation.

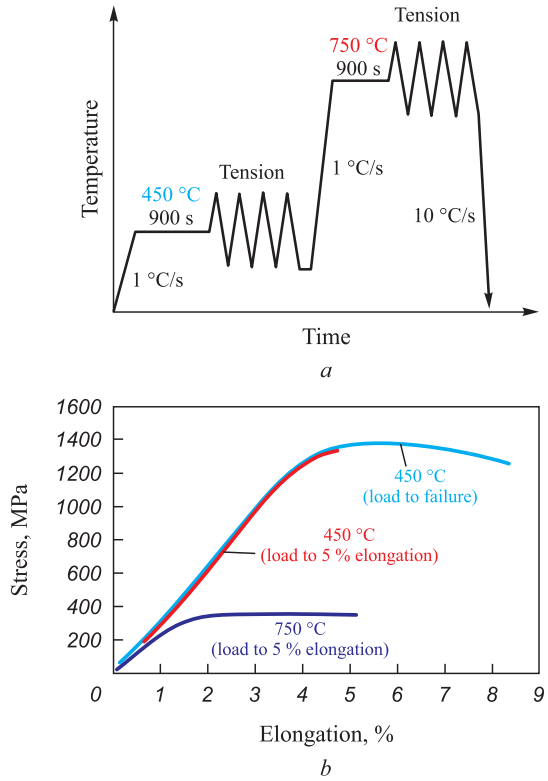

General diagram of the test process (*a*) and the corresponding stress-strain curves (*b*) of RATE steel

Общая диаграмма процесса испытания (*a*) и соответствующие кривые деформации (*b*) стали с РАПЭ

Conclusion

This study reveals that RATE steels experience strain hardening within the 450 – 750 °C operating temperature range, with higher strain hardening observed at 750 °C. The hot strength at 750 °C, with approximately 5 % relative elongation, reaches ~360 MPa. These results suggest that die tooling constructed from RATE steel can consistently operate at temperatures up to 750 °C.

Список литературы / References

1. Orlov Yu.G., Dudetskaya L.R. *Materials and Technologies for Production of Cast Die Tools*. Minsk: Belarus. Navuka; 2010:171. (In Russ.).

   Орлов Ю.Г., Дудецкая Л.Р. *Материалы и технологии изготовления литого штампового инструмента*. Минск: Беларуская навука; 2010:171.

2. Poznyak L.A. *Tool Steels*. Kyiv: Naukova Dumka; 1996:488. (In Russ.).

   Позняк Л.А. *Инструментальные стали*. Киев: Наукова думка; 1996:488.

3. Krugljakow A.A., Rogachev S.O., Lebedeva N.V., Sokolov P.Yu., Arsenkin A.M., Khatkevich V.M. On the nature of hot work hardening phenomenon in die steel with regulated austenitic transformation during exploitation. *Materials Science and Engineering: A*. 2022;833:142548. https://doi.org/10.1016/j.msea.2021.142548

4. Lebedeva N.V., Panova G.A., Kruglyakov A.A., Rogachev S.O. *Method for hardening treatment of tool from die steels*. Patent no. 2776893 RU. Publ. 28.07.2022. (In Russ.).

Пат. 2776893 RU. *Способ упрочняющей обработки инструмента из штамповых сталей* / Н.В. Лебедева, Г.А. Панова, А.А. Кругляков, С.О. Рогачев; опубл. 28.07.2022.

5. Кругляков А.А. Структура и механические свойства штамповых сталей после закалки и отпуска. *Деформация и разрушение материалов*. 2019(10):42–45. https://doi.org/10.31044/1814-4632-2019-10-42-45

Krugljakow A.A. Structure and mechanical properties of die steels after quenching and tempering. *Deformatsiya i razrushenie materialov*. 2019;(10):42–45. (In Russ.). https://doi.org/10.31044/1814-4632-2019-10-42-45

6. Nikulin S.A., Kruglyakov A.A., Rogachev S.O., Panova G.A., Lebedeva N.V. *Die steel*. Patent no. 2744584 RU. Publ. 11.03.2021.

Пат. 2744584 RU. *Штамповая сталь* / С.А. Никулин, А.А. Кругляков, С.О. Рогачев, Г.А. Панова, Н.В. Лебедева; опубл. 11.03.2021.

Information about the Authors

Aleksandr A. Kruglyakov, *Cand. Sci. (Eng.), General Director,* Scientific Production Association WBH
E-mail: dr.a.krugljakow@t-online.de

Stanislav O. Rogachev, *Cand. Sci. (Eng.), Assist. Prof. of the Chair "Metallography and Physics of Strength",* National University of Science and Technology "MISIS"; *Research Associate,* Baikov Institute of Metallurgy and Materials Science, Russian Academy of Sciences
ORCID: 0000-0001-7769-7748
E-mail: csaap@mail.ru

Aleksei V. Molyarov, *Engineer of the Chair "Metallography and Physics of Strength",* National University of Science and Technology "MISIS"
E-mail: anwil_875@mail.ru

Сведения об авторах

Александр Аркадьевич Кругляков, *к.т.н., генеральный директор,* Научно-коммерческая фирма WBH
E-mail: dr.a.krugljakow@t-online.de

Станислав Олегович Рогачев, *к.т.н., доцент кафедры металловедения и физики прочности,* Национальный исследовательский технологический университет «МИСИС»; *научный сотрудник,* Институт металлургии и материаловедения им. А.А. Байкова РАН
ORCID: 0000-0001-7769-7748
E-mail: csaap@mail.ru

Алексей Валерьевич Моляров, *инженер кафедры металловедения и физики прочности,* Национальный исследовательский технологический университет «МИСИС»
E-mail: anwil_875@mail.ru

Contribution of the Authors

A. A. Kruglyakov – conceptualization, formulation of conclusions.

S. O. Rogachev – scientific guidance, writing the text.
A. V. Molyarov – investigation, calculations.

Вклад авторов

А. А. Кругляков – формирование основной концепции, формулирование выводов.
С. О. Рогачев – научное руководство, подготовка текста.
А. В. Моляров – исследования, проведение расчетов.

Received 05.06.2023
Revised 20.06.2023
Accepted 30.07.2023

Поступила в редакцию 05.06.2023
После доработки 20.06.2023
Принята к публикации 30.07.2023

Physico-chemical basics of metallurgical processes / Физико-химические основы металлургических процессов

UDC 546.261
DOI 10.17073/0368-0797-2023-4-445-458

Review article
Обзорная статья

Carbides of transition metals: Properties, application and production. Review. Part 2. Chromium and zirconium carbides

Yu. L. Krutskii [1], **T. S. Gudyma** [1], **T. M. Krutskaya** [2], **A. O. Semenov** [3], **A. V. Utkin** [4]

[1] **Novosibirsk State Technical University** (20 K. Marksa Ave., Novosibirsk 630073, Russian Federation)
[2] **Novosibirsk State University of Architecture and Civil Engineering** (113 Leningradskaya Str., Novosibirsk 630008, Russian Federation)
[3] **National Research Tomsk Polytechnic University** (30 Lenina Str., Tomsk 634050, Russian Federation)
[4] **Institute of Solid State Chemistry and Mechanochemistry, Siberian Branch of the Russian Academy of Sciences** (18 Kutateladze Str., Novosibirsk 630090, Russian Federation)

krutskii@yandex.ru

Abstract. The properties, application, and methods for producing chromium and zirconium carbides are considered. These carbides are oxygen-free refractory metal-like compounds. As a result, they are characterized by high values of thermal and electrical conductivity. Their hardness is relatively high. Chromium and zirconium carbides exhibit significant chemical resistance in aggressive environments. For these reasons, they have found application in modern technology. Chromium carbide is used mainly as component of surfacing mixtures to create protective coatings that resist intensive abrasive wear, including at elevated temperatures (up to 800 °C) in oxidizing environments. This compound is also used in the manufacture of tungsten-free hard alloys and carbide steels. Chromium carbide, along with vanadium carbide, is used as a grain growth inhibitor in WC – Co hard alloys. Powdered zirconium carbide can be used to polish the surface of items made of ferrous and non-ferrous metals. The properties of refractory compounds depend on the content of impurities and dispersion (particle size). To solve a specific problem associated with the use of refractory compounds, it is important to choose the right method for their preparation, to determine the permissible content of impurities in the initial components. This leads to the existence of different methods for the synthesis of carbides. The main methods for their preparation are: synthesis from simple substances (metals and carbon), metallothermal and carbothermal reduction. Plasma-chemical synthesis (vapor-gas phase deposition) is also used to obtain carbide nanopowders. A characteristic is given to each of these methods. Information on the possible mechanism of the processes of carbothermal synthesis is presented.

Keywords: chromium carbide, zirconium carbide, refractory oxygen-free compounds, hardfacing, fields of application, production methods

Acknowledgements: The work was performed in accordance with the state order of the Ministry of Science and Higher Education of the Russian Federation (code FSUN-2020-0008).

For citation: Krutskii Yu.L., Gudyma T.S., Krutskaya T.M., Semenov A.O., Utkin A.V. Carbides of transition metals: Properties, application and production. Review. Part 2. Chromium and zirconium carbides. *Izvestiya. Ferrous Metallurgy*. 2023;66(4):445–458.
https://doi.org/10.17073/0368-0797-2023-4-445-458

Карбиды некоторых переходных металлов: свойства, области применения и методы получения. Часть 2. Карбиды хрома и циркония (обзор)

Ю. Л. Крутский [1], **Т. С. Гудыма** [1], **Т. М. Крутская** [2], **А. О. Семенов** [3], **А. В. Уткин** [4]

[1] **Новосибирский государственный технический университет** (Россия, 630073, Новосибирск, пр. Карла Маркса, 20)
[2] **Новосибирский государственный архитектурно-строительный университет** (Россия, 630008, Новосибирск, ул. Ленинградская, 113)
[3] **Национальный исследовательский Томский политехнический университет** (Россия, 634050, Томск, пр. Ленина 30)
[4] **Институт химии твердого тела и механохимии Сибирского отделения Российской академии наук** (Россия, 630090, Новосибирск, ул. Кутателадзе 18)

krutskii@yandex.ru

Аннотация. Рассмотрены свойства, области применения и методы получения карбидов хрома и циркония, относящихся к бескислородным тугоплавким металлоподобным соединениям с высокими тепло- и электропроводностью. Твердость их сравнительно велика. Карбиды хрома и циркония проявляют значительную химическую стойкость в агрессивных средах, что способствует их широкому применению в современной технике. Карбид хрома используется преимущественно в виде компонентов наплавочных смесей для создания покрытий, защищающих от интенсивного абразивного износа, в том числе и при повышенных температурах (до 800 °C) в окислительных средах. Это соединение применяется при изготовлении безвольфрамовых твердых сплавов и карбидосталей. Карбид хрома наряду с карбидом ванадия используется как ингибитор роста зерен в системе WC – Co твердых сплавов. Порошкообразный карбид циркония может использоваться для полирования поверхности изделий из черных и цветных металлов. Свойства тугоплавких соединений зависят от содержания примесей и дисперсности (размеров частиц). Для решения конкретной задачи, связанной с применением тугоплавких соединений, важно правильно выбрать метод их получения и определить допустимое содержание примесей в исходных компонентах. Это обусловливает применение разных методов синтеза карбидов. Основными методами их получения являются синтез из простых веществ (металлы и углерод), металлотермическое и карботермическое восстановление. Для получения нанопорошков карбидов применяется плазмохимический синтез (осаждение из парогазовой фазы). Представлена характеристика каждого из этих методов. Приведены сведения о возможном механизме процессов карботермического синтеза.

Ключевые слова: карбид хрома, карбид циркония, тугоплавкие бескислородные соединения, износостойкая наплавка, области применения, методы получения

Благодарности: Работа выполнена в соответствии с госзаданием Минобрнауки Российской Федерации (код FSUN-2023-0008).

Для цитирования: Крутский Ю.Л., Гудыма Т.С., Крутская Т.М., Семенов А.О., Уткин А.В. Карбиды некоторых переходных металлов: свойства, области применения и методы получения. Часть 2. Карбиды хрома и циркония. *Известия вузов. Черная металлургия*. 2023;66(4):446–458. https://doi.org/10.17073/0368-0797-2023-4-445-458

Introduction

Chromium and zirconium carbides exhibit a range of distinct properties, such as refractoriness, substantial chemical resistance in diverse aggressive environments, elevated hardness, as well as impressive thermal and electrical conductivity. As a result, their utilization within the realms of industry and technology has been steadily increasing. Chromium carbide finds practical application as a constituent in wear-resistant coatings, and it also serves a role in the production of tungsten-free hard alloys and carbide steels. Another avenue of application lies in its function as an inhibiting additive in tungsten carbide hard alloys. The substantial hardness of zirconium carbide renders it suitable as an abrasive for the refinement and polishing of metal products. The primary techniques for synthesizing transition metal carbides encompass carbothermal, metalthermal, and elemental source-based synthesis methods.

The objective of this study is to conduct an analysis of information pertaining to the properties, applications, and methodologies involved in the synthesis of chromium and zirconium carbides.

Basic properties of chromium and zirconium carbides

Figure depicts state diagrams for the Cr–C and Zr–C systems [1]. Within the Cr–C system, three distinct carbides ($Cr_{23}C_6$, Cr_7C_3 and Cr_3C_2) with fixed compositions are presented. Carbide Cr_3C_2 exhibits the highest melting temperature, approximately 1900 °C. When the carbon content within the considered system surpasses 40 at. %, carbon coexists with Cr_3C_2 carbide. For the production of powdered higher chromium carbides devoid of free carbon impurities, the synthesis temperature should theoretically remain below 1900 °C, aligning with the composition required for obtaining the Cr_3C_2 reaction product. In practice, even minor inconsistencies in the mixture (such as those caused by delamination during extended storage or vibration) can lead to the formation of a liquid phase within the system at temperatures as low as around 1500 °C. Hence, it is prudent to conduct the synthesis at temperatures not exceeding this threshold.

In the Zr–C system, a solitary compound, zirconium carbide, prevails, characterized by a wide range of homogeneity (approximately from 35 to 50 at. % C). Zirconium carbide ZrC boasts a melting point of about 3530 °C. A significant reduction in the melting point of zirconium carbide occurs as the carbon content diminishes (1800 °C at approximately 35 at. % C). Likewise, the microhardness experiences a notable decrease (with a C/Zr atomic ratio of 1.0, the value is 3100 kg/mm^2, and at C/Zr = 0.6, it is 1900 kg/mm^2) [2]. When the carbon content surpasses 50 at. %, carbon coexists with zirconium carbide. Consequently, to produce powdered zirconium carbide devoid of free carbon, while maintaining its high melting point and microhardness in the resulting ceramic, the synthesis temperature should not surpass 3530 °C. Moreover, the mixture's composition should align with the target reaction product, ZrC composition.

Information pertaining to certain properties of these compounds, drawn from [3], has been consolidated in Table. Both chromium and zirconium carbides exhibit robust thermodynamic stability, substantiated by their elevated heat of formation from basic elements and their isobaric-isothermal potentials. These carbides demonstrate commendably high coefficients of thermal conductivity and low resistivity, mirroring their metal-like refractory nature [4].

Examination of the chemical attributes of refractory compounds facilitates the formulation of guidelines for their application within diverse aggressive environments.

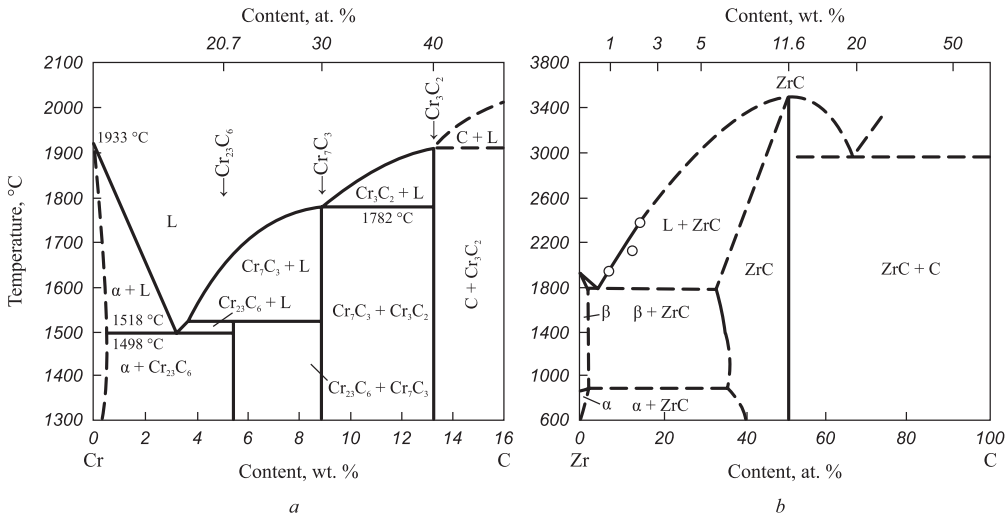

a *b*

State diagrams of the systems Cr – C (*a*) and Zr – C (*b*)

Диаграммы состояния систем Cr – C (*a*) и Zr – C (*b*)

The carbides in question exhibit stability when subjected to base solutions and numerous mineral acids. Additionally, they display resilience against the effects of elevated temperatures and atmospheric oxygen [5].

Areas of application of chromium and zirconium carbides

Application of chromium carbide

Chromium carbide is primarily employed as a constituent within surfacing mixtures, serving to create coatings that safeguard against intensive abrasive wear, including elevated temperatures of up to 800 °C within oxidizing environments. These coatings are applied through methods such as cladding or sputtering. The wear-resistant layer produced through cladding comprises chromium carbide set within a matrix of chromium, nickel [6], or chromium-nickel alloys [7 – 9]. Domestic industry has successfully mastered the production of the powder surfacing tape PL-AN111, which incorporates chromium carbide into the core powder composition. This tape finds utility in restoring surfaces within the contact and intermediate zones of blast furnace charging device cones that operate under forced conditions [10]. Another area of application lies in the creation of cermets, specifically tungsten-free hard alloys of KKhN grades (chromium carbide–nickel) [11]. Furthermore, promising prospects are observed for relatively cost-effective chromium carbide hard alloys and carbide steels with binders composed of iron and chromium, such as the Kh17N2 and Kh13M2 grades [12]. Notably, within the WC – Co hard alloy system, chromium carbide, along with vanadium carbide, serves as a grain growth inhibitor. Information regarding the properties and applications of hard alloys is expounded upon in [13]. The integration of inhibiting additives, such as these carbides, into hard alloys is commonly achieved through electrospark plasma sintering [14 – 16]. However, alternative techniques including microwave heating [17], hot isostatic pressing [18], and non-pressure sintering [19] can also be employed for this purpose. Both chromium and

Basic thermodynamic, physical and mechanical properties of chromium and zirconium carbides

Основные термодинамические, физические и механические свойства карбидов хрома и циркония

Properties	Relating to the compound	
	Cr_3C_2	ZrC
Heat of formation from elements, kJ/mol, at a temperature of 298 K	–97.91	–196.65
Isobaric-isothermal potential (Gibbs energy), kJ/mol, at a temperature of 298 K	–98.90	–193.26
Pycnometric density, kg/m^3	6880	6730
Coefficient of thermal conductivity, W/(m·K), at a temperature of 20 °C	19.1	11,6
Resistivity, μΩ·m, at a temperature of 298 K	0.75	0.49
Microhardness, GPa, at a temperature of 293 K	26.6 – 26.8	20.5 – 27.0
Coefficient of linear thermal expansion, $K^{-1}\cdot10^{-6}$, at temperatures of 300 – 1300 K	11.7	7.1
Ultimate compression strength, MPa, at a temperature of 293 K	1048	830 – 1600

vanadium carbides similarly function as grain growth inhibitors within analogues of WC–Co cermets, exemplified by composite WC – 10 wt. % Si_3N_4 [20], as well as within cermets founded upon titanium carbonitride Ti(C, N) [21]. Porous materials crafted from chromium carbide–nickel alloys exhibit marked corrosion resistance in both acidic and alkaline solutions [22]. Furthermore, chromium carbide finds application as a catalyst in the oxidation of ammonia and carbon monoxide [23].

Application of zirconium carbide

Zirconium carbide serves as an abrasive material in pastes used for the finishing and lapping of both ferrous and non-ferrous metal components [24]. Beyond its notable hardness, an added benefit lies in its relatively elevated thermal conductivity, which mitigates the risk of burns. Carbon–carbon composites (C–C) display promise as materials suited for high-temperature applications. In this context, particularly when exposed to high-speed airflow, effective protection of the (C–C) composite against high-temperature ablation is achieved through a coating of zirconium carbide. This is due to its resistant to thermal shocks [25; 26].

Chromium and zirconium carbide manufacturing methods

The properties of refractory compounds are contingent on factors like impurity content, dispersity, and stoichiometric balance. Zirconium carbide's microhardness [2] varies with its composition. Therefore, addressing specific challenges associated with refractory compounds necessitates the meticulous selection of appropriate preparation methods and the determination of acceptable impurity levels within initial constituents. This reality has led to the proliferation of diverse synthesis techniques, which are classified in [27].

The most prevalent methods for carbide synthesis encompass:

– synthesis from elemental constituents

$$xMe + y\mathrm{C} \rightarrow Me_x\mathrm{C}_y; \quad (1)$$

– metallothermal (often magnesiothermal) reduction of oxides in the presence of carbon

$$Me\mathrm{O} + \mathrm{Mg} + \mathrm{C} \rightarrow Me\mathrm{C} + \mathrm{MgO}; \quad (2)$$

– carbothermal reduction of oxides

$$Me\mathrm{O} + \mathrm{C} \rightarrow Me\mathrm{C} + \mathrm{CO}. \quad (3)$$

Synthesis reactions of refractory compounds (carbides) from elemental constituents are invariably exothermal. If the heat release reaches a threshold of 2400 kJ/kg of the mixture, the reaction initiates spontaneously. Should the heat release be inadequate, measures such as blend preheating or the utilization of mechanical activation of its components become necessary. Conversely, excessive heat release calls for the incorporation of inert additives into the mixture. These procedures are referred to as SHS processes (self-propagating high-temperature synthesis). Under optimal conditions, nearly complete conversion of the initial substances into the final products transpires, typically yielding an unreacted substance content of around 1 % by mass. Since the synthesis process is devoid of contamination, the product's purity in terms of impurities is roughly equivalent to that of the reagents [28]. Nevertheless, such processes are encumbered by the high cost of elemental powders.

During the metallothermal synthesis of carbides, it becomes imperative to subject the reaction products to treatment (typically with an acid) in order to eliminate compounds, notably oxides, stemming from the reducing metal – commonly magnesium. Owing to magnesium's comparably low boiling point (1090 °C) [29] and the substantial heat liberation inherent in magnesiothermal processes, the emission of hot blend and reaction byproducts is plausible. To preempt such scenarios, these processes are conducted within sealed reactors operating under elevated argon pressure. A notable attribute of magnesiothermal and calciumthermal reduction processes is the emergence of refractory compound particles enshrouded by layers of magnesium or calcium oxides characterized by elevated melting points [30]. Consequently, the resultant products of the reaction exhibit high dispersion. Moreover, it's essential to factor in the high cost and toxic nature of powdered magnesium [31].

It is widely considered [4; 32] that the carbothermal synthesis of carbides stands as the most promising approach for the large-scale production of these compounds. In the carbothermal method for obtaining transition metal carbides, the reagents utilized are typically non-toxic. The processes of carbide formation occur within the solid phase. Given the endothermic nature of carbide formation, these processes are conducted at elevated temperatures. To optimize synthesis parameters, the carbon monoxide (CO) pressure is reduced by performing the process in an inert gas environment or under vacuum conditions. Carbothermal reduction can also be accomplished via the sol–gel method. A distinctive trait of this approach lies in its relatively lower synthesis temperatures, which arise from the close contact between reagents within ultra-dispersed blends [3]. The resultant products are in a nanodispersed state. Nonetheless, drawbacks of the sol–gel method encompass the use of toxic reagents in several syntheses, the intricacy (including duration and multi-stage nature) of batch preparation processes, and the occurrence of incomplete reaction conversion in certain cases.

Higher chromium carbide manufacturing method

Synthesis through chromium and carbon

For chromium carbide Cr_3C_2, the heat of formation aligns closely with its enthalpy at relatively low tem-

peratures (approximately 1140 K) [3]. As a result, initiating the SHS process for a mixture of chromium and carbon at ambient temperature is impractical. Instead, this synthesis can be realized through preheating the mixture. In the case at hand, mixture's mechanical activation typically preceded the SHS process.

Mechanical activation alone doesn't inherently lead to the synthesis of chromium carbides. Research conducted in [33] demonstrated that fullerenes exhibit greater reactivity compared to graphite. While mechanical activation aids in reducing synthesis parameters (for instance, the process temperature for Cr_3C_2 carbide synthesis can be lowered by around 200 °C) [34], incomplete carbide formation reactions were noted in [35; 36]. Nevertheless, employing high-energy mechanical activation enables the production of compact Cr_3C_2 carbide products [37]. It's worth noting that mechanical activation is a time-consuming (often spanning several hours) and energy-intensive procedure.

An alternative approach involves elevating the thermality of the process. As explored in [38], the synthesis of chromium carbides can occur when a portion of carbon black is replaced with polytetrafluoroethylene $(–CF2 = CF2–)_n$. At temperatures ranging from 900 to 1000 K, this compound decomposes, yielding graphite and fluorine. The latter substance interacts with chromium, forming chromium fluorides. This reaction releases substantial heat, consequently triggering an SHS process for Cr_7C_3 carbides or Cr_3C_2 carbides with particle sizes measuring 0.5 – 2.0 μm. It is imperative to purify the reaction products from chromium fluoride CrF_2. Given the involvement of fluorine, the reactor necessitates sealing.

Metallothermal reduction

The procedure for producing cast chromium carbide through the SHS process is documented [39]. The reagents employed included chromium oxides (Cr_2O_3 and CrO_3), aluminum and graphite powders. This synthesis took place within an argon environment under pressures ranging from 4 to 20 MPa. The material had to be comminuted to attain the necessary powder. The reaction products contained up to 3 wt. % of aluminum, necessitating subsequent removal through acid treatment. These factors collectively add complexity to the process. Notably, CrO_3 oxide is highly toxic [40]. An alternate approach, the aluminothermal process, was described in [41] for synthesizing chromium carbide. While initially, chromium was reduced from aluminum oxide, the reaction mixture was subsequently maintained in an argon environment at 800 °C for two hours. The resulting product (effectively $Cr_3C_2 – Al_2O_3$ composite) consisted of particles sized between 300 and 400 μm.

Additionally, [42] explored the synthesis of chromium carbide through the magnesiothermal method:

$$3Cr_2O_3 + 9Mg + 4C = 2Cr_3C_2 + 9MgO. \quad (4)$$

Due to the process's inherent high adiabatic temperature (1950 °C), the introduction of an inert additive (Cr_3C_2) into the mixture was undertaken. This procedure transpired within an argon environment. The average size of the produced chromium carbide particles measures 2 μm. The magnesiothermal synthesis of chromium carbide is elucidated in [43]. The concoction of chromium oxide, magnesium, and acetone (as the carbon source) underwent thermal treatment within an autoclave at a temperature of 700 °C. The reagents were combined in a stoichiometric proportion to enable the reaction:

$$3Cr_2O_3 + 10Mg + 2C_3H_6O = \\ = 2Cr_3C_2 + 10MgO + C + CO + 6H_2. \quad (5)$$

Following a 15 h isothermal holding, chromium carbide with particle sizes ranging from 35 to 50 nm, enveloped by carbon layers measuring 3 – 4 nm in thickness, was successfully obtained.

Carbothermal reduction

The carbothermal reduction of chromium oxide is conducted through the comprehensive reaction:

$$3Cr_2O_3 + 13C = 2Cr_3C_2 + 9CO. \quad (6)$$

This process involves the reduction of thermodynamically robust chromium oxide through the utilization of a relatively feeble reducing agent, carbon monoxide (CO). In this context, the role of carbon is primarily focused on regenerating the generated carbon dioxide CO_2 [44]. From a thermodynamic standpoint, this process might seem implausible. Conclusions drawn from [45] suggest that the formation of chromium carbides is likely to transpire during the interaction between chromium oxide and solid carbon. In [46], the process of reducing chromium oxide using various agents (lamp carbon black, petroleum coke, thermal anthracite, semi-coke, and graphite) was investigated. The content of the reducing agent in the mixture corresponded to the stoichiometric ratio for reaction (3). The study revealed that the reduction start temperature displays weak dependency on the type of carbon material, spanning within the range of 1050 – 1100 °C. The gaseous phase predominantly consists of carbon monoxide, CO. Among the various environments, the most robust carbide formation occurs in hydrogen, followed by helium, with vacuum hosting the slowest process. Notably, the reaction products comprise a blend of Cr_3C_2 and Cr_7C_3 carbides. Authors in [46] propose carbon monoxide, CO, as the reducing agent for chromium oxide (contrary to thermodynamics). Meanwhile, [47] presents results from an exploration of chromium oxide interaction with diverse carbon materials (sucrose, carbon fiber material (CFM), and carbon black). The carbon fiber material consists of carbonization products from hydrated cellulose fibers. The mixture's reducing agent con-

tent corresponded to the stoichiometric value for reaction (6). Based on *X*-ray diffraction data, sucrose initiates Cr_3C_2 phase formation at 1200 °C, while CFM and carbon black begin at 1350 °C and 1400 °C, respectively. The lowered temperature for carbide formation with organic substances (sucrose and hydrocarbons) can be attributed to the creation of highly dispersed carbon components resulting from their thermal degradation within the oxide mixture.

Further insights into this process, focusing on gas phase control (continuous monitoring of CO and CO_2 oxides) are presented in [48; 49]. The charging material was heated within an inert gas atmosphere (helium or argon). At approximately 900 °C, a preference for carbon dioxide CO_2 emission over carbon monoxide CO emission was observed. This behavior is linked to carbon's interaction with adsorbed acidic species on its surface. Notably, the carbide phase predominantly forms on the surface of chromium oxide particles [4]. Following the establishment of an outer Cr_3C_2 carbide layer, interaction with chromium oxide commences, resulting in the formation of chromium carbide with a Cr_7C_3 composition. In cases where the initial reagent mixture contains insufficient carbon, the resulting product would exhibit a mixed-phase composition. The maximum liberation of carbon monoxide CO occurs at approximately 1200 °C (with a low content of carbon dioxide CO_2 at this temperature). If the reduction process followed the mechanism postulated in [44], the of CO and CO_2 oxides in the gas phase during chromium oxide reduction would be comparable.

The vapor pressure of chromium oxide at 1700 K (approximately 1430 °C) is approximately $7 \cdot 10^{-5}$ mm Hg (equivalent to about $9 \cdot 10^{-3}$ Pa), which is close to that of carbothermal synthesis. The vapor consists of chromium atoms, oxygen, and molecules of CrO, CrO_2, O_2 [50]. In contrast, the vapor pressure over carbon at the same temperature is significantly lower, measuring $9.13 \cdot 10^{-14}$ atm (approximately $9 \cdot 10^{-9}$ Pa) [8]. It is known that the evaporation of chromium oxide is notably enhanced in the presence of carbon [49].

The process of synthesizing chromium carbide partially involves the transfer of vaporous chromium and its oxides to the surface of the carbon reducing agent. This phenomenon is supported by the findings in references [51; 52].

Another perspective suggests that the carbothermal reduction process occurs through the direct interaction between solid oxide and carbon. According to the Cr – C system's phase diagram, a liquid phase may emerge at temperatures exceeding 1498 °C, facilitating close contact between the oxide and carbon and expediting the reduction process [51].

To summarize the aforementioned points, it can be inferred that the carbothermal reduction process of chromium oxide is quite intricate and may follow several mechanisms. Determining which one predominates is challenging.

In order to obtain reaction product consisting solely of carbide, briquettes composed of a calculated blend with an additional 5 % dextrin solution were heated in a resistance furnace to 1500 °C for 30 – 40 min and maintained at this temperature for 1.5 – 2.0 h in a hydrogen environment. The resulting carbide contained minimal impurities (wt. %: 87 of total Cr; 13.48 total C; 13.34 C bonded with a theoretical content of 86.67 Cr and 13.33 C) and exhibited an average particle size of 6.94 μm [53]. Reference [54] explored a process for producing chromium carbide using nano-sized powders of chromium oxide (average particle size less than 60 nm) and carbon black with a 14 % excess (average particle size less than 50 nm), nearly following a stoichiometric ratio to carry out reaction (3). The reduction initially yielded the lowest oxide, CrO. A single-phase product containing only Cr_3C_2 carbide was obtained at 1200 °C and held at that temperature for one hour. This suggests that under such conditions, the carbide formation process was completed. However, thermogravimetric analysis results revealed that even at 1200 °C, the weight loss (15.7 wt. %) was much lower than the value calculated based on the assumption of complete reaction (3) (41.2 wt. %). The average particle size of chromium carbide was approximately 50 nm. With an increase in synthesis time, the particles grew in size and aggregated.

In [55], a mixture of powdered chromium oxide Cr_2O_3, along with graphite or synthetic pitch, was subjected to heating in an argon gas environment, with the addition of 5 vol. % water, at varying temperatures for two hours. Experimental findings indicated that when synthetic pitch was employed as the reducing agent, a single-phase product (Cr_3C_2) formed at 1100 °C, whereas when graphite was used, this phase appeared at 1300 °C. This implies that synthetic pitch functions as a more active reducing agent compared to graphite. However, it is worth noting that the manufacturing process is time-consuming and labor-intensive. Details concerning particle dispersion were not provided. Reference [56] employed ammonium dichromate as a chromium source and carbon black as the carbon source. The mixture was heated in a vacuum environment at 1100 °C for a duration of 30 min, resulting in the formation of a single-phase product (Cr_3C_2 carbide). The produced powders were primarily composed of spherical particles with an average size of 27.2 nm. *X*-ray photoelectron spectroscopy revealed the presence of not only chromium and carbon but also oxygen. Therefore, under these specific conditions, the carbide formation process remains incomplete. The authors [56] suggest that the creation of chromium carbide progresses through the development of chromium carbide proceeds through the formation of an intermediate carbide phase

$$Cr_3C_{2-x}\ (0 \le x \le 0.5): Cr_2O_3 \rightarrow Cr_3C_{2-x} \rightarrow Cr_3C_2.$$

The synthesis of chromium carbide utilizing a novel type of carbon material known as nanofiber carbon (NFC), obtained through catalytic decomposition of light hydrocarbons, is outlined in references [57; 58]. This material is notably pure, with impurities mainly comprising catalyst remnants, constituting no more than 1 wt. %. It is distinguished by its substantial specific surface area (approximately 150 m^2/g) [59]. Experiments were conducted in an argon environment. Under optimized

conditions, the resulting material is characterized by a single phase (chromium carbide Cr_3C_2). Powder particles predominantly manifest aggregation. The average size of particles and aggregates measures 7.8 μm, displaying a wide array of size distributions. The specific surface area of the samples is 2.2 m^2/g. Oxidation of chromium carbide commences at 640 °C and nears completion at 1000 °C. The ideal synthesis parameters were identified as a molar ratio of Cr_2O_3:C = 3:13 (stoichiometric ratio for achieving Cr_3C_2 compound), and process temperature of 1300 – 1400 °C. Mention exists of the synthesis of chromium carbide using this method from ultrafine blends in references [60; 61]. Reference [60] formed a precursor (chromium tartrate) through a combination of chromium oxide CrO_3 solutions and tartaric acid, followed by drying. Similarly, in [61], a precursor was obtained from ammonium bichromate $(NH_4)_2Cr_2O_7$ and glucose. Heat treatment of the blends was performed in argon at 1100 °C [60] or in a vacuum environment (10^{-2} Pa) [61]. Particle sizes measured 1 – 2 μm [60] or approximately 30 nm [61].

Methane [62], along with its blends containing hydrogen [63] or argon [64; 65], can serve as effective reducing agents. The temperatures required for carbide formation are lower compared to those when solid carbon materials are used. While it is true that thermodynamically speaking, the use of hydrocarbons can lower the initiation temperature of reduction, this approach adds complexity to the process and raises concerns about its fire and explosion risks.

Vapor deposition

In [66], the production of ultrafine chromium carbonitride powder of $Cr_3(C_{0.8}N_{0.2})_2$, through plasma-chemical synthesis was explored. This process involved reducing chromium oxide using a nitrogen-hydrogen plasma flow containing propane–butane. However, the exhaust gases generated during this process contain hazardous hydrogen cyanide. The resulting powder had an average particle size of 35 nm, with the primary substance content ranging from 90.23 to 94.60 wt. %. It is worth noting that when stored in air, the chromium carbonitride powders exhibited significant oxygen and moisture adsorption. In comparison to coarser-grained chromium carbide powders [67], the thermal oxidative stability of this compound is relatively lower: oxidation initiates at approximately 280 °C and is nearly completed at 580 °C. A similar process was examined in reference [68]. Experimental results indicated that the interaction between chromium oxide and hydrocarbons within a plasma flow did not yield higher single-phase carbides. Another study in [69] described attempts to produce chromium carbonitride in a nitrogen plasma flow through the interaction of chromium metal powder and natural gas containing 94 vol. % methane. The resulting synthesis products contained 91.8 – 93.5 wt. % of the target compound, with particle sizes ranging from 150 to 600 nm.

In many of the referenced works ([33 – 35; 38; 39; 41 – 43; 45 – 47; 49; 51; 52; 54 – 56; 60; 62 – 65; 68] which account for approximately 83 % of the total cited references, information about the content of impurities in the final product was not provided.

Zirconium carbide manufacturing method

Synthesis through zirconium and carbon

In [70], zirconium and acetylene carbon black powders employed as initial materials. The blend, with a stoichiometric composition, underwent "dry" stirring for 2 – 3 h. Subsequently, it was compacted into briquettes to expedite diffusion processes. The synthesis occurred under a pressure of $1.2 \cdot 10^{-4}$ mm Hg (0.2 Pa). At a temperature of 1800 °C and a duration of one hour, zirconium carbide (ZrC) was successfully produced. The presence of impurities in the final product amounted to 0.6 wt. %. However, no information regarding particle dispersion was provided.

Metallothermal reduction

In [71 – 73], magnesiothermal synthesis was conducted according to the reaction

$$ZrO_2 + 2Mg + C = ZrC + 2MgO. \quad (7)$$

To mitigate the process's thermal intensity, an inert additive, such as sodium fluoride, was utilized [71], or blends were formulated with an excess of magnesium beyond stoichiometric proportions [72]. In [73], zirconium carbide was obtained after subjecting the materials to 30 h of mechanical activation. An alternative means of initiating magnesiothermal reduction involves partially oxidizing magnesium through its interaction with water [74]. This procedure leads to a high-pressure environment due to the evolution of hydrogen (pressure reaching 49.15 MPa). The resultant zirconium carbide nanoparticles were approximately 500 nm in size.

In the examined process, sodium [75] can also serve as a reducing metal. The process in question involved the reagents zirconium chloride $ZrCl_4$, sodium and toluene. By heating the solid residue produced after the excess toluene had evaporated, zirconium carbide was synthesized at a temperature of 700 °C over the course of one hour in an argon environment. It's important to note that sodium is highly susceptible to oxidation in air [40], which posed challenges during the blend preparation stage.

Carbothermal reduction

The comprehensive reaction equation is as follows

$$ZrO_2 + 3C = ZrC + 2CO. \quad (8)$$

Researchers [76] posit that the reduction of ZrO_2 oxide, which is thermodynamically robust, takes place

through carbon rather than the relatively thermodynamically weaker reducing agent (CO). The interaction likely involves the transfer of oxide vapors (ZrO_2, ZrO [50]) to the oxide's surface, followed by chemical interaction and desorption of the gaseous product (CO) resulting from the reaction. Conversely, researchers [44] lean towards the notion that CO drives the reduction of zirconium oxide, with carbon's role limited to regeneration. However, this viewpoint lacks substantial experimental support. In [77], active carbon, carbon black, and graphite powder served as carbon materials. These reagents were proportioned stoichiometrically to facilitate reaction (8). Monitoring of the reduction process was based on the quantity of released CO oxide. At temperatures of 1800 and 2000 °C, the conversion degree approached 100 %, and the oxygen content in the reaction products remained below 1 wt. % (except for instances involving thermal treatment with graphite). Carbothermal regeneration processes of titanium and zirconium oxides share certain similarities, given that zirconium carbide forms from oxycarbide ZrO_xC_y. The particle size of the obtained material predominantly fell within the range of 2.4 – 7.5 μm, accounting for 90 wt. %. Reference [48] also utilized active carbon, carbon black, and graphite powder as carbon materials. The blend was prepared in stoichiometric proportion for reaction (8) and subsequently heated in an inert gas flow (helium). The oxycarbide phase ZrO_xC_y emerged at 1450 °C, with the ZrO_2 phase already absent in samples synthesized at 2000 °C. Oxygen content in these samples remained around 0.6 wt. %. Notably, at synthesis temperatures exceeding 1450 °C, the gas phase primarily comprised CO oxide. This serves as unequivocal evidence against the feasibility of reducing zirconium oxide ZrO_2 using carbon monoxide CO, as such a reaction would yield a significant quantity of oxide CO_2 in the gas phase. However, particle size information is not provided. From a thermodynamic standpoint, reactions [78] are infeasible

$$ZrO_2 + CO = ZrC + 1.5O_2; \quad (9)$$

$$ZrO_2 + 4CO = ZrC + 3CO_2. \quad (10)$$

In [78], samples composed of compressed zirconium oxide ZrO_2 and graphite were subjected to heating within a helium environment. The formation of the ZrC phase took place at 1800 °C. The primary mechanism behind zirconium carbide formation predominantly involves carbon diffusion into zirconium oxide ZrO_2, as opposed to the vapor transfer of ZrO_2 and ZrO oxides to the carbon surface, followed by chemical interaction).

An examination of the aforementioned published data yields the following insights. Challenging is the alignment with the viewpoint of the authors in [44] concerning the reduction of zirconium dioxide with carbon monoxide. More recent experimental findings [79] suggest that the reduction process more likely transpires through the transfer of zirconium oxide vapors to the carbon material's surface, accompanied by a chemical reaction and subsequent removal of the resulting gaseous product (CO). While the possibility of solid-phase interaction involving carbon diffusion into zirconium dioxide is not excluded, reduction leads to the formation of zirconium oxycarbide ZrC_xO_y, with its oxygen content diminishing over time.

The process of generating zirconium carbide via the interaction between zirconium dioxide and carbon was outlined in [79 – 81].

A thermodynamic analysis of the process for obtaining zirconium carbide and its synthesis through heating a compressed mixture with an argon-hydrogen plasma was conducted in [79]. When employing a reactant ratio (ZrO_2 + C) in accordance with the stoichiometry of Eq. (5), the degree of transformation of zirconium dioxide into carbide approached unity within the temperature range of 1900 – 3800 K. In experiments involving a stoichiometric reactant ratio and a thermal treatment time of three minutes, the resulting product was single-phase (ZrC) with a carbon content of 4.14 wt. % and an oxygen content of 0.35 wt. %. However, information regarding the dispersity of zirconium carbide was not provided. Zirconium carbide was synthesized in [80] using zirconium dioxide and carbon black. The mixture of calcined components was ball-milled for eight hours and subsequently heated in a hydrogen environment. Optimal outcomes were achieved at a temperature of 2200 °C and a holding time of 60 min. The content of bonded carbon amounted to 11.30 wt. %, while the calculated content was 11.65 wt. %. Unfortunately, no information concerning powder dispersity was provided. In [81], the reagents comprised zirconium dioxide and graphite powders, with the blend's composition aligning with the stoichiometry of Eq. (8). Consequently, the reduction of zirconium dioxide to carbide does not involve carbon oxide (CO). The blend underwent high-energy grinding in a planetary mill for 20 h, followed by heat treatment at temperatures ranging from 1300 to 1600 °C for two hours under vacuum conditions. Full transformation of the reactants was achieved at 1400 °C. This indicates that the utilization of high-energy grinding enables a reduction in the carbide formation temperature by 400 °C. No reports of reagent contamination with grinding media and lining materials were made. The resulting powdered material consisted of agglomerates measuring approximately 7 μm in size, comprised of particles around 200 nm in size.

The synthesis of zirconium carbide utilizing nanofibrous carbon, characterized by its low impurity content (around 1 wt. %) and substantial specific surface area (approximately 150 m^2/g) [59], was explored in references [82; 83]. The blend was formulated in accordance with the stoichiometry of Eq. (5). It was observed that the use of such material led to a reduction in the process temperature by approximately 200 °C, ultimately yielding a highly dispersed single-phase product (ZrC) with an average particle size of approximately 15 μm. The impurity content remained relatively low, approximately 2 wt. %.

The series of publications provides comprehensive insights into the zirconium carbide production process via the carbothermal method from ultrafine blends. Zirconium butoxide $Zr(OC_4H_9)_4$ [84 – 86], zirconium *n*-propoxide $Zr(OC_3H_7)_4$ [87 – 89], zirconium tetrachloride $ZrCl_4$ [90 – 92], zirconium nitrate $Zr(NO_3)_4 \cdot 5H_2O$ [93], and zirconium oxychloride $ZrOCl_2 \cdot 8H_2O$ were utilized as zirconia sources [94 – 96]. The carbon sources encompassed propanol C_3H_7OH [95], butanol C_4H_9OH [84; 85], furfuryl alcohol C_5H_5OOH [92], acetylacetone $CH_3–CO–CH_2–CO–CH_3$ [89; 96], sucrose [87; 95], phenolic resin [86; 88; 91], salicylic acid $C_6H_4–OH–COOH$ [89], triethylamine $C_6H_{15}N$ [89], divinylbenzene $C_6H_4(C_2H_5)_2$ [90], glucose [94; 96], chitosan [93], 1,4-butanediol $C_4H_{10}O_2$ [96]. The reagents containing zirconium and carbon were stirred for 1 – 3 h. Subsequently, the solvent was removed either through evaporation or by subjecting the mixture to vacuum conditions. The resulting dry residue (ultrafine mixture) underwent heat treatment within an inert gaseous medium or under vacuum at conditions at temperatures ranging from 1250 to 1600 °C.

It is intriguing to note that in nearly all the aforementioned publications, the authors carried out calculations based on reaction (8) during blend preparation. Consequently, they hold the belief that the reduction of zirconium carbide from the oxide takes place through solid carbon, rather than involving carbon monoxide CO.

Vapor deposition

Zirconium carbonitride $ZrC_{0.90}N_{0.06}$ was synthesized within a nitrogen-hydrogen plasma flow through the reduction of zirconium oxide ZrO_2 with propane-butane [66]. The content of impurities (ZrO_2 and free carbon, C_{free}) within the resulting reaction products ranged from 16.88 to 19.95 wt. %. One potential explanation for such a high impurity content lies in the considerable thermodynamic stability exhibited by zirconium oxide [11]. The average particle size of the synthesized material measured around 50 nm. It's essential to highlight that the exhaust gases produced during this process contain toxic hydrogen cyanide. Additionally, observations indicated that the zirconium carbonitride powders, when exposed to air, exhibited a pronounced propensity for oxygen and moisture adsorption.

Synthesis through salt melt electrolysis

In [97], zirconium carbide powder with particle size ranging from 60 to 100 nm was successfully produced through electrolysis in a calcium chloride melt at a temperature of 1123 K (850 °C). A compressed mixture of ZrO_2/C was utilized as the anode, and the process ran for a duration of seven hours.

In several of the cited publications ([73 – 75; 78; 81; 84; 85; 89 – 92; 95 – 97], amounting to approximately 65 % of the total references), no information regarding the content of impurities in the final product was provided.

Conclusions

This text discusses refractory oxygen-free metal-like compounds, specifically chromium and zirconium carbides, highlighting their properties and applications. Chromium and zirconium carbides are characterized by high thermal and electrical conductivity, notable hardness, and chemical inertness. They find application across various engineering fields, such as abrasives, wear-resistant ceramics, and components in surfacing materials. Chromium carbide is utilized in tungsten-free hard alloys and carbide steels. Zirconium carbide shows promise as an inhibitory additive in hard alloy production and can function as a catalyst in organic synthesis. The methods for preparing these compounds are detailed and analyzed, outlining their distinctive features.

The majority of research on the synthesis of chromium and zirconium carbides focuses on their production from simple substances through carbothermal and metallothermal processes. Limited information exists on the preparation of these compounds via vapor-gas deposition. A noteworthy observation is that many cited publications lack details about the purity of the reaction products, often relying solely on *X*-ray phase analysis to gauge the completeness of the carbide formation processes. A plausible mechanism for the formation of these compounds involves the transfer of oxide vapors to the surface of carbon material particles, followed by subsequent chemical interaction. Additionally, it's conceivable that carbides may form through direct contact between solid reagents.

Список литературы / References

1. *State Diagrams of Binary Metal Systems. Reference book*. Lyakishev N.P. ed. Moscow: Mashinostroenie; 1996;1:992. (In Russ.).

   Диаграммы состояния двойных металлических систем. Справочник / Под ред. Н.П. Лякишева. Москва: Машиностроение; 1996;1:992.

2. Vinitskii I.M. Dependence of properties of monocarbides of IV-V groups transition metals on carbon content. *Poroshkovaya metallurgiya.* 1972;(6):76–82. (In Russ.).

   Виницкий И.М. Зависимость свойств монокарбидов переходных металлов IV–V групп от содержания углерода. *Порошковая металлургия*. 1972;(6):76–82.

3. *Properties, Production and Application of Refractory Compounds*. Kosolapova T.Ya. ed. Moscow: Metallurgiya;1986:928. (In Russ.).

   Свойства, получение и применение тугоплавких соединений / Под ред. Т.Я. Косолаповой. Москва: Металлургия; 1986:928.

4. Kosolapova T.Ya. *Carbides*. Moscow: Metallurgiya; 1968: 300. (In Russ.).

   Косолапова Т.Я. *Карбиды*. Москва: Металлургия; 1968: 300.

5. Kosolapova T.Ya. Chemical properties of refractory compounds. *Zhurnal VHO im. D.I. Mendeleeva.* 1979;24(3): 244–249. (In Russ.).

Косолапова Т.Я. Химические свойства тугоплавких соединений. *Журнал ВХО им. Д.И. Менделеева*. 1979;24(3):244–249.

6. Wang L., Zhou J., Yu Y., Guo C., Chen J. Effect of powders refinement on the tribological behavior of Ni-based composite coatings by laser cladding. *Applied Surface Science.* 2012;258(17):6697–6704. http://doi.org/10.1016/j.apsusc.2012.03.141

7. Matthews S., James B., Hyland M. The role of microstructure in the high temperature oxidation mechanism of Cr_3C_2–NiCr composite coatings. *Corrosion Science*. 2009;51(5): 1172–1180. http://doi.org/10.1016/j.corsci.2009.02.027

8. Chatha S.S., Sidhu H.S., Sidhu B.S. High temperature hot corrosion behavior of NiCr and Cr_3C_2–NiCr coatings on T91 boiler steel in an aggressive environment at 750 °C. *Surface and Coating Technology*. 2012;206(19-20):3839–3850. http://doi.org/10.1016/j.surfcoat.2012.01.060

9. Kaur M., Singh H., Prakash S. High-temperature behavior of a high-velocity oxy-fuel sprayed Cr_3C_2–NiCr coating. *Metallurgical and Materials Transactions A*. 2012;43: 2979–2993. http://doi.org/10.1007/s11661-012-1118-4

10. Yuzvenko Yu.A. *Surfacing*. Kyiv: Naukova dumka; 1976:71. (In Russ.).

Юзвенко Ю.А. *Наплавка*. Киев: Наукова думка; 1976: 71.

11. Klimenko V.N., Maslyuk V.A. Corrosion-resistant metal-ceramic alloys based on chromium carbide. *Tekhnologiya i organizatsiya proizvodstva*. 1983; 3: 82–85. (In Russ.).

Клименко В.Н., Маслюк В.А. Коррозионностойкие металлокерамические сплавы на основе карбида хрома. *Технология и организация производства*. 1983;3:82–85.

12. Maslyuk V.A., Yakovenko R.V., Potazhevskaya O.A., Bondar A.A. Powdered hard alloys and chromium carbides based on the Cr–Fe–C system. *Poroshkovaya metallurgiya*. 2013;(1/2):60–74. (In Russ.).

Маслюк В.А., Яковенко Р.В., Потажевская О.А., Бондар А.А. Порошковые твердые сплавы и хромистые карбидостали на основе системы Cr–Fe–C. *Порошковая металлургия*. 2013;(1/2):60–74.

13. Kurlov A.S., Gusev A.I. *Physics and Chemistry of Tungsten Carbides*. Moscow: Fizmatlit; 2013:272. (In Russ.).

Курлов А.С., Гусев А.И. *Физика и химия карбидов вольфрама*. Москва: Физматлит; 2013:272.

14. Bonache V., Salvador M.D., Rocha V.G., Borrell A. Microstructural control of ultrafine and nanocrystalline WC–12Co–VC/Cr_3C_2 mixture by spark plasma sintering. *Ceramics International*. 2011;37(3):1139–1142. http://doi.org/10.1016/j.ceramint.2010.11.026

15. Chen H., Yang Q., Wang J., Yang H., Chen L., Ruan J., Huang Q. Effects of VC/Cr_3C_2 on WC grain morphologies and mechanical properties of WC–6 wt. % Co cemented carbides. *Journal of Alloys and Compounds*. 2017;714: 245–250. https://doi.org/10.1016/j.jallcom.2017.04.187

16. Sun L., Tian'en Y., Jia C., Hiong J. VC, Cr_3C_2 doped ultrafine WC–Co cemented carbides prepared by spark plasma sintering. *International Journal of Refractory Metals and Hard Materials*. 2011;29(2):147–152. http://doi.org/10.1016/j.ijrmhm.2010.09.004

17. Zhao Z. Microwave-assisted synthesis of vanadium and chromium carbides nanocomposite and its effect on properties of WC–8Co cemented carbides. *Scripta Materialia*. 2016;120: 103–106. http://doi.org/10.1016/j.scriptamat.2016.04.024

18. Bonache V., Salvador M.D., Fernández A., Borrell A. Fabrication of full density near-nanostructured cemented carbides by combination of VC/Cr_3C_2 addition and consolidation by SPS and HIP technologies. *International Journal of Refractory Metals and Hard Materials*. 2011;29(3):202–208. http://doi.org/10.1016/j.ceramint.2010.11.026

19. Espinoza-Fernández L., Borrell A., Salvador M.D., Gutierrez-Gonzalez C.F. Sliding wear behavior of WC–Co–Cr_3C_2–VC composites fabricated by conventional and non-conventional techniques. *Wear*. 2013;307(1-2):60–67. http://doi.org/10.1016/J.WEAR.2013.08.003

20. Li Y., Zheng D., Li X., Qu S., Yang C. Cr_3C_2 and VC doped WC–Si_3N_4 composites prepared by spark plasma sintering. *International Journal of Refractory Metals and Hard Materials*. 2013;41:540–546. http://doi.org/10.1016/j.ijrmhm.2013.07.004

21. Wan W., Xiong J., Guo Z., Dong G., Yi C. Effects of Cr_3C_2 addition on the corrosion-erosion behavior of Ti(C,N)-based cermets. *Tribology International*. 2013;39:178–186. http://doi.org/10.1016/j.triboint.2013.03.019

22. Apininskaya L.M., Klimenko V.N., Maslyuk V.A., Radomyselskii I.D. Porous products made of chromium carbide alloys. *Poroshkovaya metallurgiya*. 1971;(2):33–36. (In Russ.).

Апининская Л.М., Клименко В.Н., Маслюк В.А., Радомысельский И.Д. Пористые изделия из карбидохромовых сплавов. *Порошковая металлургия*. 1971;(2):33–36.

23. Kharlamov A.I., Kirillov N.V. Catalytic properties of powders of refractory compounds of transition elements. Carbides and nitrides. *Poroshkovaya metallurgiya*. 1983;(2): 55–67. (In Russ.).

Харламов А.И., Кириллов Н.В. Каталитические свойства порошков тугоплавких соединений переходных элементов. Карбиды и нитриды. *Порошковая металлургия*. 1983;(2):55–67.

24. Adamovskii A.A. Carbides of transition metals in abrasive processing. *Poroshkovaya metallurgiya*. 2007;(11/12): 96–111. (In Russ.).

Адамовский А.А. Карбиды переходных металлов в процессах абразивной обработки. *Порошковая металлургия*. 2007;(11/12):96–111.

25. Sun W., Xiong X., Huang B.-Y., Li G.-D., Zhang H.-B., Chen Z.-K., Zheng X.-L. ZrC ablation protective coating for carbon/carbon composites. *Carbon*. 2009;47(14): 3368–3371. http://doi.org/10.1016/j.carbon.2009.07.047

26. Wang S.-L., Li K.-Z., Li H.-Y., Zhang Y.-L. Microstructure and ablation resistance of ZrC nanostructured coating for carbon/carbon composite. *Materials Letters*. 2013;107: 99–102. http://doi.org/10.1016/j.matlet.2013.05.124

27. Gurin V.N. Methods of synthesis of refractory compounds and prospects of their application for new materials creation. *Zhurnal VKhO im. D.I. Mendeleeva*. 1979;24(3):212–222. (In Russ.).

Гурин В.Н. Методы синтеза тугоплавких соединений и перспективы их применения для создания новых материалов. *Журнал ВХО им. Д.И. Менделеева*. 1979; 24(3):212–222.

28. Merzhanov A.G., Borovinskaya I.P. Self-propagating high-temperature synthesis in the chemistry and technology

of refractory compounds. *Zhurnal VKhO im. D.I. Mendeleeva*. 1979;24(3):223–227. (In Russ.).

Мержанов А.Г., Боровинская И.П. Самораспространяющийся высокотемпературный синтез в химии и технологии тугоплавких соединений. *Журнал ВХО им. Д.И. Менделеева*. 1979;24(3):223–227.

29. *Properties of Elements. Part 1. Physical Properties*. Samsonova G.V. ed. Moscow: Metallurgiya; 1976:600. (In Russ.).

Свойства элементов. Часть 1. Физические свойства / Под ред. Г.В. Самсонова. Москва: Металлургия; 1976: 600.

30. *Physicochemical Properties of Oxides*. Samsonova G.V. ed. Moscow: Metallurgiya; 1978: 472. (In Russ.).

Физико-химические свойства окислов / Под общ. ред. Г.В. Самсонова. Москва: Металлургия; 1978:472.

31. Samsonov G.V., Perminov V.P. *Magnesiothermy*. Moscow: Metallurgiya; 1971:176. (In Russ.).

Самсонов Г.В., Перминов В.П. *Магниетермия*. Москва: Металлургия; 1971:176.

32. Kieffer R., Benezovsky F. *Hard Materials*. Moscow: Metallurgiya; 1968:384. (In Russ.).

Киффер Р., Бенезовский Ф. *Твердые материалы*. Москва: Металлургия; 1968:384.

33. Liu Z.G., Tsuchiya K., Umemoto M. Mechanical milling of fullerene with carbide forming elements. *Journal of Materials Science*. 2002;37:1229–1235. http://doi.org/10.1023/A:1014383909485

34. Li L., Tang J. Synthesis of Cr_7C_3 and Cr_3C_2 by mechanical alloying. *Journal of Allows and Compounds*. 1994;209(1-2): L1–L3. http://doi.org/10.1016/0925-8388(94)91060-X

35. Gomari S., Shafari S. Microstructural characterization of nanocrystalline chromium carbides synthesized by high energy ball milling. *Journal of Allows and Compounds*. 2010;490(1-2):26–30. http://doi.org/10.1016/j.jallcom.2009.10.041

36. Pripisnov O.N., Shelekhov E.V., Rupasov S.I., Medvedev A.S. The mechanism of phase formation and features of mechanochemical synthesis of chromium carbides. *Izvestiya vuzov. Poroshkovaya metallurgiya i funktsional'nye pokrytiya*. 2014;(3):8–15. (In Russ.). http://doi.org/10.17073/1997-308X-2014-3-8-15

Приписнов О.Н., Шелехов Е.В., Рупасов С.И., Медведев А.С. Механизм фазообразования и особенности механохимического синтеза карбидов хрома. *Известия вузов. Порошковая металлургия и функциональные покрытия*. 2014;(3):8–15. http://doi.org/10.17073/1997-308X-2014-3-8-15

37. Sharafi S., Gomari S. Effects of milling and subsequent consolidation treatment on the microstructural properties and hardness of the nanocrystalline chromium carbide powders. *International Journal of Refractory Metals and Hard Materials*. 2012;30(1):57–63. http://doi.org/10.1016/j.ijrmhm.2011.07.004

38. Manukyan H.V., Nersisyan G.A., Kharatyan S.L. Activated chromium-carbon combustion and chromium carbide synthesis. *Khimicheskaya fizika*. 2001;20(11):34–37. (In Russ.).

Манукян Х.В., Нерсисян Г.А., Харатян С.Л. Активированное горение хрома с углеродом и синтез карбидов хрома. *Химическая физика*. 2001;20(11):34–37.

39. Gorshkov V.A., Komratov G.N., Yukhvid V.I. Production of cast higher chromium carbide by self-propagating high-temperature synthesis. *Poroshkovaya metallurgiya*. 1992;(11):57–60. (In Russ.).

Горшков В.А., Комратов Г.Н., Юхвид В.И. Получение литого высшего карбида хрома методом самораспространяющегося высокотемпературного синтеза. *Порошковая металлургия*. 1992;(11):57–60.

40. Rosin I.V., Tomina L.D. *General and Inorganic Chemistry. Modern Course*. Moscow: Yurait; 2012:1338. (In Russ.).

Росин И.В., Томина Л.Д. *Общая и неорганическая химия. Современный курс*. Москва: Юрайт; 2012:1338.

41. Cintho O.M., Favilla E.A.P., Capocchi J.D.T. Mechanical-thermal synthesis of chromium carbides. *Journal of Allows and Compounds*. 2007;439(1-2):189–195. http://doi.org/10.1016/j.jallcom.2006.03.102

42. Ko S-K., Won C.-W., Shon I.-J. Synthesis of Cr_3C_2 by SHS process. *Scripta Materialia*. 1997;31(6):889–895. http://doi.org/10.1016/S1359-6462(97)00181-4

43. Mahajan M., Rajpoot S., Randey O.P. In-situ synthesis of chromium carbide (Cr_3C_2) nanopowders by chemical-reduction route. *International Journal of Refractory Metals and Hard Materials*. 2015;50:113–119. http://doi.org/10.1016/J.IJRMHM.2014.12.010

44. Vodop'yanov A.G., Kozhevnikov G.N., Baranov S.V. Interaction of refractory metal oxides with carbon. *Uspekhi khimii*. 1988;LVII(9):1419–1439. (In Russ.).

Водопьянов А.Г., Кожевников Г.Н., Баранов С.В. Взаимодействие тугоплавких оксидов металлов с углеродом. *Успехи химии*. 1988;LVII(9):1419–1439.

45. Popov A.A., Ostrik P.N., Gasik M.I. Thermodynamics of reduction and formation of carbide in the Cr–C–O system. *Izvestiya. Ferrous Metallurgy*. 1986;29(10):1–3. (In Russ.).

Попов А.А., Острик П.Н., Гасик М.И. Термодинамика восстановления и карбидообразования в системе Cr–C–O. *Известия вузов. Черная металлургия*. 1986; 29(10):1–3.

46. Golodov S.M., Kolchanov V.A., Tarabrin G.K., Sorin S.B. Study of the interaction of chromium oxide with carbon. *Izvestiya. Ferrous Metallurgy*. 1984;27(5):6–9. (In Russ.).

Голодов С.М., Колчанов В.А., Тарабрин Г.К., Сорин С.Б. Исследование взаимодействия окиси хрома с углеродом. *Известия вузов. Черная металлургия*. 1984;27(5):6–9.

47. Vlasova V.M., Kakazei N.G., Minakov V.N., Sergeev V.P., Sinel'nikova V.S., Kharlamov A.I., Khorpyakov O.T. Carbide formation in chromium oxide – carbon-containing component systems. *Neorganicheskie materialy*. 1988;24(12): 1998–2003. (In Russ.).

Власова В.М., Каказей Н.Г., Минаков В.Н., Сергеев В.П., Синельникова В.С., Харламов А.И., Хорпяков О.Т. Карбидообразование в системах оксид хрома – углеродсодержащий компонент. *Неорганические материалы*. 1988;24(12):1998–2003.

48. Gruner W., Stolle S., Wetzig K. Formation of CO_x species during the carbothermal reduction of oxides of Zr, Si, Ti, Cr, W and Mo. *International Journal of Refractory Metals and Hard Materials*. 2000;18(2-3):137–145. http://doi.org/10.1016/S0263-4368(00)00013-5

49. Berger L.-M., Stolle S., Gruner W., Wetzig K. Investigation of the carbothermal reduction process of chromium oxide by micro and lab-scale methods. *International Journal of Refractory Metals and Hard Materials*. 2001;19(2): 109–121. http://doi.org/10.1016/S0263-4368(01)00003-8

50. Kazenas E.K., Tsvetkov Yu.V. *Thermodynamics of Oxide Evaporation*. Moscow: LKI; 2008:480. (In Russ.).

Казенас Е.К., Цветков Ю.В. *Термодинамика испарения оксидов*. Москва: ЛКИ. 2008:480.

51. Vodop'yanov A.G., Serebryakova A.V., Kozhevnikov G.I. On the mechanism of interaction of chromium oxide with carbon. *Metally*. 1979;(5):11–15. (In Russ.).

Водопьянов А.Г., Серебрякова А.В., Кожевников Г.И. О механизме взаимодействия окиси хрома с углеродом. *Металлы*. 1979;(5):11–15.

52. Водопьянов А.Г., Кожевников Г.Н. Диссоциация окиси хрома в присутствии углерода. *Металлы*. 1979;(6):58–62.

Vodop'yanov A.G., Kozhevnikov G.N. Dissociation of chromium oxide in the presence of carbon. *Metally*. 1979;(6): 58–62. (In Russ.).

53. Kosolapova T.Ya., Samsonov G.V. Preparation of higher chromium carbide. *Zhurnal prikladnoi khimii*. 1959;XXXII(1): 55–60. (In Russ.).

Косолапова Т.Я., Самсонов Г.В. Приготовление высшего карбида хрома. *Журнал прикладной химии*. 1959;XXXII(1):55–60.

54. Zhao Z., Zheng H., Zhang S., Song W., Mao S., Chen Y. Effect of reaction time on phase composition and microstructure of chromium carbide nanopowders. *International Journal of Refractory Metals and Hard Materials*. 2013;41: 558–562. http://doi.org/10.1016/j.ijrmhm.2013.07.007

55. Eick B.M., Youngblood J.P. Carbothermal reduction of metal-oxide powders by synthetic pitch to carbide and nitride ceramics. *Journal of Materials Science*. 2009;44:1159–1171. http://doi.org/10.1007/s10853-009-3249-6

56. Zhao Z., Zheng H., Wang Y., Mao S., Niu J., Chen Y., Shang M. Synthesis of chromium carbide (Cr_3C_2) nanopowders by the carbonization of the precursors. *International Journal of Refractory Metals and Hard Materials*. 2011;29(5):614–617. http://doi.org/10.1016/j.ijrmhm.2011.04.007

57. Krutskii Yu.L., Dyukova K.D., Bannov A.G., Ukhina A.V., Sokolov V.V., Pichugin A.Yu., Krutskaya T.M., Netskina O.V., Samoilenko V.V. Synthesis of high-dispersion higher chromium carbide powder using nanofibre carbon. *Powder Metallurgy and Functional Coatings*. 2014;(3):3–8. (In Russ.). http://doi.org/10.17073/1997-308X-2014-3-3-8

Крутский Ю.Л., Дюкова К.Д., Баннов А.Г., Ухина А.В., Соколов В.В., Пичугин А.Ю., Крутская Т.М., Нецкина О.В., Самойленко В.В. Синтез высокодисперсного порошка высшего карбида хрома с использованием нановолокнистого углерода. *Известия вузов. Порошковая металлургия и функциональные покрытия*. 2014;(3):3–8. http://doi.org/10.17073/1997-308X-2014-3-3-8

58. Krutskii Yu.L., Dyukova K.D., Kuz'min R.I., Maksimovskii E.A., Veselov S.V. Use of carbon material with developed surface for the synthesis of higher chromium carbide. *Izvestiya. Ferrous Metallurgy*. 2019;62(2):115–122. (In Russ.). http://doi.org/10.17073/0368-0797-2019-2-115-122

Крутский Ю.Л., Дюкова К.Д., Кузьмин Р.И., Максимовский Е.А., Веселов С.В. Использование углеродного материала с развитой поверхностью для синтеза высшего карбида хрома. *Известия вузов. Черная металлургия*. 2019;62(2):115–122. http://doi.org/10.17073/0368-0797-2019-2-115-122

59. Kuvshinov G.G., Mogilnykh Yu.L., Kuvshinov D.G., Yermakov D.Yu., Yermakova M.A., Salanov A.N., Rudina N.A. Mechanism of porous filamentous carbon granule formation on catalytic hydrocarbon decomposition. *Carbon*. 1999;37(8): 1239–1246. http://doi.org/10.1016/S0008-6223(98)00320-0

60. Preiss H., Schultze D., Szulzewsky K. Carbothermal synthesis of vanadium and chromium carbides from solution-derived precursors. *Journal of the European Ceramic Society*. 1999;19(2):187–194. http://doi.org/10.1016/S0955-2219(98)00191-5

61. Zhao Z., Zheng H., Liu S., Shen J., Song W., Chen J. Low temperature synthesis of chromium carbide (Cr_3C_2) nanopowders by a novel precursor method. *International Journal of Refractory Metals and Hard Materials*. 2015;48:46–50. http://doi.org/10.1016/j.ijrmhm.2014.07.026

62. Khoshandam B., Kumar R.V. Producing chromium carbide using reduction of chromium oxide with methane. *American Institute of Chemical Engineers Journal*. 2006;52(3): 1094–1102. http://doi.org/10.1002/aic.10712

63. Wang S.-H., Lin H.-T., Nayak P.K., Chang C.-Y., Huang J.-L. Carbothermal reduction process for synthesis of nanosized chromium carbide via metal-organic vapor deposition. *Thin Solid Films*. 2010;518(24):7360–7365. http://doi.org/10.1016/j.tsf.2010.05.001

64. Ostrovski O., Guangqing Z. Reduction and carburization of metal oxides by methane-containing gas. *American Institute of Chemical Engineers Journal*. 2006;52(1): 300–310. http://doi.org/10.1002/aic.10628

65. Ebrahimi-Kahrizsangi R., Zadeh H.M., Nemati V. Synthesis of chromium carbide by reduction of chromium oxide with methane. *International Journal of Refractory Metals and Hard Materials*. 2010;28(3):412–415. http://doi.org/10.1016/J.IJRMHM.2010.01.001

66. Saburov V.P., Cherepanov A.N., Zhukov M.F., Krushenko G.G., Galevskii G.V., Borisov V.T *Plasma Chemical Synthesis of Ultra-Dispersed Powders and Their Use for Modifying Metals and Alloys. Vol. 12. Low-Temperature Plasma*. Novosibirsk: Nauka, Sibirskaya izdatel'skaya firma RAS; 1995:344. (In Russ.).

Сабуров В.П., Черепанов А.Н., Жуков М.Ф., Крушенко Г.Г., Галевский Г.В., Борисов В.Т. *Плазмохимический синтез ультрадисперсных порошков и их применение для модифицирования металлов и сплавов. Т. 12. Низкотемпературная плазма*. Новосибирск: Наука, Сибирская издательская фирма РАН; 1995:344.

67. Krutskii Yu.L., Galevskii G.V., Kornilov A.A. Oxidation of ultra-dispersed powders of boron, vanadium and chromium carbides. *Poroshkovaya metallurgiya*. 1983;(2):47–50. (In Russ.).

Крутский Ю.Л., Галевский Г.В., Корнилов А.А. Окисление ультрадисперсных порошков карбидов бора, ванадия и хрома. *Порошковая металлургия*. 1983;(2):47–50.

68. Isaeva N.V., Blagoveshchenskii Yu.V., Blagoveshchenskaya N.V., Mel'nik Y.I., Samokhin A.V., Alekseev N.V., Astashov A.G. Production of nanopowders and carbide mixtures using low-temperature plasma. *Powder Metallurgy and Functional Coatings*. 2013;(3):7–14. (In Russ.).

Исаева Н.В., Благовещенский Ю.В., Благовещенская Н.В., Мельник Ю.И., Самохин А.В., Алексеев Н.В., Асташов А.Г. Получение нанопорошков и твердосплавных смесей с применением низкотемпературной плазмы.

Известия вузов. Порошковая металлургия и функциональные покрытия. 2013;(3):7–14.

69. Nozdrin I.V., Shiryaeva L.S., Rudneva V.V. Plasma synthesis and physical and chemical certification of nanochromium carbide. *Izvestiya. Ferrous Metallurgy*. 2012;55(12):3–8. (In Russ.).

Ноздрин И.В., Ширяева Л.С., Руднева В.В. Плазменный синтез и химико-физическая аттестация нанокарбида хрома. *Известия вузов. Черная металлургия*. 2012; 55(12): 3–8.

70. Naumenko V.Ya. Production of transition metal carbides of groups IV-V in their homogeneity areas. *Poroshkovaya metallurgiya*. 1970;10:20–22. (In Russ.).

Науменко В.Я. Получение карбидов переходных металлов IV–V групп в областях их гомогенности. *Порошковая металлургия*. 1970;(10):20–22.

71. Won H.I., Nersisyan H., Won C.W., Lee H.H. Simple synthesis of nano-sized refractory metal carbides by combustion process. *Journal of Materials Science*. 2011;46: 6000–6006. http://doi.org/10.1007/s10853-011-5562-0

72. Li J., Fu Z.Y., Wang W.M., Wang H., Lee S.H., Niihara K. Preparation of ZrC by self-propagating high-temperature synthesis. *Ceramics International*. 2010;36(5):1681–1686. http://doi.org/10.1016/j.ceramint.2010.03.013

73. Davoodi D., Hassanzadeh-Tabrizi S.A., Emami A.H., Salanshour S. A low temperature mechanochemical synthesis of nanostructured ZrC powder by a magnesiothermic reaction. *Ceramics International*. 2015;41(7):8397–8401. http://doi.org/10.1016/j.ceramint.2015.03.034

74. Zhou L., Yang L., Shao L., Chen B., Meng F., Qian Y., Hu L. General fabrication of boride, carbide and nitride nanocrystals via a metal-hydrolysis-assisted process. *Inorganic Chemistry*. 2017;56(5):2440–2447. http://doi.org/10.1021/acs.inorgchem.6b02501

75. Mandavi M., Ramazani M., Darvishi Z. Investigation of template effect on zirconium carbide synthesis process in carbotherhermal method at low temperature condition. *Advanced Powder Technology*. 2016;27(4):1547–1551. http://doi.org/10.1016/j.apt.2016.05.016

76. Elyutin V.P., Pavlov J.A., Polyakov V.P., Sheboldaev S.B. *Interaction of Metal Oxides with Carbon*. Moscow: Metallurgiya; 1976:360. (In Russ.).

Елютин В.П., Павлов Ю.А., Поляков В.П., Шеболдаев С.Б. *Взаимодействие окислов металлов с углеродом*. Москва: Металлургия; 1976:360.

77. Stolle S., Gruner W., Pitschke W., Berger L.-M., Wetzig K. Comparative microscale investigations of the carbothermal synthesis of (Ti, Zr, Si) carbides with oxide intermediates of different volatilities. *International Journal of Refractory Metals and Hard Materials*. 2000;18(1):61–72. http://doi.org/10.1016/S0263-4368(00)00018-4

78. Sondhi A., Morandi C., Reidy R.F., Scharf T.W. Theoretical and experimental investigations on the mechanism of carbothermal reduction of zirconia. *Ceramics International*. 2013;39(4):4489–4497. https://doi.org/10.1016/j.ceramint.2012.11.043

79. Moiseev G.K., Popov S.K., Ovchinnikov L.A., Vatolin N.A. Formation of titanium and zirconium carbides when their oxides interact with carbon in low-temperature plasma. *Izvestiya An SSSR. Neorganicheskie materialy*. 1982;18(9):1521–1524. (In Russ.).

Моисеев Г.К., Попов С.К., Овчинников Л.А., Ватолин Н.А. Образование карбидов титана и циркония при взаимодействии их оксидов с углеродом в низкотемпературной плазме. *Известия АН СССР. Неорганические материалы*. 1982;18(9):1521–1524.

80. Shumilova R.G., Kosolapova T.Ya. Production of zirconium carbide on a semi-industrial scale. *Poroshkovaya metallurgiya*. 1968;(4):86–89. (In Russ.).

Шумилова Р.Г., Косолапова Т.Я. Получение карбида циркония в полупромышленном масштабе. *Порошковая металлургия*. 1968;(4):86–89.

81. Seo M., Kang S., Kim Y., Ryu S.-S. Preparation of highly dispersed ultra-fine ZrC by combination of carbothermal reduction of ball-milled ZrO_2 and C mixture and bead milling. *International Journal of Refractory Metals and Hard Materials*. 2013;41:345–350. http://doi.org/10.1016/j.ijrmhm.2013.05.007

82. Krutskii Yu.L., Dyukova K.D., Bannov A.G., Maksimovskii E.A., Ukhina A.V., Krutskaya T.M., Netskina O.V., Kuznetsova V.V. Synthesis of fine zirconium carbide powder with carbon nanofibers. *Analysis and Data Processing Systems*. 2015;60(3):192–205. (In Russ.). http://doi.org/10.17212/1814-1196-2015-3-192-205

Крутский Ю.Л., Дюкова К.Д., Баннов А.Г., Максимовский Е.А., Ухина А.В., Крутская Т.М., Нецкина О.В., Кузнецова В.В. Синтез высокодисперсного порошка карбида циркония с использованием нановолокнистого углерода. *Научный вестник НГТУ*. 2015;60(3):192–205. http://doi.org/10.17212/1814-1196-2015-3-192-205

83. Krutskii Yu.L., Maksimovskii E.A., Popov M.V., Netskina O.V., Cherkasova N.Yu., Kvashina T.S., Chushenkov V.I., Smirnov A.I., Felof'yanova A.V., Aparnev A.I. Synthesis of highly dispersed zirconium carbide. *Russian Journal of Applied Chemistry*. 2018;91(3):428–435. http://doi.org/10.1134/S107042721803014X

84. Leconte Y., Maskrot H., Combemale L., Herlin-Boime N., Reynaud C. Application of the laser pyrolysis to the synthesis of SiC, TiC and ZrC pre-ceramics nanopowders. *Journal of Analytical and Applied Pyrolysis*. 2007;79(1-2):465–470. http://doi.org/10.1016/j.jaap.2006.11.009

85. Combemale L., Leconte Y., Portier X., Herlin-Boime N., Reynaud C. Synthesis of nanosized zirconium carbide by laser pyrolysis route. *Journal of Alloys and Compounds*. 2009;483(1-2):468–472. http://doi.org/10.1016/j.jallcom.2008.07.159

86. Sacks M.D., Wang C.-A., Yang Z., Jain A. Carbothermal reduction synthesis of nanocrystalline zirconium carbide and hafnium carbide powders using solution-derived precursors. *Journal of Materials Science*. 2004;39:6057–6066. http://doi.org/10.1023/B:JMSC.0000041702.76858.A7

87. Dolle M., Gosset D., Bogicevic C., Carolak F., Simeone D., Baldinozzi G. Synthesis of nanosized zirconium carbide by a sol-gel route. *Journal of the European Ceramic Society*. 2007;27(4):2061–2067. http://doi.org/10.1016/J.JEURCERAMSOC.2006.06.005

88. Yan Y., Huang Z., Liu X., Jiang D. Carbothermal synthesis of ultra-fine zirconium carbide powders using inorganic precursors via sol-gel method. *Journal of Sol-Gel Science and Technology*. 2007;44:81–85. http://doi.org/10.1007/s10971-007-1595-x

89. Tao X.Y., Qiu W.F., Li H., Zhao T. One pot synthesis of a soluble polymer for zirconium carbide. *Chinese Chemical Letters*. 2010;21(5):620–623. http://doi.org/10.1016/j.cclet.2010.01.002

90. Zhao D., Hu H., Zhang C., Zhang Y., Wang J. A simple way to prepare precursors for zirconium carbide. *Journal of Materials Science*. 2010;45:6401–6405. http://doi.org/10.1007/s10853-010-4722-y

91. Yan C., Liu R., Cao Y., Zhang C., Zhang D. Carbothermal synthesis of submicrometer zirconium carbide from polyzirconoxane and phenolic resin by the facile one-pot reaction. *Journal of the American Ceramic Society*. 2012;95(11): 3366–3369. http://doi.org/10.1111/j.1551-2916.2012.05456.x

92. Ang C., Williams T., Seeber A., Wang H., Cheng Y.-B. Synthesis and evolution of zirconium carbide via sol-gel route: Features of nanoparticle oxide carbon reactions. *Journal of the American Ceramic Society*. 2013;96(4):1099–1106. http://doi.org/10.1111/jace.12260

93. Yan C., Liu R., Cao Y., Zhang C., Chang D. Synthesis of zirconium carbide powders using chitosan as carbon source. *Ceramics International*. 2013;39(3):3409–3412. http://doi.org/10.1016/j.ceramint.2012.09.032

94. Chu A., Qin M., Rafi-ud-din, Zhang L., Lu H., Jia B., Qu X. Carbothermal synthesis of ZrC powders using a combustion synthesis precursor. *International Journal of Refractory Metals and Hard Materials*. 2013;36:204–210. http://doi.org/10.1016/J.IJRMHM.2012.08.016

95. Xie J., Fu Z., Wang Y., Lee S.W., Niihara K. Synthesis of nanosized zirconium carbide powders by a combinational method of sol-gel and pulse current heating. *Journal of the European Ceramic Society*. 2014;34(1):13e.1–13e.7. http://doi.org/10.1016/j.jeurceramsoc.2013.07.003

96. Wu H., Zhang W., Zhang J. Pyrolysis synthesis and microstructure of zirconium carbide from new preceramic polymers. *Ceramics International*. 2014;40(4):5967–5972. http://doi.org/10.1016/j.ceramint.2013.11.044

97. Dai L., Wang H., Zhou H., Yu Y., Zhu J., Li Y., Wang L. Direct electrochemical synthesis of zirconium carbide from zirconia. *Ceramics International*. 2015;41(3):4182–4188. http://doi.org/10.1016/j.ceramint.2014.12.101

Information about the Authors

Yurii L. Krutskii, *Cand. Sci. (Eng.), Assist. Prof. of the Chair "Chemistry and Chemical Technology"*, Novosibirsk State Technical University
ORCID: 0000-0003-2524-4143
E-mail: krutskii@yandex.ru

Tat'yana S. Gudyma, *Postgraduate of the Chair "Chemistry and Chemical Technology"*, Novosibirsk State Technical University
ORCID: 0000-0002-4724-3371
E-mail: gudymatan@mail.ru

Tat'yana M. Krutskaya, *Cand. Sci. (Chem.), Assist. Prof. of the Chair of Physics and Chemistry*, Novosibirsk State University of Architecture and Civil Engineering
ORCID: 0000-0001-8003-4523
E-mail: t.krutskaya@mail.ru

Andrei O. Semenov, *Senior Lecturer of Division of Nuclear Fuel Cycle of School of Nuclear Science and Engineering*, National Research Tomsk Polytechnic University
ORCID: 0000-0002-0172-3732
E-mail: semenov_ao@tpu.ru

Aleksei V. Utkin, *Cand. Sci. (Chem.)., Senior Researcher of the Laboratory of Chemical Materials Science*, Institute of Solid State Chemistry and Mechanochemistry, Siberian Branch of the Russian Academy of Sciences
ORCID: 0000-0003-2709-322X
E-mail: utkin@solid.nsc.ru

Сведения об авторах

Юрий Леонидович Крутский, *к.т.н, доцент кафедры химии и химической технологии*, Новосибирский государственный технический университет
ORCID: 0000-0003-2524-4143
E-mail: krutskii@yandex.ru

Татьяна Сергеевна Гудыма, *аспирант кафедры химии и химической технологии*, Новосибирский государственный технический университет
ORCID: 0000-0002-4724-3371
E-mail: gudymatan@mail.ru

Татьяна Михайловна Крутская, *к.х.н., доцент кафедры физики и химии*, Новосибирский государственный архитектурно-строительный университет
ORCID: 0000-0001-8003-4523
E-mail: t.krutskaya@mail.ru

Андрей Олегович Семенов, *старший преподаватель отделения ядерного топливного цикла Инженерной школы ядерных технологий*, Национальный исследовательский Томский политехнический университет
ORCID: 0000-0002-0172-3732
E-mail: semenov_ao@tpu.ru

Алексей Владимирович Уткин, *к.х.н., старший научный сотрудник лаборатории химического материаловедения*, Институт химии твердого тела и механохимии Сибирского отделения РАН
ORCID: 0000-0003-2709-322X
E-mail: utkin@solid.nsc.ru

Contribution of the Authors

Yu. L. Krutskii – writing the text.
T. S. Gudyma – writing the text.
T. M. Krutskaya – search for literary data in the SciFinder system.
A. O. Semenov – search for literary data in the SciFinder system.
A. V. Utkin – writing the text.

Вклад авторов

Ю. Л. Крутский – составление текста статьи.
Т. С. Гудыма – работа с текстом статьи.
Т. М. Крутская – поиск статей в системе SciFinder.
А. О. Семенов – поиск статей в системе SciFinder.
А. В. Уткин – работа над текстом статьи.

Received 24.02.2022
Revised 10.06.2022
Accepted 15.03.2023

Поступила в редакцию 24.02.2022
После доработки 10.06.2022
Принята к публикации 15.03.2023

Physico-chemical basics of metallurgical processes / Физико-химические основы металлургических процессов

UDC 669.71
DOI 10.17073/0368-0797-2023-4-459-470

Original article
Оригинальная статья

Thermodynamic assessment of conditions for co-reduction of zinc and iron by carbon from oxides of concentrates and waste from metallurgical enterprises

N. F. Yakushevich, E. V. Protopopov, M. V. Temlyantsev, I. V. Strokina

Siberian State Industrial University (42 Kirova Str., Novokuznetsk, Kemerovo Region – Kuzbass 654007, Russian Federation)

protopopov@sibsiu.ru

Abstract. The paper considers theoretical issues of reduction of zinc and iron by carbon from oxides of concentrates and zinc-containing metallurgical waste (dust and sludge of metallurgical furnaces). The described parallel reduction of zinc and iron by carbon from oxides undergoes with the formation of solid metal solution of Fe–Zn containing up to 46 wt. % of zinc, melts and the vapor–gas phase of $CO–CO_2–Zn$, the equilibrium composition of which is determined by the temperature and zinc content in solid solutions and melts. The authors determined the activity and elasticity of zinc vapor in solid solutions and melts of the Fe–Zn system and the activity of components in slag melts of the $ZnO–SiO_2$ system. Thermodynamic assessment showed that in the absence of solid carbon, the reduction of zinc from oxide by carbon monoxide is possible at temperatures above 1320 °C, and reduction by iron is possible in the temperature range of 1320–1500 °C. During reduction from slag melts at reduced activity values of zinc and iron oxides and elevated temperatures, reduction of zinc is carried out more efficiently than reduction of iron. In the presence of solid carbon in all temperature ranges (above 620 °C) and concentrations of zinc and iron monoxides at values $a_{ZnO} > 0$, $a_{FeO} > 0.4$, reduction of iron undergoes more efficiently ($\Delta G^{\circ}_{FeO} < \Delta G^{\circ}_{ZnO}$). In the case of co-reduction of iron and zinc, the primary reduction product is solid iron. Thermodynamically, the possible introduction of zinc atoms into a solid solution of α-Fe is practically not realized due to the high elasticity of zinc vapor even at low concentrations in the outer layers on the surfaces of crystalline nuclei of α-Fe, which causes the possibility of a sufficiently deep degree of reduction and sublimation of zinc during its carbon-thermal reduction from concentrates and waste from metallurgical enterprises.

Keywords: zinc, metallurgical zinc – containing wastes, state diagrams of Fe – Zn, Fe – Zn – O – C, $ZnO – SiO_2$ systems, zinc activity in solid solutions and Fe – Zn melts, component activity in slag melts, zinc vapor elasticity over solid solutions and melts of Fe – Zn

For citation: Yakushevich N.F., Protopopov E.V., Temlyantsev M.V., Strokina I.V. Thermodynamic assessment of conditions for co-reduction of zinc and iron by carbon from oxides of concentrates and waste from metallurgical enterprises. *Izvestiya. Ferrous Metallurgy*. 2023;66(4):459–470. https://doi.org/10.17073/0368-0797-2023-4-459-470

Термодинамическая оценка условий совместного восстановления цинка и железа углеродом из оксидов концентратов и отходов металлургических производств

Н. Ф. Якушевич, Е. В. Протопопов, М. В. Темлянцев, И. В. Строкина

Сибирский государственный индустриальный университет (Россия, 654007, Кемеровская обл. – Кузбасс, Новокузнецк, ул. Кирова, 42)

protopopov@sibsiu.ru

Аннотация. Рассматриваются теоретические вопросы восстановления цинка и железа углеродом из оксидов концентратов и цинксодержащих металлургических отходов (пыли и шламы металлургических печей). Показана возможность параллельного восстановления цинка и железа углеродом из оксидов с образованием твердых металлических растворов Fe–Zn, содержащих до 46 % цинка (по массе), расплавов и парогазовой фазы $CO–CO_2–Zn$, равновесный состав которой определяется температурой и содержанием цинка в твердых растворах и расплавах. Определены активности и упругости пара цинка в твердых растворах и расплавах системы Fe–Zn и активности

компонентов в шлаковых расплавах системы $ZnO-SiO_2$. Термодинамическая оценка показывает, что при отсутствии твердого углерода восстановление цинка из оксида оксидом углерода CO возможно при температурах выше 1320 °C, а восстановление железом возможно в интервале температур 1320 – 1500 °C. При восстановлении из шлаковых расплавов при пониженных значениях активностей оксидов цинка и железа и повышенных температурах восстановление цинка осуществляется более эффективно, чем восстановление железа. В присутствии твердого углерода во всех диапазонах температур (выше 620 °C) и концентраций оксидов цинка ZnO и железа FeO при значениях $a_{ZnO} > 0$, $a_{FeO} > 0{,}4$ восстановление железа проходит более эффективно ($\Delta G^{\circ}_{FeO} < \Delta G^{\circ}_{ZnO}$). При совместном восстановлении железа и цинка первичным продуктом восстановления является твердое железо. Термодинамически возможное внедрение атомов цинка в твердый раствор α-железа практически не реализуется из-за высокой упругости пара цинка уже при небольших его концентрациях в наружных слоях на поверхностях кристаллических зародышей α-железа, что обуславливает возможность достаточно глубокой степени восстановления и возгонки цинка при углеродотермическом восстановлении его из концентратов и отходов металлургических производств.

Ключевые слова: цинк, металлургические цинксодержащие отходы, диаграммы состояния систем Fe – Zn, Fe – Zn – O – C, $ZnO-SiO_2$, активности цинка в твердых растворах и расплавах Fe – Zn, активности компонентов в шлаковых расплавах, упругость пара цинка над твердыми растворами и расплавами Fe – Zn

Для цитирования: Якушевич Н.Ф., Протопопов Е.В., Темлянцев М.В., Строкина И.В. Термодинамическая оценка условий совместного восстановления цинка и железа углеродом из оксидов концентратов и отходов металлургических производств. *Известия вузов. Черная металлургия*. 2023;66(4):459–470. https://doi.org/10.17073/0368-0797-2023-4-459-470

Introduction

The reduction of zinc by carbon from concentrates or metallurgical waste (dust, sludge) constitutes the primary intermediate stage in the technologies for producing zinc and zinc oxide (ZnO). Various technological options are known, implemented at temperatures ranging from 1100 to 1290 °C, including heat treatment in drum furnaces (Waelz process), multi-hearth shaft furnaces (PRIMUS process), ring furnaces (DRIVIRON process), and others. Typically, these technologies facilitate the "distillation" of zinc obtained during the vapor reduction process. Subsequently, the captured zinc vapor is condensed in apparatuses, or zinc oxide is obtained in the form of a pulverized concentrate containing up to 65 wt. % (rotary kilns) or up to 96 wt. % (multi-hearth furnaces) zinc oxide suitable for the production of electrolytic zinc metal. These zinc oxide products find application in various industries, including paint, rubber, etc. [1 – 3].

The residue remaining post zinc distillation, commonly in the form of slags containing up to 30 % iron or metallized pellets, which may contain up to 50 % (PRIMUS process) or up to 96 % (DRIVIRON process) of reduced iron metal, serves as raw material in the smelting of cast iron, steel, and ferroalloys [2].

Despite the requirement for theoretical justification for numerous technological variants, the parameters of most utilized modes are established upon the findings of kinetic studies on the reactions involving iron and zinc oxides with carbon dioxide. The practical determination of suitable parameters and designs for the involved units is crucial in this context.

A comprehensive thermodynamic analysis of the co-reduction of iron and zinc oxides is notably lacking, with insufficient consideration given to the formation of solid solutions and Fe – Zn melts, as well as chemical compounds like $ZnO \cdot Fe_2O_3$ (zinc ferrite), (Mn, Zn)Fe_2O_4 (franklinite), $ZnO \cdot Fe_2O_3 - 2ZnO \cdot 5Fe_2O_3$ solutions. Additionally, there is an absence of information on the activities of components in Fe – Zn solid solutions, metal and slag melts, or the composition of the vapor-gas phase above these solutions and melts. The simplified schemes outlining the multiparameter mechanism of physicochemical interactions within the Fe – Zn – C – O system do not provide adequate guidance for accurately selecting the parameters of the technological regime for a specific process.

This study focuses on conducting a thermodynamic assessment of the conditions for co-reduction of zinc and iron by carbon, utilizing oxides present in metallurgical production waste such as dust and sludge. These waste materials are generated during the melting of cast iron and steel in electric arc steel-smelting furnaces and converters.

Thermodynamic analysis

Table presents the approximate composition of zinc-containing materials used in carbon-thermal reduction processes [1; 2; 4; 5].

According to [6], zincite (ZnO) and hematite (Fe_2O_3) combine to form the compound zinc ferrite ($ZnO \cdot Fe_2O_3$), or franklinite (Zn, Mn)Fe_2O_4 in the presence of manganese oxide MnO. This compound remains stable in the temperature range of 700 – 1100 °C. These compounds, particularly with an excess of Fe_2O_3, create solid solutions of hematite – ferrite (or franklinite) up to the stoichiometric ratio of $2ZnO + 5Fe_2O_3$. These solutions maintain the spinel structure in its pure form up to 1100 °C. If the Fe_2O_3:ZnO ratio exceeds 2.5, sintered products contain magnetite (Fe_3O_4), is present in the sintered products; whereas a ratio lower than 1.0 results in the presence of zincite.

In dusts from arc steel smelting furnaces, characterized by 50 – 60 % Fe_2O_3, 0.5 – 4.0 % MnO and approximately 10 – 25 % ZnO [1; 2] (with a Fe_2O_3:(ZnO + MnO) ratio > 3), franklinite and magnetite are consistently present. Notably, FeO and ZnO are typically absent under these conditions.

The co-reduction of iron and zinc from dust waste follows a complex multi-stage scheme. At the first stage,

Composition of zinc-containing materials

Состав цинксодержащих материалов

Material	Content, wt. %														Reference
	Zn	Fe	SiO_2	CaO	MgO	Al_2O_3	C	Mn	Pb	Na_2O	K_2O	S	Cl	F	
Concentrate	45 – 55	5 – 15	1.0 – 5.5	0.3 – 1.2	0.2 – 0.7	1.2 – 2.7	–	–				28 – 32			[1]
EAF dust (15 – 20 kg/t steel)	18.2	30.5	4.6	7.0	2.0	1.0	2.1	2.0 – 4.0		1.5 – 2.0	2.0 – 2.5	0.45		up to 5.8	[2]
Clinker (slag of Waelz process)	1.2	30.5	28.2	7.3	2.1	1.9	1.0		3.0 – 5.0			0.4			[4]
EAF dust	12.35	44.77	3.9	7.02	9.21	0.38	10.8	2 – 4		2.94	1.0	0.4	1 – 2	0.1 – 0.4	A*
Concentrated products	45 – 55	5 – 15	1.0 – 5.5	0.3 – 1.2	0.2 – 0.7	1.2 – 2.7	–	–				28 – 32			[1]
Converter dust	5.95	34.27	3.13	15.68	7.72	1.37	10.80	0.94		1.66	2.48	0.25			A*
Zinc pitch	18 – 21	13 – 30	24 – 29	2 – 5					1.5 – 5.0				4 – 8		[2]
Converter sludge	8 – 17	3.7	5 – 10	10 – 18					0.2 – 0.3				1 – 3		[2]
Blast furnace sludge from West Siberian Metallurgical Combine	6 – 10	28 – 35	4 – 8	3.0 – 5.9	1.7 – 2.0	1.6 – 4.0	18 – 34			1.0 – 1.6	0.10 – 0.15	2.4 – 3.3			[5]
Pyrolysis product of rubber tires	8.24	5.55	12.38	1.93	0.48	1.69	56.81	0.12		1.63	0.44	4.20			A*

Note. A* based on the analysis results of samples from EVRAZ JSC.

within a reducing atmosphere, zinc ferrite readily undergoes decomposition through the reaction

$$ZnO{\cdot}Fe_2O_3 + 1/3CO = ZnO + 2/3Fe_3O_4 + 1/3CO_2. \quad (1)$$

At the second stage, higher iron oxides present in zinc-containing materials, along with the magnetite formed during the ferrite decomposition, are reduced by gaseous carbon monoxide CO in accordance with the reactions:

$$3Fe_2O_3 + CO = 2Fe_3O_4 + CO_2; \quad (2)$$

$$Fe_3O_4 + CO = 3FeO + CO_2. \quad (3)$$

Reaction (3) is achieved at 550 °C when the carbon monoxide content (in the gas phase composed of CO and CO_2) is approximately 50 %. At 640 °C, the equilibrium P_{CO} is roughly 0.4. At higher temperatures, reaction (3) can occur at low concentrations of carbon monoxide (CO): at 1000 °C $P_{CO} \approx 0{,}2$ atm; at 1200 °C $P_{CO} \approx 0.1$ atm [7].

At the third stage, reduction of iron from wustite with carbon monoxide CO occurs through the reaction

$$FeO(s) + CO = Fe(s) + CO_2 \quad (4)$$

this reduction process takes place at elevated concentrations of carbon monoxide CO in the gas phase. Specifically, at 700 °C $P_{CO} \geq 0.6$ atm, $CO{:}CO_2 \approx 1.5$; at 400 °C $P_{CO} \geq 0.68$ atm, $CO{:}CO_2 \approx 2$; at 1300 °C $P_{CO} \geq 0.76$ atm, $CO{:}CO_2 \approx 2.7$ [8]).

The reduction of zinc from oxide occurs through the reaction

$$ZnO(s) + CO = Zn(l, g) + CO_2, \quad (5)$$

however, this process is intricate due to intense zinc evaporation and the formation of α-Fe–Zn solid solutions and Fe–Zn melts.

In the presence of solid carbon or the potential for its formation during the decomposition of carbon monoxide (CO), the reduction of oxides at all stages can be achieved through direct contact interaction with solid carbon, known as direct reduction. Thermodynamically, this process is more favorable; however, its efficient implementation requires fine grinding and thorough mixing of the reagents to maximize the interaction surface. The composition of the equilibrium gas phase in this case is constrained by the equilibrium of the Boudoir reaction

$$CO_2 + C = 2CO. \quad (6)$$

For the practical implementation of carbon-thermal reduction technologies, it is crucial to determine the parameters of phase-chemical interactions occurring at the third and final stage of the process.

The thermodynamic analysis was based on the following initial data: one of the latest versions of the state diagram of the iron–zinc system [9], which notably differs from those previously presented in reference literature (refer to Fig. 1 in [10]); the phase chemical equilibrium diagram of the Fe–C–O system (see Fig. 4 in [11]); and reference data concerning the thermodynamic properties of iron, zinc, and carbon oxides [12 – 14].

According to the state diagram of Fe–Zn alloys [9], zinc undergoes melting at a temperature of 419.6 °C (forming a eutectic with less than 0.1 % Fe at 419.4 °C). As the temperature increases to 531 °C, the solubility of iron in the zinc melt rises, reaching approximately 2.5 %. Upon exceeding the equilibrium iron concentrations, a solid solution, known as the ζ phase (Zn ≈ 94 ÷ 97 %), precipitates from the melt. At 531 °C, the ζ phase undergoes decomposition through a peritectic reaction, giving rise to the δ_1 phase (solid solution Zn ≈ 88 ÷ 92 %). The δ_1 phase coexists with the "Γ_1" phase (81 – 86 % Zn), until 550 °C, at which point it decomposes, forming the "Γ" phase. The "Γ" phase coexists with the δ and α-iron phases up to 667 – 780 °C. In the temperature range of 667 – 780 °C, it coexists with α-ferrite and a liquid melt containing iron ranging from 2.5 to 8.5 %. At 780 °C, the "Γ" phase undergoes decomposi-

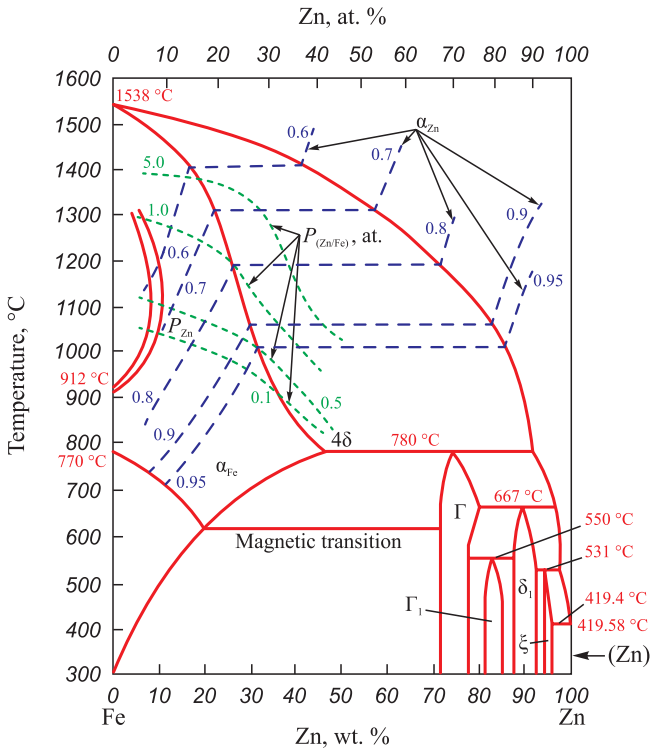

Fig. 1. State diagram of the Fe–Zn system:
– – – – zinc activity in solid solutions and Fe–Zn melts;
——— – P_{Zn} – elasticity of zinc vapor over Fe–Zn solid solutions;
– – – – α_{Zn} – Fe – Zn solid solutions

Рис. 1. Диаграмма состояния системы Fe–Zn:
– – – – активности цинка в твердых растворах и расплавах Fe–Zn;
——— – P_{Zn} – упругость пара цинка над твердыми растворами Fe–Zn;
– – – – α_{Zn} – твердые растворы Fe–Zn

tion through a peritectic reaction into a liquid melt containing approximately 8 % iron and a solid solution based on α ferrite with a zinc content of 46 %. At temperatures lower (300 °C) and higher (up to 1535 °C), the zinc content in the ferrite solution decreases nearly to zero. Consequently, the region of Fe – Zn solid solutions extends within the range of zinc concentrations of 0 – 46 % in the solution and temperatures of 0 – 1535 °C. Additionally, there exists a broader two-phase region, encompassing iron-based solid solutions containing 0 – 46 % Zn and liquid Fe – Zn melts with a zinc content ranging from 0 (at 153 °C) to 92 % (at 780 °C).

Fe – Zn solid solutions based on α ferrite undergo a magnetic transformation within the temperature range of 769 °C (0 % Zn) to 623 °C (20 % Zn).

Zinc exhibits high vapor elasticity, and its vapor pressure above pure zinc follows the equation

$$\lg P^{\circ}_{Zn} = -\frac{6171}{T} + 5.423,$$

according to this equation $P^{\circ}_{Zn} = 0.1$ atm at 720 °C, $P^{\circ}_{Zn} = 1$ atm at 907 °C, $P^{\circ}_{Zn} = 10$ atm at 1183 °C, $P^{\circ}_{Zn} = 57$ atm at 1500 °C. Equilibrium zinc vapor pressures above solid solutions of α-Fe – Zn and melts vary in accordance with changes in the activity of zinc in them and temperature, described by the equation $a_{ZnO} = f(x_{Zn}, T)$.

Due to the lack of data on the activities of components in the Fe – Zn system, the Fe – Cu system was employed as a prototype. In the Fe – Cu system, a broad range of solid solutions based on α-Fe – Cu ferrite (Cu ≈ 0 ÷ 8 %) exists, bordering in the temperature range of 1094 – 1484 °C with an even wider two-phase region: solid solution (α-Fe) – melt (Cu = $8_{(1484\,°C)} \div 97_{(1094\,°)}$ %) [10]. Substantial positive deviations from Raoult's law are observed in Fe – Cu melts. At 1550 °C in Fe – Cu melts with a copper content of 0 – 4 % $\gamma_{Cu} = 10.1$. With an increase in the concentration of copper in the melt, the activity of copper decreases: at $x_{Cu} = 0.1$ (10 %) – $\gamma_{Cu} = 5.4$, $a_{Cu} = 0.56$; at $x_{Cu} = 0.2$ (18 %) – $\gamma_{Cu} = 13.8$, $a_{Cu} = 0.71$; at $x_{Cu} = 0.4$ (37 %) – $\gamma_{Cu} = 2.0$, $a_{Cu} = 0.8$; at $x_{Cu} = 0.8$ (70 %) – $\gamma_{Cu} = 1.2$, $a_{Cu} = 0.89$ [15]. It is noteworthy that in homogeneous melts with positive deviations from Raoult's law, these positive deviations increase as the temperature decreases. When the concentration dependence lines reach $a_i = f(x_i, T)$ = const for compositions corresponding to x_i of the liquidus at a given temperature, the values of a_i within the two-phase region remain constant until the x_i of the solidus is reached. Simultaneously, positive deviations from Raoult's law increase even more. Furthermore, the activity of components in a homogeneous solid solution decreases as their concentration in the solution decreases.

The values of activities and activity coefficients of zinc in Fe – Zn solid solutions and melts, as per these assumptions, are depicted in Fig. 2.

In melts with high zinc content (more than 50 %), zinc activity coefficients exhibit minimal deviation from unity, and zinc activities demonstrate slight positive deviations from Raoult's law. In solid solutions with a zinc content ranging from 5 to 25 % and temperatures between 1000 and 1400 °C, the activity of zinc varies from 0.5 to 0.9, and the activity coefficients are $\gamma_{Zn} = 5 \div 9$, indicating substantial positive deviations from Raoult's law.

Consequently, even above solid solutions (α-Fe, Zn) containing relatively small amounts of zinc (5 – 10 %), the vapor pressure of zinc is substantial. The equilibrium values of zinc activities in solid solutions and melts, along with the vapor pressure of zinc above solid solutions, are plotted on the state diagram of the Fe – Zn system (Fig. 1). Based on the provided data, it can be inferred that at a zinc content in the α-iron solid solution of 5 – 10 %, the vapor pressure of zinc at $t \approx 1050$ °C reaches 0.5 atm, and at 1300 °C, it surpasses 1 atm. As the zinc concentration in the solid solution increases, the vapor pressure of zinc also increases. For instance, $t \approx 1050$ °C, it attains 0.1 atm and 0.5 atm at 5 and 20 % zinc content, respectively.

The outcomes of thermodynamic analysis of the reduction of iron and zinc from oxides are depicted in Fig. 3 as dependences of the functions $\Delta G° = f(T)$, reduced to 1 mole of oxygen in the initial gas phase for oxide formation reactions, and the corresponding number of moles of the initial oxide for reduction reactions.

The reduction of iron from wustite by carbon monoxide CO through reaction (4)

$$2FeO(s, l) + 2CO = 2Fe(s) + 2CO_2$$

initiates at 580 °C in the absence of solid carbon (point *F* in Fig. 3, where the lines $\Delta G° = f(T)$ for reactions (6) and (7) intersect):

$$2CO + O_2 = 2CO_2;$$

$$2Fe(s) + O_2 = 2FeO(s). \qquad (7)$$

For reaction (4) at $t = 580$ °C $\Delta G^{\circ}_{(4)} = 0$ ((point *F′*), $P_{CO}:P_{CO_2} = 1$, $P_{O_2} \approx 10^{-25}$ atm; at $t = 1200$ °C $\Delta G^{\circ}_{(4)} = -25$ kJ; at $t = 1500$ °C $\Delta G^{\circ}_{(4)} = -55$ kJ.

The reduction of zinc from zincite by carbon monoxide CO through reaction (5)

$$2ZnO(s) + 2CO = 2Zn(g) + 2CO_2$$

commences at higher temperatures. For the point *L′* in Fig. 3 $t_{start} \approx 1320$ °C, $\Delta G^{\circ}_{(5)} = 0$, $P_{O_2} \approx 10^{-10}$ atm; at $t = 1500$ °C $\Delta G^{\circ}_{(5)} = -55$ kJ. At $t = 1500$ °C the lines $\Delta G° = f(T)$ for reactions (4) and (5) at intersect at $\Delta G^{\circ}_{(4)} = \Delta G^{\circ}_{(5)} = -55$ kJ (point *D* in Fig. 3).

At temperatures lower than 1500 °C $\Delta G^{\circ}_{(4)} < \Delta G^{\circ}_{(5)}$, at $t > 1500$ °C $\Delta G^{\circ}_{(5)} < \Delta G^{\circ}_{(4)}$. It can be assumed that in

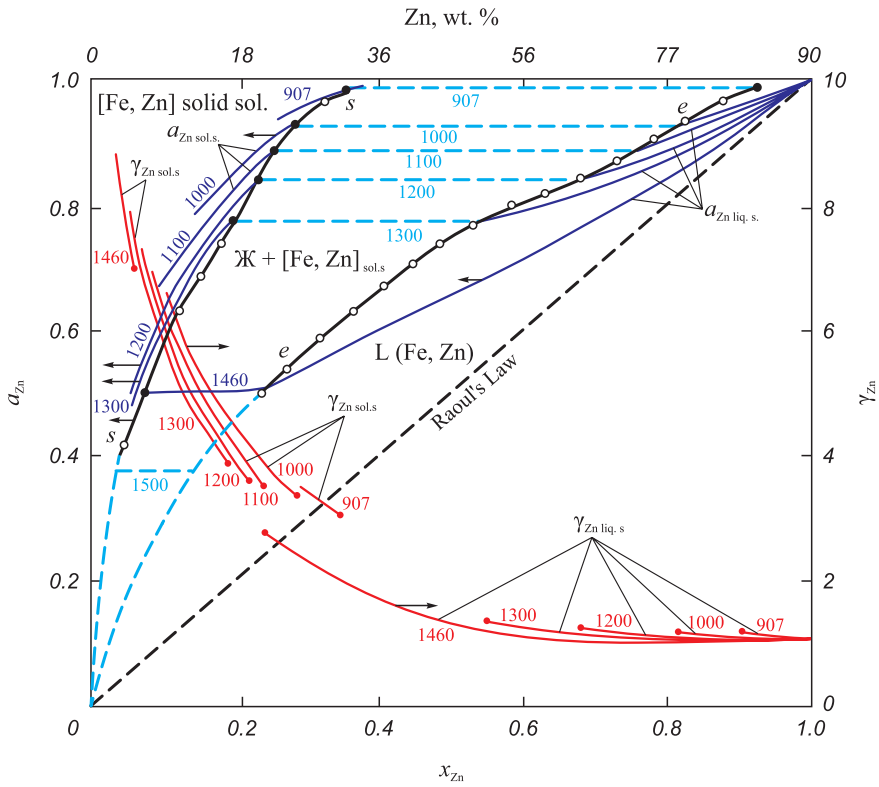

Fig. 2. Dependence of zinc activity and activity coefficient on composition and temperature

Рис. 2. Зависимость активности и коэффициента активности цинка от состава и температуры

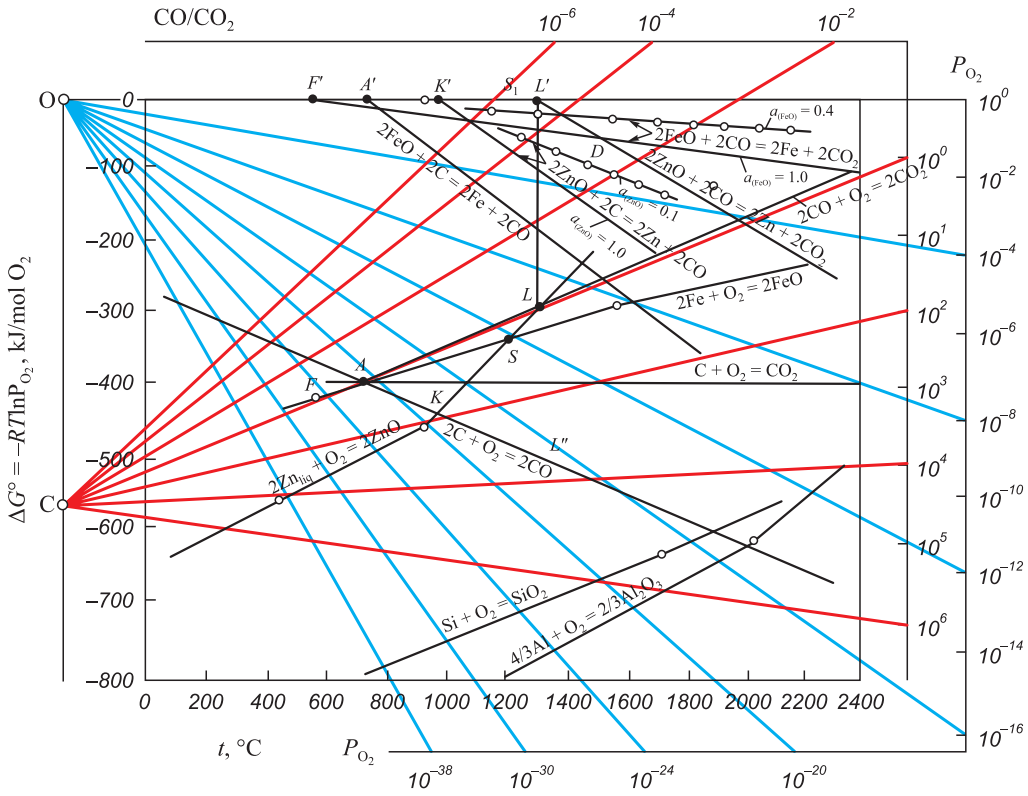

Fig. 3. Dependence of Gibbs energy and equilibrium compositions of the gas phase ($CO:CO_2$; P_{O_2}) on temperature for reactions of oxides formation and for reactions of reduction of iron and zinc by carbon and CO oxide

Рис. 3. Зависимость энергии Гиббса и равновесных составов газовой фазы ($CO:CO_2$; P_{O_2}) от температуры для реакций образования оксидов и для реакций восстановления железа и цинка углеродом и оксидом CO

the temperature range of 1320 – 1500 °C, under the conditions of a reducing atmosphere required for the production of iron metal by reaction (1) – (P_{CO}:P_{CO_2} > 1, P_{O_2} < 10^{-8} atm), reduced iron can act as a zinc-reducing agent from zincite. At higher temperatures, zinc vapor can reduce iron from wustite:

$$\mathrm{Fe(s, l) + ZnO(s)} \underset{>1500\ °C}{\overset{1320\div1500\ °C}{\rightleftharpoons}} \mathrm{Zn(g) + FeO(s, l)}. \quad (8)$$

Thus, the reduction of zinc from zincite by carbon monoxide CO is possible only at temperatures above 1320 °C (400 °C above the boiling point of zinc), with zinc obtained only in the vapor state. In practice, reactions (4), (5), and (8) proceed in parallel, and the reduced iron acts as a catalyst for reaction (5). The practical realization of the indirect reduction process is not realistic due to the low values of $\Delta G°$ for reactions (4), (5), (8).

The processes of iron and zinc reduction from oxides by solid carbon are governed by reactions (9) and (10):

$$\mathrm{2FeO(s, l) + 2C(s) = 2Fe(s, l) + 2CO}; \quad (9)$$

$$\mathrm{2ZnO(s) + 2C(s) = 2Zn(l, g) + 2CO}. \quad (10)$$

The initiation of reduction for reaction (9) is characterized in Fig. 3 by point *A*: the intersection of lines $\Delta G° = f(T)$ for reactions (6) and (11):

$$\mathrm{2C + O_2 = 2CO}, \quad (11)$$

for reaction (10), it is marked by point *K*: the intersection of lines $\Delta G° = f(T)$ for reactions (11) and (12):

$$\mathrm{2Zn(g) + O_2 = 2ZnO(s)}. \quad (12)$$

Parameters of point *A*: $t_{start} \approx 650$ °C, P_{CO}:$P_{CO_2} \approx 1.1$, $P_{O_2} \approx 10^{-21}$ atm; $\Delta G^{\circ}_{(9)start} = 0$ (point *A′*); for point *K*: $t_{start} \approx 960$ °C (approximately 330 °C lower than for reaction (5)), P_{CO}:$P_{CO_2} \approx 10^2$, $P_{O_2} \approx 10^{-19}$atm; $\Delta G^{\circ}_{(10)start} = 0$ (point *K′*).

Above 960 °C, in the entire temperature range, reaction (9) has a significant advantage over reaction (10) ($\Delta G^{\circ}_{(9)} - \Delta G^{\circ}_{(10)} = -80$ kJ).

During the co-reduction of iron and zinc, the presence of carbon facilitates the formation of the ternary carbide Fe_3ZnC [12]. This carbide coexists at temperatures of at least 780 °C with α-iron (with a zinc content in a solid solution based on α-iron lower than 46 % and carbon higher than 4 %) and the "Γ" phase with a zinc content of 71 – 74 %. The "Γ" phase decomposes at 780 °C through a peritectic reaction (13) with the formation of α-iron and a liquid phase containing approximately 7 % Fe, 89 % Zn, 4 % C:

$$\text{“}\Gamma\text{”} \rightarrow (\alpha\text{-Fe + Zn}) + \mathrm{l}. \quad (13)$$

The presence of carbon restricts the reduction processes by limiting the composition of the gas phase (CO:CO_2 ratio) in accordance with the equilibrium constant of the Boudoir reaction (6).

The presented volumetric diagram (Fig. 4, face *A*) indicates that in the presence of solid carbon, the reduction temperature of iron from wustite corresponds to $t_{start} \approx 690$ °C (for the formation of cementite Fe_3C $t_{start} \approx 680$ °C) with the CO:CO_2 ratio in the gas phase approximately 1.5. In the presence of excess carbon, the concentration of carbon monoxide CO in the gas phase aligns with the equilibrium for reaction (6). The CO:CO_2 ratio at 690 °C is approximately 1.5; at 900 °C, it is approximately 19; at higher temperatures, the content of carbon monoxide CO is almost 100 % (CO:$CO_2 \geq 10^2$) (Fig. 4).

Similarly, during the reduction of zinc by carbon according to reaction (10) at the start temperature of the reduction $t_{start} \approx 960$ °C and higher CO:$CO_2 \geq 10^2$.

It is worth noting that at low temperatures (below 1200 °C), the activities of iron and carbon show slight deviations from their molar concentrations [14], and their variations in Fe – Zn solid solutions and melts do not significantly affect the equilibrium of reactions (9) and (10).

During the carbothermal co-reduction of a mixture of zinc and iron oxides, the primary reduction product consists of crystalline iron nuclei formed by reactions (1) (in the temperature range 580 – 1535 °C) and (5) (above 700 °C until the formation of the iron-carbon melt). The reduction of zinc with its transition into iron nuclei, along with the formation of solid solutions based on α-iron, begins almost simultaneously with the emergence of a new phase (α-iron). This process is similar to what occurs during the co-reduction of manganese and silicon, where primary small drops of metal (MnC_x) with 5 – 8 % silicon are present [16]. In the melting of calcium carbide, in the primary drops of metal formed in the low-temperature levels of the ore smelting furnace bath, up to 8 % silicon in the ferrous alloy is also detected. It is noteworthy that in Mn – Si and Fe – Si alloys, there are strong negative deviations from Raoult's law ($\gamma_{Si} \approx 10^{-3}$), and in Fe – Zn alloys with low zinc concentrations ($x_{Zn} < 0.2$), there are positive deviations $\gamma_{Zn[Fe]} = 4 \div 10$ (Fig. 2). Considering the high vapor elasticity of zinc and the potential formation of low-melting films of melts on the surface of α-iron nuclei, along with the intense evaporation of zinc from their surfaces, and the kinetic challenges associated with zinc diffusion inside solid-phase nuclei, it can be assumed that most of the zinc transitions into the vapor-gas phase. Consequently, the equilibrium states of solid metal – slag – gas are practically unattainable due to these factors.

The calculated thermodynamic parameters of the Fe – Zn – O – C system are illustrated in Fig. 4. The analysis reveals that achieving a concentration of 5 ÷ 10 % Zn in the α-Fe solid solution is possible at temperatures

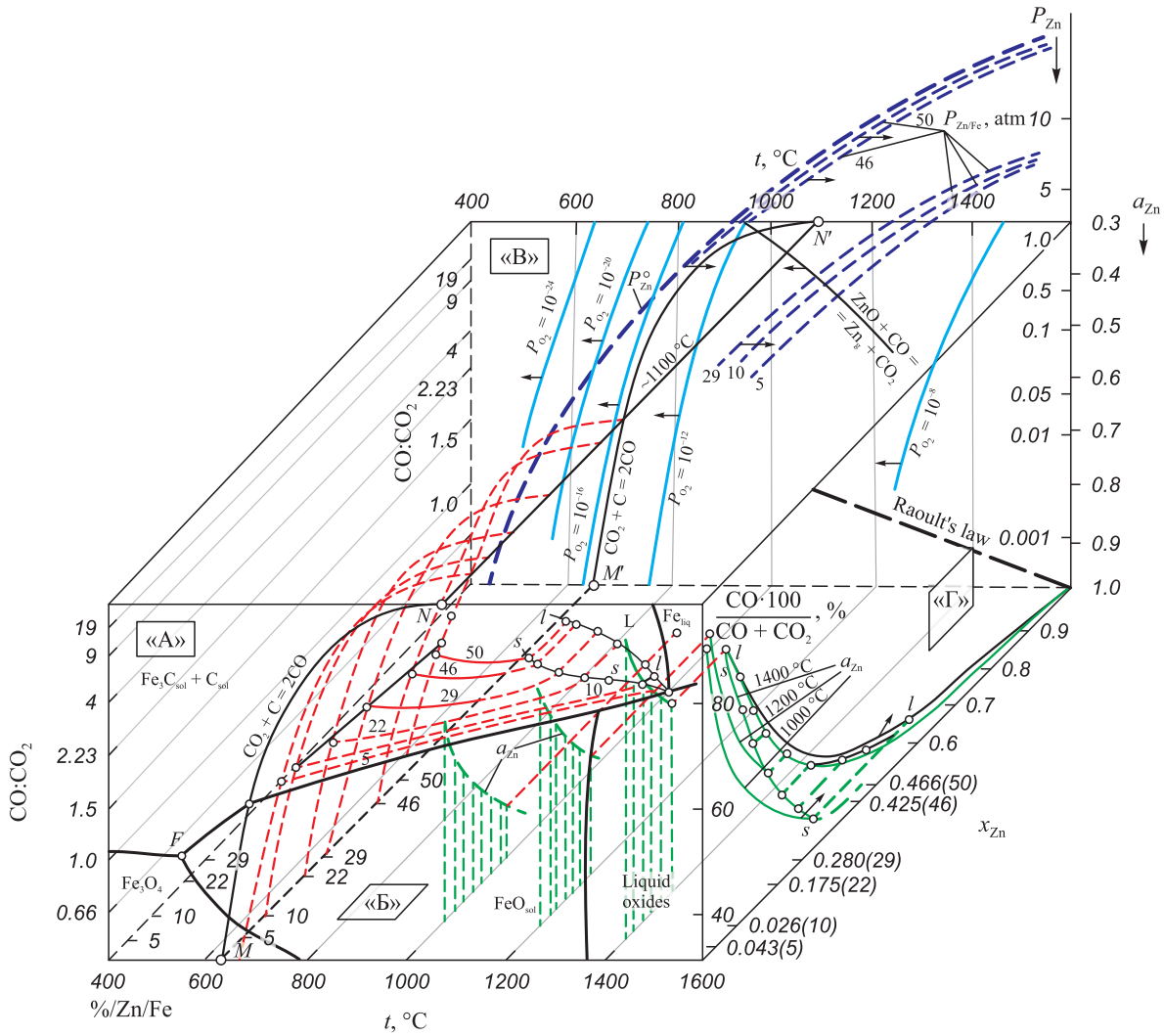

Fig. 4. Physico-chemical parameters of the Fe–Zn–O–C system (–o– – lines of liquidus (l – l) and solidus (s – s)

Рис. 4. Физико-химические параметры системы Fe–Zn–O–C (–o– – линии ликвидуса (l – l) и солидуса (s – s)

between 700 – 800 °C, with $a_{Zn} = 0.9$, and an equilibrium vapor pressure of zinc at approximately 0.01 atm (Fig. 1). In surface films that are supersaturated with zinc $P_{Zn} > 0.1$ atm, reaching 1 atm at 1300 – 1200 °C.

Results and discussion

The feasibility of co-reducing iron and zinc, leading to the formation of Fe–Zn solid solutions, is highly contingent on various factors such as temperature, heating rate, isothermal holding time, solubility, and the energy of formation of solutions.

For instance, when carbon interacts with silica particles smaller than 100 μm, the reduction rate increases by 2 – 3 orders of magnitude [17].

It can be postulated that factors such as the degree of grinding, mixing, and compacting of reagents, involving briquetting and agglomeration, could lead to a substantial increase in the reaction surface area. This increase, accompanied by elevated excess energy due to mechano-energetic activation during mechanical processes, might result in a lower initiation temperature for the co-reduction of iron and zinc, a rapid acceleration of reactions, and the potential formation of Fe–Zn solid solutions with a notably high concentration of zinc.

The optimal mixing of iron and zinc oxides is achieved when the components are combined at the molecular level in chemical compounds such as ferrite and franklinite, or at high temperatures in slag melts. Research [1] has demonstrated that zinc recovery from ferrite occurs more rapidly and at lower temperatures (~800 °C) compared to pure zincite (~1000 °C). Even at temperatures between 800 – 900 °C, zinc is significantly reduced (at 800 °C $P^{\circ}_{Zn} \approx 0.6$ atm; at 900 °C $P^{\circ}_{Zn} > 0.9$ atm).

The reduction of iron and zinc from slag melts by carbon monoxide CO is influenced by temperature, the composition of the gas phase, the melt composition, and, consequently, the activity of FeO oxide in the melt. Additionally, it depends on the physical characteristics of the melt, including homogeneity, viscosity, interfa-

cial surface tension between slag-metal and slag – gas, the degree of surface interaction influenced by the amount of slag and gas, as well as the degree of bubbling and emulsification of heterogeneous slag.

When reducing iron and zinc from slag with solid carbon, properties of the carbon reducing agent, including reactivity, porosity, density, fractional composition, and wettability with metal and slag melts, become significant factors.

In the FeO – SiO_2 system slags saturated with silica, the activity of iron oxide FeO when its content in the melt is 0 – 55 % ($x_{FeO} < 0.5$) exhibits little dependence on the composition and temperature (at 1350 – 1600 °C $a_{FeO} = 0.36 \div 0.37$ [10; 18]. In the presence of basic oxides, for example, like slags of the FeO – SiO_2 – (CaO + MgO) system, positive deviations from Raoult's law are observed at 1600 °C in the FeO concentration range of 0 – 50 %, with the magnitude increasing with higher slag basicity R = CaO:SiO_2 and lower temperature. For instance, at 1600 °C in slags saturated with silica (SiO_2 = 50 ÷ 60 %), and iron oxide FeO content of 10, 20, 30 and 40 %, the activities a_{FeO} are 0.15, 0.29, 0.45, and 0.55, respectively. Increasing slag basicity R to 1 results in approximately a 1.5 times increase in the activity of iron oxide. Similar findings were obtained in [1; 19] at 1250 and 1200 °C for slags containing 25 – 60 % FeO with basicity ranging from 0.33 – 1.0.

Therefore, from slags with $R < 1$ at $a_{FeO} < 1$ the reduction of iron by carbon monoxide CO is more challenging compared to pure oxide.

A similar conclusion can be drawn regarding reaction (5). The shift of lines of equilibrium $\Delta G° = f(T)$ for reaction (4) at $a_{FeO} = 0.4$ is shown in Fig. 3.

In most carbothermal technological processes designed for zinc recovery from concentrates and industrial waste (e.g., Waelz process, PRIMUS, etc.), measures are taken to prevent the formation of large amounts of low-melting liquid metal and complex oxide eutectic melts at process temperatures ranging from 1150 – 1250 °C. This is achieved by incorporating sand and an excess (up to four times the stoichiometric requirement) of a larger (up to 5 mm) carbonaceous reducing agent into the charge mixture as thickeners. The addition of these thickeners results in the formation of a viscous heterogeneous slag with a high content of silicon oxide (up to 30 – 40 %), leading to a significant decrease in the activity of the main oxides, including ZnO, in the slag. This complicates the recovery of zinc.

The interaction between zinc and silicon oxides gives rise to a double chemical compound, 2ZnO·SiO_2 commonly known as willemite, with a ZnO content of 73 %. Willemite undergoes congruent melting at 1512 °C and forms eutectics with ZnO (SiO_2 – 21 %, t = 1505 °C) and with SiO_2 (SiO_2 – 43 %, t = 1430 °C) (Fig. 5, *a*). At temperatures below 1430 °C within the ZnO concentrations in the range of 0 – 73 %, only solid phases coexist in the ZnO – SiO_2 system: SiO_2 and 2ZnO·SiO_2.

In the presence or addition of basic oxides (CaO, MgO, FeO, MnO) to the charge mixture, the melting temperature of the slag decreases (in the $e_1 - E_t$ direction, as shown in Fig. 5, *a*) reaching the temperatures of ternary or more complex eutectics (around ~1000 °C), and even lower in the presence of Na_2O (down to 800 °C). This can lead to the formation of complex zinc-containing compounds, such as $xMeO \cdot yZnO \cdot zSiO_2$ (x, y, z = 1 or 2).

The activity of zinc oxide a_{Zn} in eutectic melts can vary significantly and reach 0.1, significantly complicating the reduction of zinc. Fig. 3 illustrates the change in the parameters of the function $\Delta G° = f(T)$ for reaction (10) at $a_{Zn} = 1$ and $a_{Zn} = 0.1$. At 1200 °C, the difference between $\Delta G_{(10)}$ at $a_{Zn} = 1$ and $a_{Zn} = 0.1$ is ~30 % (70 and 50 kJ). It has been observed that in slags with a zinc content of 0.5 – 10 %, the replacement of calcium oxide with iron oxide FeO does not alter the activity coefficient of zinc oxide. However, a change in the content of the mole fraction of silicon oxide from 0.26 – 0.30 to 0.35 – 0.40 reduces the activity coefficient of zinc oxide by 2.1 – 2.5 times. Further increases in the SiO_2 content in the slag to 44 – 46 mol. % (slags saturated with silica) does not affect the value of the activity coefficient of zinc oxide.

Changes in the activities of components in the ZnO – SiO_2 system at 1500 and 1600 °C are shown in Fig. 5, *b* (the diagram shows isoactivity lines $a_{ZnO} = f(x_{SiO_2}, t = \text{const})$ and $a_{ZnO} = f(x_{SiO_2}, t = \text{const})$ (Fig. 5, *a*). The presence of two phase regions in the state diagram of the ZnO – SiO_2 system determined the sign alternating dependence of the activity isotherms of the components and their intersection with the lines of Raoult's law at points $R_i(a_i = x_i, \gamma_i = 1)$, which makes it possible to fairly correctly represent the course of activity isotherms [10].

It was demonstrated in [20] that in three-component (and more complex) systems, even in acidic slags (at the line of saturation with silica) with the addition of basic oxides (CaO, MgO, etc.), their activity in primary slags formed at the beginning of melting change by orders of magnitude (from 0.1 – 0.6 to ~0.001). Accurate information for a specific technological option and a given mode (charge composition, temperature) can be obtained through experimental studies.

Conclusions

Utilizing existing reference data and kinetic studies, a thermodynamic assessment of the co-reduction conditions of zinc and iron by carbon from oxides present in concentrates and by-products of metallurgical processes (such as dust and sludge generated during steel melting in electric arc furnaces and converters) was conducted.

Graphs depicting the zinc activity in solid metal solutions based on α-iron and Fe – Zn melts were created, illustrating their composition and temperature dependence.

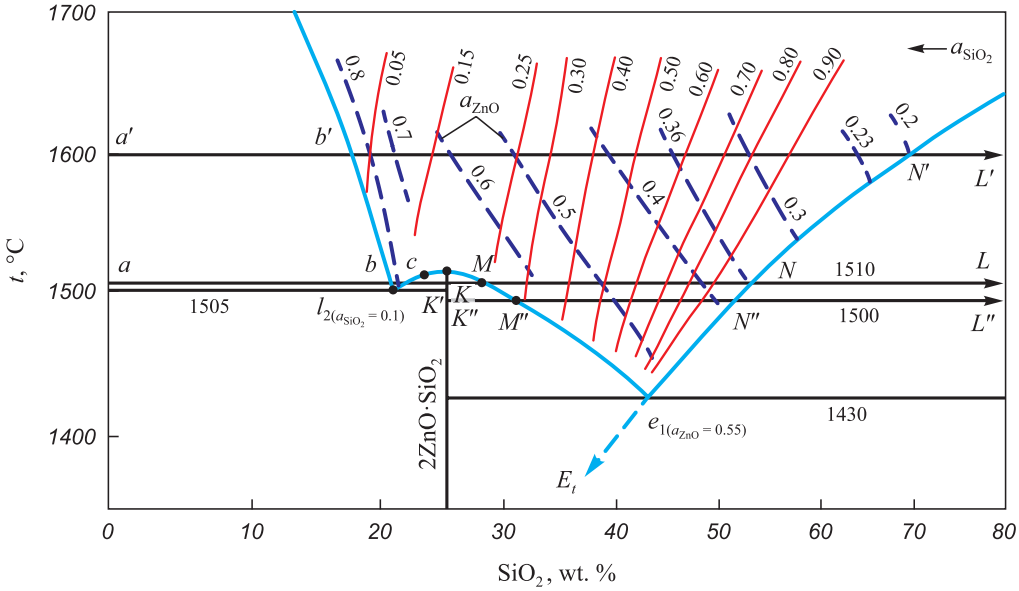

a

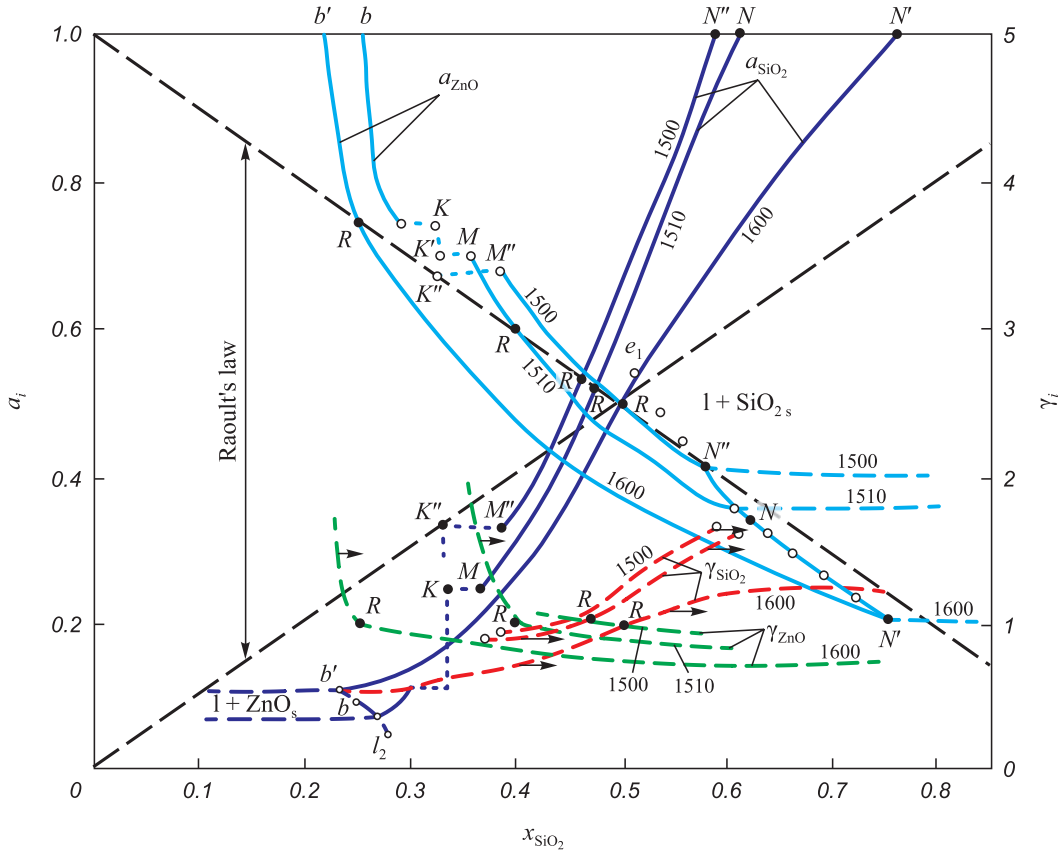

b

Fig. 5. Diagram of the state of the ZnO – SiO$_2$ system (*a*) and the activity and activity coefficients of the components in the ZnO – SiO$_2$ system (*b*): –o– – N'–N–N'' – l_1 and $в'$–$в$–l_2 – boundaries of the two-phase zones l + ZnO(s)

Рис. 5. Диаграмма состояния системы ZnO – SiO$_2$ (*a*) и активности и коэффициенты активности компонентов в системе ZnO – SiO$_2$ (*b*): –o– – N'–N–N'' – l_1 и $в'$–$в$–l_2 – границы двухфазных областей l + ZnO(s)

The activities of a_{ZnO} and a_{SiO_2} in ZnO – SiO$_2$ homogeneous melts at 1500 and 1600 °C were also charted. It is evident that in silica-saturated slags, the activity of zinc oxides decreases from 0.37 at 1430 °C to 0.2 at 1600 °C.

The absence of solid carbon in the system allows zinc recovery from oxide by carbon monoxide CO at temperatures above 1320 °C. However, with the presence of solid carbon, zinc reduction can occur at lower temperatures

(300 – 350 °C). At 1200 °C and $a_{ZnO} = 1$ $\Delta G_{(10)} \approx 50$ kJ, at ~1350 °C $\Delta G_{(10)} = 100$ kJ. The reduction from slags at $a_{ZnO} \leq 0.1$ requires higher temperatures (by 150 – 300 °C, respectively).

During co-reduction of zinc and iron from oxides with solid carbon, the primary reduction product is solid α-iron. At temperatures above 1000 °C, reduced iron acts as a reducing agent and catalyst for the zinc reduction reaction.

Zinc exhibits intensive evaporation from Fe – Zn metal melts and α-Fe – Zn solid solutions, including solid crystalline nuclei. Even with a zinc content in solutions of less than 5 % at 1300 °C, the equilibrium pressure of zinc vapor above the solutions reaches 1 atm, facilitating a high degree of dezincification of zinc-containing concentrates and metallurgical waste through carbothermal reduction methods.

References / Список литературы

1. Lakernik M.M. *Electrothermy in Metallurgy of Copper, Lead, Zinc*. Moscow: Metallurgiya; 1971:296. (In Russ.).

   Лакерник М.М. *Электротермия в металлургии меди, свинца, цинка*. Москва: Металлургия; 1971:296.
2. Tarasov A.V., Besser A.D., Mal'tsev V.I. *Metallurgical Processing of Secondary Zinc Raw Materials*. Moscow: Gintsvetmet; 2004:219. (In Russ.).

   Тарасов А.В., Бессер А.Д., Мальцев В.И. *Металлургическая переработка вторичного цинкового сырья*. Москва: Гинцветмет; 2004:219.
3. Saramak D., Krawczykowski D., Gawenda T. Investigations of zinc recovery from metallurgical waste. *IOP Conference Series: Materials Science and Engineering*. 2018;427:012017. https://doi.org/10.1088/1757-899X/427/1/012017
4. Kozlov P.A. *Veltz-Process*. Moscow: Ruda i metally; 2002:175. (In Russ.).

   Козлов П.А. *Вельц-процесс*. Москва: ИД «Руда и металлы», 2002:175.
5. Kuznetsov S.N., Volynkina E.P., Protopopov E.V., Zorya I.V. *Metallurgical Technologies for Processing Technogenic Deposits, Industrial and Household Waste*. Novosibirsk: Publishing House of the SB RAS; 2014:294. (In Russ.).

   Металлургические технологии переработки техногенных месторождений, промышленных и бытовых отходов / С.Н. Кузнецов, Е.П. Волынкина, Е.В. Протопопов, И.В. Зоря. Новосибирск: Изд-во СО РАН; 2014:294.
6. Ivanovskaya M.I., Tolstik A.I., Kotikov D.A., Pan'kov V.V. Structural features of Zn – Mn-ferrite synthesized by pyrilysis sputtering. *Zhurnal fizicheskoi khimii*. 2009;83(12): 2283–2288. (In Russ.).

   Ивановская М.И., Толстик А.И., Котиков Д.А., Паньков В.В. Структурные особенности Zn – Mn-феррита, синтезированного методом распылительного пиролиза. *Журнал физической химии*. 2009;83(12):2283–2288.
7. Dinel't V.M., Anikin A.E., Strakhov V.M. Reduction of iron ore by means of lignite semicoke. *Coke and chemistry*. 2011;54(5):165–168. https://doi.org/10.3103/S1068364X11050048
8. Nokhrina O.I., Rozhihina I.D., Hodosov I.E. The use of coal in a solid phase reduction of iron oxide. *IOP Conference Series: Materials Science and Engineering*. 2015;91:012045. https://doi.org/10.1088/1757-899X/91/1/012045
9. *State Diagrams of Double Metal Systems. Guide*. Lyakishev N.P. ed. Moscow: Mashinostroenie; 1997:1024. (In Russ.).

   Диаграммы состояния двойных металлических систем. Справочник / Под общ. ред. Н.П. Лякишева. Москва: Машиностроение; 1997:1024.
10. Elliott John F., Gleiser Molly, Ramakrishna V. *Thermochemistry for Steelmaking*. Addison – Wesley Inc.; 1963.

    Эллиот Д.Ф., Глейзер М., Рамакршина В. *Термохимия сталеплавильных процессов*. Москва: Металлургия; 1969:252.
11. Shcherban A.P. Dependence of interphase distribution coefficients on temperature and concentration of components in double metal systems. *East European Journal of Physics*. 2020;(4):63–68. https://doi.org/10.26565/2312-4334-2020-4-08
12. Kubaschewski O. *Iron – Binary Phase Diagrams*. Berlin; 1982.

    Кубашевски О. *Диаграммы состояния двойных и многокомпонентных систем на основе железа*. Москва: Металлургия, 1985:184.
13. Khina B.B., Goranskiy G.G. Thermodynamic properties of multicomponent amorphous alloys in Fe–Si–B–Ni and Fe–Si–B–Ni–CO–Cr–Mo systems. *Advanced Materials and Technologies*. 2016;(2):8–15. https://doi.org/10.17277/amt.2016.02.pp.008-015
14. Massardier V., Merlin J., Le Patezour E., Soler M. Mn–C interaction in Fe–C–Mn steels: Study by thermoelectric power and internal friction. *Metallurgical and Materials Transactions A*. 2005;36:1745–1755. https://doi.org/10.1007/s11661-005-0039-x
15. Yakushevich N. F., Kaveshnikov A.A. Thermodynamic analysis of the CaO – SiO_2 – TiO_2 system as part of invariant equilibria. *Izvestiya. Ferrous Metallurgy*. 2004;47(6):7–11. (In Russ.).

    Якушевич Н. Ф., Кавешников А.А. Термодинамический анализ системы CaO – SiO_2 – TiO_2 в состояниях инвариантных равновесий. *Известия вузов. Черная металлургия*. 2004;47(6):7–11.
16. *Schlackenatlas*. Verein Deutscher Eisenhüttenleute, Verlag Stahleisen; 1981:282. (In Germ.).

    Атлас шлаков / Перевод с нем. Г.И. Жмойдина / Под ред. И.С. Куликова. Москва: Металлургия; 1985:208.
17. Nikolaychuk P.A. Thermodynamic evaluation of electrochemical stability of Me – Si systems (Me = 4th row transition metal). *Journal of Siberian Federal University. Chemistry*. 2015;8(2):160–180. https://doi.org/10.17516/1998-2836-2015-8-2-160-180
18. Bertoli A.C., Garcia J.S., Trevisan M.G., Ramalho T.C., Freitas M.P. Interactions fulvate-metal (Zn^{2+}, Cu^{2+} and Fe^{2+}): theoretical investigation of thermodynamic, structural and spectroscopic properties. *Biometals*. 2016;29:275–285. https://doi.org/10.1007/s10534-016-9914-8
19. Prostakova V., Shishin D., Shevchenko M., Jak E. Termodynamic optimization of the Al_2O_3 – FeO – Fe_2O_3 – SiO_2 oxide system. *Calphad*. 2019;67:101680. https://doi.org/10.1016/j.calphad.2019.101680

20. Sokol'skii V.E., Galinich V.I., Kazimirov V.P., Batalin G.I., Shovskii V.A. Structure of the molten ternary silicate systems $MnO–TiO_2–SiO_2$ and $MnO–ZrO_2–SiO_2$. *Melts*. 1989;1(6): 513–519.

Information about the Authors

Nikolai F. Yakushevich, *Dr. Sci. (Eng.), Prof.-Consultant of the Chair of Non-Ferrous Metals and Chemical Engineering,* Siberian State Industrial University
E-mail: Yakushevich@cmet.sibsiu

Evgenii V. Protopopov, *Dr. Sci. (Eng.), Prof. of the Chair of Ferrous Metallurgy,* Siberian State Industrial University
ORCID: 0000-0002-7554-2168
E-mail: protopopov@sibsiu.ru

Mikhail V. Temlyantsev, *Dr. Sci. (Eng.), Prof., Vice-Rector for Educational and Tutorial Work,* Siberian State Industrial University
ORCID: 0000-0001-7985-5666
E-mail: uchebn_otdel@sibsiu.ru

Irina V. Strokina, *Cand. Sci. (Eng.), Senior Lecturer of the Chair of Non-Ferrous Metals and Chemical Engineering,* Siberian State Industrial University
ORCID: 0000-0003-3719-8949
E-mail: chuzhinova.iv@yandex.ru

Сведения об авторах

Николай Филиппович Якушевич, *д.т.н., профессор-консультант кафедры металлургии цветных металлов и химической технологии,* Сибирский государственный индустриальный университет
E-mail: Yakushevich@cmet.sibsiu

Евгений Валентинович Протопопов, *д.т.н., профессор кафедры металлургии черных металлов,* Сибирский государственный индустриальный университет
ORCID: 0000-0002-7554-2168
E-mail: protopopov@sibsiu.ru

Михаил Викторович Темлянцев, *д.т.н., профессор, проректор по учебной и воспитательной работе,* Сибирский государственный индустриальный университет
ORCID: 0000-0001-7985-5666
E-mail: uchebn_otdel@sibsiu.ru

Ирина Владимировна Строкина, *к.т.н., старший преподаватель кафедры металлургии цветных металлов и химической технологии,* Сибирский государственный индустриальный университет
ORCID: 0000-0003-3719-8949
E-mail: chuzhinova.iv@yandex.ru

Contribution of the Authors

N. F. Yakushevich – statement of the task, analysis of literary data, complex thermodynamic analysis of co-reduction Zn and Fe by carbon, writing the text.

E. V. Protopopov – analysis of selected data to calculate the thermodynamic parameters of co-reduction of zinc and iron by carbon.

M. V. Temlyantsev – statement of the task, calculation of thermodynamic parameters of co-reduction of Zn and Fe by carbon, analysis of literary data, processing of the results, editing the final versions of the article.
I. V. Strokina – calculation of thermodynamic parameters of co-reduction of Zn and Fe by carbon, obtaining results, preparing drawings and tables.

Вклад авторов

Н. Ф. Якушевич – постановка задачи, анализ литературных источников, проведение комплексного термодинамического анализа процесса совместного восстановления цинка и железа углеродом, написание текста статьи.
Е. В. Протопопов – проведение анализа подобранных источников информации для расчета термодинамических параметров процесса совместного восстановления цинка и железа углеродом.
М. В. Темлянцев – постановка задачи, расчет термодинамических параметров совместного восстановления цинка и железа углеродом, анализ литературных источников, обработка результатов, редактирование финальной версии статьи.
И. В. Строкина – проведение расчетов термодинамических параметров процесса совместного восстановления цинка и железа углеродом, получение результатов, подготовка рисунков и таблицы для статьи.

Received 14.04.2022
Revised 15.03.2023
Accepted 20.03.2023

Поступила в редакцию 14.04.2022
После доработки 15.03.2023
Принята к публикации 20.03.2023

Physico-chemical basics of metallurgical processes / **Физико-химические основы металлургических процессов**

UDC 669.168
DOI 10.17073/0368-0797-2023-4-471-478

Original article
Оригинальная статья

Physical properties and structure of boron-containing slags during reduction period of AOD process

R. R. Shartdinov, **A. A. Babenko, A. G. Upolovnikova, A. N. Smetannikov**

Institute of Metallurgy, Ural Branch of the Russian Academy of Sciences (101 Amundsena Str., Yekaterinburg 620016, Russian Federation)

rr.shartdinov@gmail.com

Abstract. The effect of basicity and content of boron oxide on viscosity, crystallization temperature, phase composition, and structure of the $CaO-SiO_2-B_2O_3-12\ \%\ Cr_2O_3-3\ \%\ Al_2O_3-8\ \%\ MgO$ fluorine-free slag system in the range of boron oxide content 3 – 6 % and basicity 1.0 – 2.5 is studied by vibrational viscometry, thermodynamic phase composition modeling (HSC Chemistry 6.12 (Outokumpu)), and Raman spectroscopy. It was found that physical properties of the studied slags mainly depend on the balance between the degree of structure polymerization, nature of the bond with it, and phase composition. With a low basicity of 1.0, slags are "long" and an increase in the content of boron oxide from 3 to 6 % makes them more fusible, reducing the crystallization temperature of the slag from 1340 to 1224 °C, and its viscosity from 1.0 – 0.8 to ~0.25 Pa·s at 1600 – 1660 °C, despite the significant complication of the structure, reflected in the growth of the bridging oxygen index BO from 1.10 to 1.49. With an increase in basicity, slags transfer from "long" to "short" and the content of calcium oxide increases, which, being a donor of free oxygen ions (O^{2-}), acts as a modifier of the slag structure. Thus, with a basicity of $B = (CaO/SiO_2) = 2.5$, slags have a simpler structure (BO = 0.50 – 0.53) relative to slags with a basicity of 1.0, while the addition of boron oxide complicates it only slightly (an increase in BO from 0.5 up to 0.53). Increasing the concentration of B_2O_3 lowers the crystallization temperature from 1674 to 1605 °C and the viscosity from 1.0 to 0.3 Pa·s at 1660 °C as a result of the formation of low-melting compounds (mostly $2CaO \cdot B_2O_3$).

Keywords: AOD-slag, boron oxide, chromium oxide, structure, viscosity, phase composition, crystallization temperature

Acknowledgements: The work was performed as part of the state task of the Institute of Metallurgy of the Ural Branch of the Russian Academy of Sciences using the equipment of the CCP "Composition of Matter" of the Institute of High-Precision Electronics of the Ural Branch of the Russian Academy of Sciences.

For citation: Shartdinov R.R., Babenko A.A., Upolovnikova A.G., Smetannikov A.N. Physical properties and structure of boron-containing slags during reduction period of AOD process. *Izvestiya. Ferrous Metallurgy*. 2023;66(4):471–478.
https://doi.org/10.17073/0368-0797-2023-4-471-478

Физические свойства и структура борсодержащих шлаков восстановительного периода АКР-процесса

Р. Р. Шартдинов, **А. А. Бабенко, А. Г. Уполовникова, А. Н. Сметанников**

Институт металлургии Уральского отделения Российской академии наук (Россия, 620016, Свердловская обл., Екатеринбург, ул. Амудсена, 101)

rr.shartdinov@gmail.com

Аннотация. Влияние основности и содержания оксида бора на вязкость, температуру кристаллизации, фазовый состав и структуру безфтористых шлаков системы $CaO-SiO_2-B_2O_3-12\ \%\ Cr_2O_3-3\ \%\ Al_2O_3-8\ \%\ MgO$ в диапазоне содержания оксида бора от 3 до 6 % и основности 1,0 – 2,5 были изучены посредством вибрационной вискозиметрии, термодинамического моделирования фазового состава (HSC Chemistry 6.12 (Outokumpu)) и рамановской спектроскопии. Было установлено, что физические свойства изучаемых шлаков главным образом зависят от баланса между степенью полимеризации структуры, природы связи в ней и фазового состава. При низкой основности (примерно 1,0) шлаки являются «длинными» и рост содержания оксида бора с 3 до 6 % делает их более легкоплавкими, снижая температуру кристаллизации шлака с 1340 до 1224 °C, а вязкость – с 1,0 – 0,8 примерно до 0,25 Па·с при температуре 1600 – 1660 °C, несмотря на значительное усложнение структуры, отражающееся в росте показателя мостикового кислорода BO с 1,10 до 1,49. С повышением основности шлаки из «длинных» переходят в «короткие». Растет содержание оксида кальция, который, являясь донором свободных ионов кислорода (O^{2-}), выступает в роли модификатора структуры шлака. При основности $B = (CaO/SiO_2) = 2,5$ шлаки обладают более

простой структурой (BO = 0,50 – 0,53) относительно шлаков с основностью 1,0, при этом добавление оксида бора усложняет ее лишь незначительно (рост показателя BO с 0,50 до 0,53). Увеличение концентрации B_2O_3 понижает температуру кристаллизации с 1674 до 1605 °C и вязкость – с 1,0 до 0,3 Па·с при температуре 1660 °C в результате образования легкоплавких соединений ($2CaO·B_2O_3$).

Ключевые слова: АКР-шлак, оксид бора, оксид хрома, структура, вязкость, фазовый состав, температура кристаллизации

Благодарности: Работа выполнена в рамках исполнения государственного задания Института металлургии Уральского отделения Российской академии наук с использованием оборудования ЦКП «Состав вещества» Института высокоточной электроники Уральского отделения Российской академии наук.

Для цитирования: Шартдинов Р.Р., Бабенко А.А., Уполовникова А.Г., Сметанников А.Н. Физические свойства и структура борсодержащих шлаков восстановительного периода АКР-процесса. *Известия вузов. Черная металлургия*. 2023;66(4):471–478.
https://doi.org/10.17073/0368-0797-2023-4-471-478

Introduction

Currently, the primary method employed for the smelting of low-carbon stainless steel is the argon oxygen decarburization (AOD). This technology, originated by Union Carbide Corp. in the USA in 1968, became widely adopted, and by the onset of the 21st century, approximately three-quarters of all stainless steel production used this technique [1].

The AOD process consists of two distinct phases: oxidation and reduction. The primary objective of the oxidation period is to decarbonize the metal by introducing a mixture of oxygen and inert gas, thereby attaining the required carbon concentrations while minimizing the oxidation of chromium. Subsequently, the reduction period ensues, during which the metal is purged solely with inert gas to enhance mixing and reintegrate oxidized chromium into the metal, accomplished through the addition of aluminum or silicon additives. Concluding the reduction phase, the metal undergoes desulfurization, resulting in the formation of slag characterized by low FeO oxide content and a basicity ranging from 2.0 to 2.5 [1]. Nevertheless, the effectiveness of achieving profound metal desulfurization and the efficient reduction of chromium is not solely dependent on the chemical activity of the oxide system components; it also relies on creating favorable kinetic conditions for the processes [1 – 3].

The kinetics of the processes involved in metal desulfurization and chromium reduction are predominantly influenced by the fluid mobility of the generated slags [1; 4]. The diffusion rates of sulfur and chromium oxide within the slag are inversely proportional to its viscosity [2]. To promote low viscosity in the resultant slag, fluorspar is frequently employed as a flux [1; 5; 6]. However, the utilization of the CaF_2 compound poses a significant drawback due to the generation of environmentally harmful volatile fluorides at elevated temperatures during the process [3; 7]. The advancement of this process is accompanied by a reduction in the refining properties of the resulting slags, an escalation in environmental impact, and a corrosive effect on equipment. Therefore, there is a need to develop refining slags with enhanced fluid mobility that do not incorporate fluorspar. A viable solution to this challenge is the incorporation of boron oxide, which, through interactions with the primary components of the generated slags, forms low melting eutectics ($CaO·B_2O_3$ and $2CaO·B_2O_3$ with melting points of 1130 and 1280 °C), ensuring heightened fluid mobility.

In this study, the viscosity (η), crystallization temperature (t_{cr}), phase composition, and structure of slags in the $CaO – SiO_2 – B_2O_3 – 12\ \%\ Cr_2O_3 – 3\ \%\ Al_2O_3 – 8\ \%\ MgO$ system were investigated across a range of boron oxide content from 3 to 6 % and basicity levels of 1.0 – 2.5. This investigation employed vibration viscometry, thermodynamic simulation of phase composition (HSC Chemistry 6.12 (Outokumpu)), and Raman spectroscopy.

Materials and experimental methods

In order to investigate the properties of slags within the $CaO – SiO_2 – B_2O_3 – 12\ \%\ Cr_2O_3 – 3\ \%\ Al_2O_3 – 8\ \%\ MgO$ system, slags were prepared, and their composition outlined in Table 1.

Table 1

Composition of the experimental slags

Таблица 1. **Состав экспериментальных шлаков**

Slag sample	Content in slag, %						*B*	t_{cr}, °C
	CaO	SiO_2	B_2O_3	MgO	Al_2O_3	Cr_2O_3		
1	37.00	37.00	3	8	3	12	1.0	1340
2	52.86	21.14	3	8	3	12	2.5	1674
3	50.71	20.29	6	8	3	12	2.5	1605
4	35.50	35.50	6	8	3	12	1.0	1224

The slag was melted in a resistance furnace using molybdenum crucibles in an argon atmosphere, with oxides of analytical grade calcined for 2 – 3 h at a temperature of 800 °C (oxide B_2O_3 at 100 °C).

Viscosity measurements of the resulting slags were conducted employing a vibration viscometer [8] in molybdenum crucibles under an argon atmosphere. Temperature measurement was executed using a tungsten–rhenium thermocouple. The data obtained, characterizing slag viscosity as a function of temperature, were utilized to construct graphs in $\ln\eta - 1/T$ coordinates. The inflection point of the viscosity polytherms in these coordinates, following Frenkel's theory of viscous flow, indicates the temperature at which slag crystallization initiates [9].

Thermodynamic simulation of the phase composition of experimental slag samples was performed using the HSC Chemistry 6.12 software package (Outokumpu) [10].

The structure of experimental slag samples was examined using a U 1000 Raman microscope-spectrometer with a laser featuring an exciting wavelength of 532 nm. The resulting spectra are presented graphically within the wavenumber range of 400 – 1500 cm^{-1}.

Results and discussion

The measured viscosity of the slags within the oxide system under investigation is illustrated in Fig. 1, and in Fig. 2, they are depicted in $\ln\eta - 1/T$ coordinates; the onset temperature of crystallization was determined based on the inflection in the dependency (Table 1).

Throughout the study, Raman spectra of the examined slags *1 – 4* were acquired (Fig. 3).

It is postulated that the extent of slag polymerization is primarily influenced by the high-frequency silicate range of 800 – 1200 cm^{-1}, corresponding to $[SiO_4]$ tetrahedra. For a comprehensive understanding of the slag structure, deconvolution of the Raman spectra within this range was conducted using the Gaussian method [11]. The distinctive peaks of elements Q^n_{Si} ($[SiO_4]$ with the number of bridging oxygen n) and others are detailed in Table 2, with the results of the deconvolution presented in Fig. 4.

A plausible method for representing the degree of slag polymerization is through the average quantity of bridging oxygen (BO). This metric is articulated as the number of bridging oxygen atoms multiplied by the relative

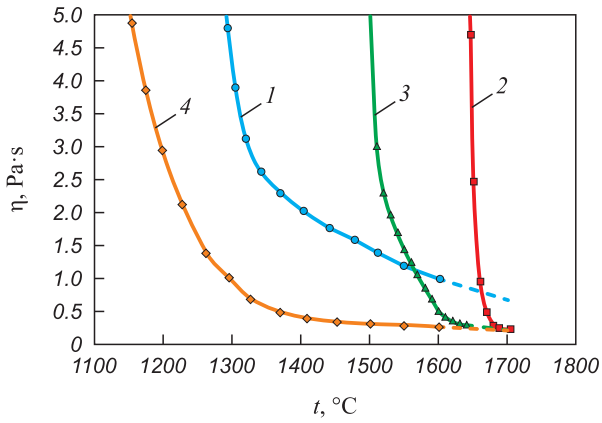

Fig. 1. Dependence of slag viscosity (*1 – 4*) on temperature

Рис. 1. Зависимость вязкости шлаков (*1 – 4*) от температуры

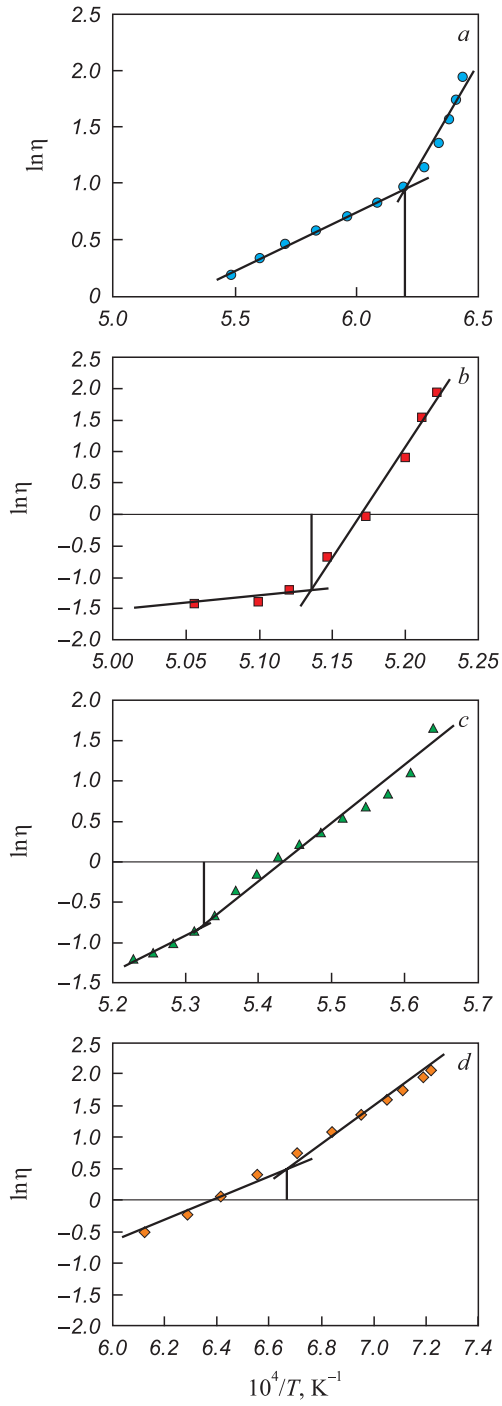

Fig. 2. Dependence of the logarithm of viscosity (lnη) on the inverse absolute temperature (1/*T*) for slags *1 – 4* (*a – d*)

Рис. 2. Зависимость логарифма вязкости (lnη) от обратной абсолютной температуры (1/*T*) для шлаков *1 – 4* (*a – d*)

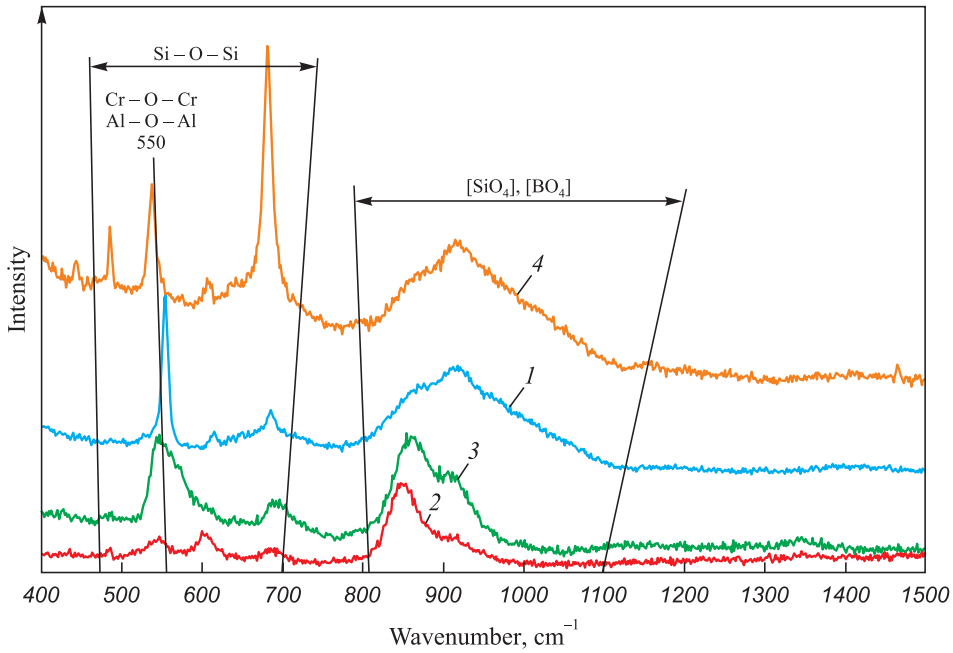

Fig. 3. Raman spectra of the slag samples *1* (B = 1.0; 3 % B_2O_3), *2* (B = 2.5; 3 % B_2O_3), *3* (B = 2.5; 6 % B_2O_3), *4* (B = 1.0; 6 % B_2O_3)

Рис. 3. Рамановские спектры образцов шлаков *1* (B = 1,0; 3 % B_2O_3), *2* (B = 2,5; 3 % B_2O_3), *3* (B = 2,5; 6 % B_2O_3), *4* (B = 1,0; 6 % B_2O_3)

fraction of each structural unit $[SiO_4]$ and is calculated using the formula outlined in Table 3:

$$BO = 0 \cdot Q^0_{Si} + 1 \cdot Q^1_{Si} + 2 \cdot Q^2_{Si} + 3 \cdot Q^3_{Si} + 4 \cdot Q^4_{Si}.$$

Table 4 showcases the outcomes of the thermodynamic simulation of the phase composition of experimental slag samples. The results, determined by the melting temperatures of the formed phases, were categorically divided into three groups: low temperature (1130 – 1280 °C), medium temperature (1460 – 1600 °C), and high temperature (1710 – 2852 °C) phases.

Acidic slags with a basicity of 1.0 (samples *1* and *4*) fall into the category of "long" slags (Fig. 1), characterized by a high degree of polymerization (Table 3). Fig. 3 does not display peaks corresponding to the $[BO_3]$ compound. It can be inferred that the B_2O_3 oxide is incorporated into the structure through 3D tetrahedra of the $[BO_4]$ compound, aligning with wave numbers of 900 – 920 cm^{-1} (Table 2).

As per the deconvolution results, slag 1, with a basicity of 1.0 and 3 % B_2O_3, possesses a BO index value of 1.1. Its structure is predominantly represented by the $[SiO_4]$ compound without bridging oxygen, along with 1

Table 2

Correspondence of wave numbers and structures

Таблица 2. **Соответствие волновых чисел и структур**

Element	Wavenumber, cm^{-1}	Structure	References
Q^0_{Si}	850 – 880	w/o bridging oxygen in $[SiO_4]$	[12; 13]
Q^1_{Si}	900 – 920	with one o bridging oxygen in $[SiO_4]$	
Q^2_{Si}	950 – 980	with two o bridging oxygens in $[SiO_4]$	
Q^3_{Si}	1040 – 1060	with three o bridging oxygens in $[SiO_4]$	
Q^4_{Si}	1060, 1190	with four o bridging oxygens in $[SiO_4]$	
Si – O – Si	500 – 650	Si – O^0 symmetric deformation vibrations	[14]
Al – O – Al	550	Al – O^0 vibrations	[15]
Cr – O – Cr	520 – 540	Cr – O^0 non-symmetric valence vibrations	[16]
$[BO_3]$	1350 – 1530	B – O^- valence vibrations in $[BO_3]^-$	[17; 18]
$[BO_4]$	900 – 920	B – O^0 symmetric valence vibrations in $[BO_4]$	[18]

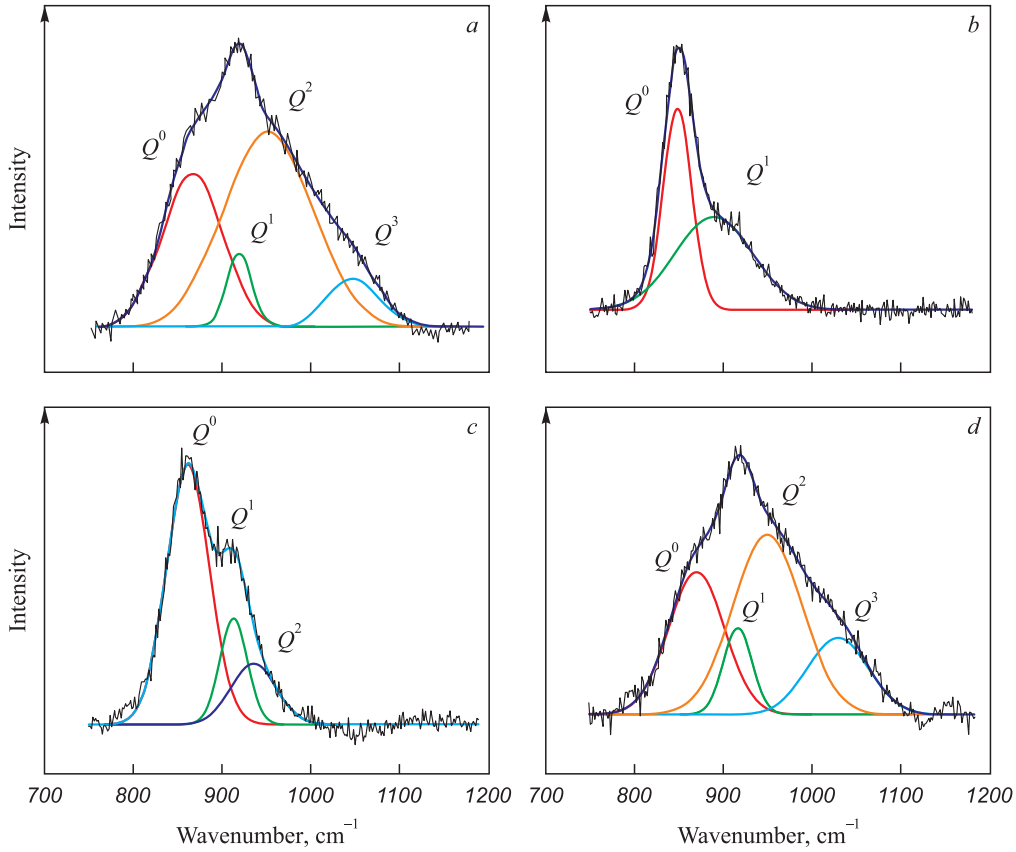

Fig. 4. Deconvolated spectra for the slags *1 – 4* (*a – d*)

Рис. 4. Деконволированные спектры для шлаков *1 – 4* (*a – d*)

and 2 bridging oxygen, with proportions of 0.39, 0.17 and 0.41, respectively. The combination of a relatively complex silicon–oxygen network structure (BO = 1.1) with a high concentration of high-temperature phases (32.23 %) leads to the formation of slag characterized by high viscosity of 1.0 – 0.8 Pa·s at 1600 – 1660 °C and a crystallization temperature of 1340 °C (Table 1).

Increasing the boron oxide content to 6 % induces even greater polymerization in slag *4* (BO = 1.49). This leads to an elevated proportion of Q^2 (0.45) and Q^3 (0.17), primarily due to changes in Q^0 and Q^1 values. At the same time, the proportion of low-melting compounds in the slag rises to 26.3 %, while the content of high-temperature phases decreases to 30.66 %. Despite the presence of a more intricate silicon-oxygen structure (BO = 1.49), in the form of [BO_4] tetrahedra, weakens the complex silicon-oxygen lattice. This weakening occurs as the resulting B – O^0 bonds are weaker than the Si – O^0 bonds. This "weakening" of the slag structure, combined with an increase in the proportion of low-melting compounds, results in a reduced viscosity of slag *4* to approximately 0.25 Pa·s at a temperature of 1600 – 1660 °C.

Table 3

Fractions of silicate structural elements

Таблица 3. **Доли силикатных структурных элементов**

Slag sample	Structural element				BO
	Q^0_{Si}	Q^1_{Si}	Q^2_{Si}	Q^3_{Si}	
1	0.39	0.17	0.41	0.03	1.10
2	0.50	0.50	0	0	0.50
3	0.63	0.21	0.16	0	0.53
4	0.29	0.09	0.45	0.17	1.49

Slags *2* and *3*, characterized by high basicity of 2.5, exhibit a "shorter" nature with a low degree of polymerization (refer to Fig. 1 and Table 3). As the basicity of these slags increases to 2.5, the peak in the silicate region of the spectrum (800 – 1200 cm^{-1}) shifts towards a decrease in wavenumber (Fig. 3). This shift is attributed to calcium oxide (CaO), acting as a slag structure modifier by providing free oxygen ions (O^{2-}). These free oxygen ions react with bridging oxygen (O^0) in silicates, resulting in a reduction in the complexity of Si–O bonds in the slag structure. Consequently, an increase in CaO content promotes the development of the depolymerization process [19 – 23]. Peaks in the wavenumber range of 500 – 650 cm^{-1} correspond to the Cr – O – Cr, Si – O – Si and Al – O – Al bonds. With an increase in

Table 4

Phase composition of the experimental slags at 1650 °C

Таблица 4. **Фазовый состав экспериментальных шлаков при температуре 1650 °C**

Phases	Fusing temperature, °C	Phase content in slag sample, %			
		1	*2*	*3*	*4*
Low temperature phases					
$CaO \cdot B_2O_3$	1130	1.88	0.06	0.28	4.10
$2CaO \cdot B_2O_3$	1280	4.47	2.81	7.55	8.22
$CaO \cdot MgO \cdot 2SiO_2$	1391	13.49	0.07	0.22	13.95
	Total	19.84	2.94	8.05	26.27
Medium temperature phases					
$2CaO \cdot MgO \cdot 2SiO_2$	1454	4.35	0.43	0.83	3.77
$3CaO \cdot B_2O_3$	1460	0.52	6.46	10.09	0.80
$3CaO \cdot 2SiO_2$	1460	9.76	5.89	6.69	7.18
$CaO \cdot MgO \cdot SiO_2$	1503	8.93	5.17	6.98	8.39
$3CaO \cdot Al_2O_3$	1539	0	0.44	0.12	0
$CaO \cdot SiO_2$	1540	17.99	3.22	4.37	17.06
$CaO \cdot Al_2O_3 \cdot SiO_2$	1550	0.45	0.03	0.06	0.42
$CaO \cdot Al_2O_3 \cdot 2SiO_2$	1550	2.71	0	0.01	2.80
$3CaO \cdot MgO \cdot 2SiO_2$	1575	2.14	4.18	4.72	1.56
$2CaO \cdot Al2O_3 \cdot SiO_2$	1590	0.67	0.89	1.00	0.53
$CaO \cdot Al_2O_3$	1600	0.27	2.10	1.64	0.23
	Total	47.77	28.81	36.52	42.75
High temperature phases					
SiO_2	1710	4.70	0.04	0.10	5.31
$2MgO \cdot SiO_2$	1890	1.19	0.11	0.26	1.32
Al_2O_3	2040	0.74	0.29	0.39	0.76
$3CaO \cdot SiO_2$	2070	0.06	4.22	1.94	0.04
$CaO \cdot Cr_2O_3$	2100	5.49	14.92	14.00	4.80
$2CaO \cdot SiO_2$	2130	9.61	34.04	26.89	7.66
$MgO \cdot Al_2O_3$	2135	0.86	1.10	1.47	0.87
Cr_2O_3	2435	7.99	1.10	1.77	8.33
CaO	2570	0.24	5.04	2.77	0.21
MgO	2852	1.34	4.56	4.27	1.36
	Total	32.23	65.43	53.86	30.66

basicity, these peaks smooth out, indicating a weakening of the bonds.

Slag *2*, containing 3 % boron oxide, possesses the least complex structure (BO = 0.5). It is characterized by an equal number of Q^0 and Q^1 values featuring a simple silicon-oxygen structure with a small amount of bridging oxygen. The slag is distinguished by a high proportion of refractory phases (more than 65 %) and a small proportion of low-melting phases (2.94 %). Consequently, its crystallization temperature is 1676 °C, and viscosity is 1.0 Pa·s at a temperature of 1660 °C.

Increasing the boron oxide content to 6 % in slag *3* has virtually no effect on its polymerization compared to slag *2* (the amount of bridging oxygen does not exceed 0.53). The structure contains Q^0, Q^1 and Q^2, with proportion of 0.63, 0.21 and 0.16, respectively. However, an increase in the content of low-melting phases to 8.05 % and a decrease in the proportion of refractory phases to 53.86 % positively influence the crystallization temperature (1605 °C) and slag viscosity, which decreased to 0.5 – 0.3 Pa·s in the range of 1600 – 1660 °C.

The obtained data on the influence of slag basicity and boron oxide content on phase composition, structure, viscosity, and crystallization temperature highlight that slag viscosity depends on the balance between the degree of polymerization of the structure, the nature of the bonds within it, and the phase composition.

Conclusions

The study has yielded new data on the impact of basicity and boron oxide content on the viscosity, crystallization temperature, phase composition, and structure of slags within the $CaO-SiO_2-B_2O_3-12\ \%\ Cr_2O_3-3\ \%\ Al_2O_3-8\ \%\ MgO$ system, spanning a range of boron oxide content from 3 to 6 % and basicity from 1.0 to 2.5.

The findings reveal that the physical properties of the investigated slags predominantly hinge on the delicate equilibrium between the degree of polymerization of the structure, the nature of the bonds within it, and the phase composition. At a low basicity of 1.0, augmenting the boron oxide content from 3 to 6 % renders the slag more fusible, leading to a reduction in the crystallization temperature from 1340 to 1224 °C and a decrease in viscosity from 1.0 – 0.8 to approximately 0.25 Pa·s at a temperature of 1600 – 1660 °C. This occurs despite a notable increase in structural complexity, as reflected in the rise of the BO index from 1.10 to 1.49.

In the case of high basicity ($B = 2.5$), the slags exhibit a simpler structure (BO = 0.50 – 0.53), and the addition of boron oxide only marginally complicates it (from 0.50 to 0.53). An increase in B_2O_3 content results in a reduction of the crystallization temperature from 1674 to 1605 °C and a decrease in viscosity from 1.0 to 0.3 Pa·s at a temperature of 1660 °C, attributed to the formation of low-melting compounds.

References / Список литературы

1. Tokovoi O.K. *Argon Oxygen Refining of Stainless Steel*. Chelyabinsk: ITs YuUrGU; 2015:250. (In Russ.).

Токовой О.К. *Аргонокислородное рафинирование нержавеющей стали*. Челябинск: ИЦ ЮУрГУ; 2015:250.

2. Popel' S.I., Sotnikov A.I., Boronenkov V.N. *Theory of Metallurgical Processes*. Moscow: Metallurgiya; 1986:463. (In Russ.).

   Попель С.И., Сотников А.И., Бороненков В.Н. *Теория металлургических процессов*. Москва: Металлургия; 1986:463.

3. Dyudkin D.A., Kisilenko V.V. *Production of Steel. In 3 vols. Vol. 3. Out-of-Furnace Steel Metallurgy*. Moscow: Teplotekhnik; 2010:544. (In Russ.).

   Дюдкин Д.А., Кисиленко В.В. *Производство стали. В 3-х томах. Т. 3. Внепечная металлургия стали*. Москва: Теплотехник; 2010:544.

4. Yavoiskii V.I., Yavoiskii A.V. *Scientific Foundations of Modern Production Processes of Steel*. Moscow: Metallurgiya; 1987:184. (In Russ.).

   Явойский В.И., Явойский А.В. *Научные основы современных процессов производства стали*. Москва: Металлургия; 1987:184.

5. Magidson I.A., Morozov A.S., Sidorenko M.F., etc. Viscosity of chromium slags. *Izvestiya. Ferrous Metallurgy*.1973;16(11):61–64. (In Russ.).

   Магидсон И.А., Морозов А.С., Сидоренко М.Ф. и др. Вязкость хромистых шлаков. *Известия вузов. Черная металлургия*. 1973;16(11):61–64.

6. Kalicka Z., Kawecka-Cebula E., Pytel K. Application of the Iida model for estimation of slag viscosity for Al_2O_3–Cr_2O_3–CaO–CaF_2 systems. *Archives of Metallurgy and Materials*. 2009;54(1):179–187.

7. Povolotskii D.Ya., Roshchin V.E., Gribanov V.P., etc. Influence of SiO_2 on the volatility of slags of Al_2O_3–Al_2O_3–CaF_2 system. *Izvestiya. Ferrous metallurgy*. 1982;25(8):39–42. (In Russ.).

   Поволоцкий Д.Я., Рощин В.Е., Грибанов В.П. и др. Влияние SiO_2 на летучесть шлаков системы Al_2O_3–Al_2O_3–CaF_2. *Известия вузов. Черная металлургия*. 1982;25(8):39–42.

8. Shtengel'meier S.V., Prusov V.A., Bogechov V.A. Improving viscosity measuring with a vibration viscometer. *Zavodskaya laboratoriya*. 1985;(9):56–57. (In Russ.).

   Штенгельмейер С.В., Прусов В.А., Богечов В.А. Усовершенствование методики измерения вязкости вибрационным вискозиметром. *Заводская лаборатория*. 1985;9:56–57.

9. Voskoboinikov V.G., etc. *Properties of Blast Furnace Slags*. Moscow: Metallurgiya; 1975:180. (In Russ.).

   Воскобойников В.Г. и др. *Свойства доменных шлаков*. Москва: Металлургия; 1975:180.

10. Roine A. *HSC 6.0 Chemistry Reactions and Equilibrium Software with Extensive Thermochemical Database and Flowshut*. Pori.: Outokumpu research Oy; 2006:448.

11. Mysen B.O., Virgo D., Scarfe C.M. Relations between the anionic structure and viscosity of silicate melts-a Raman spectroscopic study. *American Mineralogist*. 1980;65(7): 690–710.

12. McMillan P. Structural studies of silicate glasses and melts-applications and limitations of Raman spectroscopy. *American Mineralogist*. 1984;69(6):622–644.

13. Matson D.W., Sharma S.K., Philpotts J.A. The structure of high-silica alkali-silicate glasses. A Raman spectroscopic investigation. *Journal of Non-Crystalline Solids*. 1983;58(2-3): 323–352. https://doi.org/10.1016/0022-3093(83)90032-7

14. McMillan P.F., Poe B.T., Gillet P.H., Reynard B. A study of SiO_2 glass and supercooled liquid to 1950 K via high-temperature Raman spectroscopy. *Geochimica et Cosmochimica Acta*. 2001;58(17):3653–3662. https://doi.org/10.1016/0016-7037(94)90156-2

15. Kim T.S., Park J.H. Structure-viscosity relationship of low-silica calcium aluminosilicate melts. *ISIJ International*. 2014;54(9):2031–2038. https://doi.org/10.2355/isijinternational.54.2031

16. Dines T.J., Inglis S. Raman spectroscopic study of supported chromium (VI) oxide catalysts. *Physical Chemistry Chemical Physics*. 2003;5(6):1320–1328. https://doi.org/10.1039/b211857b

17. Kim Y., Morita K. Relationship between molten oxide structure and thermal conductivity in the CaO–SiO_2–B_2O_3 system. *ISIJ International*. 2014;54(9):2077–2083. https://doi.org/10.2355/isijinternational.54.2077

18. Cochain B., Neuville D.R., Henderson G.S., McCammon C.A., Pinet O., Richet P. Effects of the iron content and redox state on the structure of sodium borosilicate glasses: A Raman, Mössbauer and boron K-Edge XANES spectroscopy study. *Journal of the American Ceramic Society*. 2012;95(3):962–971. https://doi.org/10.1111/j.1551-2916.2011.05020.x

19. Mysen B.O., Virgo D., Seifert F.A. The structure of silicate melts: Implications for chemical and physical properties of natural magma. *Reviews of Geophysics*. 1982;20(3): 353–382. https://doi.org/10.1029/RG020i003p00353

20. Mysen B.O. Relationships between silicate melt structure and petrologic processes. *Earth-Science Reviews*. 1990;27(4): 281–365. https://doi.org/10.1016/0012-8252(90)90055-Z

21. Mills K.C. The influence of structure on the physico-chemical properties of slags. *ISIJ International*. 1993;33(1): 148–155. https://doi.org/10.2355/isijinternational.33.148

22. Park J.H. Structure–property correlations of CaO–SiO_2–MnO slag derived from Raman spectroscopy. *ISIJ International*. 2012;52(9):1627–1636. https://doi.org/10.2355/isijinternational.52.1627

23. Park J.H. Composition-structure-property relationships of CaO–*M*O–SiO_2 (M = Mg^{2+}, Mn^{2+}) systems derived from micro-Raman spectroscopy. *Journal of Non-Crystalline Solids*. 2012;358(23):3096–3012. https://doi.org/10.1016/j.jnoncrysol.2012.08.014

Information about the Authors

Ruslan R. Shartdinov, *Junior Researcher of the Laboratory of Steel and Ferroalloys,* Institute of Metallurgy, Ural Branch of the Russian Academy of Sciences
ORCID: 0000-0003-0852-1161
E-mail: rr.shartdinov@gmail.com

Anatolii A. Babenko, *Dr. Sci. (Eng.), Prof., Chief Researcher of the Laboratory of Steel and Ferroalloys,* Institute of Metallurgy, Ural Branch of the Russian Academy of Sciences
ORCID: 0000-0003-0734-6162
E-mail: babenko251@gmail.com

Alena G. Upolovnikova, *Cand. Sci. (Eng.), Senior Researcher of the Laboratory of Steel and Ferroalloys,* Institute of Metallurgy, Ural Branch of the Russian Academy of Sciences
ORCID: 0000-0002-6698-5565
E-mail: upol.ru@mail.ru

Artem N. Smetannikov, *Junior Researcher of the Laboratory of Steel and Ferroalloys,* Institute of Metallurgy, Ural Branch of the Russian Academy of Sciences
ORCID: 0000-0001-9206-0905
E-mail: artem.smetannikov.89@mail.ru

Сведения об авторах

Руслан Рафикович Шартдинов, *младший научный сотрудник лаборатории стали и ферросплавов,* Институт Уральского отделения РАН
ORCID: 0000-0003-0852-1161
E-mail: rr.shartdinov@gmail.com

Анатолий Алексеевич Бабенко, *д.т.н., профессор, ведущий научный сотрудник,* Институт металлургии Уральского отделения РАН
ORCID: 0000-0003-0734-6162
E-mail: babenko251@gmail.com

Алена Геннадьевна Уполовникова, *к.т.н., старший научный сотрудник лаборатории стали и ферросплавов,* Институт Уральского отделения РАН
ORCID: 0000-0002-6698-5565
E-mail: upol.ru@mail.ru

Артем Николаевич Сметанников, *младший научный сотрудник лаборатории стали и ферросплавов,* Институт Уральского отделения РАН
ORCID: 0000-0001-9206-0905
E-mail: artem.smetannikov.89@mail.ru

Contribution of the Authors

R. R. Shartdinov – conducting the experiment, processing and analysis of the research results, writing and editing the text.
A. A. Babenko – scientific guidance, analysis of the research results, writing and editing the text.
A. G. Upolovnikova – modeling, analysis of the research results, editing the text.
A. N. Smetannikov – conducting the experiment, analysis of the research results.

Вклад авторов

Р. Р. Шартдинов – проведение эксперимента, обработка, анализ, написание статьи, редактирование статьи.
А. А. Бабенко – научное руководство, анализ результатов, написание статьи, редактирование статьи.
А. Г. Уполовникова – моделирование, анализ, редактирование статьи
А. Н. Сметанников – проведение эксперимента, анализ.

Received 18.04.2023
Revised 12.05.2023
Accepted 22.05.2023

Поступила в редакцию 18.04.2023
После доработки 12.05.2023
Принята к публикации 22.05.2023

Physico-chemical basics of metallurgical processes / Физико-химические основы металлургических процессов

UDC 669.053.2
DOI 10.17073/0368-0797-2023-4-479-484

Original article
Оригинальная статья

Selective solid-phase reduction of iron in phosphorous oolite ores

B. Suleimen, **S. P. Salikhov, F. Sh. Sharipov, V. E. Roshchin**

South Ural State University (76 Lenina Ave., Chelyabinsk 454080, Russian Federation)

bakytsuleimen@mail.ru

Abstract. Selective solid-phase reduction of iron and phosphorus in oolite ores of the Lisakovsky and Ayat deposits was experimentally studied. Using X-ray phase analysis, the phase composition of the initial ores and samples after reduction roasting was determined. Goethite, magnetite and quartz were found in the ores of both deposits. Phosphorus in the ore of the Ayat deposit is in the form of aluminum phosphate and iron hydrophosphate, and in the samples of the Lisakovsky ore – as a component of calcium hydrophosphate. Experiments on reduction roasting were carried out in a resistance furnace at 1000 °C with holding time of 5 h. After roasting in CO atmosphere, α-Fe appears in the samples, while phosphorus remains as a component of iron, calcium and aluminum phosphates. After roasting in a mixture with graphite, phosphorus is reduced by solid carbon from iron and calcium phosphates and passes into metal, but remains as a component of aluminum phosphate. Studies using microroentgenospectral analysis show that phosphorus content in the metal phase after reduction with solid carbon is 2.0 – 3.5 at. %. When CO is reduced in the atmosphere, phosphorus in the metallic phase is practically not detected. At the same time, the amount of residual iron in the oxide phase after carbon monoxide reduction significantly exceeds the amount of iron after reduction in a mixture with carbon. The experimental results confirm the possibility of selective reduction of iron by carbon oxide CO without phosphorus reduction.

Keywords: oolitic iron ore, reduction roasting, carbon monoxide, selective reduction, metallization, metallic iron, phosphorus

For citation: Suleimen B., Salikhov S.P., Sharipov F.Sh., Roshchin V.E. Selective solid-phase reduction of iron in phosphorous oolite ores. *Izvestiya. Ferrous Metallurgy*. 2023;66(4):479–484. https://doi.org/10.17073/0368-0797-2023-4-479-484

Селективное твердофазное восстановление железа в фосфористых оолитовых рудах

Б. Сулеймен, **С. П. Салихов, Ф. Ш. Шарипов, В. Е. Рощин**

Южно-Уральский государственный университет (Россия, 454080, Челябинск, пр. Ленина, 76)

bakytsuleimen@mail.ru

Аннотация. Представлены результаты экспериментальных исследований по селективному твердофазному восстановлению железа и фосфора в оолитовых рудах Лисаковского и Аятского месторождений. С использованием рентгенофазового анализа определен фазовый состав исходных руд и образцов после восстановительного обжига. В рудах обоих месторождений обнаруживаются гетит, магнетит и кварц. Фосфор в руде Аятского месторождения находится в виде фосфата алюминия и гидрофосфата железа, а в образцах Лисаковской руды – в составе гидрофосфата кальция. Эксперименты по восстановительному обжигу проводились в печи сопротивления при температуре 1000 °C и времени выдержки 5 ч. После обжига в атмосфере CO в образцах появляется α-железо, в то время как фосфор остается в составе фосфатов железа, кальция и алюминия. После обжига в смеси с графитом фосфор восстанавливается твердым углеродом из фосфатов железа и кальция и переходит в металл, однако остается в составе фосфата алюминия. Исследования с использованием микрорентгеноспектрального анализа показывают, что содержание фосфора в металлической фазе после восстановления твердым углеродом составляет 2,0 – 3,5 % (ат.). При восстановлении в атмосфере CO фосфора в металлической фазе практически не обнаруживается. При этом количество остаточного железа в оксидной фазе после восстановления угарным газом значительно превышает количество железа после восстановления в смеси с углеродом. Результаты экспериментов подтверждают возможность селективного восстановления железа оксидом углерода CO без восстановления фосфора.

Ключевые слова: оолитовая железная руда, восстановительный обжиг, оксид углерода CO, селективное восстановление, металлизация, металлическое железо, фосфор

Для цитирования: Сулеймен Б., Салихов С.П., Шарипов Ф.Ш., Рощин В.Е. Селективное твердофазное восстановление железа в фосфористых оолитовых рудах. *Известия вузов. Черная металлургия*. 2023;66(4):479–484. https://doi.org/10.17073/0368-0797-2023-4-479-484

Introduction

In light of the increased production of ferrous metals and the use of ores with low iron content, the integrated utilization of mineral raw materials in ferrous metallurgy has gained growing relevance [1 – 3]. In recent years, significant attention has been directed towards the challenges associated with the extraction [4 – 6] and processing [7] of iron from oolitic iron ores characterized by high phosphorus content. Additionally, considerable focus has been placed on the enrichment [8] and dephosphorization [9] of these ores. Extensive reserves of oolitic ores are present in Asian countries [10; 11], Africa [12; 13], Europe, and North America [13 – 15]. The Ayat and Lisakovsky deposits, situated in Kazakhstan, are examples of such deposits. Although these two large deposits share similar iron contents, they exhibit variations in phosphorus, vanadium, and aluminum content.

The unconsolidated fraction of Ayat ores comprises fragments of oolites, micrograins of quartz, and alumina, while the cohesive portion consists of oolites bound together by a clay-cement matrix [16]. The average iron content for this deposit is 37.1 %. The ores exhibit 16.4 % SiO_2, 6 % Al_2O_3 and 0.37 % P. Lisakovsky ores constitute a loose blend of brown iron ore oolites and quartz sand grains, featuring an iron content ranging from 30 to 40 % and a notably high phosphorus content (up to 0.8 %) [17]. The beneficiation of such ores necessitates the implementation of intricate and costly processing flowcharts. Unfortunately, the current methods do not effectively remove phosphorus, thereby impacting the technological aspects of metallurgical processing. Within the blast furnace, where roasting (in the shaft) and melting (in the hearth) occur in a reducing atmosphere, phosphorus undergoes complete reduction, transforming into metal. The elimination of phosphorus from cast iron, whether in ladles or steelmaking units, incurs additional expenditures in terms of materials, energy, and time. Consequently, dephosphorization before or during the iron production process emerges as a crucial step when utilizing high-phosphorus oolitic ores.

In [18 – 20], investigations were conducted into the feasibility of selectively reducing iron in the ores from the Ayat deposit through solid-phase reduction. According to the findings from these studies, selective iron reduction can be accomplished through exposure to carbon monoxide at a temperature of 1000 °C.

The objective of this study is to conduct a comparative analysis of the solid-phase selective reduction process of iron, without concurrent phosphorus reduction, in oolitic ores sourced from the Ayat and Lisakovsky deposits.

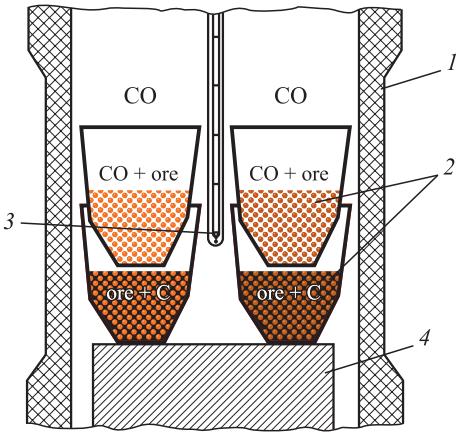

Fig. 1. Layout of crucibles with ore samples in working space of the Tamman furnace:
1 – graphite heater; *2* – crucibles with samples; *3* – thermocouple; *4* – stand

Рис. 1. Схема расположения тиглей с образцами руд в рабочем пространстве печи Таммана:
1 – графитовый нагреватель; *2* – тигли с образцами; *3* – термопара; *4* – подставка

Experimental

The study utilized samples of oolitic iron ores obtained from the Ayat and Lisakovsky deposits. The experiments were conducted within a closed Tamman furnace featuring a graphite heater, ensuring the establishment of a reducing atmosphere in the furnace space. Employing the calculation method outlined in [21], the equilibrium composition of the gas phase in the furnace's working space at a temperature of 1000 °C and a pressure of 0.1 MPa was determined to be 34.58 % CO, 0.07 % CO_2 and 65.35 % N_2.

Four corundum crucibles (Fig. 1) were positioned in the working space of the furnace, each containing ore samples ranging in size from 0.4 to 1.0 mm. The ore samples in the upper crucibles interacted with CO oxide in the gas phase, while those in the lower crucibles were mixed with graphite powder and engaged with solid carbon. The furnace was gradually heated to a temperature of 1000 °C over 60 min and maintained at this temperature for a duration of 5 h. Temperature control was facilitated using a tungsten rhenium thermocouple WR5/WR20. The selection of temperature and holding time was based on insights gleaned from prior experiments [18 – 20].

Upon completion of the holding period, the crucibles containing the samples were gradually cooled along with the furnace until reaching room temperature. To eliminate carbon residues, a mixture of samples with graphite powder was dispersed, and representative samples were

extracted for *X*-ray spectral and *X*-ray phase microanalyses.

A subset of the samples was impregnated with epoxy resin, followed by grinding and polishing. The resultant polished sections were subjected to examination using a JSM-6460LV electron microscope (JEOL), equipped with an energy-dispersive analyzer (Oxford Instruments). This analysis aimed to ascertain the elemental composition at specific points and across areas through *X*-ray spectral microanalysis. *X*-ray phase analysis (XRF) of both the original and metallized samples was conducted using a Rigaku Ultima IV diffractometer. The resulting diffraction patterns were interpreted using the Match! 3 software.

Results

Fig. 2 presents the XRF results of the original ore samples, revealing the presence of goethite FeO(OH), magnetite Fe_3O_4 and quartz SiO_2 in both samples. The Ayat deposit ore contains phosphorus in the form of aluminum phosphate $AlPO_4$ and iron hydrogen phosphate $FePO_4 \cdot 2H_2O$. In contrast, the Lisakovsky ore samples include phosphorus in the composition of calcium hydrogen phosphate $CaHPO_4 \cdot 2H_2O$.

Fig. 3 displays the XRF results after reduction roasting. The diffraction pattern of samples reduced in a CO oxide atmosphere (Fig. 3, *a*) exhibits a higher number of peaks, indicating a greater variety of phases compared to samples roasted in contact with graphite powder (Fig. 3, *b*).

According to the XRF results, all samples contain α-iron, magnetite Fe_3O_4, quartz SiO_2 and berlinite $AlPO_4$. In samples subjected to CO atmosphere, phosphorus manifests itself in the composition of iron and calcium phosphates, namely FeP_2O_7 and $FePO_4$, CaP_2O_6 and $Ca_3(PO_4)_2$ (Fig. 3, *a*). Conversely, samples in contact with carbon do not contain iron or calcium phosphates. The Lisakovsky ore exhibits the presence of calcium oxide CaO (Fig. 3, *b*).

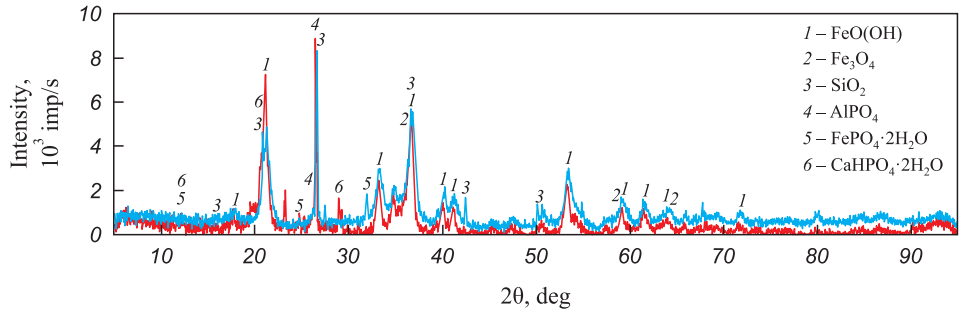

Fig. 2. Diffractograms of samples of initial ores from Lisakovsky (▬) and Ayat (▬) deposits

Рис. 2. Дифрактограммы образцов исходных руд Лисаковского (▬) и Аятского (▬) месторождений

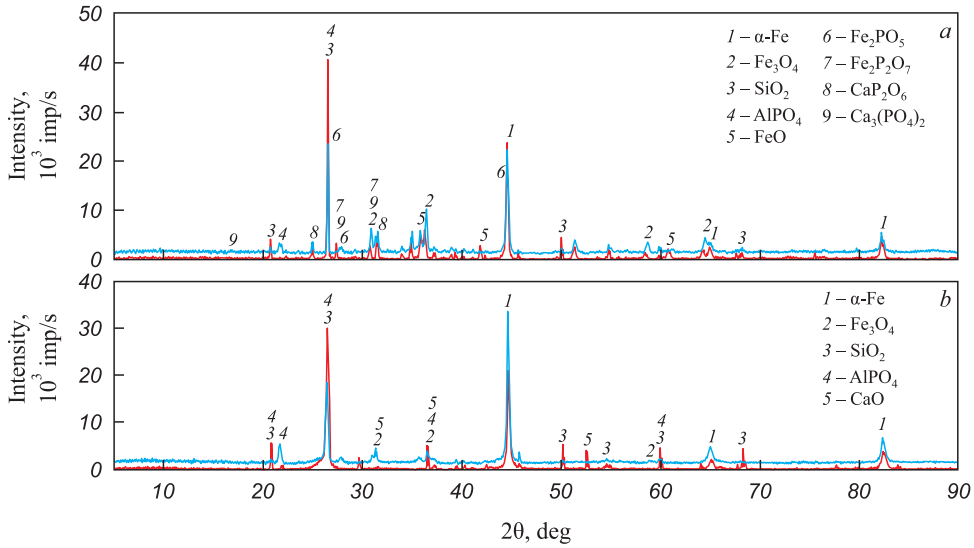

Fig.3. Diffractogram of the ores from Lisakovsky (▬) and Ayat (▬) deposits after reduction roasting in CO atmosphere (*a*) and in contact with solid carbon (*b*)

Рис.3. Дифрактограммы руд Лисаковского (▬) и Аятского (▬) месторождений после восстановительного обжига в атмосфере CO (*a*) и в контакте с твердым углеродом (*b*)

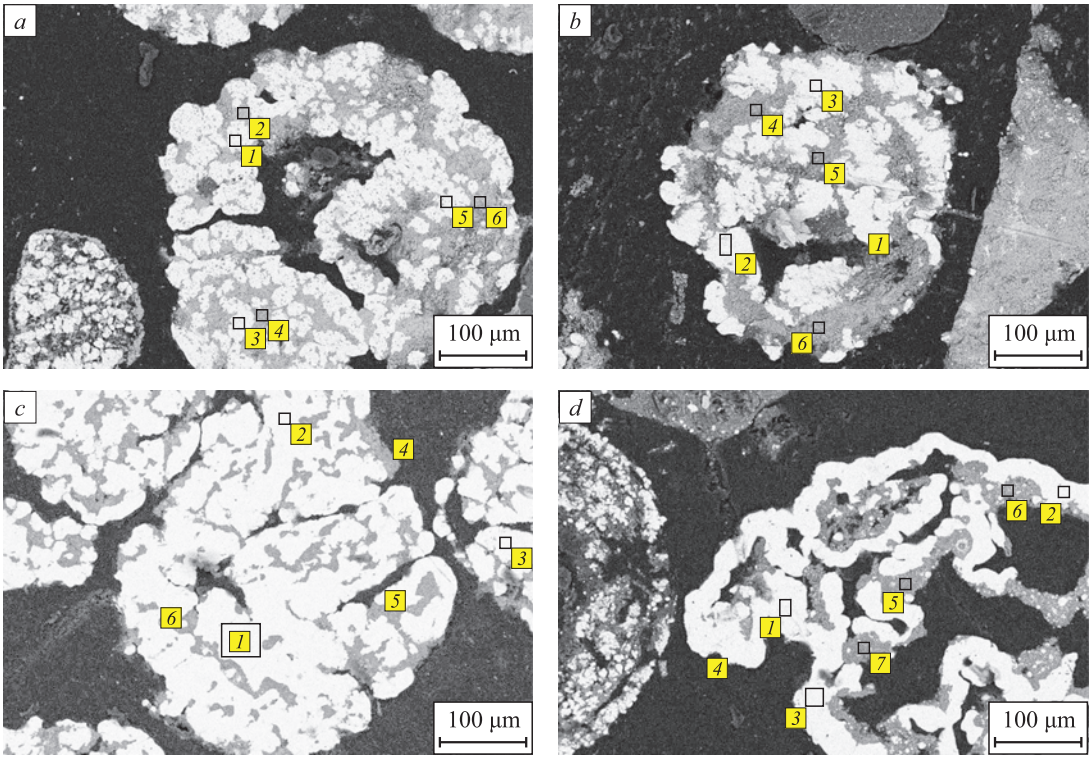

Fig. 4. Distribution of metallic and non-metallic phases in the samples of ores of Lisakovsky (*a*, *c*) and Ayat (*b*, *d*) deposits after reduction roasting in CO atmosphere (*a*, *b*) and in contact with carbon (*c*, *d*)

Рис. 4. Распределение металлических и неметаллических фаз в образцах руд Лисаковского (*a*, *c*) и Аятского (*b*, *d*) месторождений после восстановительного обжига в атмосфере CO (*a*, *b*) и в контакте с углеродом (*c*, *d*)

Average content of elements according to results of the metallized samples analysis

Среднее содержание элементов по результатам анализа металлизованных образцов

Points/Analyzed sites	Content of elements, % (at.)							
	O	Mg	Al	Si	P	Ca	Mn	Fe
Spectrum *1*, *3*, *5* (Fig. 4, *a*)	–	–	–	–	0.1	–	–	99.9
Spectrum *2*, *4*, *6* (Fig. 4, *a*)	63.0	0.4	10.0	5.3	1.6	0.1	0.3	19.3
Spectrum *1*, *2*, *3* (Fig. 4, *b*)	–	–	–	–	0.1	–	–	99.9
Spectrum *4*, *5*, *6* (Fig. 4, *b*)	61.8	1.1	10.1	6.2	1.2	0.6	0.4	18.6
Spectrum *1*, *2*, *3* (Fig. 4, *c*)	–	–	–	–	3.5	–	–	96.5
Spectrum *4*, *5*, *6* (Fig. 4, *c*)	63.5	2.2	15.3	11.5	0.5	1.6	0.7	4.7
Spectrum *1*, *2*, *3*, *4* (Fig. 4, *d*)	–	–	–	–	2.0	–	–	98.0
Spectrum *5*, *6*, *7* (Fig. 4, *d*)	63.5	1.3	15.3	9.2	0.2	2.8	0.6	7.1

An examination of polished sections of roasted ores revealed that, whether in contact with carbon or in a CO atmosphere, the metallic phase of iron formed both on the surface and within the ore particles (Fig. 4). Notably, reduction with solid carbon resulted in the creation of more distinctly defined and dense metallic structures (Fig. 4, *d*).

The table provides the average results of *X*-ray spectral microanalysis, indicating the elemental content at specific points and sites of analysis in the metallized ore samples. As an illustration, based on the analysis results from sites *1*, *3* and *5* (Fig. 4, *a*), the average phosphorus content is 0.1 %, while the iron content is 99.9 % (at.).

Post-roasting in contact with carbon, iron in samples from both deposits undergoes nearly complete reduction, with residual oxides containing only 5 – 7 % iron. Conversely, when reduced in a CO atmosphere, the iron content in the oxide phase remains around 20 %. Notably, in iron reduced in a CO atmosphere, the phosphorus content in the metal does not exceed 0.1 %. In contrast, after the reduction of iron with solid carbon, the phosphorus content ranges between 2.5 – 3.0 %.

Discussion

The XRF results indicate that the initial ores comprise phases of goethite, magnetite, hydrophosphates of iron and calcium, quartz, and aluminum phosphate. In all metallized samples, goethite disappears, the α-iron phase emerges, and the SiO_2 phase persists. Phosphorus in samples after reduction in a CO atmosphere is found in the form of CaP_2O_6 or $Ca_3(PO_4)_2$, $FePO_4$ or FeP_2O_7 and $AlPO_4$. In contrast, samples reduced with carbon show phosphorus exclusively in the $AlPO_4$ phase. Under these conditions, phosphorus undergoes reduction from calcium and iron phosphates, converting into metal. The obtained results are confirmed by the examination of the samples using an electron microscope after reduction roasting. In the Ayat and Lisakovsky deposit samples, phosphorus is virtually not reduced after reduction in a CO atmosphere; however, in a mixture with solid carbon, phosphorus reduction occurs and is detectable through *X*-ray spectral microanalysis in the metal phase.

The increased phosphorus content in Lisakovsky ore does not alter the previously identified patterns of its recovery but rather reinforces the obtained findings. Thus, carbon monoxide does not reduce phosphorus from oolitic ore compounds, while phosphorus reduction is achieved through the utilization of solid carbon.

The results obtained affirm the feasibility of selectively reducing iron with carbon monoxide in oolitic ores characterized by high phosphorus content from different deposits.

Conclusions

Lisakovsky and Ayat oolitic ores share a similarity in iron content but exhibit variations in phosphorus content, where phosphorus is present in the form of calcium, iron, and aluminum phosphates. At a temperature of 1000 °C and with a holding time of 5 h, carbon monoxide fails to reduce phosphorus from iron and calcium hydrophosphates, as well as from aluminum phosphates. In contrast, under the same conditions, when in contact with solid carbon, phosphorus undergoes complete reduction, transitioning into the metal phase from calcium and iron hydrophosphates. However, reduction from aluminum phosphate does not occur.

References / Список литературы

1. Smirnov K.I., Gamov P.A. Pyro-metallurgical processing of ilmenite concentrate with production of iron and titanium oxides. *Solid State Phenomena*. 2021;316:385–389. https://doi.org/10.4028/www.scientific.net/SSP.316.385
2. Smirnov K., Gamov P.A. Specific features of metal reduction from ilmenite concentrate. *AIP Conference Proceedings*. 2022;2456(1):020052. https://doi.org/10.1063/5.0074718
3. Kosdauletov N.K., Roshchin V.R. Solid-phase reduction and separation of iron and phosphorus from manganese oxides in ferromanganese ore. *Defect and Diffusion Forum*. 2021;410:281–286. https://doi.org/10.4028/www.scientific.net/DDF.410.281
4. Li K., Ni W., Zhu M., Zheng M., Li Y. Iron extraction from oolitic iron ore by a deep reduction process. *Journal of Iron and Steel Research International*. 2011;18(8):9–13. http://doi.org/10.1016/S1006-706X(11)60096-4
5. Sun Y.S., Han Y.X., Gao P., Wang Z.H., Ren D.Z. Recovery of iron from high phosphorus oolitic iron ore using coal-based reduction followed by magnetic separation. *International Journal of Minerals, Metallurgy, and Materials*. 2013;20(5):411–419. https://doi.org/10.1007/s12613-013-0744-1
6. Zhou W., Han Y., Sun Y., Gao P., Li Y. Review of research on iron extraction and phosphorus reduction of high phosphorus oolitic hematite. *Metal Mines*. 2019;(2):10–11. https://doi.org/10.19614/j.cnki.jsks.201902002
7. Zhou W., Han Y., Sun Y., Gao P., Li Y. Recycling iron from oolitic hematite via microwave fluidization roasting and magnetic separation. *Minerals Engineering*. 2021;164:106851. https://doi.org/10.1016/j.mineng.2021.106851
8. Chandio A.D., Channa I.A., Shaik A.A., Madad S., Rizvi S.B.H., Shah A.A., Alhazaa A. Beneficiation of low-grade Dilband iron ore by reduction roasting. *Metals*. 2023;13(2):296. https://doi.org/10.3390/met13020296
9. Wu S., Sun T., Kou J., Xu H. A new iron recovery and dephosphorization approach from highphosphorus oolitic iron ore via oxidation roasting-gas-based reduction and magnetic separation process. *Powder Technology*. 2023;413:118043. https://doi.org/10.1016/j.powtec.2022.118043
10. Manieh A.A. Oolite liberation of oolitic iron ore, Wadi Fatima, Saudi Arabia. *International Journal of Mineral Processing*. 1984;13(3):187–192. https://doi.org/10.1016/0301-7516(84)90002-4
11. Abro M.M., Pathan A.G., Mallah A.H. Liberation of oolitic hematite grains from iron ore. *Mehran University Research, Journal of Engineering Technology*. 2011;30:329–338.
12. El Sharkawi M.M., Mesaed A., Mortada M.E. *Stratigraphic Setting and Paleoenvironment of the Coniacian-Santonian Ironstones of Aswan, South Egypt*. 1996.
13. Champetier Y., Hamdadou E., Hamdadou M. Examples of biogenic support of mineralization in two oolitic iron ores-Lorraine (France) and Gara Djebilet (Algeria). *Sedimentary Geology*.1987;51(3-4):249–255. https://doi.org/10.1016/0037-0738(87)90050-9
14. Tigunov L.P., Anufrieva S.I., Bronitskaya E.S., Krivokoneva G.K., Sokolova V.N., Alikberov V.M., Sladkova G.A., Fainshtein G.G., Parovinchak M.S. Modern technological decisions of processing ferriferous ores of the Bakcharsky deposit. *Razvedka i okhrana nedr*. 2010;(2):37–43. (In Russ.).

    Тигунов Л.П., Ануфриева С.И., Броницкая Е.С., Кривоконева Г.К., Соколова В.Н., Аликберов В.М., Сладкова Г.А., Файнштейн Г.Г., Паровинчак М.С. Современные технологические решения переработки железосодержащих руд Бакчарского месторождения. *Разведка и охрана недр*. 2010;(2):37–43.
15. Özdemir Ö., Deutsch E.R. Magnetic properties of oolitic iron ore on Bell Island, Newfoundland. *Earth and Planetary*

Science Letters. 1984;69(2):427–441.
https://doi.org/10.1016/0012-821X(84)90201-2

16. Suleimen B., Salikhov S.P., Roshchin V.E. Study of the iron ores of the Ayat deposit of the oolite-type. *Mining Informational and Analytical Bulletin (Scientific and Technical Journal)*. 2022;(10-1):50–58. (In Russ.).
https://doi.org/10.25018/0236_1493_2022_101_0_50

Сулеймен Б., Салихов С.П., Рощин В.Е. Изучение железных руд Аятского месторождения оолитового типа. *Горный информационно-аналитический бюллетень*. 2022;(10-1):50–58.
https://doi.org/10.25018/0236_1493_2022_101_0_50

17. Kaskataeva K.B., Kryazheva T.V., Sadchikov A.V., D'yakonov V.V. Characteristics of ores of the Lisakovsky deposit for their complex processing. *Izvestiya Tomskogo politekhnicheskogo universiteta. Inzhiniring georesursov*. 2021;332(5):7–16. (In Russ.).

Каскатаева К.Б., Кряжева Т.В., Садчиков А.В., Дьяконов В.В. Характеристика руд Лисаковского месторождения с целью их комплексной переработки. *Известия Томского политехнического университета. Инжиниринг георесурсов*. 2021;332(5):7–16.

18. Salikhov S.P., Suleimen B., Roshchin V.E. Selective reduction of iron and phosphorus from oolite ore. *Izvestiya. Ferrous Metallurgy*. 2020;63(7):560–567. (In Russ.).
https://doi.org/10.17073/0368-0797-2020-7-560-567

Салихов С.П., Сулеймен Б., Рощин В.Е. Селективное восстановление железа и фосфора из оолитовой руды. *Известия вузов. Черная металлургия*. 2020;63(7):560–567.
https://doi.org/10.17073/0368-0797-2020-7-560-567

19. Suleimen B., Salikhov S.P. Behavior of extrusion briquettes (Brex) and pellets from oolite iron ore in solid-phase metallization. *AIP Conference Proceedings*. 2022;2456(1):020054.
https://doi.org/10.1063/5.0075188

20. Suleimen B., Salikhov S.P. Metallization of oolitic iron ore after oxidation firing. *Solid State Phenomena*. 2021;316:390–395.
https://doi.org/10.4028/www.scientific.net/SSP.316.390

21. Mikhailov G.G., Leonovich B.I., Kuznetsov Yu.S. *Thermodynamics of Metallurgical Processes and Systems*. Moscow: MISIS; 2009:520. (In Russ.).

Михайлов Г.Г., Леонович Б.И., Кузнецов Ю.С. *Термодинамика металлургических процессов и систем*. Москва: ИД МИСиС; 2009:520.

Information about the Authors

***Bakyt Suleimen**, Research Associate of the Research Laboratory "Hydrogen Technologies in Metallurgy",* South Ural State University
ORCID: bakytsuleimen@mail.ru
E-mail: 0000-0001-9306-1045

***Semen P. Salikhov**, Cand. Sci. (Eng.), Assist. Prof. of the Chair of Pyrometallurgical and Foundry Technologies,* South Ural State University
ORCID: salikhovsp@susu.ru
E-mail: 0000-0002-8818-0450

***Farkhod Sh. Sharipov**, MA Student of the Chair of Pyrometallurgical and Foundry Technologies,* South Ural State University
E-mail: saripovf17@mail.ru

***Vasilii E. Roshchin**, Dr. Sci. (Eng.), Prof. of the Chair of Pyrometallurgical and Foundry Technologies,* South Ural State University
ORCID: 0000-0003-3648-8821
E-mail: roshchinve@susu.ru

Сведения об авторах

***Бакыт Сулеймен**, научный сотрудник научно-исследовательской лаборатории «Водородные технологии в металлургии»,* Южно-Уральский государственный университет
ORCID: bakytsuleimen@mail.ru
E-mail: 0000-0001-9306-1045

***Семен Павлович Салихов**, к.т.н., доцент кафедры пирометаллургических и литейных технологий,* Южно-Уральский государственный университет
ORCID: salikhovsp@susu.ru
E-mail: 0000-0002-8818-0450

***Фарход Шукурович Шарипов**, магистрант кафедры пирометаллургических и литейных технологий,* Южно-Уральский государственный университет
E-mail: saripovf17@mail.ru

***Василий Ефимович Рощин**, д.т.н., профессор кафедры пирометаллургических и литейных технологий,* Южно-Уральский государственный университет
ORCID: 0000-0003-3648-8821
E-mail: roshchinve@susu.ru

Contribution of the Authors

B. Suleimen – analytical data review, conducting experiments, determining chemical and phase composition of the samples, preparing the text and illustrations.
S. P. Salikhov – statement and solution of the task, analysis of the experimental results, editing of the text and illustrations.
F. Sh. Sharipov – graphic presentation of the results, conducting experiments.
V. E. Roshchin – scientific guidance, formation of the goal of the study and conclusions based on the experimental results.

Вклад авторов

Б. Сулеймен – аналитический обзор, проведение экспериментов, определение химического и фазового составов образцов, подготовка текста и иллюстраций статьи.
С. П. Салихов – постановка и решение задачи, анализ результатов эксперимента, редактирование текста и иллюстраций.
Ф. Ш. Шарипов – графическое оформление полученных результатов, проведение экспериментов.
В. Е. Рощин – научное руководство исследованиями, формирование цели исследования и выводов по результатам экспериментов.

Received 14.03.2023
Revised 19.06.2023
Accepted 28.06.2023

Поступила в редакцию 14.03.2023
После доработки 19.06.2023
Принята к публикации 28.06.2023

Innovation in metallurgical industrial and laboratory equipment, technologies and materials

Инновации в металлургическом промышленном и лабораторном оборудовании, технологиях и материалах

UDC 621.746+621.771
DOI 10.17073/0368-0797-2023-4-485-491

Original article
Оригинальная статья

Stress state of billet – mandrel system during production of hollow steel billet in a unit for continuous casting and deformation. Part 1

O. S. Lekhov[1], **A. V. Mikhalev**[2], **S. O. Nepryakhin**[3]

[1] **Russian State Vocational Pedagogical University** (11 Mashinostroitelei Str., Yekaterinburg 620012, Russian Federation)
[2] **JSC "Ural Pipe Plant"** (28 Sakko i Vantsetti Str., Pervouralsk, Sverdlovsk Region 623107, Russian Federation)
[3] **Ural Federal University named after the First President of Russia B.N. Yeltsin** (28 Mira Str., Yekaterinburg 620002, Russian Federation)

MXLehov38@yandex.ru

Abstract. The substantiation of the relevance of obtaining continuous cast steel pipe hollow billet is given from the position of improving the quality of pipes made of carbon and alloy steels is given. The article presents an assessment of the quality of the inner surface of pipes made of solid steel pipe billet. A new technology is proposed for the production of hollow steel pipe billets on a resource-saving unit of combined continuous casting and deformation. The photo of the continuous casting and deformation section of JSC Ural Pipe Plant is given, where a pilot unit of combined continuous casting and deformation is installed. The paper presents the results of a theoretical study of stress-strain state of the mandrel and sections of a pipe billet when it is compressed by the strikers of the unit of combined continuous casting and deformation. The authors discuss the general model of the mold – striker system. The initial data on calculation, dimensions of the hollow pipe billet and a description of the calibration of strikers for compression of a hollow steel billet are given. The temperature field of a hollow billet was determined. To simulate the stress-strain state of the metal in the roll pass and the mandrel, four contact pairs were considered. Calculations were made by the finite element method. The dimensions of the final element in the roll pass of hollow billet were determined. The authors established the values and patterns of changes in metal displacements and axial stresses in the roll pass during the production of hollow steel billets in the unit of combined continuous casting and deformation (strikers are made along a constant radius). The stress state of metal in the roll pass was assessed from the standpoint of improving the quality of hollow steel billets.

Keywords: unit, continuous casting, anvil, deformation, hollow billet, stress, finite element

For citation: Lekhov O.S., Mikhalev A.V., Nepryakhin S.O. Stressed state of the billet – mandrel system during production of hollow steel billet in a unit for continuous casting and deformation. Part 1. *Izvestiya. Ferrous Metallurgy*. 2023;66(4):485–491.
https://doi.org/10.17073/0368-0797-2023-4-485-491

Напряженное состояние системы заготовка – оправка при получении стальной полой заготовки на установке непрерывного литья и деформации. Часть 1

О. С. Лехов[1], **А. В. Михалев**[2], **С. О. Непряхин**[3]

[1] **Российский государственный профессионально-педагогический университет** (Россия, 620012, Екатеринбург, ул. Машиностроителей, 11)
[2] **ОАО «Уральский трубный завод»** (Россия, 623107, Свердловская обл., Первоуральск, ул. Сакко и Ванцетти, 28)
[3] **Уральский федеральный университет имени первого Президента России Б.Н. Ельцина** (Россия, 620002, Екатеринбург, ул. Мира, 19)

MXLehov38@yandex.ru

Аннотация. Приводится обоснование актуальности получения непрерывнолитых стальных трубных полых заготовок с позиции улучшения качества труб из углеродистых и легированных сталей. Представлена оценка качества внутренней поверхности труб, прокатанных из стальных сплошных трубных заготовок. Предлагается новая технология получения стальных трубных полых заготовок на ресурсосберегающей установке совмещенного процесса непрерывного литья и деформации. Приводится фотография участка непрерывного литья и деформации ОАО «Уральский трубный завод», показана опытная установка совмещенного процесса непрерывного литья и деформации. Статья содержит результаты теоретического исследования напряженно-деформированного состояния оправки и участков трубной заготовки при обжатии ее бойками установки совмещенного процесса непрерывного литья и деформации. В статье рассматривается общая модель системы кристаллизатор – бойки. Приведены исходные данные для расчета, размеры полой трубной заготовки и описание калибровки бойков для обжатия стальной полой заготовки. Рассматривается температурное поле полой заготовки. Для моделирования напряженно-деформированного состояния металла в очагах деформации и оправке рассматриваются четыре контактные пары. Излагается методика расчета с использованием метода конечных элементов и приводятся размеры конечного элемента в очагах деформации полой заготовки. Установлены величины и закономерности изменения перемещений металла и осевых напряжений в очагах деформации при получении стальных полых заготовок на установке совмещенного процесса непрерывного литья и деформации (бойки выполнены по постоянному радиусу). Авторы дают оценку напряженного состояния металла в очагах деформации с позиции улучшения качества стальных полых заготовок при получении на установке непрерывного литья и деформации.

Ключевые слова: установка, непрерывное литье, боек, деформация, полая заготовка, напряжение, конечный элемент

Для цитирования: Лехов О.С., Михалев А.В., Непряхин С.О. Напряженное состояние системы заготовка – оправка при получении стальной полой заготовки на установке непрерывного литья и деформирования. Часть 1. *Известия вузов. Черная металлургия*. 2023;66(4):486–491. https://doi.org/10.17073/0368-0797-2023-4-485-491

Introduction

In light of the increased output, expansion of the seamless pipes range, and the strengthening of quality requirements, there is a pressing need for research related to the development of new methods and units for producing continuous cast steel pipe hollow billets from carbon and alloy steels. It has been discovered that the quality of the inner surface of pipes produced from hollow billets is superior compared to pipes rolled from solid billets. This is due to the fact that segregation and shrinkage porosity are located within the wall of continuous cast hollow billets, whereas they are concentrated in the core zone of solid billet.

A new technology has been developed for the industrial production of steel pipe hollow billets using a unit for combined continuous casting and deformation (Fig. 1) [1 – 3].

The proposed technology involves the formation of a steel annular shell with a wall that contains the liquid phase in a single-piece copper mold. This is followed by the compressing of the wall crusts using strikers, resulting in the displacement of the liquid phase. Afterward, the hardened shell wall is compressed around its entire circumference in a single pass, and the finished hollow billet is calibrated.

Research materials and method

A theoretical study was undertaken to evaluate the new technology for producing hollow steel billets and to establish the fundamental parameters of the unit. A general model of the mold, striker, mandrel, and wall crusts of a hollow billet is depicted in Fig. 2. Dimensions of the deformation areas during bending and compressing of the hollow billet walls by the strikers, the calibration section, and the mandrel are provided. In order to achieve this, it is essential to determine the stress-strain state (SSS) of the metal in the deformation zones during bending and compressing of the hollow billet wall, as well as when subjecting the mandrel to stress during production of a steel hollow billet in the unit.

The elastoplastic contact problem, taking into account significant displacements and deformations, was solved to compute the SSS [4 – 6].

The calculations were performed using the finite element method within the versatile ANSYS 15.0 software

Fig. 1. Unit of continuous casting and deformation:
1 – induction furnace; *2* – DC electric motor;
3 – synchronizer geared system; *4* – bed

Рис. 1. Установка непрерывного литья и деформации:
1 – индукционная печь; *2* – электродвигатель постоянного тока;
3 – редуктор-синхронизатор; *4* – станина установки

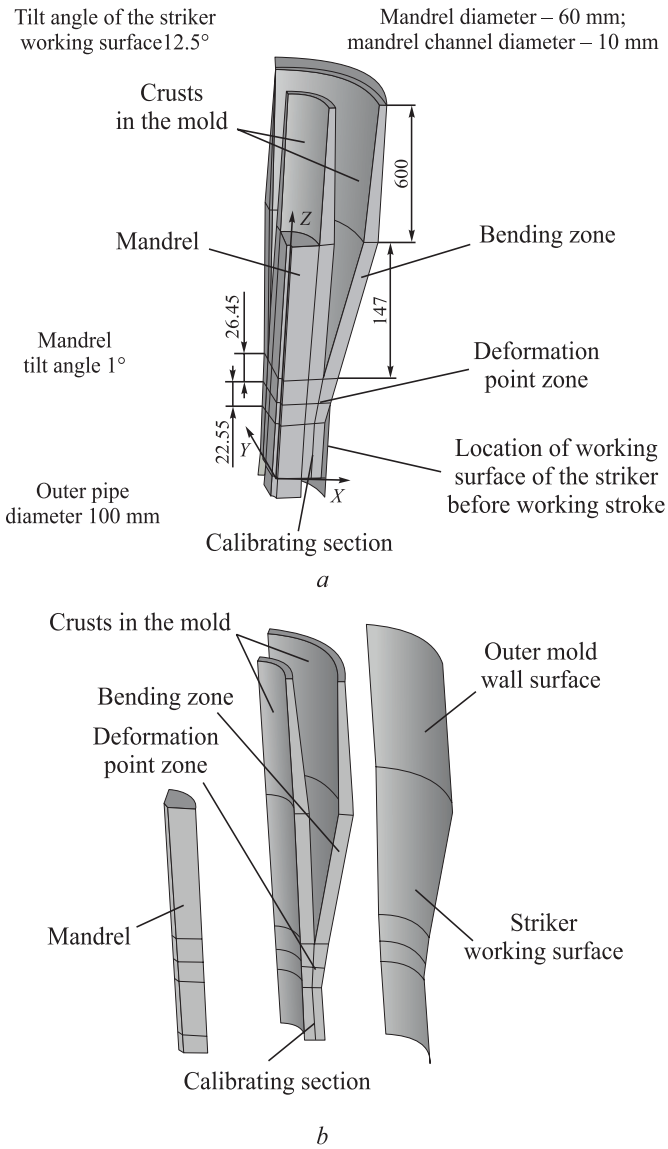

Fig. 2. Geometry of the mandrel, crusts in the mold, bending zone, roll pass, and striker:
a – general model; *b* – model elements

Рис. 2. Геометрия оправки, корочек в кристаллизаторе, зоны гибки, очага деформации и бойка:
a – общая модель; *b* – элементы модели

package [7 – 9]. Fig. 2 provides a comprehensive overview of the components of the unit of combined continuous casting and deformation, which forms the basis of the calculation model. The key dimensions are as follows: outer pipe diameter – 100 mm, mandrel diameter – 60 mm, internal mandrel channel – 10 mm, calibrating section length – 60 mm, deformation zone – 49 mm, crust thickness in the bending zone – 15 mm, and a 30 mm liquid phase situated between the crusts where ferrostatic pressure has an impact. The tilt angle of the striker working surface is 12.5°, and the mandrel tilt is 1°. The temperature of the inner surface of the pipe billet shell, specifically on the side subjected to ferrostatic pressure, is 1450 °C, while the temperature of the outer surfaces of the shells (in contact with the mandrel, mold walls, and strikers) is 1200 °C. The temperature distribution follows a logarithmic law across the thickness of the mandrel and shells. The temperature of the pipe billet as it enters the striker is assumed to be 1200 °C, and after it exits the striker, it drops to 1000 °C. The angular speed of the eccentric shafts is 40 rpm. At this speed, the contact time of the billet with the strikers during the working stroke is 0.375 s, while the idle time is 1.125 s. Both the mandrel and the striker are made from steel grade 4Kh4VMFS, while the pipe billet is composed of steel grade 09G2S. article [1] discusses the dependence of the elastic modulus and the resistance to plastic deformation on the degree, rate of deformation, and temperature for the steel under consideration. Graphs illustrating this dependence are provided for the temperature range of 1200 – 1450 °C.

To calculate the stress-strain state of the mandrel and various sections of the pipe billet while it is being compressed by the strikers moving along the eccentric shaft, a finite element model was developed [10 – 12]. This model encompasses the crusts of pipe billet inside the mold, the mold walls in contact with the crusts, the mandrel, the bending section, and the deformation and striker zones. In this context, the crusts inside the mold, the mandrel, the bending section, and the deformation zone are treated as solid bodies. The material of these components, as well as the calibrating section, is assumed to be elastoplastic. The striker and the mold walls are modeled as perfectly rigid, which simplifies the problem's dimensionality [13 – 16]. The primary dimensions of the model elements are depicted in Fig. 2. The finite element mesh utilizes SOLID185, CONTA 174, and TARGE 170 elements. The size of the finite element in the bending zone, deformation zone, and the calibrating section is set to 1 mm, while in other areas, it is 2 mm.

Four contact pairs were established to replicate the stress-strain conditions of the mandrel, the bending zone, and the deformation zone: between the mandrel and the bending and deformation zones; between the inner crust of the billet inside the mold and the mold wall; between the outer crust of the billet within the mold and the mold wall; between the bending section zone, the deformation zone, and the working surface of the striker.

To simplify the calculation due to symmetry, the analysis was performed on one quarter of the elements within the model. Consequently, kinematic boundary conditions (ensuring the absence of normal displacements) were imposed on the symmetry surfaces. The simulation involved compression of the billet by the striker, causing a 5 mm displacement of the striker along the *X*-axis, along with a simultaneous downward motion of the striker by 5 mm (displacement along the *Z*-axis).

Results and discussion

The calculation results are presented along the lines passing through specific points (Fig. 3), located in the *Y* plane at $Y = 0$.

The compression force exerted by the striker along the *X*-axis amounts to 722 MPa, along the *Y*-axis it measures 399 MPa, and the pulling force along the *Z*-axis is 42 MPa.

The calculation results are tabulated in the following table, specifying the particular values of displacements and stresses at points *1 – 15*. Since the maximum and minimum values of these parameters do not consistently correspond to points *1* and *15*, the maximum and minimum displacements and stresses along these three lines are additionally provided.

The distribution of stresses in the deformation zones along the three reference axes (*SX*, *SY*, *SZ*) is illustrated in Figure 4, depicting the compression of the billet by the striker by 5 mm while simultaneously lowering the striker by 5 mm, with the working surface of the striker oriented along the fixed radius.

The axial stress diagrams reveal that, as the strikers compress the hollow billet, the maximum compressive stress *SX* reaches –147.9 MPa on their contact surface at point *3*. Concurrently, stresses *SY* and *SZ* are significantly lower or

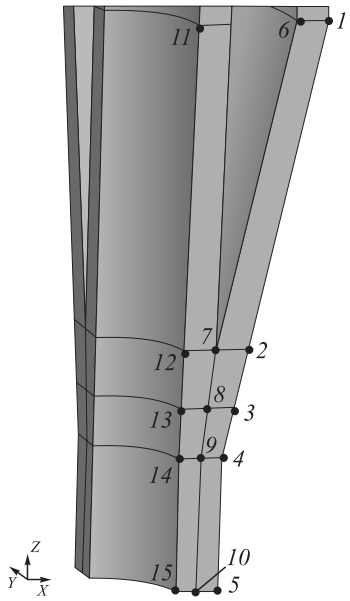

Fig. 3. Position of the points to represent the calculation results

Рис. 3. Положение точек для представления результатов расчета

Results of calculation of displacements and stresses

Результаты расчета перемещений и напряжений

Point	Displacement, mm		Stress, MPa			
	UX	*UZ*	*SX*	*SY*	*SZ*	*SXZ*
Results along the line passing through points *1 – 5*						
1	–3.2	0.8	–0.5	–32.8	–7.0	–0.5
2	–4.1	–1.1	–91.2	–42.0	–3.1	–6.8
3	–5.0	–4.8	–147.9	–102.2	–86.4	–19.8
4	–0.2	–5.2	–0.2	19.8	17.5	–0.1
5	0	–5.2	–1.7	–8.7	–0.7	0.3
Min along the line *1 – 5*	0	1.1	0.2	22.7	24.1	16.1
Max along the line *1 – 5*	–5.0	–5.2	–147.9	–102.2	–105.4	–22.9
Results along the line passing through points *6 – 10*						
6	–3.3	1.8	0.6	–3.6	11.9	3.0
7	–2.0	–0.1	–83.5	–39.9	–32.3	–6.8
8	–2.9	–3.7	–164.6	–89.0	–53.0	–4.2
9	–0.4	–5.5	–37.8	–19.4	–26.9	–17.2
10	0	–5.2	–8.8	–6.9	0.1	–0.2
Min along the line *6 – 10*	0	1.8	0.9	13.7	13.7	3.8
Max along the line *6 – 10*	–4.0	–5.5	–164.6	–89.6	–56.3	–20.9
Results along the line passing through points *11 – 15*						
11	0	0.2	0	–1.0	–7.9	–0.1
12	–0.1	0	–94.4	–68.3	–60.2	25.2
13	–0.2	–1.4	–175.5	–116.4	–102.4	–44.6
14	0	–5.2	–48.6	–16.1	–14.1	–14.5
15	0	–5.2	–15.7	–10.0	–0.1	–4.5
Min along the line *11 – 15*	0	0.6	0	10.9	1.6	25.2
Max along the line *11 – 15*	–0.2	–5.3	–179.0	–116.4	–102.4	–49.9

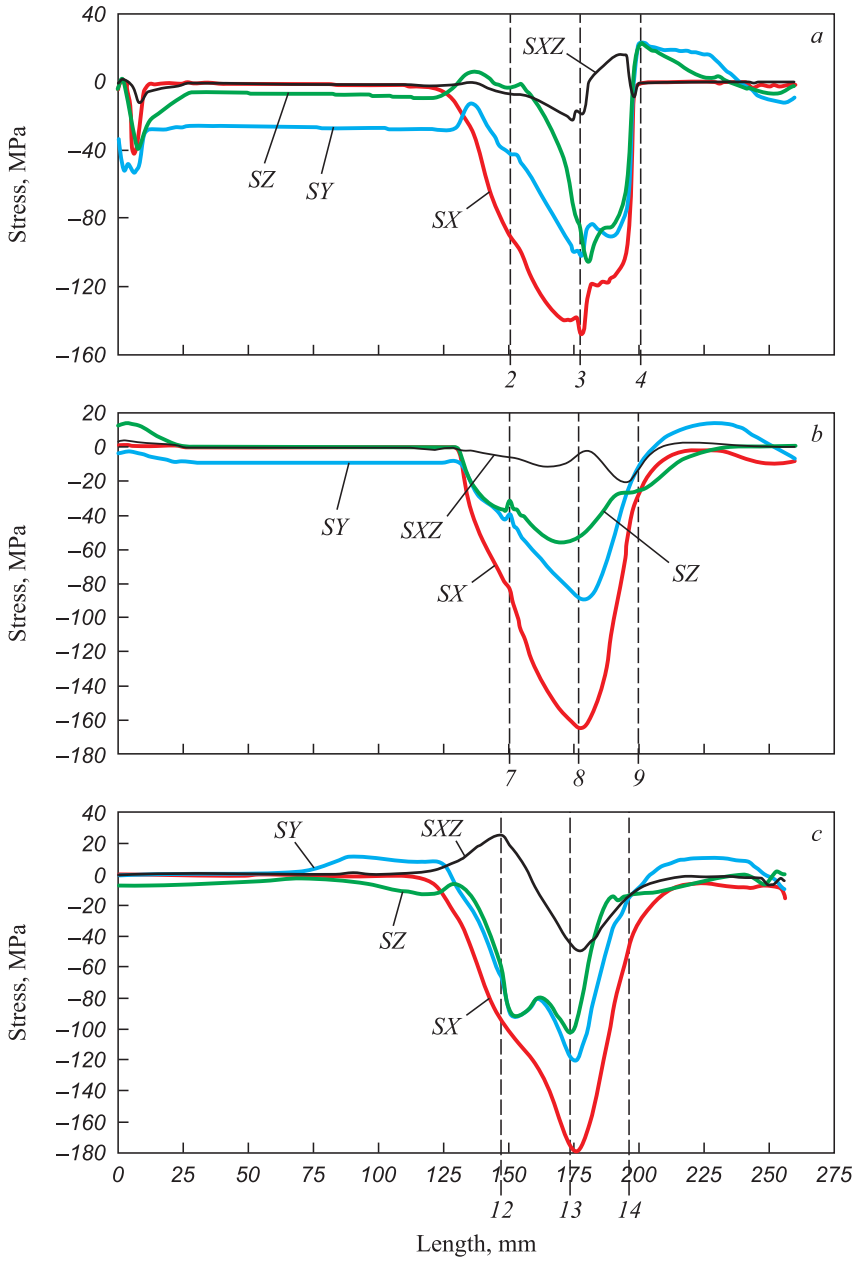

Fig. 4. Nature of stresses along the line drawn through points *1 – 5* (*a*), *6 – 10* (*b*) and *11 – 15* (*c*)

Рис. 4. Характер напряжений по линии, проведенной через точки *1 – 5* (*a*), *6 – 10* (*b*) и *11 – 15* (*c*)

equal to –102.2 and –86.4 MPa (Fig. 4). The highest shear stress, *SXZ*, at point *3* is 19.8 MPa. As we move along the line where the wall crusts of the hollow billet meet, the nature of axial stresses changes. The highest value, which is –164.6 MPa, corresponds to stress *SX* at point *8*, while stresses along the other reference axes are notably lower (Fig. 4, *b* and Table). It's worth noting that the maximum axial stresses, *SX*, *SY* and *SZ*, are observed on the contact surface of the billet with the mandrel at point *13*, with values of –179.0, –116.4 and –102.4 MPa, respectively (Fig. 4, *c*). Additionally, the maximum shear stress is also located at this point, measuring 44.6 MPa.

The results presented demonstrate that during the cyclic deformation of the hardened steel shell wall by the strikers, significant compression stresses, reaching up to –179.0 MPa, occur along all three reference axes. This indicates that the shell wall, when compressed by calibrated strikers, experiences nearly uniform compression from all directions. This is particularly significant when processing continuously cast metal to produce high-quality steel hollow billets [17 – 20].

Conclusion

The article details a new technology for producing hollow steel billets using a resource-efficient and compact unit for combined continuous casting and deformation. The study revealed distinct patterns in metal displacements

and axial stresses within the cyclic deformation zones during the production of hollow steel billets using the unit. It was observed that when the wall of a hollow billet undergoes deformation, the metal experiences uniform compression from all directions. This phenomenon greatly contributes to the production of high-quality steel pipe billets.

References / Список литературы

1. Lekhov O.S., Mikhalev A.V. *Unit of Continuous Casting and Deformation for Production of Steel Sheets and Billets*. Moscow: Vologda: Infra-Inzheneriya; 2021:304. (In Russ.).

   Лехов О.С., Михалев А.В. *Установка непрерывного литья и деформации для производства стальных листов и сортовых заготовок*. Москва: Вологда: Инфра-Инженерия; 2021:304.
2. Lekhov O.S., Guzanov B.N., Lisin I.V., Bilalov D.Kh. Investigation of the combined process of continuous casting and cyclic deformation for the production of steel sheets. *Stal'*. 2016;(1):59–62. (In Russ.).

   Лехов О.С., Гузанов Б.Н., Лисин И.В., Билалов Д.Х. Исследование совмещенного процесса непрерывной разливки и циклической деформации для получения листов из стали. *Сталь*. 2016;(1):59–62.
3. Fujii H., Ohashi T., Hiromoto T. On the formation of the internal cracks in continuously cast slabs. *Tetsu-to-Hagane*. 1978;18(8):510–518. https://doi.org/10.2355/tetsutohagane1955.62.14_1813
4. Lekhov O.S., Mikhalev A.V., Shevelev M.M. Load and strain status of CCM backups and stripe deformation at production of steel sheets for welded pipes. Report 1. *Izvestiya. Ferrous Metallurgy*. 2018;61(4):268–273. (In Russ.). https://doi.org/10.17073/0368-0797-2018-4-268-273

   Лехов О.С., Михалев А.В., Шевелев М.М. Нагруженность и напряженное состояние бойков установки непрерывного литья и деформации полосы при получении листов из стали для сварных труб. Сообщение 1. *Известия вузов. Черная металлургия*. 2018;61(4):268–273. https://doi.org/10.17073/0368-0797-2018-4-268-273
5. Sorimachi K., Emi T. Elastoplastic stress analysis of bulging as a major cause of internal cracks in continuously cast slabs. *Tetsu-to-Hagane*. 1977;63(8):1297–1304. https://doi.org/10.2355/tetsutohagane1955.63.8_1297
6. Vyunnenberg K. Production of continuously cast blanks that meet the highest quality requirements. In: *Proceedings of the Sixth Int. Congress of Iron and Steel. Vol. 3*. Moscow: Mashinostroenie; 1990:364–376. (In Russ.).

   Вюнненберг К. Производство непрерывнолитых заготовок отвечающих высшим требованиям качества. В кн.: *Труды шестого международного конгресса железа и стали. Т. 3*. Москва: Машиностроение; 1990:364–376.
7. *ANSYS. Structural Analysis Guide*. Rel. 15.0.
8. Bogatov A.A., Nukhov D.Sh., P'yankov K.P. Finite element modeling of plate rolling. *Metallurg*. 2015;(2):19–23. (In Russ.).

   Богатов А.А., Нухов Д.Ш., Пьянков К.П. Конечно-элементное моделирование процесса толстолистовой прокатки. *Металлург*. 2015;(2):19–23.
9. Takashima Y., Yanagimoto I. Finite element analysis of flange spread behavior in H-beam universal rolling. *Steel Research International*. 2011;82(10):1240–1247. https://doi.org/10.1002/srin.201100078
10. Karrech A., Seibi A. Analytical model of the expansion in of tubes under tension. *Journal of Materials Processing Technology*. 2010;210:336–362.
11. Kazakov A.L., Spevak L.F. Numeral and analytical studies of nonlinear parabolic equation with boundary conditions of a special form. *Applied Mathematical Modelling*. 2013;37(10-13): 6918–6928. https://doi.org/10.1016/j.apm.2013.02.026
12. Kobayashi S., Oh S.-I., Altan T. *Metal Forming and Finite-Element Method*. New York: Oxford University Press; 1989:377.
13. Jansson N. Optimized sparse matrix assembly in finite element solvers with one-sided communication. *High Performance Computing for Computational Science – VECPAR 2012*. Springer: Berlin, Heidelberg; 2013:128–139.
14. Matsumia T., Nakamura Y. Mathematical model of slab bulging during continuous casting. In: *Applied Mathematical and Physical Models in Iron and Steel Industry*. *Proceedings of the 3rd Process Technological Conference, Pittsburgh, Pa, 28–31 March 1982*. New York: 1982:264–270.
15. Park C.Y., Yang D.Y. A study of void crushing in large forgings: II. Estimation of bonding efficiency by finite-element analysis. *Journal of Materials Processing Technology*. 1997;72(1):32–41.
16. Efimenko L.A., Prygaev A.K. *Determination of Actual Mechanical Properties of Pipeline Metal Based on Hardness Measurement*. Moscow: Izd-vo RTU nefti i gaza; 2007:18. (In Russ.).

    Ефименко Л.А., Прыгаев А.К. *Определение фактических механических свойств металла трубопроводов на основе измерения твердости*. Москва: изд. РТУ нефти и газа; 2007:18.
17. Kudrya A.V. Critical factors of metallurgical quality of high-strength steels. In: *Perspective Materials. Vol. V*. Tol'yatti: izd. TSU; 2013:332–362. (In Russ.).

    Кудря А.В. Критические факторы металлургического качества сталей повышенной прочности. В кн.: *Перспективные материалы. Т. V*. Тольятти: изд. ТГУ; 2013: 332–362.
18. Kazakov A.A., Kiselev D.V. Modern methods for assessing the quality of materials structure based on panoramic studies with TXIXOMET image analyzer. In: *Perspective Materials. Vol. V*. Tol'yatti: izd. TSU; 2013:270–329. (In Russ.).

    Казаков А.А., Киселев Д.В. Современные методы оценки качества структуры материалов на основе панорамных исследований на основе анализатора изображений TXIXOMET. В кн.: *Перспективные материалы. Т. V*. Тольятти: изд. ТГУ; 2013:270–329.
19. Kyung-Moon L., Hu-Chul L. Grain refinement and mechanical properties of asymmetrically rolled low carbon steel. *Journal of Materials Processing Technology*. 2010;210(12):1574–1579. https://doi.org/10.1016/j.jmatprotec.2010.05.004
20. Efron L.I. *Metal Science in "Big" Metallurgy. Pipe Steels*. Moscow: Metallurgizdat; 2012:696. (In Russ.).

    Эфрон Л.И. *Металловедение в «большой» металлургии. Трубные стали*. Москва: Металлургиздат; 2012:696.

Information about the Authors

Oleg S. Lekhov, *Dr. Sci. (Eng.), Prof. of the Chair of Engineering and Vocational Training in Machinery and Metallurgy,* Russian State Professional Pedagogical University
E-mail: MXLehov38@yandex.ru

Aleksandr V. Mikhalev, *Cand. Sci. (Eng.), General Director,* JSC "Ural Pipe Plant"
E-mail: mialex@trubprom.com

Sergei O. Nepryakhin, *Cand. Sci. (Eng.), Assist. Prof. of the Chair "Metal Forming",* Ural Federal University named after the First President of Russia B.N. Yeltsin
E-mail: s.o.nepriakhin@urfu.ru

Сведения об авторах

Олег Степанович Лехов, *д.т.н., профессор кафедры инжиниринга и профессионального обучения в машиностроении и металлургии,* Российский государственный профессионально-педагогический университет
E-mail: MXLehov38@yandex.ru

Александр Викторович Михалев, *к.т.н., генеральный директор,* ОАО «Уральский трубный завод»
E-mail: mialex@trubprom.com

Сергей Олегович Непряхин, *к.т.н., доцент кафедры обработки металлов давлением,* Уральский федеральный университет имени первого Президента России Б.Н. Ельцина
E-mail: s.o.nepriakhin@urfu.ru

Contribution of the Authors

O. S. Lechov – preparation of introduction, setting the task, analysis of the calculation results.
A. V. Mikhalev – introduction, setting the task, analysis of the research results.
S. O. Nepryakhin – analysis of the calculation results.

Вклад авторов

О. С. Лехов – введение, постановка задачи, анализ результатов расчета.
А. В. Михалев – введение, постановка задачи, анализ результатов исследований.
С. О. Непряхин – анализ результатов расчета.

Received 24.04.2022
Revised 03.03.2023
Accepted 10.03.2023

Поступила в редакцию 24.04.2022
После доработки 03.03.2023
Принята к публикации 10.03.2023

Innovation in metallurgical industrial and laboratory equipment, technologies and materials
Инновации в металлургическом промышленном и лабораторном оборудовании, технологиях и материалах

UDC 621.365.5:669.187.2
DOI 10.17073/0368-0797-2023-4-492-497

Original article
Оригинальная статья

Investigation of electromagnetic furnaces with a C-shaped magnetic core

G. E. Levshin

Polzunov Altai State Technical University (46 Lenina Ave, Barnaul, Altai Territory 656038, Russian Federation)

levshing@mail.ru

Abstract. The paper describes design features, methodology and results of the study of 10 induction electromagnetic crucible furnaces with a *C*-shaped magnetic core (MC). The core is covered by turns of an electric coil (EC) of small volume up to ~14.56 dm^3. The furnaces have MC from a set of used transformer plates with a working volume of ~ 28.5 – 30.8 dm^3, a capacitor bank (CB), the number of turns w = 23 – 50 of copper or aluminum wire, voltage 380 – 390 V, frequency 50 Hz. The water-cooled EC is placed in a rubber tank and creates a horizontal electromagnetic flow with induction of ≈70 mT, which is amplified by MC and directed beyond EC into a larger working volume of ~30.7 dm^3 between its poles with induction up to ≈100 mT. When placing a steel crucible in the volume, induction increases up to 125 – 150 mT and the experimental furnace EMC-30.7-23A with a capacity of 44 kVA allows melting 21 kg of silumin at a speed of 10 °C/min in 65 min, which is faster than in the resistance furnace CAT-0.16 with a power of 40 kW in 2 h. With strong compression of MC plates, the noise decreases from 80 – 85 to 40 – 48 dB. To increase the furnace efficiency, it is proposed to use pole plates with a width of 155 mm, mineral wool in the thermal insulation of the crucible, tuning capacitors in CB, and EC from copper cable. For melting of high-temperature alloys, it is advisable to connect this furnace to a step-up transformer in order to increase the current density from 3.7 to the permissible 20 A/mm^2, power in the EC – CB circuit, and EC induction. The authors suggest to continue research on electromagnetic furnaces made from cheap transformer scrap to determine the scope.

Keywords: induction electromagnetic melting furnace, magnetic circuit, electric coil, magnetomotive force, capacitor bank, crucible

For citation: Levshin G.E. Investigation of electromagnetic furnaces with a C-shaped magnetic core. *Izvestiya. Ferrous Metallurgy*. 2023;66(4): 492–497. *https://doi.org/10.17073/0368-0797-2023-4-492-497*

Исследование электромагнитных печей с С-образным магнитопроводом

Г. Е. Левшин

Алтайский государственный технический университет им. И.И. Ползунова (Россия, 656038, Алтайский край, Барнаул, пр. Ленина, 46)

levshing@mail.ru

Аннотация. Рассмотрены особенности конструкции, методика и результаты исследования 10 индукционных электромагнитных тигельных печей с *С*-образным магнитопроводом (МПр), сердечник которого охватывают витки электрической катушки (ЭК) малого объема (примерно до 14,56 дм^3). В печи применяют наборный МПр из использованных трансформаторных пластин с рабочим объемом примерно 28,5 – 30,8 дм^3, напряжение 380 – 390 В, частоту 50 Гц, конденсаторную батарею (КБ), количество витков w = 23 – 50 медного или алюминиевого провода. Охлаждаемая водой ЭК размещена в резиновом резервуаре и создает горизонтальный электромагнитный поток с индукцией 70 мТл, который усиливается МПр и направляется за пределы ЭК в больший рабочий объем (примерно 30,7 дм^3) между его полюсами с индукцией примерно до 100 мТл. При размещении стального тигля в объеме индукция возрастает до 125 – 150 мТл и экспериментальная печь ЭМС-30,7-23А мощностью 44 кВ·А позволяет за 65 мин расплавить 21 кг силумина со скоростью 10 °С/мин. В печи сопротивления САТ-0,16 мощностью 40 кВт аналогичный процесс протекает за 2 ч. При сильном сжатии пластин МПр шум уменьшается с 80 – 85 до 40 – 48 дБ. Для повышения эффективности печи предлагается использовать полюсные пластины шириной 155 мм; минеральную вату в теплоизоляции тигля, подстроечные конденсаторы в КБ, ЭК из медного кабеля. Целесообразно для плавки высокотемпературных сплавов подключить рассматриваемую печь к повышающему напряжение трансформатору, чтобы увеличить плотность тока с 3,7 до допускаемой 20 А/мм^2, мощность в контуре ЭК – КБ, индукцию. Предлагается для определения области применения продолжить исследования электромагнитных печей, изготовленных и из дешевого трансформаторного лома.

Ключевые слова: индукционная электромагнитная плавильная печь, магнитопровод, электрическая катушка, магнитодвижущая сила, конденсаторная батарея, тигель

Для цитирования: Левшин Г.Е. Исследование электромагнитных печей с С-образным магнитопроводом. *Известия вузов. Черная металлургия*. 2023;66(4):492–497. https://doi.org/10.17073/0368-0797-2023-4-492-497

Introduction

There are two types of induction melting furnaces used in metal casting:

– a crucible inductor furnace creates a vertical electromagnetic flow and is commonly equipped with *I*-shaped outer core-type open magnetic cores (MC);

– a channel furnace (transformer) with closed MC [1; 2].

In 2013, furnaces of the third type known as crucible induction electromagnetic furnaces, with curved *O*-, *U*- and *C*-shaped magnetic cores that create a horizontal working electromagnetic flow, were patented [3; 4]. These furnaces differ significantly in design, energy consumption, and process performance capabilities compared to the first type of furnaces. A comparison between inductor furnaces and electromagnetic crucible furnaces revealed several advantages of the latter [5; 6], which were further confirmed through investigations of the parameters and technology of melting aluminum and copper alloys in a *U*-shaped magnetic core electromagnetic furnace [7; 8].

A similar investigation into the operation of a *C*-shaped MC design furnace, referred to as an EMC furnace, holds both scientific and practical significance. This EMC furnace features a horizontal open *C*-shaped MC *1* with two poles and core wrapped around by turns of an electric coil *4* (EC), incased in a protective sealed shell *6* for a cooling agent (Fig. 1, *a*). The magnetic core *1* forms the furnace shell, which can be permanently installed or equipped with a tilting mechanism. The electric coil *4* and magnetic core *1* collaborate to create intensive working flow between their facing poles, affecting the crucible *2* with its charge-containing bath *3*, suspended on trunnions *7* or installed on a base *5* (Fig. 1, *a*) [3; 4]. The operational principles of this furnace are extensively described in [5; 6].

No similar and detailed engineering solutions for induction melting crucible EMC furnaces, their operating parameters, and rational scope of application were discovered in the Google Scholar and Scopus databases [7 – 9]. Furthermore, they were not found on the websites of major induction melting furnace manufacturers[1, 2, 3, 4, 5, 6, 7, 8, 9].

The objective of this paper is to investigate the design and operating parameters of EMC furnaces when melting silumin. This investigation aims to gather essential operational data necessary for design, calculation, and determining the rational scope of application.

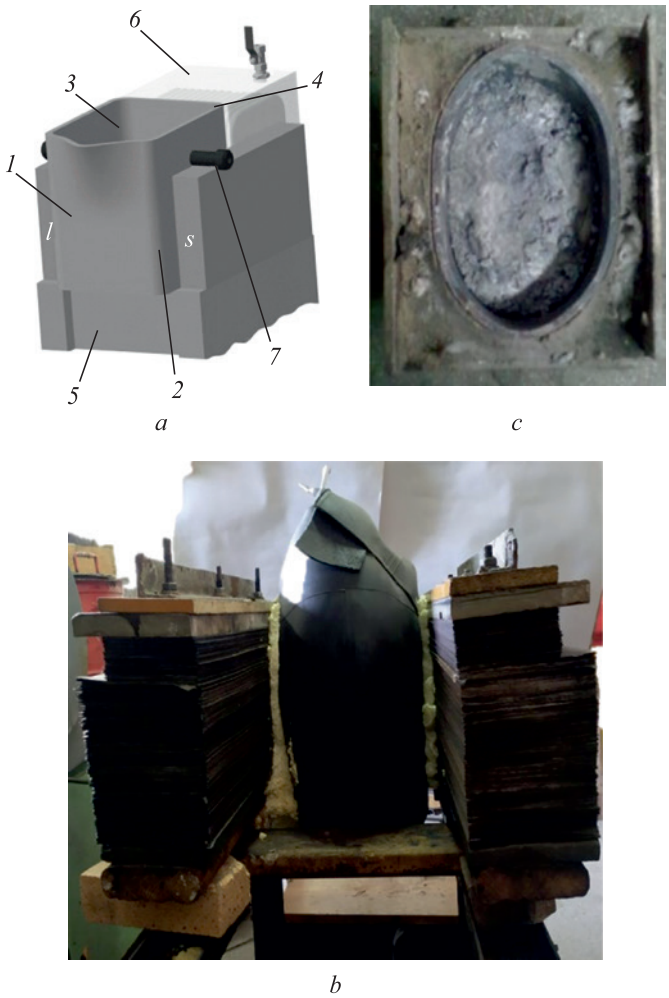

Fig. 1. Layout of electromagnetic furnace with a C-shaped magnetic core (*a*), photo of the furnace (*b*) with a flexible tank (without shell) and an oval crucible (*c*):
1 – MC; *2* – crucible; *3* – bath; *4* – EC; *5* – base; *6* – shell; *7* – trunnions

Рис. 1. Схема электромагнитной печи ЭМС (*a*), фото печи (*b*) с гибким резервуаром (без кожуха) и овального тигля (*c*):
1 – МПр; *2* – тигель; *3* – ванна; *4* – ЭК; *5* – основание; *6* – кожух; *7* – цапфы

[1] Indutherm Erwärmungsanlagen GmbH. URL: http://www.indutherm.de/ru/ (Accessed: 09.02.2023).

[2] EFD Induction GmbH. URL: http://www.efd-induction.com/ru/ (Accessed: 09.02.2023).

[3] Ajax TOCCO Magnethermic GmbH. URL: http://www.ajaxtocco.de (Accessed: 09.02.2023).

[4] РЭЛТЕК. URL: http://www.reltec.biz (Accessed: 09.02.2023).

[5] TG Indutionsanlagen GmbH. URL: http://www.itg-induktion.de (Accessed: 09.02.2023).

[6] Otto Junker GmbH. URL: http://www.otto-junker.de (Accessed: 09.02.2023).

[7] ABP Induction Systems GmbH. URL: http://www.abpinduction.com/ru/ (Accessed: 09.02.2023).

[8] ABB Process Industries GmbH Giessereien Umformwerke. URL: http://www.abb.de (Accessed: 09.02.2023).

[9] Ias Induktions Anlagen Service GmbH CO KG. URL: http://www.ias-gmbh.de (Accessed: 09.02.2023).

The tests were conducted on ten manufactured furnaces[10] (Fig. 1, *b*).

Investigation objects

The magnetic core of the furnaces is manually assembled utilizing used transformer plates with thickness of 0.35 and 0.40 mm. For pole heights h_p of approximately 195 mm, wider plates measuring 175×615 mm are employed for the core, and 155×700 mm plates are used for the pole part. In order to increase h_p to 240 mm maximize the effective volume V_e the furnaces were arranged in layers with an approximate height of 45 mm. In this configuration, plates measuring 55 mm, 90 mm or 120 mm in width are placed on the pole, while plates measuring 175 mm in width are used for the core. These plates are compressed using thick asbestos-cement and wooden spacers, belt ties, or steel studs insulated with electro-cardboard (Fig. 1, *b*). The pole length l_{work} in the range of 305 to 330 mm ($h_p/l_{work} \approx 0.79$).

The electric coil (EC) was manually wrapped around a dielectric frame using a stranded copper (C) flexible wire of the CF type with rubber insulation, having a cross-sectional area of approximately 78.5 mm^2 and 130.0 mm^2, or aluminum (A) wire with a 62 mm^2 cross-sectional area and three layers of paper insulation. The length of the EC lec measured 2.8 dm, the door section was up to 5.2 dm^2, and the cavity volume V_{ec} was up to 4.56 dm^3. The turns of the coil had either three or four bars, which were connected by a terminal at the EC outlets. To cool the EC, it was placed under running water, and a bundle of bars was inserted into a high-voltage-thermoplastic (HVT) tube to provide double electrical insulation. The EC itself was situated in a 13 dm^3 tank. The section of the cross-sectional area and the number of turns took into account the conditions required to achieve a specific induction level and allowable heating of the EC when subjected to increased current, especially at voltages exceeding 390 V. The number of turns w for the EC included options like 28M, 30M, 37M, 50A, 40A, 30A or 23A. This choice had an impact on the length of the EC, and, therefore, on the length l_w of the MC. The tank was placed inside a protective asbestos-cement shell, which also reduced the length l_p of the poles of the MC and the working volume of the furnace $V_w = h_c l_c l_w$, dm^3 (here $h_w l_w = S_w$ represents the working surface of the furnace pole).

The furnaces manufactured from transformer scrap were designed as EMC-V_p-w-M (or A):

– EMC-24.6-28M, EMS -24.6-37M,
– EMC-28.2-30M,
– EMC-28.7-23A,
– EMC-30.7-30A, EMC-30.7-40A, EMC-30.7-23A,
– EMC-30.8-28M, EMC-30.8-50A,
– EMC-35-50A.

Method of experiment

The service experience of the furnace with a *U*-shaped magnetic core was utilized [5; 6]. EMC furnaces were supplied with single-phase current I_{ec} ($f = 50$ Hz) from the industrial grid at a voltage of $U \approx 380 \div 390$ V. To explore the impact of the capacitor bank's capacity C_{CB} on furnace parameters, they were connected to the capacitor bank, and EC were connected in parallel. The C_{CB} capacity was gradually increased by connecting old capacitor banks of KC2 and KM2 type (GOST 1282 – 68) with a rated capacity of $C = 80 \div 800$ μF, with some variations in capacity. No tuning capacitors were employed to approximate current resonance in EC (I_{ec}) and CB (I_{CB}).

Steel cylindrical crucibles were used, with both round and oval sections, constructed from a heavy-wall (8 mm) tube with an outer diameter of 220 mm, along with an oxygen cylinder. These were housed within a portable asbestos-cement box featuring two types of thermal insulation: sand-clay-liquid glass mixture (Fig. 1, *c*); mineral wool combined with sheet asbestos.

The magnetomotive force (MMF) of EC $I_{ec}w$, current density *j*, powers (total $S_{ec} \approx S_{L-C}$, circulating in the *L – C*-circuit, active *P*, and inductive Q_L), total impedance *Z* and inductive reactance *x*, power factor cosφ, and electromagnetic induction L_{em} of the EMC furnace, active I_a and inductive I_L currents were all computed based on electrical measurement results, employing electrical engineering formulas [5; 6; 10].

Integral criteria for energy intensity were also calculated, including magnetic $K_m = I_{ec}w/V_w$, electromagnetic $K_{em} = I_{ec}w/(B_e V_p)$, electric heating $K_{eh} = S_{ec}/V_e$, and power supply $K_{eh} = S_{feed}/V_w$ [5; 6]. These criteria facilitate the comparison of various furnace parameters.

The temperature of a 21 kg silumin ingot AK7 was measured using a TRM-1 tool with a thermocouple XA enclosed in ceramic "beads"; temperature readings were recorded without applying scaling corrections. Temperatures of the top and bottom core surfaces of MC were measured using a multimeter M838 with thermocouples XA (without hoods). The temperature of the box walls, including the crucible and the skid, were measured using mercury thermometers.

The induction on the side and end surfaces of MC, both with and without the crucible, were measured at a distance from it and between the poles using a flat milliteslameter probe Sh1-15. Measurements were taken in three horizontal and seven vertical rows of points located 220 mm away from the ends of MC. To prevent potential damage to a Hall sensor due to rapid crucible heating, the probe was positioned up to 5 mm away from the right side of the crucible and the right pole. A DT-8851/52 tool, along with smart-

[10] S. Yu. Sergeev, D. S. Kuldyaykin, A. V. Levagin, V. V. Kondrikov, K. A. Mazko, E. S. Bayandin, A. S. Zinoviev, R. M. Gainulin, P. A. Navalikhin took part in the work under the support of Aluminum Casting Plant JSC (city of Barnaul).

phones offered reliable reading proximity, was used to measure noise level.

Experiment result and discussion

Results reflecting changes in the average values of feed currents $I_{feed} = I_{tot}$, as well as I_{ec} and I_{CB}, circulating in the EC – CB ($L - C$) circuit, depending on the capacity of C_{CB} are presented in Fig. 2. The current I_{ec} increases from 780 to 912 A, and the current I_{CB} rises to around 920 A at an approximate C_{CB} capacity of 8,134 μF (where these graphs intersect). What makes this particularly interesting is the decrease in the current Ifeed reducing from approximately 780 to 113 A at the same C_{CB} capacity. This significantly lowers the power consumed from the circuit, transitioning from $S_{ec} = I_{feed}U_{feed} = 780 \cdot 390 = 304{,}200$ W up to $S_{feed} = 113 \cdot 390 = 44{,}070$ W (approximately a sevenfold reduction). Further reduction in power consumption can be achieved through the use of tuning capacitors.

From experiments involving the heating and melting of a 21 kg silumin ingot in EMC furnaces equipped with a working volume V_w, EC, and crucibles, the most successful experience was observed in furnace EMC-30.7-23A featuring an oval crucible within a lining mix. This furnace achieved a silumin melting temperature of 650 °C within 65 min, with an average heating rate of 10 °C/min. High heating speed (14 – 19 °C/min) were maintained until the 30th min, reaching a temperature of 519 °C (Fig. 3). The heating speed decreased to 6 °C/min (reaching 560 °C), and then further to 3 °C/min. One of the reasons for this speed decrease is the heating of the box wall and increased heat loss outward. However, after the 60th min, the speed increased again to 6 °C/min due to overheating during melting.

The core of MC is heated unevenly (Fig. 3). The lower surface, measuring 175 mm in width, reaches temperatures of approximately 160 °C as the melting process concludes, while the upper surface, characterized by narrow 120 mm plates intersecting, heats up to 268 °C. The increased heating in this section of the core can be attributed to the lower specific weight of the narrow plates.

Heating of the outer walls of the box remains nearly uniform and does not exceed 170 °C (Fig. 3). This temperature can be reduced by increasing the thickness (as space allows) or by using linings made from materials with low thermal conductivity, such as lightweight chamotte, mineral wool, and others. The steel crucible "burned out", causing the melt to flow through cracks in the lining and the left wall of the box, emptying into the tank below the furnace at the end of the melting process. These cracks were formed due to recurring thermal deformations of the steel crucible, lining, and asbestos-cement walls. The top of the steel skid was heated by the leakage field to approximately 120 °C.

This heating of all elements contributed to the following performance parameters of the EMC-30.7-23A furnace (without the crucible):

– $C_{CB} \approx 8{,}134$ μF;
– $I_{ec} \approx 911$ A; $I_{CB} \approx 893$ A; $I_{feed} \approx 113$ A;
– $S_{L-C} \approx 355$ kV·A; $S_{feed} \approx 44$ kV·A; $S_{L-C}/S_{feed} = 8$;
– $j \approx 3.7$ A/mm^2;
– $Z \approx 0.428$ Ω;
– $L_{em} \approx 0.001363$ H;
– $I_{ek}w \approx 20{,}953$ A; $H_c \approx 74{,}800$ A/m;
– $B_{cm} = 94$ mT; $B_{ms} = 47$ mT; $B_{ec} = (B_{cm} + B_{ms})/2 \approx 70$ mT;
– $K_m \approx 682.5$ A/dm^3;
– $K_{em} > 6.825$ A/(dm^3·mT);
– $K_{en} > 11.6$ kV·A/dm^3; $K_{ec} > 1.43$ kV·A/dm^3.

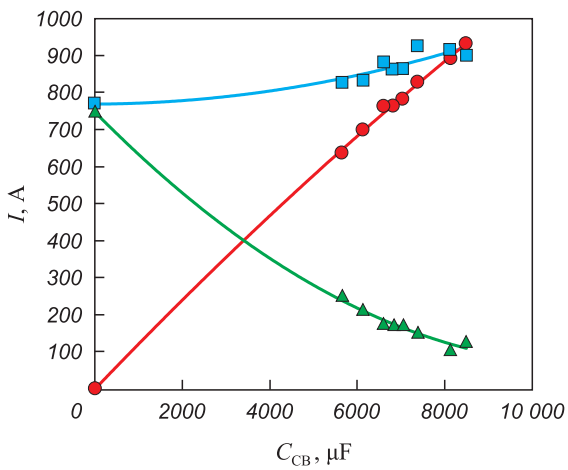

Fig. 2. Dependence of currents of $I_{current}$ (▲), I_{ec} (■) and I_{CB} (●) on capacity C_{CB} of EMS-30.7-23A furnace

Рис. 2. Зависимость токов $I_{пит}$ (▲), $I_{эк}$ (■) и $I_{кб}$ (●) от емкости $C_{кб}$ печи ЭМС-30,7-23А

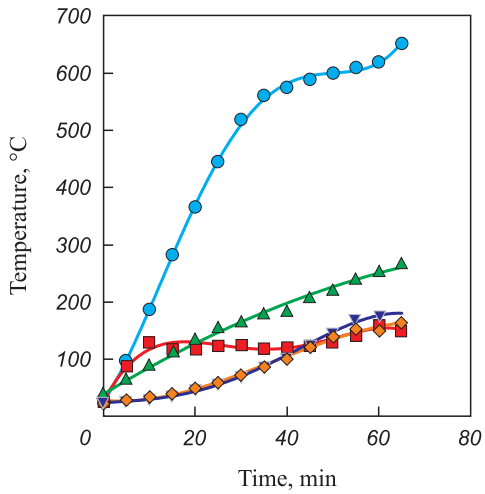

Fig. 3. Dependence of temperature of ingot and elements of EMS-30.7-23A furnace on time:
● – TRM-1; ■ – bottom of the core; ▲ – top of the core;
▼ – at the crucible on the left; ◆ – at the crucible on the right

Рис. 3. Зависимость температуры слитка и элементов печи ЭМС-30,7-23А от времени:
● – ТРМ-1; ■ – низ сердечника; ▲ – верх сердечника;
▼ – у тигля слева; ◆ – у тигля справа

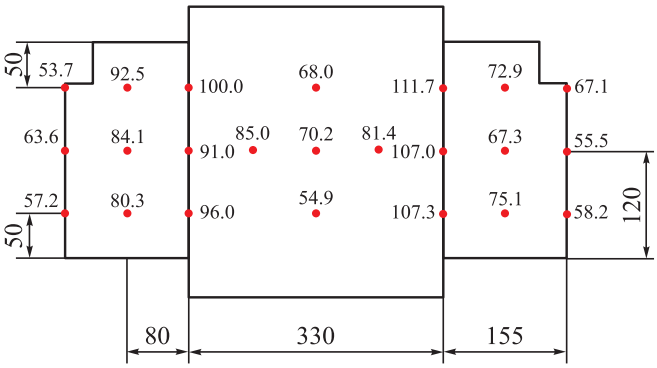

Fig. 4. Layout of points and results of induction measurement on MC surface and between its poles without crucible

Рис. 4. Схема расположения точек и результаты измерения индукции на поверхности МПр и между его полюсами без тигля

An analysis of the results of induction measurements on the surface of MC (with/without crucible) reveals the following (Fig. 4):

– expectedly increased induction B_d at the poles of the MC (91.0 – 111.2/125 – 150 mT);

– lower induction at the end faces of the MC (67.3 – – 92.5/65 – 82 mT);

– lower induction at the outer surfaces of the MC (53.7 – – 67.1/52 – 69 mT);

– the expectedly lowest induction is in the center between the poles (55 – 70 mT without crucible).

The distribution of induction Be at the middle horizontal section points (Fig. 4) between the poles without the crucible (91 – 85 – 70 – 81.4 – 107 mT) reveals that the electromagnetic field is non-uniform and exhibits a horizontal gradient of 0.6 mT/mm directed from the center of l_{work} towards the poles.

The induction B_p is approximately 100 mT at the poles of MC, which significantly limits the volume V_w to approximately 30.7 dm^3. This induction level greatly surpasses the induction in EC (B_{ek} = 70 mT), despite EC having a much smaller volume V_{ec} of approximately 14.56 dm^3. This difference in induction is due to the magnetization of MC by the EC field. The induction of the leakage field of MC decreases rapidly with distance l following the equation $B_{dis} \approx 0.00121^2 - 0.6987l + 134.88$.

When a steel crucible with a diameter of 220 mm is installed, the induction B_p at the poles and between the crucible and the poles has noticeably and expectedly increased (approximately 1.25 – 1.50 times). This can be explained by the presence of a ferromagnetic body with a diameter of 220 mm and two smaller gaps of 55 mm each within an open magnetic circuit with one larger air gap of length l_{work} = 330 mm. This configuration reduces the total magnetic resistance of the circuit and thus increases the induction at the poles. Such an increase in induction is highly beneficial when melting a ferromagnetic charge, as discussed in [11].

With the plates of MC being compressed more tightly, the noise level decreases at a distance of 600 mm from the furnace and 200 mm above EC, going from 80–85 dB (when compressed with belts) down to 40–48 dB (when compressed with pins). This signifies a substantial reduction in noise levels, decreasing from 80–85 dB to 40–48 dB with a strong compression of MC plates.

Conclusion

The experimental furnace EMC-30.7-23A, with a capacity of 44 kW, enables the melting of 21 kg of silumin at a rate of 10 °C/min in just 65 min. In contrast, a resistance furnace CAT-0.16, with a power of 40 kW, requires 120 min to achieve the same result (at a rate of 5.4 °C/min).

To further improve the efficiency of heating and the operation of the furnace, it is advisable to increase the h_p/l_{work} ratio from 0.79 to 1.0, broaden the pole plates to 155 mm, and incorporate mineral wool in the thermal insulation of the crucible. Additionally, tuning capacitors in CB and EC made from copper wire can be used.

Magnetizing the MC with a weak field at an induction level of B_{ec} = 70 mT in EC, having a relatively small volume V_{ec} of approximately 14.56 dm^3, allows the field to be safely shifted beyond the limits of EC. This results in a notable increase in the induction B_p by around 100 mT within a significantly larger volume V_p (approximately 30.7 dm^3). This reduction in EC size and electricity consumption, coupled with enhanced reliability, positively impacts the EC and overall furnace performance.

For testing the melting of copper alloys and cast iron, it is advisable to connect the furnace to a step-up transformer, which will increase the current density from 3.7 A/mm^2 to the allowable 20 A/mm^2. This increase significantly boosts the currents I_{ec}, I_{CB}, power S_{L-C}, MMF $I_{ec}w$, induction (B_{ec} and B_p), and enhances criteria such as K_{em}, K_{en}, K_{ec}.

Building upon these successful experiences, it becomes feasible to create small-sized EMC furnaces from cost-effective transformer scrap. Further investigations can then be conducted to improve the parameters and determine their range of application, including heating charges, melting various types of alloys, holding and finishing molten materials, and facilitating the transfer of the crucible for casting purposes, among other applications.

References / Список литературы

1. Sakharevich A.N. Induction crucible furnaces. Design features, operation. *Lit'e i metallurgiya*. 2012;(3):242–245. (In Russ.).

   Сахаревич А.Н. Индукционные тигельные печи. Конструктивные отличия, эксплуатация. *Литье и металлургия*. 2012;(3):242–245.

2. Malyarov A.I. *Foundry Furnaces*. Moscow: Mashinostroenie; 2014:256. (In Russ.).

   Маляров А.И. *Печи литейных цехов*. Москва: Машиностроение; 2014:256.

3. Levshin G.E., Sergeev S.Yu. *Electromagnetic crucible melting furnace with C-shaped magnetic core and horizontal magnetic flux*. Pat. RF 2536311. *Byulleten' izobretenii*. 2014. (In Russ.).

Пат. 2536311 РФ. *Электромагнитная тигельная плавильная печь с С-образным магнитопроводом и горизонтальным магнитным потоком* / Левшин Г.Е., Сергеев С.Ю.; заявл. 12.03.2013; опубл. 20.12.2014.

4. Levshin G.E. Comparison of induction furnaces with vertical and horizontal electromagnetic flux. *Metallurgiya mashinostroeniya*. 2015;(5):2–6. (In Russ.).

Левшин Г.Е. Сравнение индукционных печей с вертикальным и горизонтальным электромагнитным потоком. *Металлургия машиностроения*. 2015;(5):2–6.

5. Levshin G.E. Parameters of electromagnetic induction furnace with U-shaped magnetic core. *Metallurgiya mashinostroeniya*. 2017;(2):11–16. (In Russ.).

Левшин Г.Е. О параметрах электромагнитной индукционной печи с U-образным магнитопроводом. *Металлургия машиностроения*. 2017;(2):11–16.

6. Levshin G.E. Electrotechnology of smelting in an electromagnetic furnace with U-shaped magnetic circuit. *Elektrotekhnika*. 2018;(5):73–76. (In Russ.).

Левшин Г.Е. Электротехнология плавки в электромагнитной печи с U-образным магнитопроводом. *Электротехника*. 2018;(5):73–76.

7. Kachanov A.N., Kachanov N.A., Korenkov D.A. Classification and field of application of low-temperature induction heating systems with the opened magnetic conductors. *Vestnik MEI*. 2016;(2):36–40. (In Russ.).

Качанов А.Н., Качанов Н.А., Коренков Д.А. Классификация и область применения систем низкотемпературного индукционного нагрева с разомкнутыми магнитопроводами. *Вестник МЭИ*. 2016;(2):36–40.

8. Rudnev V., Loveless D., Cook R.L. *Handbook of Induction Heating*. New York: CRC Press; 2017:772. https://doi.org/10.1201/9781315117485

9. Lupi S. *Fundamentals of Electroheat*. Switzerland: Springer Int. Publ.; 2017:1–55.

10. Marchenko A.L., Opadchii Yu.F. *Electrotechnics and Electronics. Vol. 1*. Moscow: Infra-M; 2015:574. (In Russ.).

Марченко А.Л., Опадчий Ю.Ф. *Электротехника и электроника. Т. 1. Электротехника*. Москва: Инфра-М; 2015:574.

11. Levshin G.E. Magnetisation of ferromagnetic charge at induction heating. *Izvestiya. Ferrous Metallurgy*. 2022;65(2):85–91. (In Russ.). https://doi.org/10.17073/0368-0797-2022-2-85-91

Левшин Г.Е. Намагничивание ферромагнитной шихты при индукционном нагреве. *Известия вузов. Черная металлургия*. 2022;65(2):85–91. https://doi.org/10.17073/0368-0797-2022-2-85-91

Information about the Author

Gennadii E. Levshin, *Dr. Sci. (Eng.), Prof. of the Chair of Engineering Technology and Equipment,* Polzunov Altai State Technical University
E-mail: levshing@mail.ru

Сведения об авторе

Геннадий Егорович Левшин, *д.т.н., профессор кафедры машиностроительной технологии и оборудования,* Алтайский государственный технический университет им. И.И. Ползунова
E-mail: levshing@mail.ru

Received 30.08.2022
Revised 20.12.2022
Accepted 09.02.2023

Поступила в редакцию 30.08.2022
После доработки 20.12.2022
Принята к публикации 09.02.2023

Economic efficiency of metallurgical production / Экономическая эффективность металлургического производства

UDC 338.2
DOI 10.17073/0368-0797-2023-4-498-507

Original article
Оригинальная статья

Institutionalization of ESG-principles at the international level and in the Russian Federation, their impact on ferrous metallurgy enterprises. Part 2

O. V. Glushakova, O. P. Chernikova

Siberian State Industrial University (42 Kirova Str., Novokuznetsk, Kemerovo Region – Kuzbass 654007, Russian Federation)

chernikovaop@yandex.ru

Abstract. Currently, a new development trend is being formed in the world associated with the decarbonization of economies. This process is based on the institutionalization of ESG-principles – an approach to doing business, characterized by the involvement of companies in solving environmental, social and governance problems. The process of institutionalization of ESG-principles at the international level was initiated in 1948 with the adoption of the Universal Declaration of Human Rights under the auspices of the UN. The active involvement of Russia in the formation of the institutional framework in the field of ESG has begun only in 2020. The reason for this was the ratification of a number of international documents, as well as the active promotion of climate policy by many countries of the world. The stages of the institutionalization process at the international level discussed in detail in Report 1. The decarbonization of economies creates development risks for industries whose products are characterized by high carbon and energy intensity. Ferrous metallurgy also belongs to them. This report presents the results of a study of the effectiveness of measures taken by the Russian Government in the field of reducing atmospheric air pollution in large industrial centers of the ferrous metallurgy based on data from the Unified Information System for Monitoring Air Quality, as well as the results of an analysis of the ESG-practices of the largest Russian ferrous enterprises and compliance with carbon intensity and energy intensity of their products according to the criteria of sustainable (including green) development projects established in our country. As a result of the study, it was found that despite the use of ESG-principles in their activities, the specific emissions of CO_2-equivalent of the largest iron and steel enterprises significantly exceed the criteria for sustainable (including green) development projects established by the Russian Government.

Keywords: institutionalization, ESG-principles, carbon intensity, energy intensity, ferrous metallurgy, ferrous metallurgy products

For citation: Glushakova O.V., Chernikova O.P. Institutionalization of ESG-principles at the international level and in the Russian Federation, their impact on the activities of ferrous metallurgy enterprises. Part 2. *Izvestiya. Ferrous Metallurgy*. 2023;66(4):498–507.
https://doi.org/10.17073/0368-0797-2023-4-498-507

Институализация ESG-принципов на международном уровне и в Российской Федерации, их влияние на деятельность предприятий черной металлургии. Часть 2

О. В. Глушакова, О. П. Черникова

Сибирский государственный индустриальный университет (Россия, 654007, Кемеровская обл. – Кузбасс, Новокузнецк, ул. Кирова, 42)

chernikovaop@yandex.ru

Аннотация. В настоящее время в мире формируется новый тренд, связанный с декарбонизацией экономик. В его основе – принципиально новый подход к ведению предпринимательской деятельности с учетом соблюдения принципов ESG (*Environmental – Social – Governance*), характеризующийся вовлеченностью компаний в решение экологических, социальных и управленческих проблем. Начало процессу институциализации ESG-принципов на международном уровне было положено в 1948 г. с принятием Всеобщей декларации прав человека под эгидой ООН. Активное включение России в формирование институциональных рамок в области ESG произошло только в 2020 г. Основанием для этого послужила ратификация ряда международных документов, а также активное продвижение многими странами мира климатической политики. Подробно этапы процесса институциализации ESG-принципов

на международном уровне и в России рассмотрены ранее. Декарбонизация экономик формирует риски развития для отраслей, продукция которых характеризуется высокой углеродоемкостью и энергоемкостью (например, черная металлургия). В работе представлены результаты исследования эффективности принятых Правительством РФ мер в области снижения уровня загрязнения атмосферного воздуха в крупных промышленных центрах черной металлургии на основе данных Единой информационной системы мониторинга качества атмосферного воздуха, а также результаты анализа ESG-практик крупнейших российских предприятий черной металлургии и соответствия углеродоемкости и энергоемкости выпускаемой ими продукции установленным в России критериям проектов устойчивого (в том числе «зеленого») развития. В результате исследования установлено, что, несмотря на использование ESG-принципов в своей деятельности, удельные выбросы CO_2-эквивалента крупнейших предприятий черной металлургии значительно превышают установленные Правительством РФ значения критериев проектов устойчивого (в том числе «зеленого») развития.

Ключевые слова: институциализация, ESG-принципы, углеродоемкость, энергоемкость, черная металлургия, продукция черной металлургии

Для цитирования: Глушакова О.В., Черникова О.П. Институализация ESG-принципов на международном уровне и в Российской Федерации, их влияние на деятельность предприятий черной металлургии. Часть 2. *Известия вузов. Черная металлургия*. 2023;66(4):498–507. *https://doi.org/10.17073/0368-0797-2023-4-498-507*

Introduction

Since 2020, Russia has been actively developing its institutional framework in the field of ESG. In addition to ratifying international documents such as the UN Framework Convention on Climate Change (1992), the Kyoto Protocol (1997), and the Paris Climate Agreement (2015), this initiative is driven by the global trend of many countries actively advocating for climate policies aimed at mitigating greenhouse gas emissions.

One of the objectives outlined in the Strategy for the Development of Russia's Ferrous Metallurgy for the period 2014 – 2020 and the prospective plan until 2030 [1] is to diminish the adverse environmental impact of the industry's enterprises. This involves reducing emissions of harmful substances into the atmosphere, minimizing pollution discharges, and advancing climate protection through mechanisms that enhance the energy efficiency of metallurgical production, consequently reducing the carbon footprint.

Russian and international scholars are currently directing their attention towards investigating the environmental impact of ferrous metallurgy enterprises. The study presented in [2] delves into the analysis of air pollutant emissions from ferrous metallurgy enterprises, considering the influence of external factors. In [3], there is a discussion on the influence of contemporary environmental initiatives on the international trade of ferrous metallurgy products. Notably, [4 – 6] provide evidence that China's metallurgical industry has the potential to transition to low-carbon production, thereby reducing carbon oxide (CO_2) emissions into the atmosphere. These papers also affirm the effectiveness of novel taxation instruments in achieving this goal. Papers [7; 8] disclose issues related to the management of sustainable development within metallurgical enterprises, while work [9] specifically examines the environmental challenges associated with the development of ferrous metallurgy in the European North of Russia. The current trends in the development of ferrous metallurgy and efforts to enhance its energy and environmental efficiency are comprehensively analyzed in [10]. The research presented in [11] delves into technologies aimed at optimizing the recycling of waste generated by ferrous metallurgy. Paper [12] addresses the challenges associated with energy efficiency and environmental management within the ferrous metallurgy sector. The outcomes of studies[1, 2] focused on decarbonization of economies, including the utilization of carbon emission trading, are discussed. Furthermore, the effectiveness of carbon tax in reducing carbon oxide (CO_2) emissions into the atmosphere is explored in studies[3, 4, 5, 6, 7]. Additionally, the impact of the volume of carbon oxide (CO_2) emissions on companies' P/E ratio is investigated in study[8].

---

[1] Ellerman A.D., Jacoby H.D., Decaux A. The Effects on Developing Countries of the Kyoto Protocol and Carbon Dioxide Emissions Trading (December 1998). https://ssrn.com/abstract=569250 (Accessed: 15.03.2022).

[2] Milunovich G., Stegman A., Cotton D. Review of Carbon Trading Theory and Practice. https://ssrn.com/abstract=989271 or http://dx.doi.org/10.2139/ssrn.989271. (Accessed: 15.03.2022).

[3] Felix P. Does a Carbon Tax Reduce CO_2 Emissions? Evidence From British Columbia. https://ssrn.com/abstract=3329512 or http://dx.doi.org/10.2139/ssrn.3329512. (Accessed: 15.03.2022).

[4] Rivers N., Schaufele B. Salience of Carbon Taxes in the Gasoline Market (October 22, 2014). https://ssrn.com/abstract=2131468 or http://dx.doi.org/10.2139/ssrn.2131468 (Accessed: 15.03.2022).

[5] Elliott J., Foster I., Kortum S.S., Khun J. G., Munson T.,Weisbach D. Unilateral Carbon Taxes, Border Tax Adjustments, and Carbon Leakage (February 27, 2012). University of Chicago Institute for Law & Economics Olin Research Paper No. 600, https://ssrn.com/abstract=2072696 or http://dx.doi.org/10.2139/ssrn.2072696 (Accessed: 15.03.2022).

[6] Metcalf G.E., Weisbach D.A. Design of a Carbon Tax (January 8, 2009). U of Chicago Law & Economics, Olin Working Paper No. 447, U of Chicago, Public Law Working Paper No. 254, https://ssrn.com/abstract=1324854 or http://dx.doi.org/10.2139/ssrn.1324854 (Accessed: 15.03.2022).

[7] Hsu Shi-Ling. Nine Reasons to Adopt a Carbon Tax (May 17, 2009). https://ssrn.com/abstract=1405944 or http://dx.doi.org/10.2139/ssrn.1405944 (Accessed: 15.03.2022).

[8] Bolton P., Kacperczyk M.T. Do Investors Care about Carbon Risk? (October 30, 2020). Columbia Business School Research Paper Forthcoming, Journal of Financial Economics (JFE), Forthcoming. European Corporate Governance Institute – Finance Working Paper 711/2020. https://ssrn.com/abstract=3398441 or http://dx.doi.org/10.2139/ssrn.3398441 (Accessed: 15.03.2022).

Materials and methods

This study employs both chronological and institutional approaches, allowing for a coherent examination of the evolution of the ESG institutional framework on both international and Russian levels. Throughout the research, we scrutinized the content of international documents adopted under the auspices of the UN and other international organizations, which reflect the development of ESG-principles. Additionally, we analyzed Russian legislation in the field of ESG. The investigation relied on methods such as analysis, synthesis, comparison, and grouping. We examined climate, ecological, corporate social responsibility, and sustainability reports from major Russian ferrous metallurgy enterprises, ESG rankings, official statistical reports published by the Federal State Statistics Service, and the Enerdata statistical yearbook.

Results and discussion

Russia is currently conducting an experiment on setting quotas for emissions of atmospheric pollutants involving the implementation of emission quotas for atmospheric pollutants in 12 major urban industrial areas designated as cities with high and very high levels of atmospheric air pollution. A comprehensive system of compensatory measures has been developed, focusing on the reduction of negative environmental impacts. These measures include the renovation, technical re-equipment, and remodeling of facilities.

In 2020, Russia launched the Unified Information System for Monitoring (UISM) atmospheric air quality [13]. Over the ensuing period, statistics on the initial monitoring results have been accumulated [14]. The air quality is actively monitored in twelve cities across the Russian Federation, such as Cherepovets, Novokuznetsk, Lipetsk, Chelyabinsk, Nizhniy Tagil, Magnitogorsk, and others, where major ferrous metallurgy enterprises are operational. Monitoring is conducted in real-time through Roshydromet observation posts situated in close proximity to major metallurgical facilities, including Cherepovets Steel Mill, United West Siberian Metallurgical Plant, Novolipetsk Steel, Nizhniy Tagil Iron and Steel Works, Chelyabinsk Metallurgical Plant, and Magnitogorsk Iron and Steel Works – recognized as primary sources of pollution. In Cherepovets, Novokuznetsk, and Lipetsk, both average daily and average monthly Standards Index (SI) values for atmospheric air pollution are recorded during monitoring, while in Chelyabinsk, only the SI average daily value is registered. The monitoring of air quality includes the assessment of the average daily concentration of various pollutants such as suspended solids, sulfur oxide (SO_2), carbon oxide, nitrogen oxides (NO and NO_2), ozone, hydrogen sulfide, ammonia, and particles of 1, 2, 5, and 10 microns in size. As of now, the UISM does not record the average daily concentration of carbon oxide (CO_2). During the survey period (January – March 2022), data on air quality in Nizhniy Tagil and Magnitogorsk were unavailable due to ongoing technical works on the websites. The measurement results are interpreted based on the SI values, where a range from 0 to 1 indicates low atmospheric air pollution, 2 to 4 signifies pollution higher than normal, 5 to 10 indicates high pollution, and values above 10 represent very high pollution levels. Table 1 provides the interpretation of the average monthly SI values for atmospheric air pollution in Cherepovets, Novokuznetsk, and Lipetsk for the years 2020 – 2021.

In 2020, an average monthly SI value for atmospheric air pollution in Chelyabinsk was not recorded. The average monthly SI values for atmospheric air pollution in Chelyabinsk in 2021 are presented in Table 2.

The analysis of the obtained results leads to the conclusion that the primary focus in improving the environmental well-being of major industrial centers is the technical upgrading and remodeling of metallurgical enterprises. Despite the ongoing experiment involving the setting of quotas for harmful emissions and the implementation of compensatory measures, there are still instances of high, very high, and higher-than-normal SI values for atmospheric air pollution. In 2021, Cherepovets recorded an average monthly SI value corresponding to very high and high pollution levels for 7 out of 12 months. Novokuznetsk experienced this for 4 months out of 12, while Lipetsk recorded such values for 6 months out of 12. Additionally, Chelyabinsk had higher-than-normal average daily SI values from June to December 2021, with recurrence rates ranging from 1 to 19 days per month. In July, August, and October 2021, the values were high, occurring 1 to 2 days per month, and in August and October, they were very high, occurring once per month.

It is evident that the existing financial mechanisms, such as the state program of the Russian Federation "Environmental Protection," inclusive of the national project "Ecology" and the federal project "Clean Air," will likely fall short of adequately addressing the identified problem. Consequently, Russia is presently in the process of establishing an institutional framework designed to enhance the motivation of economic entities to incorporate ESG principles into their operations. Additionally, this framework aims to provide incentives for investors, including institutional investors, to make responsible investment decisions.

Given the current realities and the potential introduction of transboundary carbon regulation mechanisms, it becomes evident that carbon-intensive industries, including ferrous metallurgy, must genuinely adopt environmentally friendly practices rather than merely express-

Table 1

Interpretation of the average monthly SI values of atmospheric air pollution

Таблица 1. **Сведения об интерпретации среднемесячных значений СИ загрязнения атмосферного воздуха**

Month	Cherepovets (Cherepovets Steel Mill of PJSC Severstal)	Novokuznetsk (EVRAZ United West Siberian Metallurgical Plant)	Lipetsk (PJSC Novolipetsk Steel)
Interpretation of the average monthly SI value of atmospheric air pollution in 2020			
January	n/a	n/a	n/a
February	n/a	High	n/a
March	Very high	Higher-than-normal	Very high
April	Higher-than-normal	Higher-than-normal	Higher-than-normal
May	High	Low	Higher-than-normal
June	Low	Low	High
July	Low	Low	Very high
August	Higher-than-normal	Low	Low
September	High	Low	Higher-than-normal
October	Low	High	Higher-than-normal
November	High	Higher-than-normal	n/a
December	n/a	Very high	n/a
Interpretation of the average monthly SI value of atmospheric air pollution in 2021			
January	n/a	Higher-than-normal	n/a
February	Higher-than-normal	Very high	n/a
March	Higher-than-normal	Higher-than-normal	High
April	Low	Higher-than-normal	Very high
May	Very high	High	Very high
June	Very high	Low	Very high
July	Very high	Low	High
August	Very high	Higher-than-normal	Higher-than-normal
September	Very high	Higher-than-normal	n/a
October	High	Higher-than-normal	Higher-than-normal
November	High	Very high	Very high
December	Higher-than-normal	High	Low

Table 2

Data on the average daily SI values of atmospheric air pollution in Chelyabinsk[9]

Таблица 2. **Сведения о среднесуточных значениях СИ загрязнения атмосферного воздуха в городе Челябинск**[9]

Month (2021)	Number of days per month in which the atmospheric air pollution corresponded to the respective SI scale value			
	Low	Higher-than-normal	High	Very high
January	n/a	n/a	n/a	n/a
February	28	–	–	–
March	31	–	–	–
April	30	–	–	–
May	31	–	–	–
June	17	13	–	–
July	15	15	1	–
August	9	19	2	1
September	–	15	–	–
October	22	6	2	1
November	29	1	–	–
December	29	2		

ing commitment in words. Ongoing applied research is exploring the use of hydrogen in cast iron and steel production. However, experts indicate that the time frame for the initiation of the first pilot projects in this domain spans from three to five years, with the adaptation of this technology for full-scale production expected to require a considerably longer duration[10].

Analysis of ESG-practices of the major metallurgical companies in Russia

PJSC Severstal (Cherepovets Steel Mill, Cherepovets)

The company's official website features a dedicated "Sustainable Development" section providing insights into its strategy with short-, medium-, and long-term targets for reducing greenhouse gas emissions:

1. Abating greenhouse gas emissions by 3 % per 1 ton of liquid steel by the end of 2023, compared to 2020 (projected to be 2001 tons of CO_2 equivalent per ton of steel in 2023).

[9] Unified information system for monitoring atmospheric air quality. URL: http://www.feerc.ru/uisem/portal/ (Accessed: 20.03.2022).

[10] By 2023, Novatek and Severstal are to launch a joint hydrogen project. URL: https://www.vedomosti.ru/business/articles/2021/06/03/872835-novatek-severstal (Accessed: 20.03.2022).

2. Reducing greenhouse gas emissions per 1 ton of liquid steel by 10 % by the end of 2030 compared to the 2020 baseline.

3. A long-term goal is currently under development, with plans to present the concept in 2022. These objectives align with the criteria for sustainable (including green) development in the Russian Federation and the requirements for the verification system of the projects for sustainable (including green) development in the Russian Federation, as outlined in the Decree of the Government of the Russian Federation No. 1587 of 21.09.2021.

4. Reducing air pollutant emissions by 13 % by 2025 compared to the 2020 baseline.

5. Main energy saving objective: achieve an energy intensity of 5.55 Gcal/t of steel produced by 2026 through the implementation of an energy-saving program.

According to the website, the company is considering According to the company's website, PJSC Severstal is actively considering scenarios for implementing climate policies. These scenarios include:

1. SSP126 scenario: Aligned with the Paris Agreement, anticipating a global average temperature increase of +1.8 °C by 2100).

2. SSP245 scenario: An intermediate scenario projecting a temperature increase of +2.8 °C by 2100;

3. SSP585 scenario: The worst-case scenario, envisioning a temperature increase of +4.4 °C by 2100. It's noteworthy that achieving the long-term goal outlined in these scenarios is uncertain and beyond the control of current climate policy stakeholders, including signatories of the Paris Agreement, given the extremely distant time horizon.

The company has published an updated climate report for the year 2021, available on its official website[11], continuing a tradition of regularly releasing sustainability reports since 2010[12]. PJSC Severstal has established an in-house climate-related risks and energy management system. The company's climate memorandum, outlining five principles of its climate policy, is accessible on its website[13].

Severstal has developed an occupational health and safety strategy[14].

[11] PJSC Severstal's 2021 Climate Report. URL: https://www.severstal.com/contant-static/file/82493/Climate-report-rus.pdf (Accessed: 16.03.2022).

[12] PJSC Severstal's 2010 – 2020 Sustainability Reports. URL: https://www.severstal.com/rus/sustainable-development/documents/reports (Accessed: 18.03.2022).

[13] PJSC Severstal's Climate Memorandum. URL: https://www.severstal.com/rus/sustainable-development/climate/ (Accessed 30.03.2022).

[14] Updated PJSC Severstal's strategy on occupational health and safety (January 2022). URL: https://www.severstal.com/contant-static/file/82240/Severstal_HSE_Strategy_update_RU.pdf (Accessed: 17.03.2022).

EVRAZ United West Siberian Metallurgical Plant, Novokuznetsk

EVRAZ Nizhniy Tagil Iron and Steel Works, Nizhniy Tagil

EVRAZ has established five-year environmental targets spanning from 2018 to 2022. One of these targets is to reduce greenhouse gas emissions to below 2.0 tons of CO_2-equivalent per 1 ton of steel by 2022.

In alignment with global efforts to address climate change, EVRAZ has set an additional target to decrease the energy intensity of steel production by 15 % by 2025, using the 2018 baseline as a reference point, aiming for 24.23 GJ per 1 ton of steel.

EVRAZ Group outlines various scenarios for the implementation of its climate policy, including:

1. RCP 2.6 scenario: The most innovative and low-carbon trajectory, illustrating global efforts to limit emissions and restrict the temperature rise to 0.4 – 1.6 °C by 2100.

2. RCP 4.5 scenario: This scenario aligns closely with the Paris Agreement, implying a temperature increase from 1.1 to 2.6 °C by 2100.

3. RCP 8.5 scenario: Considered a business-as-usual scenario, it represents the most intensive use of fossil fuels with minimal actions to combat climate change. This scenario projects an average global temperature increase of 2.6 – 4.8 °C by 2100.

In October 2020, EVRAZ published its first Climate Change Report[15], signaling the company's commitment to addressing climate-related risks. The company has established a comprehensive energy management system, and sustainability reports have been regularly published since 2018. Reports for the years 2018 – 2020 are currently accessible on the EVRAZ Group's public website[16].

PJSC Novolipetsk Steel, Lipetsk

PJSC Novolipetsk Steel in Lipetsk has established a medium-term goal to reduce greenhouse gas emissions to 1.84 tons of CO_2-equivalent per 1 ton of steel by 2023, as reported by public sources.

Despite this goal, the official reports available on the company's website do not provide detailed scenarios

[15] EVRAZ Climate Change Report. URL: https://www.evraz.com/ru/sustainability/data-center/climate-change-reports/ (Accessed: 17.03.2022).

[16] EVRAZ 2018 – 2020 Sustainability Reports. URL: https://www.evraz.com/ru/sustainability/data-center/sustainability-reports/ (Accessed: 17.03.2022).

outlining the implementation of Novolipetsk Steel's climate policy.

The company has not made a separate climate report available on its official website. Instead, information related to the mid-term strategic goal of its climate policy until 2023, as well as results achieved in abating greenhouse gas emissions, can be found in the 2019 "Ecology" Report.

PJSC Novolipetsk Steel announces the implementation of an integrated system addressing climate-related risks and energy management. While the company's website includes the Environmental Protection Report for the year 2019, there is an absence of a more recent report[17]. Corporate Social Responsibility Reports have been published on the official website since 2009. The reports "On Environmental Activities" have been accessible on the official website since 2013, with the first report "On Sustainable Development" presented in 2015, and the first "Ecology" Report posted in 2016[18].

MECHEL (Chelyabinsk Metallurgical Plant, Chelyabinsk)

As per the information available on the official website, there is a stated objective to achieve a 17 % reduction in the intensity of greenhouse gas and pollutant emissions into the atmospheric air at the Chelyabinsk production site by 2025. However, the baseline period for this reduction target is not specified.

The official website of the MECHEL Group does not provide any detailed information on the implementation scenarios of the company's climate policy, and it lacks climate reports. Additionally, there is no indication of whether the company has established a climate-related risks and energy management system.

While the MECHEL Group's official website contains general documents regarding environmental policy and energy efficiency, it does not offer specific environmental protection reports[19], ecological reports, or integrated reports as of now.

PJSC Magnitogorsk Iron and Steel Works, Magnitogorsk

The enterprise's website includes a "Sustainable Development" section, outlining a target to reduce the intensity of greenhouse gas emissions into the atmospheric air by 20 % by 2025 compared to the 2018 baseline, aiming for 1.8 tons of CO_2-equivalent per ton of steel. The specified criterion for achieving this goal is defined as reducing the comprehensive air pollution index to 5.0 units by 2025.

The 2019 Sustainability Report[20] and the 2020 Integrated Annual Report[21] do not provide information on the implementation of the company's climate policy. Although these documents declare the mid-term strategic goal of the climate policy until 2025 and highlight achievements in greenhouse gas emission reduction, a dedicated climate report as a separate document is currently not accessible on the official website of PJSC Magnitogorsk Iron and Steel Works.

Open data analysis

The analysis of the official websites of the major Russian cast iron and steel producers reveals that most of these companies align with the principles of sustainable development and engage in monitoring greenhouse gas emissions and energy intensity of their products, as shown in Table 3. However, MECHEL stands out as an exception, as its official website lacks GRI climate or other relevant reports. Similarly, these reports are not available on the official website of the Russian Union of Industrialists and Entrepreneurs. It remains unclear whether MECHEL does not assess the carbon and energy intensity of its products or does not disclose this information to all stakeholders.

Despite the integration of ESG-principles into their activities, the specific emissions of major ferrous metallurgy enterprises in 2020 ranged from 1.90 to 2.18 tons of CO_2-equivalent per 1 ton of steel (Table 3).

These figures are significantly higher than the criteria established by the Decree of the Government of the Russian Federation No. 1587 of 21.09.2021. According to these criteria, the carbon intensity of carbon steel should be less than 0.283 tons of CO_2-equivalent per 1 ton of products, and that of high-alloy steel should be less than 0.352 ton of CO_2-equivalent per 1 ton of products. This implies that the actual emissions of CO_2-equivalent are 5 to 8 times higher than the values set by the sustainable development project criteria established by the Decree of the Government of the Russian Federation No. 1587 of 21.09.2021.

RAEX analytical agency provided information on ESG ranking as of 15.03.2022 for 160 Russian compa-

[17] The 2019 Environmental Protection Report of PJSC Novolipetsk Steel. URL: https://nlmk.com/upload/iblock/8d4/NLMK_ecology_22.04.pdf (Accessed: 18.03.2022).

[18] PJSC Novolipetsk Steel Corporate Social Responsibility Reports; PJSC Novolipetsk Steel Sustainability Reports; PJSC Novolipetsk Steel "Ecology" Report. URL: https://nlmk.com/ru/ir/results/csr-reports/ (Accessed: 18.03.2022).

[19] MECHEL official website. URL: https://www.mechel.ru/development/environmental/ (Accessed: 18.03.2022).

[20] Sustainability Report of PJSC Magnitogorsk Iron and Steel Works. URL: https://mmk.ru/ru/sustainability/social-responsibility/ (Accessed: 18.03.2022).

[21] The 2020 Integrated Annual Report of PJSC Magnitogorsk Iron and Steel Works. URL: https://mmk.ru/ru/investor/results-and-reports/sustainability-reports/ (Accessed: 18.03.2022).

Table 3

Analysis of greenhouse gas emissions and energy intensity of steel production of the largest Russian metallurgical enterprises[12–21]

Таблица 3. **Анализ выбросов парниковых газов и энергоемкости производства стали крупнейшими металлургическими предприятиями России[12–21]**

Enterprise	Environmental costs, RUB bn			Volume of greenhouse gas emissions, mln tons of CO_2 e				Specific emissions, t of CO_2-equivalent per 1 t of steel*****					Energy intensity of steel production, GJ/t of cast steel		
	2018	2019	2020	2017	2018	2019	2020	2017	2018	2019	2020	2021	2018	2019	2020
PJSC Severstal (Cherepovets Steel Mill, Cherepovets)	3.4	3.8	5.6	27.53	27.77	28.11	27.86	2.097	2.056	2.084	2.063	2.093	24.08****	24.45****	24.7****
EVRAZ (EVRAZ United West Siberian Metallurgical Plant, Novokuznetsk; EVRAZ Nizhniy Tagil Iron and Steel Works, Nizhniy Tagil)	59.9**	59.1**	89.8**	36.68	34.56	39.06	н/д	2.02	2.01	1.97	1.970	n/a	28.50	27.50	25.6
PJSC Novolipetsk Steel	175.0**	202.0**	n/a	33.60	34.20	32.00	н/д	1.95	1.92	1.92	1.900	n/a	22.88****	23.60****	n/a
MECHEL (Chelyabinsk Metallurgical Plant, Izhstal, Urals Stampings Plant, Vyartsilya Metal Products Plant, Bratsk Ferroalloy Plant)	n/a	n/a	n/a	n/a	n/a	n/a	n/a	n/a	n/a	n/a	n/a	n/a	n/a	n/a	n/a
PJSC Magnitogorsk Iron and Steel Works	8.9	8.7	7.2	31.07	29.49	27.49	25.20***	2.40	2.25	2.13	2.180	n/a	25.40	26.08	21.9

N o t e s . ** – environmental costs for EVRAZ and PJSC Novolipetsk Steel are presented in mln USD;

*** – the 2020 Integrated Report of PJSC Magnitogorsk Iron and Steel Works presents the predicted value of greenhouse gas emissions for 2020;

**** – Severstal›s 2020 Sustainability Report provides data on the energy intensity of producing 1 ton of steel in Gcal (data on energy intensity of cast iron and steel in similar units are presented by PJSC Novolipetsk Steel in the 2019 “Ecology” Report); to ensure comparability of data on energy intensity of steel at other Russian metallurgical enterprises, the authors of the article converted the energy intensity of producing 1 ton of steel into GJ;

***** – according to the criteria of the projects for sustainable (including green) development in the Russian Federation and the requirements for the verification system of the projects for sustainable (including green) development in the Russian Federation approved by the Decree of the Government of the Russian Federation No. 1587 of 21.09.2021, the carbon intensity of carbon steel should be less than 0.283 t of CO_2-equivalent per 1 t of products, and that of high-alloy steel should be less than 0.352 t of CO_2-equivalent per 1 t of products; in 2017, the global average level of specific emissions from the production of 1 ton of steel amounted to 2.3 t of CO_2 e/t; in 2018, this value was 2.29 t of CO_2 e/t; in 2019 – 2.31 t of CO_2 e/t; and in 2020 – 2.33 t of CO_2 e/t.

Table 4

Position of the largest Russian metallurgical enterprises in the ESG-ranking dated 03/15/2022[22]

Таблица 4. **Позиция крупнейших российских металлургических предприятий России в ESG-рэнкинге от 15.03.2022 г.**[22]

Enterprise	Rating position in the area			Total ranking
	"Environment" (*E*)	"Social sphere" (*S*)	"Corporate Governance" (*G*)	
PJSC Novolipetsk Steel	4	14	9	4
PJSC Severstal	9	5	32	9
EVRAZ	24	17	25	21
PJSC Magnitogorsk Iron and Steel Works	31	19	14	22
MECHEL	158	132	93	122

nies. The positions of steelmaking leaders in the ESG ranking are presented in Table 4.

As per Clause 1 of Article 31.1 of Federal Law No. 7-FZ dated 10.01.2002 (as amended on 30.12.2021) "On Environmental Protection," entities and individuals engaged in economic or other activities at Category *I* facilities are mandated to apply for an Integrated Environmental Permit. Concurrently, in accordance with Clause 12 of Article 31.1 of the aforementioned law, entities and individuals engaged in economic or other activities at Category *II* facilities are eligible to obtain an Integrated Environmental Permit, provided they possess Best Available Techniques (BAT) Reference Documents.

In April 2018, the Ministry of Natural Resources and Ecology of the Russian Federation sanctioned a list of 300 deemed detrimental to the environment falling under Category *I*, contributing no less than 60 % to the total pollutant emissions in the Russian Federation (commonly known as the "List 300") [15]. This list encompasses major ferrous metallurgy industrial sites, including Cherepovets Industrial Site, EVRAZ United West Siberian Metallurgical Plant, Magnitogorsk Industrial Site-1 and Magnitogorsk Industrial Site-2, Chelyabinsk Metallurgical Plant, and JSC Karelskiy Okatysh Industrial Site. In compliance with Clause 6 of Article 11 of Federal Law No. 219-FZ dated 21.07.2014, "On Amendments to the Federal Law 'On Environmental Protection' and certain legislative acts of the Russian Federation," Category *I* facilities included in the "List 300" were obligated to apply to Rosprirodnadzor for an Integrated Environmental Permit between 01.01.2019 and 31.12.2022. Regrettably, during the period from 2019 to 2021, none of Russia's metallurgical companies obtained Integrated Environmental Permits (ESG-IEPs)[23].

We are currently witnessing global transformations as countries worldwide transition towards a low-carbon economy. Experts from the Task Force on Climate-related Financial Disclosures (TCFD) emphasize that addressing the challenges of climate change may necessitate significant innovations in the political, legal, technological, and market domains. While acknowledging the humane concept of sustainable development, focused on reducing carbon footprint and preserving Earth's biodiversity, it is crucial to recognize that, in the context of the 2022 global geopolitical crisis and considering economic sanctions imposed against Russia by most countries, the promotion of ESG-principles, particularly their environmental aspect, is perceived as a tool of political and economic pressure. Notably, the content of the Glasgow Climate Pact is significant. This document advocates for the reduction of coal power and the discontinuation of "inefficient subsidies" for fossil fuels.

Russia stands as one of the major exporters of ferrous metallurgy products, with key destinations including Turkey, Taiwan, the USA, Italy, Mexico, Belgium, the Netherlands, Germany, Spain, South Korea, among others [16]. In light of the global commitment to ESG-principles and climate policies by most nations, compliance with these principles is essential. Simultaneously, the world has not yet identified a suitable substitute for metallurgical industry products, which find extensive applications in construction, engineering, shipbuilding, medicine, IT, and various other fields.

Conclusions

The analysis of average monthly SI values for atmospheric air pollution in Cherepovets, Novokuznetsk, and Lipetsk from 2020 to 2021, along with the average daily SI values in Chelyabinsk for 2021, reveals persistent high, very high, and higher-then-normal levels of atmos-

[22] ESG-Рэнкинг российских компаний (от 15.03.2022). https://raex-rr.com/ESG/ESG_companies/ESG_rating_companies/2022.3/ (Accessed: 18.03.2022).

[23] Перечень объектов негативного воздействия на окружающую среду, на которые выданы комплексные экологические разрешения. Официальный сайт Росприроднадзора. URL: https://rpn.gov.ru/opendata/7703381225-objectker (Accessed: 10.03.2022).

pheric air pollution despite the implementation of quotas for harmful emissions and compensatory measures. Our examination of the official websites of major metallurgical companies in Russia, including PJSC Severstal, EVRAZ, PJSC Novolipetsk Steel, PJSC Magnitogorsk Iron and Steel Works, and MECHEL, focused on determining their adherence ESG-principles. It is evident that PJSC Severstal and EVRAZ are actively engaging with ESG-principles. Both companies publish sustainability and climate reports on their official websites, addressing climate policy scenarios and monitoring the carbon and energy intensity of their products. Furthermore, the climate reports of PJSC Severstal and EVRAZ outline short-, medium-, and, in the case of PJSC Severstal, long-term targets for reducing greenhouse gas emissions intensity into the atmosphere. PJSC Novolipetsk Steel has made available its Environmental Protection Report and Corporate Social Responsibility Reports on its official website. Similarly, PJSC Magnitogorsk Iron and Steel Works has published the Sustainability Report and the Integrated Annual Report. There are no climate reports available, and the goals for reducing greenhouse gas intensity are exclusively formulated for the medium term. MECHEL's website lacks environmental protection, ecological, climate, or integrated reports, and the mid-term objective for reducing greenhouse gas emissions lacks a specific baseline period reference. In 2020, major ferrous metallurgy enterprises exceeded the specific emissions of CO_2-equivalent per ton of products by 5 to 8 times the values stipulated by the sustainable development project criteria outlined in the Decree of the Government of the Russian Federation No. 1587 dated 21.09.2021. None of the aforementioned metallurgical companies obtained Integrated Environmental Permits (ESG-IEPs) from 2019 to 2021. Considering the emerging global trend towards decarbonizing economies, reducing carbon and energy intensity in products becomes imperative for enhancing the competitiveness of domestic ferrous metallurgy enterprises in the global market and ensuring sustainable development for the Russian economy. To promote ESG-principles in Russia, it is essential for the government to implement measures supporting research on low-carbon technologies, especially in ferrous metallurgy. Institutional investors should also actively participate in the implementation of ESG-principles to contribute to the overall sustainability of industries.

References / Список литературы

1. *On approval of the Strategy for the development of the Russian ferrous metallurgy for 2014-2020 and for the period until 2030 and the Strategy for the development of the non-ferrous metallurgy of Russia for 2014-2020 and for the period until 2030: Order of the Ministry of Industry and Trade of Russia dated 05.05.2014 No. 839.* https://www.garant.ru/products/ipo/prime/doc/70595824/ (Accsessed 14.04.2022).(In Russ.).

   Об утверждении Стратегии развития черной металлургии России на 2014 – 2020 гг. и на перспективу до 2030 г. и Стратегии развития цветной металлургии России на 2014 – 2020 гг. и на перспективу до 2030 года: Приказ Минпромторга России от 05.05.2014 № 839. https://www.garant.ru/products/ipo/prime/doc/70595824/ (Дата обращения 14.04.2022).

2. Ryabkov I.L., Yashalova N.N. The influence of external factors on ferrous metallurgy enterprises activity. *Baikal Research Journal*. 2020;11(3):6. (In Russ.). https://doi.org/10.17150/2411-6262.2020.11(3).6

   Рябков И.Л., Яшалова Н.Н. Влияние внешних факторов на деятельность предприятий черной металлургии. *Baikal Research Journal*. 2020;11(3):6. https://doi.org/10.17150/2411-6262.2020.11(3).6

3. Shteinberg E.E. Impact of modern environmental initiatives on international trade in ferrous metal products. *Russian foreign economic bulletin*. 2021;(1):121-128. (In Russ.). https://doi.org/10.24412/2072-8042-2021-1-121-128

   Штейнберг Е.Е. Влияние современных экологических инициатив на международную торговлю продукцией черной металлургии. *Российский внешнеэкономический вестник*. 2021;(1):121–128. https://doi.org/10.24412/2072-8042-2021-1-121-128

4. Lin B., Xu M. Good subsidies or bad subsidies? Evidence from low-carbon transition in China's metallurgical industry. *Energy Economics*. 2019;83:52–60. https://doi.org/10.1016/j.eneco.2019.06.015

5. Lin B., Xu M. Exploring the green total factor productivity of China's metallurgical industry under carbon tax: A perspective on factor substitution. *Journal of Cleaner Production*. 2019;233:1322–1333. https://doi.org/10.1016/j.jclepro.2019.06.137

6. Du Z., Lin B. Analysis of carbon emissions reduction of China's metallurgical industry. *Journal of Cleaner Production*. 2018;176:1177–1184. https://doi.org/10.1016/j.jclepro.2017.11.178

7. Stalinskaya E.V., Okhten' A.A. The conceptual framework for strategic management of a metallurgical enterprise's sustainable development. *Ekonomika promyshlennosti*. 2012;(1-2(57-58)):353–360. (In Russ.).

   Сталинская Е.В., Охтень А.А. Концептуальные основы стратегического управления устойчивым развитием металлургического предприятия. *Экономика промышленности*. 2012;(1-2(57-58)):353–360.

8. Amosova Yu.E., Matveeva M.A. Ecologically cleaner production as an element of sustainable development of metallurgical enterprises. *Bulletin of the South Ural State University. Series: Metallurgy*. 2019;19(1):43–49. (In Russ.).

   Амосова Ю.Е., Матвеева М.А. Экологически чистое производство как элемент устойчивого развития металлургических предприятий. *Вестник Южно-уральского государственного университета. Серия: Металлургия*. 2019;19(1):43–49.

9. Samarina V.P. Ferrous metallurgy of the European North of Russia: economic, ecological and information-communication development problems. *Sever i rynok: formirovanie ehkonomicheskogo poryadka*. 2016;(2(49)):77–84.

   Самарина В.П. Черная металлургия европейского севера России: экономические, экологические и информационно-

коммуникационные проблемы развития. *Север и рынок: формирование экономического порядка*. 2016;(2(49)):77–84.

10. Podgorodetskii G.S., Shul'ts L.A. Modern directions of development and improvement of energy and ecological efficiency of the steel industry. *Ecology and Industry of Russia*. 2016;20(4):46–52. (In Russ.). https://doi.org/10.18412/1816-0395-2016-4-46-52

Подгородецкий Г.С., Шульц Л.А. Современные направления развития и повышения энерго-экологической эффективности черной металлургии. *Экология и промышленность России*. 2016;20(4):46–52. https://doi.org/10.18412/1816-0395-2016-4-46-52

11. Khansman T., Fontana P., Chiappero A., Bot I., Rot D.L. Technologies for optimal recycling of ferrous metallurgy waste. *Chernye metally*. 2008;(10):32–37.

Хансман Т., Фонтана П., Чиапперо А., Бот И., Рот Д.Л. Технологии оптимального рециклинга отходов черной металлургии. *Черные металлы*. 2008;(10):32–37.

12. Genda Zh.T., Ioksh M., Shtil' G., Endeman G. Energy efficiency and environmental management in ferrous metallurgy. *Chernye metally*. 2011;(2):41-50.

Генда Ж.Т., Йокш М., Штиль Г., Эндеман Г. Энергетическая эффективность и природоохранный менеджмент в черной металлургии. *Черные металлы*. 2011;(2):41–50.

13. *On the creation and operation of the federal state information system for monitoring atmospheric air quality in the urban districts of Bratsk, Krasnoyarsk, Lipetsk, Magnitogorsk, Mednogorsk, Nizhny Tagil, Novokuznetsk, Norilsk, Omsk, Chelyabinsk, Cherepovets and Chita: Decree of the Government of the Russian Federation of December 24, 2019 no. 1806.* https://base.garant.ru/73361359/ (Accessed 14.04.2022). (In Russ.).

О создании и эксплуатации федеральной государственной информационной системы мониторинга качества атмосферного воздуха в городских округах Братск, Красноярск, Липецк, Магнитогорск, Медногорск, Нижний Тагил, Новокузнецк, Норильск, Омск, Челябинск, Череповец и Чита: Постановление Правительства РФ от 24.12.2019 № 1806. https://base.garant.ru/73361359/ (Дата обращения 14.04.2022).

14. *List of instructions for the implementation of the Message of the President to the Federal Assembly: approved by the President of the Russian Federation on February 27, 2019, no. 294.* https://docs.cntd.ru/document/553820169 (Accessed 14.04.2022). (In Russ.).

Перечень поручений по реализации Послания Президента Федеральному Собранию: утв. Президентом РФ 27.02.2019 № Пр-294. https://docs.cntd.ru/document/553820169 (Дата обращения 14.04.2022).

15. *On approval of the list of objects with a negative impact on the environment, belonging to category I, whose contribution to total emissions, discharges of pollutants in the Russian Federation is at least 60 percent: Order of the Ministry of Natural Resources and Ecology of the Russian Federation dated 18.04. 2018 No. 154.* https://www.consultant.ru/document/cons_doc_LAW_301627/ (Accsessed 14.04.2022). (In Russ.).

Об утверждении перечня объектов, оказывающих негативное воздействие на окружающую среду, относящихся к I категории, вклад которых в суммарные выбросы, сбросы загрязняющих веществ в Российской Федерации составляет не менее чем 60 процентов: Приказ Министерства природных ресурсов и экологии РФ от 18.04. 2018 г. № 154. https://www.consultant.ru/document/cons_doc_LAW_301627/ (Дата обращения 14.04.2022).

16. Chernobrovin V.P. Ferrous metallurgy of Russia in dynamics (1970–2018). *Bulletin of the South Ural State University. Series: Metallurgy*. 2020;20(1):7–17. (In Russ).

Чернобровин В.П. Черная металлургия России в динамике (1970–2018 гг.). *Вестник Южно-Уральского государственного университета. Серия: Металлургия*. 2020;20(1):7–17.

Information about the Authors

Ol'ga V. Glushakova, *dDr. Sci. (Economics), Assist. Prof., Prof. of the Chair of Economics, Accounting and Finance,* Siberian State Industrial University
ORCID: 0000-0002-9268-415X
E-mail: trinity@ktk.company

Oksana P. Chernikova, *Cand. Sci. (Economics), Assist. Prof., Head of the Chair of Economics, Accounting and Finance,* Siberian State Industrial University
ORCID: 0000-0002-5410-6623
E-mail: chernikovaop@yandex.ru

Сведения об авторах

Ольга Владимировна Глушакова, *д.э.н., доцент, профессор кафедры экономики, учета и финансов,* Сибирский государственный индустриальный университет
ORCID: 0000-0002-9268-415X
E-mail: trinity@ktk.company

Оксана Петровна Черникова, *к.э.н., доцент, заведующий кафедрой экономики, учета и финансов,* Сибирский государственный индустриальный университет
ORCID: 0000-0002-5410-6623
E-mail: chernikovaop@yandex.ru

Contribution of the Authors

O. V. Glushakova – formation of the concept, analysis of the results, writing the text.
O. P. Chernikova – literature review, writing the text.

Вклад авторов

О. В. Глушакова – формирование концепции работы, анализ результатов, написание статьи.
О. П. Черникова – обзор литературы, написание статьи.

Received 14.01.2022
Revised 16.05.2022
Accepted 18.05.2022

Поступила в редакцию 14.04.2022
После доработки 16.05.2022
Принята к публикации 18.05.2022

Над номером работали:

Л.И. Леонтьев, *главный редактор*

Е.В. Протопопов, *заместитель главного редактора*

Е.А. Ивани, *заместитель главного редактора*

Л.П. Бащенко, *заместитель ответственного секретаря*

Е.Ю. Потапова, *заместитель главного редактора по развитию*

О.А. Долицкая, *научный редактор*

Е.М. Запольская, *ведущий редактор*

А.О. Гашникова, *ведущий редактор*

В.В. Расенець, *верстка, иллюстрации*

Г.Ю. Острогорская, *менеджер по работе с клиентами*

Подписано в печать 25.08.2023. Формат 60×90 $^{1}/_{8}$. Бум. офсетная № 1.
Печать цифровая. Усл. печ. л. 15,0. Заказ 17955. Цена свободная.

Отпечатано в типографии Издательского Дома МИСИС.
119049, Москва, Ленинский пр-кт, д. 4, стр. 1.
Тел./факс: (499) 236-76-17

Зарегистрирован Федеральной службой по надзору в сфере связи, информационных технологий и массовых коммуникаций. Свидетельство о регистрации ПИ № ФС77-35456.

Подписной индекс 70383.